Гордана Јаковљевић

Мултидимензионални модел коришћења података даљинске детекције и геопросторних сервиса у управљању водним ресурсима сагласно INSPIRE и ОДВ спецификацијама

ДОКТОРСКА ДИСЕРТАЦИЈА

Multidimensional model of use remote sensing data and geospatial services in water management according to INSPIRE and WFD specification

Ph.D. THESIS

Нови Сад, 2020

УНИВЕРЗИТЕТ У НОВОМ САДУ ● ФАКУЛТЕТ ТЕХНИЧКИХ НАУКА
21000 НОВИ САД, Трг Доситеја Обрадовића 6

КЉУЧНА ДОКУМЕНТАЦИЈСКА ИНФОРМАЦИЈА

Редни број, **РБР**:	
Идентификациони број, **ИБР**:	ДО 03/2016
Тип документације, **ТД**:	Монографска публикација
Тип записа, **ТЗ**:	Текстуални штампани материјал
Врста рада, **ВР**:	Докторска дисертација
Аутор, **АУ**:	Гордана Јаковљевић
Ментор, **МН**:	Проф. др Миро Говедарица
Наслов рада, **НР**:	Мултидимензионални модел коришћења података даљинске детекције и геопросторних сервиса у управљању водним ресурсима сагласно INSPIRE и ОДВ спецификацијама
Језик публикације, **ЈП**:	Енглески
Језик извода, **ЈИ**:	Српски/енглески
Земља публиковања, **ЗП**:	Република Србија
Уже географско подручје, **УГП**:	АП Војводина, Нови Сад
Година, **ГО**:	2020.
Издавач, **ИЗ**:	Ауторски репринт
Место и адреса, **МА**:	Факултет техничких наука, 21 000 Нови Сад, Трг Доситеја Обрадовића 6
Физички опис рада, **ФО**: (поглавља/страна/ цитата/табела/слика/графика/прилога)	5/170/441/30/48/-/4
Научна област, **НО**:	Геодетско инжењерство
Научна дисциплина, **НД**:	Геоинформатика, даљинска детекција
Предметна одредница/Кључне речи, **ПО**:	Даљинска детекција, вјештачка интелигенција, процесирање у облаку, мониторинг водних ресурс
УДК	
Чува се, **ЧУ**:	Библиотека Факултета техничких наука у Новом Саду
Важна напомена, **ВН**:	
Извод, **ИЗ**:	У оквиру ове докторске дисертације испитивана је могућност употребе различитих технологија даљинске детекције у управљању водним ресурсима у складу са ОДВ и INSPIRE спецификацијама. Развијен је мултидимензионални модел који се састоји од аутоматизованих процедура обраде примарно базираних на алгоритмима вјештачке интелигенције. На овај начин омогућена је обрада и дистрибуцију података у релном или блиско реалном времену. Централно мјесто у моделу чини посматрање водног ресурса као геопросторног објекта са геометријским, тополошким и атрибутивним карактеристикама. Резултујуће информације могу бити коришћене у имплентацији ОДВ.
Датум прихватања теме, **ДП**:	
Датум одбране, **ДО**:	

Чланови комисије, **КО**:		
	Председник:	др Александар Ристић, редовни професор
	Члан:	др Флор Алварез Табоада, ванредни професор
	Члан:	др Драган Стојановић, редовни професор
	Члан:	др Срђан Колаковић, редовни професор
	Члан:	др Душан Јовановић, доцент
	Члан, ментор:	др Миро Говедарица, редовни професор

Потпис ментора

Accession number, **ANO**:	
Identification number, **INO**:	DO 03/2016
Document type, **DT**:	Monographic publication
Type of record, **TR**:	Textual printed document
Contents code, **CC**:	Ph.D. thesis
Author, **AU**:	Gordana Jakovljević, M.Sc.
Mentor, **MN**:	Prof. Miro Govedarica, Ph.D.
Title, **TI**:	Multidimensional model of use remote sensing data and geospatial services in water management according to INSPIRE and WFD specification
Language of text, **LT**:	English
Language of abstract, **LA**:	Serbian/English
Country of publication, **CP**:	Republic of Serbia
Locality of publication, **LP**:	AP Vojvodina, Novi Sad
Publication year, **PY**:	2020.
Publisher, **PB**:	Author's reprint
Publication place, **PP**:	Faculty of Technical Sciences, 21 000 Novi Sad, Trg Dositeja Obradovića
Physical description, **PD**: (chapters/pages/ref./tables/pictures/graphs/appendixes)	5/170/441/30/48/-/4
Scientific field, **SF**:	Geodetic engineering
Scientific discipline, **SD**:	Geoinformatics, Remote sensing
Subject/Key words, **S**/**KW**:	Remote sensing, artificial intelligence, cloud processing, water resource management
UC	
Holding data, **HD**:	The Library of Faculty of Technical Sciences, Novi Sad, Serbia
Note, **N**:	
Abstract, **AB**:	Within the framework of the presented Ph.D., the usability of different remote sensing technologies in water management, according to INSPIRE and WFD specification, was studied. A multidimensional model has been developed consisting of automated processing procedures which are primarily based on artificial intelligence algorithms. In this way, it is possible to process and distribute data in real or near real-time. The central place in the model represnets the observation of the water resource as a geospatial object with geometric, topological and attributive characteristics. The resulting information can be used in WFD implementation.
Accepted by the Scientific Board on, **ASB**:	
Defended on, **DE**:	

Within the framework of the presented Ph.D., the usability of different remote sensing technologies in water management, according to INSPIRE and WFD specification, was studied. A multidimensional model has been developed consisting of automated processing procedures which are primarily based on artificial intelligence algorithms. In this way, it is possible to process and distribute data in real or near real-time. The central place in the model represnets the observation of the water resource as a geospatial object with geometric, topological and attributive characteristics. The resulting information can be used in WFD implementation.

Defended Board, **DB**:			
	President:	Aleksandat Ristić, Ph.D. Full Professor	
	Member:	Flor Alvarez-Taboada, Ph.D. Associate Professor	
	Member:	Dragan Stojanović, Ph.D. Full Professor	Menthor's sign
	Member:	Prof Srđan Kolaković, Ph.D. Full Professor	
	Member:	Prof Dušan Jovanović, Ph.D. Assistant Professor	
	Member, Mentor:	Prof Miro Govedarica, Ph.D. Full Professor	

Acknowledgment

Abstract

Water is vital for the life of humans, animals, plants, and functioning of ecosystems. Human health, food security, economic growth, and energy production are all water-dependent. Growing population and urbanization, intensive industrial development, agriculture, increasing demand, and misuse of water have increased water stress, making water a scarce and expensive resource, especially in undeveloped countries. Water bodies are among most sensitive ecological environments. The comprehensive and efficient monitoring of water quality and quaninty need be established in order to understand currant status, polluters and to prevent feature dergradation of aquatic systems.

In this study, multidimensional model of use remote sensing data and geospatial services in water resourse management according to WFD and INSPIRE directive was proposed. The developed multidimensional model represents the integrated approach covering all phases from acquisition to distribution of data, by providing clearly defined methodologies for automatic extraction of water body geometry, topology, and attributes and state-of-the-art accuracy comparing with studies with similar environment complexity. The model is based on modern IT and geospatial technologies, including cloud storage, cloud computing, AI, and big data. In this way, it is possible to process, distribute, and use data acquired by remote sensing technologies in real-time or near real-time, which represents a significant step forward in processing concepts.

The implementation framework based on Google Colab, Python, and Jupyter enabled the development of a ready-to-use solution which don't demand any usage of user's hardware or installation of software. Moreover, the implementation framework is completely based on open-source libraries and platforms and, therefore free of cost. The only condition for usage of this model is the internet connection. This is especially important for enabling monitoring in undeveloped countries.

Multidimensional mode improves several aspects of monitoring results. From the geometrical point of view, the multidimensional model significantly increases the frequency of monitoring, providing a better understanding of flow dynamics. In addition to increased temporal resolution, the primary advantage of water resource attribute monitoring based on remote sensing data is the monitoring of spatial variations.

The AI provides full automation of processing procedures, avoiding the need for human operators. Due to that, water managers with low technical knowledge can monitor water resources at the state level in near-real-time. The development of the model in line with standards and requirements of WFD and INSPIRE directive, added use-value and interoperability to data allowing exchange between different stockholders and support of the decision-making process.

Consequently, the model produces highly accurate and actionable information to support the decision-making process. More importantly, created information, with appropriated WISE and INSPIRE data structure, provides a classification of water body status and should be used to fulfill the WFD reporting obligations. Additionally, resulting information can be used as the for monitoring of process towards the achievement of SDG, including Indicator 6.3.2., Indicator 6.4.2., Indicator 6.6.1., and Indicator 14.1.1.

Сажетак

Вода је основни услов за живот људи, животиња, биљка и функционисање цјелокупног екосистема. Здравље људи, доступност хране, економски раст и производња енергије су зависни од воде. Раст популације и урбанизација, убрзан развој индустирије, пољопривреда као и пораст потражње су повећали стрес воде, чинећи воду оскудним и скупим ресурсом наручито у неразвијеним замљама.

У 2017, само 71 % свјетске популације је имао приступ сигурној питкој води, и само 45 % је користио сигурне санитарне услуге, остављајући 2.2 милијарде људи без сигурне исправне питке воде, укључујући 785 милиона без чак основне питке воде и 4.2 милијарде без сигурног управљања санитарним услугама (UNESC).

Генерална скупштина Уједињених Нација је кроз Резолуцију 64/292, која је усвојена 28.06.2010. године, препознала приступ сигурној питкој води и санитаријама као основно људско право јер вода и санитарије представљају основу за реализацију свих других људских права (UNGA). 2030 AOP (UN) наглашава значај воде за одржив развоја као и значај одрживог управљања водама за спрјечавање даљег смањења квантитета и кавалитета воде. Посебно, треба обезбиједити смањење загађења отпадним материјама и пластиком. У Европи, ОДВ успоставља оквир за превенцију даљег погоршања статуса вода и заштиту акватичних система, обезбјеђујући свеобухватне смјернице за ефикасан и потпун мониторинг и класификацију статуса водних тијела (EPC). Додатно, оба документа наглашавају потребу за трансформисањем начина управљања водним ресусрима и значај мониторинга за детекцију примарних загађивача и карактеризацију њиховог утицаја на свеукупни статус водних тијела.

Геопросторне технологије, геосензори и системи даљинске детекције су постали саставни дио свакодневнице. Предности коришћења ових технологија у рјешавању еколошких проблема су препознате на глобалном нивоу кроз Интегрисани оквир геопросторних информација који „обезбјеђује основе и смјернице за развој, интеграцију, јачање и максимизацију управљања геопросторним информацијама и сродним ресурсима у свим земљама (IGIF).“ Додатно, значај и све већа улога геопросторних информација у достизању циљева дефинисаних у AOP су наглашени у циљу 17 и у докумнетима развијеним од стране УН Комитета експерата за глобално управљање геопросторним информацијама (UN GGIM)

(UN GGIM) се фокусира на примјену геопросторних технологија као и геопросторних трендова у управљању животним окружењем. Локацијско базирани сервиси, GNSS, сателитски снимци, ажурне дигиталне карте постали су доступни у реалном времену широком кругу корисника и саставни су дио свакодневних активности, а не само у домену коришћења од стране специјализованих корисника. Да би ефикасно управљали екосистемом, нове напредне процедуре процесирања засноване на ВИ треба да обезбиједе анализу велике количине података у реалном времену са високим степеном доступности и ефикасности. (UN GGIM) наглашава потенцијал ВИ у производњи и управљању екосистемима и значај благовремено креираних геопростоних информација, дефинишући аутоматизацију као кључан корак у примјени ВИ рјешења.

Упркос петобајтима бесплатно доступних података и анализи према тренутним студијама, даљинска детекција још увек није коришћена у управљању водама у пуном капацитету, практична имплементација у мониторингу и управљању и даље је ограничена. Ограничена употреба података даљинске детекције је углавном изазвана недостатком техничке стручности и знања за разумијевање могућности и ограничења ове технологије, разумијевањем квалитета и несигурности резултата, као и могућности њихове употребе уз недостатак јасно дефинисане методологије употребе и недостатка ресурса за процесирање. Менаџери за управљање водама су примарно заинтересовани за конкретне информације које ће им пружити подршку у процесу доношења одлука, без потребе да

кроз додатну едукацију разумију како су те информације креиране, очекујући аутаматизам који ће им пружити жељену информацију. Модели који се тренутно користе за процесирање података даљинске детекције у области управљања водама третирају само један аспект водних тијела тј. геометрију, топологију или атрибуте кроз комплексне процедуре обраде временски захтјевне. Тренутни модели поред недостатка комплетности процесирања имају и низак степен генерализације јер су процедуре најчешће развијене за потребе специфичног циља и подручја смањујући могућност да дати модел буде примјењен у друге сврхе и за друге регионе. Додатно, на перформансе снажно утиче знање и техничка оспособљеност оператера.

Сходно томе, главни циљ ове дисертације је развој ВИ базираног модела обраде и дистрибуције података о водним ресурсима прикупљених даљинском детекцијом и савременим геопросторним техникама у реалном и блиско реалном времену. Термин подаци о водним ресурсима у овом раду третирају скуп података дефинисан INSPIRE и ОДВ директивом, као и WISE имплементацијом уважавајући геометријске, тополошке и атрибутивне карактеристике водног ресурса као геопросторног објекта.

Да би се постигао овај главни циљ, дефинисани су сљедећи подциљеви:
• Развој модела заснованог на свеобухватној примјени стандарда у овој области од аквизиције преко обраде до дистрибуције, уважавајући тренутно стање геопросторних технологије, геосензорских система за прикупљање података, ИТ платформи и технологија,
• Развој ВИ модел за идентификацију геометријских карактеристака водног ресурса,
• Развој ВИ модела за идентификацију атрибутивних карактеристика водног ресурса, и
• Развој ВИ модела за идентификацију тополошких карактеристика водног ресурса.

Протеклих година уложени су значајни напори у развијање метода за аутоматску детекцију водних тијела. Различити приступи и медоте су развијене у циљу рјешавања основних проблема у овој области као што је раздвајање воде од површина са ниским степеном рефлексије (као што су облаци или изграђена подручја) на мултиспектралним снимцима, пораст рефлексије усљед вјетра на радаским снимцима или висок степен варијације интензитета и висине у LiDAR подацима. Традиционалне методе класификације могу се подијелити на: пиксел базирану и објект базирану у зависности од основне једнице процесирања, пиксел или објект. Пиксел базиране методе су широко примјењене за класификацију индивидуалних пиксела на основу спектралне рефлексије не узимајући у обзир контекстуалне или просторне информације. Постоје два главна ограничења приступа заснованог на пикселима: мјешовити пиксели и „со и бибера“ ефекат. Мјешовити пиксел је дефинисан као један пиксел који садржи карактеристике више класа. Обично је повезан са класификацијом снимака ниске и умјерене просторне резолуције. Друго ограничење представља то што контекстуалне информције о сусједним пикелима нису коришћене у процесу класификације. Са порастом просторне резолуције, величина подручја представљеног једним пикселом опада. На снимцима веома високе резолуције, величина пиксела је значајно мања од објекта од интереса што доводи до повећања варијансе између класа у поређењу са снимцима средње и ниске просторне разолуције. Због тога, традиционални пиксел базирани приступ класификује пикселе у различите класе од сусједног подручја узрокујући „со и бибер“ ефекат. Наведена ограничења могу бити ефикасно отклоњена повећањем просторне реолуције (мјешовити пиксели) или примјеном објекат-базиране анализе слике (ОБИА) („со и бибер“ ефекат). ОБИА приступ се састоји од два основна корака: сегментације и класификације. Алгоритам за сегментацију спаја пикселе у објекте на основу једног или више критеријума хомогености креирајући основне елементе за ОБИА-у. ОБИА поред спектралних карактеристика користи и карактеристике објекта тј. додатне спектралне информације у поређењу са пиксел базираним приступом (средња вриједност по бендовима, минимална и максимална вриједност, односе, варијансу), геометријске карактеристеике, просторне или тополошке

односе. Основно ограничење примјене ОБИА-е је то што одређивање одговарајуће вриједности за параметре није тривијално и обично се заснива на интерактивном приступу „покушај и грешка“. Поред тог, сегментација слике је захтјевна са становишта перформси рачунара и времена обраде, стога процесирање велики количина података је изазовно. Преглед коришћених метода за детекцију водних тијела на основу различитих типова података даљинске детекције је приказан у Табели 1. Оно што се уочава у табели на први поглед је недостатак истраживања у овој области на начин да се водни ресурс третира уважавајући цјеловитост карактеристика, односно уважавајући геометријске, тополошке и атрибутивне карактеристике водног ресурса као геопросторног објекта.

Табела 1. Преглед метода и типова података који су коришћени за креирање информација о водотоцима. Наранџаста боја представља мултиспектралне, црвена радараске снимке док плава боја означава LiDAR податке. Нумеричке вриједности представљају број радова.

Просторна резолуција		Пиксел базирани				ОБИА			Облак тачака			Ручно
		Праг	Регресија	Машинско учење	Дубинско учење	Праг	Регресија	Машинско учење	Праг	Регресија	Машинско учење	
Геометрија	Веома висока и висока	2		3	3							
		3		3					2		1	
						1						
	Умјерена	10		5	3							
		6		4		1		1				
Атрибути	Веома висока и висока	1	10	6		4		3				2
		2	4	1		3		1				5
		1	1			1		1				
	Умјерена		16	8		1						
			3	1				1				
	Ниска		12	1								
Топологија	Веома висока и висока	1										
		3										
	Умјерена	5		1								
		2										
	Ниска											
Интегрисано (геометрија, тополологија, атрибути												

За класификацију водних тијела на основу мултиспектралних снимака најчешће је коришћен пиксел базиран приступ у комбинацији са методама прага, машинским учењем и алгоритмима дубинског учења. Методе базиране на спектралним индексима и методом прага омогућују класификацију са тачношћу између 64% и 99%, слично комбинација пиксел базираног приступа и метода подржавајућих векторских машина (енг. support vector machine (SVM)) постиже (72%-99.6%), алгоритма највеће вјероватноће (енг. maximum likelihood classifier) (70%-97%) и случајне шуме (енг. Random forest) (78%-82%). У поређеју са различитим алгоритмима машинског учења, SVM омогућује највећу тачност. (Duro, Franklin и Dube) су извршили поређење пиксел базираног приступа и ОБИА

за класификацију земљишног покривача/коришћења земљишта, укључујући и класификацију воде на основу снимака умјерене резолуције. Резултати указују да не постоји значајна предност у коришћењу ОБИА у поређењу са пиксел базираним приступом при детекцији водених површина на основу снимака умјерене резолуције.

Картирање геометрије водних тијела на осниву радарских снимака коришћењем пиксел базираног приступа и методе прага резултује просјечном тачношћу између 88% и 98%, пиксел базирани приступ и алгоритми машинског учења (70% -99%), док објектно базиране методе имају тачност у распону од 98% до 99,7%. Поред тога, не постоји значајна разлика у перформансама пиксел базираног (90% - 99%), објект базираног (95% - 99%) и алгоритама за директну класификацију облака тачака (97% - 99%) за картирање водних тијела на основу *LiDAR* података.

Анализа претходних истраживања показује да методе за моделовање везе између резултата лабораторијских анализа теренских узорака воде и површинске рефлексије могу бити класификоване у двије групе: традиционална линеарна регресија и алгоритме машинског учења. У недавно објављеним радовима, алгоритми машинског учења као што су неуронске мреже и *SVM* су интензивно коршћени у овој области остварујући већу тачност. Мониторинг макрофита, вегетације у зонама плављења и структуре врсте је најчешће базирано на снимцима веома високе резолуције и објектно базираним методама.

Међутим, ове традиционалне методе се ослањају на карактеристике или правила која су идентификовали истраживачи како би се смањила сложеност података. Методе дубинског учења имају потенцијал да аутоматски идентификују карактеристике високог значаја из података, елиминишући потребу за стручношћу и комплексним издвајањем карактеристика, међутим нису коришћени у пуном каспацвитету. Конволуцијске неуронске мреже (енг. *Convolutional Neural Network (CNN)*) има већу тачност у односу на друге традиционалне методе (90% - 99,3%).

Илустративно је да се примјена ових нових технологија (Табела 1.) још увијек ограничава на рјешења и подршку појединачним функционално ограниченим активностима у процесима прикупљања података, обраде и дистрибуције. Обично резултат овакве обраде је ограничен скуп вриједности атрибута и/или информација о геометрији односно топологији. Посматрање система управљања водним ресурсима често је ограничено само на један аспект примјене односно једну димензију система.

Приступ примјењен у овом раду је првенствено базиран на свеобухватном погледу на процесе који се извршавају у систему од тренутка аквизиције преко обраде до дистрибуције података уважавајући стандарде и стање у овој области, аутоматизујући процесе и посматрајући систем са различитих аспеката односно димензија.

Мултидимензионални модел употребе геопросторних технологија у управљања водним ресурсима третира поглед на систем са аспекта:

- Свеобухватне примјене стандарда у овој области од аквизиције преко обраде до дистрибуције и употребе (*ISO, INSPIRE,* ОДВ...),
- Локацијско базираних карактеристика водних ресурса (дефинисани оквири за геореференцирање, водни ресурс је геопросторни објекат са елементима геометрије, топологије и атрибута),
- Тренутно доступних геопросторних технологија (*GNNS,* Даљинска детекција, LiDAR, фотограметрија),
- Тренутно доступних геосензорских система за прикупљање података (оптички, радарски,...),
- Тренутно доступних ИТ платформи и технологија (*big data,* вјештачка интелигенција, хардвер као сервис, софтвер као сервис, *Python, …*),
- Вријеме аквизиције, обраде и дистрибуције података (временски одложено, блиско реално вријеме, реално вријеме), и

- Количине прикупљених података у јединици времена (један податак, хиљаде података, милион података).

Централно мјесто у моделу чини посматрање водног ресурса као геопросторног објеката са геометријским, тополошким и атрибутивним карактеристикама. Тако дефинисаним и посматраним геопросторним објектом се управља у комплетном модеу. Атрибутивне, геометријске и тополошке карактерстике тавког објекта су одређене кроз димензију захтјева дефинисаних примјеном стандарда у области управљања водним ресурсима и искуства из постојећих имплементираних система у обаласти. Вриједност тих карактеристика се у овом моделу одређује аутоматизованим процедурама примарно базираним на ВИ и сензорким системима. Оваквим приступом је омогућено да се користе подаци са геосензорских система у реалном времену и да се обрада података и дистрибуција такође изврши у реалном или блискореалном времену, што представља значајан искорак у концептима обраде геопросторних података. Овакав модел значајно скраћује вријеме од тренутка прикупљања података на терену до тренутка добијања управљачке информације. Управо савремени системи за аквизицију геопросторних података у реалном времену могу да представљају примарни и препоручени, али не и једини улазни скуп података у овом моделу и тим омогућује управљање водним ресурсима у реалном времену. Примарни модели обраде геопросторних података (обрада сателитских снимака даљинском детекцијом, снимака фотограметријом, облака тачака прикупљеног ласерским скенирањем) и данас су још увијек системи са временски одложеним резултатума обраде са значајним коришћењем ресурса система (људи, опреме, финансија) у којима специјалистичка знања играју кључну улогу. ВИ рјешења у оквиру овог модела омогућавају аутоматизоване процедуре обраде геопросторних података и смањен утицај специјалисте на процес обраде. Доступност ових рјешења у окружењу софтвер као сервис и *cloud* инфраструктури додатно олакшава коришћење модела.

Мултидимензионални модел употребе података даљинске детекције у управљању водама се састоји од 7 потпуно аутоматизованих алгоритама. Детекција геометрије водних тијела је омогућена на основу три алгоритма и то: алгоритам базиран на *CNN* и мултиспектралним снимцима, алгоритам базиран на *CNN* и радарским снимцима и алгоритам базиран на неуронским мрежама, методи прага и *LiDAR* подацима. За креирање атрибута водних тијела користе се два алгоритма: алгоритам за детекцију плутајуће пластике базиран на *UAV* снимцима и *CNN* и за мониторинг параметара квалитета воде који је базиран на оптичким снимцима и неуронским мрежама. На крају, развије је алгоритам за аутоматско креирање топологије ријечне мреже на основу оптичких и радарских снимака.

Алгоритми за аутоматизовану обраду података даљинске детекције састоје се из 4 фазе: фаза препроцесинг, развоја модела, оцјене тачности и тестирања. Фаза препроцесинг обухвата креирање скупова података за обуку алгоритама дубинског учења као што су креирање маски водних тијела за екстракцију геометрије са оптичких или радарских снимака или интеграција података теренског узорковања и површинске рефлексије за праћење атрибутивних карактеристика. Маске су у овом истраживању аутоматски креиране на основу Сентинел 2 Нивоа 2 сателитских снимака и *region grow* алгоритма. Процес крирање обучавајућих података за мониторинг параметара квалитета је такође у потпуности аутоматизован. Креирани скупови су у поступцима развоја модела подјељени на 80% (тренинг) према 20% (валидација).

Фаза обуке подразумијева калибрацију *CNN* односно *ANN* алгоритам. За семантичку сегментацију водних тијела на основу оптичких (Сентинел 2) и радарских снимака (Сентинел 1) и детекцију видљивих отпадних материја на основу UAV снимака коришћена је ResUNet 50 архитектура. Како тачност дубинских неуронских мрежа зависи од величине скупа за обуку коришћен је трансфер знања (енг. *transfer learning*) тј. коршћена *ResNet 50* мрежа је претренирана на ImageNet бази. Плитки слојеви мреже су коришћени у изворном

облику док су посљедњи лејери фино подешени (енг. *fine-tuning*) на креираним подацима за обуку како би се омогућила детекција предмета од интереса са већом тачношћу. За моделовање везе између вриједности теренског узорковања и површинске рефлексије коришћене су *ANN* мреже. Архитектура мреже је одређена на основу методе покушаја и грешака. Развијени модели се могу користити за аутоматски монитоиринг великог броја водних тијела распрострањених на великим географским подручјима.

Фаза оцјене тачности подразумијева рачунање одговарјућих параметара тачности који су базирани на поређењу резултат предикције валидационог сета и тачних вриједности. За сваки специфични задатак у овом истраживању одабрани су параметри који омогућују свеобухватну анализу перформантности предложених алгоритама.

Фаза тестирања обухвата коришћење развијених алгоритама за детекцију геометрије водних тијела, мониторинг параметара квалитета и екстракцију ријечне мреже на територији Републике Србије.

Предложени мултидимензионални модел представља интегрисани приступ који обухвата све фазе од аквизиције до дистрибуције података, обезбјеђујући јасно дефинисану методологију за аутоматску екстракцију геометрије, топологије и атрибута водних тијела.

Модел је базиран на тренутно актуелним *IT* и геопросторним технологијама укључујући аквизицију, чување и обраду података у *cloud*-у, ВИ и *big data*. Развијени мултидимензионални модел користи податке који су сачувани у *cloud*-у што омогућује ефикаснији приступ и дистрибуцију резултата. На овој начин, могуће је екстраховати потребне информације из петобајт великих база значајно смањујући број задатака чија реализација захтјева доста ресурса и времена. Приступ базама које садрже 40 година дуге историјске и тренутне податке даљинске детекције са глобалном покривеношћу је круцијално за креирање великих база за тренирање које су неопходне за успјешност ВИ алгоритама и монитоирнг водних ресурса, а блиско реалном времену на основу тренираних ВИ алгоритмима. Имплементациони оквир базиран је на *Google Colab, Python,* и *Jupyter* што омогућава развој рјешења која су спремна за употребу и не захтијевају коришћење ресурса корисниковог хардвера или инсталацију нових софтвера. Комплетан имплементациони оквир је заснован на употреби платформи и библиотека отвореног приступа, стога је развијено рјешење могуће користити без додатних лиценцних ограничења, потпуно бесплатно. Једини услов за коришћење овог модела је интернет конекција. Ово је нарочито важно јер примјеном овог модела, омогућава се мониторинг и у економски неразвијеним земљама.

Употреба ВИ омогућује потпуно аутоматизацију процедура процесирање елиминишући потребу за операторима са специјалистичким знањима. Стога, менаџери у водном сектору са ниским техничким знањима могу вршити мониторинг водинх ресурса у блиско реалном времену. Модел је развијен у складу са стандардима и захтијевима ОДВ и *INSPIRE* директиве што обезбјеђује употребну вирједност креираних информација пружајући подршку у процесу доношења одлука и размјену података између учесника на различитим нивоима.

Додатно, мултидимензионални модел унапређује неколико аспекта резултата мониторинга. Са становишта геометрије, мултидимензионални модел значајно повећава фреквенцију мониторинга омогућујући боље разумијевање динамике тока. Поред унапређења временске резолуције, главна предност коришћења података даљинске детекције у мониорингу атрибута водних тијела је мониторинг просторних варијација. Насупрот традиционалном приступу гдје је статус водних тијела одређен у само неколико тачака, подаци даљинске детекције и развијени модел омогућује одређивање концентрације параметара квалитета воде у сваком пикселу омогућујући идентификацију загађивача и разумијевање њиховог утицаја на свеукупни статус водних тијела.

Узимајући у обзир дефнисане хипотезе и презентоване резултате, може се закључити да су све хипотезе потврђене. Предложени мутидимензионални модел потврђује да

подаци о водним ресурсима захтијевани од стране ОДВ и *INSPIRE* директиве могу бити прикупљени, процесирани и дистрибуирани коришћењем тренутно доступних геопросторних технологија. Експериментални резултати указуја да: тренутни и историјски подаци даљинске детекције могу обезбиједити свеобухватни преглед карактеристика водних тијела на регионалном нивоу са високом просторном и временском резолуцијом, ВИ омогућује развој аутоматизованих процедура обраде података даљинске детекције у реалном или блиско реалном времену, посматрање водних ресурса као геопросторних објеката омогућује интегрисано и аутоматизовано управљање водама, и модерне *it* технологије, *cloud* системи и подаци отвореног приступа омогућују промјене традиционалног и дефинисање нових процедура обраде.

Подаци даљинске детекције, са побољшаном просторном и временском резолуцијом, имају велики потенцијал за детекцију водних тијела и мониторинг њихове динамике. У овој тези, *ResUNet 50* мрежа је кроишћена за аутоматску детекцију водних тијела на основу Сентинел 1 и Сентинел 2 сателитских снимака обезбјеђујући повећање тачности (*F1*: 0.87 и 0.89 респективно) у поређењу са другим студијама са истим нивом комплексности животне средине. Поређење тачности током фазе валидације и тестирање Сентинел 1 (*F1*: 0.87 вс. 0.90) и Сенитнел 2 (*F1*: 0.89 вс. 0.92) указује на високу способност генерализације и могућност употребе дефинисаних алгоритама за аутоматску детекцију водних тијела и на другим географским подручјима. Додатно, претренирана *ResUNet 50* мрежа обезбјеђује сличне разултате и за радарске и оптичке снимке потврђујући да пренос знања може бити ефикасно коришћен када се изворне и циљане базе података значајно разликују. Што се тиче перформанси Сентинела 1 и Сентинела 2 за картирање водних тијела, Сентинел 2 пружа нешто боље резултате. *Recall* вриједност је иста (С1: 0.95 вс. С2: 0.96), док Сентинел 2 има већу прецизност а симим тим и незнатно већи *F1* и *KHAT* коефицијент. Изузетно висока вриједност *recall* и визуелна инпекција резултата показују да *ResUNet 50* није осјетљив на површ са ниским степеном рефлексије као што су изграђена подручја, путеви или сјене, што представља једнан од основних извора грешака током класификације водних тијела на основу података даљинске детекције. Главни недостатак у процесу класификације водних тијела на основу оптичких снимака, у овој дисертацији представљају мјешовити пиксели. Број мјешовитих пиксела може бити смањен *pan sharping*-ом *SWIR* опсега или коришћењем снимака са већом просторним резолуцијом. С друге стране, тачност на основу радарских снимака је смањена усљед присуства високе вегетације и жбуња дуж ријечних обала наручито за уске ријеке, високе осјетљивости радарских сензора на садржај воде и сличним карактеристикама одбијених таласа између воде и непропусних површина у рарлним предјелима. Визуелна инспекција резултата показује да предложени приступ тачно и комплетно детектује границе водних тијела чија је ширина већа од 40 метара без обзира на варијације у топографији терена, коришћењу земљишта/земљишном покривачу, и атмосферским условима. Мања водна тијела је тешко детектовати, узрокујући недостатке појединих дијелова или изостављање комплетног водног тијела. На основу презентованих резултата може се закључити да предложени приступ може бит коришћен за тачно и бесплатно аутоматско детектовање водних тијела и мониторинга промјена, у блиско реалном времену са високом фреквенцијом на великим географским подручјима. Додатно, интеграција радарских и оптичких снимака обезбјеђује монитоинг водних тијела у свим временским условима.

Поред оптичких и радрских снимака, могућност употребе *LiDAR* података за детекцију водних ресурса је анализирана. Први корак у предложеној методологији је класификације облака тачака и креирање дигиталног модела терена. У овој тези, класификација облака тачака и филтрирање тачака тла је базирана на алгоритмима дубинског учења. Предложена методологија значајно побољшава процес класификације тачака тла, осигуравајући креирање дигиталног модела терена са одговарајућом тачношћу за датекцију водних тијела и картирање плавних подручја у складу са стандардима

дафинисаним у Европској директиви о процјени и управљању ризицима од поплава. Главна предност предложене методологије је директна класификација облака тачаке, без препроцесирања и растеризације, што значајно редукује коришћене ресурсе и вријеме обраде а самим тим рјешава једно од највећих ограничења када се ради о густим облацима тачака. Додатна предност је потпуна аутоматизација процеса обраде, омућавајући корисницима да користећи сирови облак тачака креирају дигитални модел терена. Поређење тачност алгоритама који су тренирани на балансираним и дебалансираним сетовима података указује да ефикасност метода ребалансирање у великој мјери зависи од природе класификационог задатка и може се користит само уколико омогућује да резултујући, вјештачки генерисани, подаци имају исту расподјелу као и оригинални подаци. Резултати оцјене тачности класификације *LiDAR* облака тачака показује да је грешка мања од 5 cm за 99.72% тачака. Креирани дигитални модел терена, нормлизовани дигитални модел површина, интензитет и густина тачака су коришћени као улазни подаци за ефикасну класикацију водних тијела у смислу времена обраде и захтијеваних ресурса. Додатно, резултати су поређени са водним тијелима аутоматски детектованих на основу спектралних индекса и просторних карактеристика са Сентинел 2 снимака. Презентовани резултати указују да: (1) водна тијела детектована на основу LiDAR-а показују савршено поклапање са стварношћу, (2) *LiDAR* подаци омогућују значајно већу тачност у поређењу са Сентинелом 2, што је и очекивано због веће просторне резолуције, (3) прецизни *LiDAR* подаци и генерисани дигиталног модела терена имају велики потенцијал у погледу екстракције водних тијела. Међутим, ограничена доступност и високи трошкови аквизиције ограничавају њихову примјену. У будућности, употреба алгоритма дубинског учења за директну класификацију водних тијела на основу облака тачака треба додатно бити верификована.

Подаци даљинске детекције у коњукцији са резултатима теренског узорковања воде, могу се успјешно користити за праћење параметара квалитета воде, као што су хлорофил а, растворени кисеоник, суспендоване материје, тотални азот и тотални фосфор, са високом просторном и временском резолуцијом и смањеним трошковима имплементације. Предложени приступ је базиран на подацима отвореног приступа и рјешењима отвореног кода. Тренирање алгоритма је засновано на временским серијама које обухватају 20 година историјских података теренског узорковања и одговарајућих Ландсат 8 сателитских снимака. Веза између провршинске рефлексије и резултата теренског узорковања моделована је употребом вјештачких неуронских мрежа. Тачност креираних резултата је оцијењенапомоћу средње квадратне грешке (СКГ) и нормализоване средње квадратне грешке (нСКГ). Највећа тачност је забиљежена за растворени кисеоник и суспендоване материје (нСКГ: 0,57%, односно 0,97%) док је најмања тачност остварена за хлорофил а (нСКГ: 3,68%). Анализа величине скупова коришћених за обуку и резултујуће тачности указује да је број узорака и тачност неуронске мреже у директној вези. Са друге стране, *SVM* показује мању осјетљивост на мале скупове података и мјешовите пикселе. Стога, *SVM* надмашује неуронске мреже када је доступан мали број узорака за обуку и у том случају препоручује се његово коришћење за праћење квалитета воде. Оцјена тачности добијених резултата показује да су Ландсат 8 подаци погодни за праћење квалитета воде. Иако, 40 година дуга Ландсат мисија могућава коришћење историјских података и повећање обучавајућег скупа, временска резолуција од 16 дана ограничава њихову примјену у мониторингу квалитета водних тијела, нарочито у подручјима са великим степеном годишње облачности. Усљед тога, мање од 10% теренских узорака се може интегрисати са Ландсат површинском рефлексијом уколико је максимални размак између узорковања и прелета сателита 3 дана. Поред тог, мониторинг уских водних тијела је ограничен просторном резолуцијом од 30 m. Већа просторна и временска резолуција Сентинел 2 података представља бољу алтернативу за праћење квалитета воде јер омогућава већу тачност и 25% веће скупове података за 50% мање времена у поређењу са Ландсатом 8.

Главно ограничење за употребу оптичких сателитских снимака у монитоирнгу квалитета је осјетљивост сензора на облаке и маглу. Облаци узрокују значајне и непредвидеиве празнине у подацима што отежава планирање кампања теренског узорковања. Додатно, употреба даљинске детекције у мониторингу је ограничена тренутно коришћеном методологијом теренског узорковања. Како би се ријешила наведена ограничења, препоручује се коришћење сензора за аутоматско праћење квалитета на дневном или омогућујући интеграцију са подацима даљинске детекције. Уколико велико број сензора није коришћен за праћење водног тијела, интеграција података даљинске детекције, оптимизованих кампања узорковања и напредних метода процесирања је једина задовољавајућа методологија за праћење удаљених и великих водних тијела и свеобухватну процјену квалитета воде на регионалном и глобалном нивоу. Најзначајнија предност даљинске деткеције у поређењу са традиционалним и аутоматским мониторингом је праћење просторних варијација квалитета воде. Подаци о просторним варијацијама су од изузетног значаја за идентификацију и конторилу загађивача, представљајући основу за израду активационих планова за спрјечавање загађења, будуће деградације водних ресурса и заштиту јавног здравља.

Аутоматска детекција видљивих отпадних материја на основу ортофота високе резолуције може се постићи употребом *ResUNet 50* алгоритма за семантичку сегментацију. Међу тестираним алгоритмима (*ResUNet 50, ResUNext 50, XceptionUNet, InceptionUResNet v2*), *ResUNet 50* показао је стабилну перформантност за детекцију и класификацију плутајуће пластике на основу различитих скупова података, са различитом просторном резолуцијом, за плутајуће или подводне маркере ($F1 > 0.73$). *ResUNext50* и *XceptionUNet* модели довели су до прецјењивања плутајуће пластике због погрешне класификације водних пиксела. Са друге стране, развијени модел је показао погодност за детекцију плутајуће пластике, пластике у плиткој води као и на копно али са нижом тачношћу у односу на плутајућу пластику. Смањење површине детектоване пластике од само 3,4% додатно је потврдило могућност коришћења модела за мониторинг загађења пластиком и коришћења у оптимизацији кампања чишћења. Могуће је тачно детектовати и класификаовати три различита типа пластике (полиетилен терефталат (ПЕТ), Оријентисани полистирен (ОПС) иНајлон) коришћењем *ResUNet 50* модел (*F1*: ОПС: 0,86; Најлон: 0,88; ПЕТ: 0,92) који је најосјетљивији на мале примјене у количинама рефлектоване енергије. Просторне резолуције и величине пластике која се може детектовати су директно повезане тј. са смањењем прострне резолуције долази до смањења тачности класификације. Стога највећа тачност за све типове пластике је остварена коришћењем ортофота просторне резолуције од 4 mm. За све тестиране резолуције, модел не може детектовати све пикселе пластике али обезбјеђује високу вјероватноћу да детектовани пиксели одговарају пластици у стварности. Штавише, алгоритму је потребан најмање један чист пиксел (пиксел који садржи само тај материјал) за детекцију пластике на површини воде и два чиста пиксела за детекцију подводне пластике. Резултати остварени на основу ортофота просторне резолуције од 18 mm и дефинисаног модела задовољавају захтјеве тачности дефинисане у складу са *UNEP/IOC* (Cheshire, Adler and Barbière), *NOAA* (Opfer, Arthur и Lippiatt) и *OSPAR* (OSPAR) стандардима док *CSIRO* (Hardesty, Lawson и van der Velde) захтијева коришћење ортофота са просторном резолуцијом од 4 mm. Узимајући у обзир резултате класификације ортофота од 4 mm као референтне, највеће повећање површине детектоване пластике остварено је за ортофото од 23 mm (ОСП: 16,1%; Најлон: 33,2%; ПЕТ: 22,3%). Најмања разлика за ОСП и најлон класу је постигнута за просторну резолуцију од 18 mm, док најмање одступање површине детектоване ПЕТ пластике је остварено коришћењем ортофота од 30 mm . Приликом планирања UAV премјера за потребе детекције плутајуће пластике потребно је: (1) постићи компромис између просторне резолуције и површине подручја студије, (2) користити двије беспилотне летјелице са истом шемом лета, прву која ће прикупити слике потребне за детекцију пластике док друга

летјелица, са мањом висином лета, а самим тим већом резолуцијом, треба да обезбједи ортофото високе резолуције за потребе креирање података за обуку, (3) постићи синхронизацију два лета како би се смањио временски размак између премјера и омогућило њихово интегрисано коришћење, (4) планирати летове током облачног времена како би се смањио ефекат сунчевог сјаја (енг. *Sun-glint effect*), (5) брзина вјетра треба да буде што мања, тако да квалитет резултујућег ортофота није угрожен.

Детектована водна тијела на основу оптичких, радарских и *LiDAR* података су даље процесирана у циљу креирања ријечне мреже и анализе тополошких односа између њених елемената. Предложени модел за аутоматску анализу ријечне мреже омогућује екстракцију ријечне мреже на великим подручјима. Визуелна контрола остварених резултата указује да алгоритам обезбјеђује континуирану тачност без обзира на различит тип или величину водних тијела. Није уочена разлика у тачности резултата креираних за континуиране или ријеке са рукавцима, главне водотоке или притоке, ријеке које имају раван ток или меандрирају, као ни за широке или уске ријеке. Такође, алгоритам успјешно креира централну линију за рукавце и мртваје. Резултујућа ријечна мрежа је потпино повезана јер алгоритам обезбјеђује конекцију између централних линија главних водотока и притока. Стога је омогућена и тачна детекција чворова који представљају основни елемент ријечне мреже. Комплетност и тачност креиране ријечне мреже је обезбијеђена високом тачношћу класификације водних тијела, конекцијом између одвојених ријечних сегмената на нивоу полигона, отклањању празнина у полигонима које не представљају ријечна острва. Презентовани приступ за екстракцију ријечне мреже адресира главна ограничења претходних студије. Штавише, омогућује детекцију обе компоненте ријечне мреже док се све претходне студије баве само креирањем централне линије. Тачност и комплетност криране мреже је ограничена просторном резолуцијом сателитских снимака. Ријеке чија је ширина једнака или ужа од 40 m нису детектоване у потпуности. Стога, присуство празнина узрокује дисконтинуитет ријечне мреже и топлошке грешке.

Технологије даљинске детекције са континуираном аквизицијом и доступношћу података у реалном или блиско реалном времену имају велики потенцијал за пружање подршке у управљању водним ресирсима и процесу доношења одлука. Међутим, практична примјена даљинске детекције у овој области је и даље ограничена збиг недостатака техничких компентентности и знања неопходног за разумијевање могућности и ограничења технологије, недостатак јасно дефинисаних процедура обраде и високи захтјеви са становишта ресурса за обраду.

Резултати презентовани у овој дисертацији показују да презентовани мултидимензионални модел рјешава та ограничења. Главна предност модела је: јасно дефинисана методологија за мониторинг геометрије, топологије и атрибута водних ресурса на основу података даљинске детекције, потпуна аутоматизација процедуре, имплементација базирана на подацима и сервисима отвореног приступа што је омогућило развој бесплатног рјешења, спремног за употребу без инсталација програма и захтјева за ресурсима на клијенском рачунару. Овај модел је у потпуности развијен у складу са захтјевима ОДВ, *WISE* и *INSPIRE* директивом као и препорукама водећих истраживања у овој области. Стога модел, обезбјеђује високу тачност и употребљиве информације које пружају подршку у процесу доношења одлука. Још важније, резултујуће информације са одговарјућом *WISE* и *INSPIRE* структуром, омогућују класификацију статуса водних тијела и могу бити коришћене за испуњавање обавезног извјештавања дефинисаног у ОДВ. Поред тога, добијене информације могу се користити за праћење достизања циљева и индикатора одрживог развоја, укључујући индикатор 6.3.2., Индикатор 6.4.2., Индикатор 6.6.1. Ииндикатор 14.1.1.

Contents

List of published papers

Excerpts of this thesis have been published in following peer-reviewed journal and conference proceeding:

1. **Jakovljević, G.;** Govedarica, M.; Alvarez-Taboada, F.; A Deep Learning Model for Automatic Plastic Mapping Using Unnamed Aerial Vehicle (UAV) Data, Remote Sens. 2020, 12, 1515; doi:10.3390/rs12091515. **(Chapter 4.5.2.)**

2. **Jakovljević, G**.; Govedarica, M.; Álvarez-Taboada, F.; Waterbody mapping: a comparison of remotely sensed and GIS open data sources, International Journal of Remote Sensing, 2018, DOI: 10.1080/01431161.2018.1538584 **(Chapter 3.3.1.1.)**

3. **Jakovljević, G**.; Govedarica, M.; Alvarez-Taboada, F.; Pajić, V.; Accuracy Assessment of Deep Learning Based Classification of LiDAR and UAV Points Clouds for DTM Creation and Flood Risk Mapping, Geosciences 2019, 9(7), 323; https://doi.org/10.3390/geosciences9070323 **(Chapter 4.3.2.1.)**

4. Govedarica, M.; **Jakovljević, G.;** Monitoring spatial and temporal variation of water quality parameters using time series of open multispectral data, Proc. SPIE 11174, Seventh International Conference on Remote Sensing and Geoinformation of the Environment (RSCy2019), 111740Y (27 June 2019); https://doi.org/10.1117/12.2533708 **(Chapter 4.4.1.)**

5. **Jakovljević, G.;** Govedarica, M.; Álvarez-Taboada, F.; Assessment of biological and physic chemical water quality parameters using Landsat 8 time series, Proc. SPIE 10783, Remote Sensing for Agriculture, Ecosystems, and Hydrology XX, 107831F (10 October 2018). **(Chapter 4.4.1.)**

6. Govedarica, M.; **Jakovljević, G.;** Álvarez-Taboada, F.; Flood risk assessment based on LiDAR and UAV points clouds and DEM, Proc. SPIE 10783, Remote Sensing for Agriculture, Ecosystems, and Hydrology XX, 107830B (10 October 2018); https://doi.org/10.1117/12.2513278 **(Chapter 4.3.2.2.)**

7. **Jakovljević G.,** Govedarica M. Water Body Extraction and Flood Risk Assessment Using Lidar and Open Data. In: Leal Filho W., Trbic G., Filipovic D. (eds) Climate Change Adaptation in Eastern Europe. Climate Change Management. Springer, Cham., 2019, https://doi.org/10.1007/978-3-030-03383-5_7 **(Chapter 4.4.2.)**

8. **Jakovljević, G.;** Govedarica, M.; Jovanović, D.; The role of geospatial technology in the EU Water Frame Directive implementation, FIG Working Week 2018, Istanbul, Turkey. **(Chapter 4.1.)**

9. **Jakovljević, G.;** Govedarica, M.; Álvarez-Taboada, F.; Remote Sensing Data in Mapping Plastics at Surface Water Bodies, FIG Working Week, 2019, Hanoi, Vietnam. **(Chapter 4.5.2.)**

List of Figures

List of Tables

Abbreviations and Symbols

9IM	9-intersection models
AI	Artificial Intelligence
ALI	Earth Observing-1 Advanced Land Imager
ANN	Artificial Neural Network
ASTER GDEM	Advanced Spaceborne Thermal Emission and Reflection Radiometer Global Digital Elevation Model
ASWM	Automatic Subpixel Water Mapping Method
AWEI	Automated Water Extraction Index
B	Blue band
BGA	Blue-green algae
BN	Batch Normalization
BOD	Biochemical Oxygen Demand
BOMBER	Bio-Optical Model Based tool for Estimating water quality and bottom properties from Remote sensing images
CART	Classification and Regression Trees
CDOM	Colored Dissolved Organic Matter
CEN	European Committee for Standards
Chl-a	chlorophyll a
CNN	Convolution Neural Networks
COD	Chemical Oxygen Demand
CRF	Conditional Random Fields,
CSIRO	Commonwealth Scientific and Industrial Research Organization
CVA	Change Vector Analysis
DNN	Deep Neural Network
DT	Decision Tree
EC	Electrical Conductivity.
EGM96	1996 Earth Gravitational Model
ELR	Extreme Learning machine Regression
EO	Earth Observation
EQR	Ecological Quality Ratio
ETM+	Enhanced Thematic Mapper Plus
EU	European Union
FCLS	Fully Constrained Least Squares
FCN	Fully Convolutional Network
fDOM	fluorescent Dissolved Organic Matter
FPC	First Principal Component
G	Green band
GB	Gradient Boosting
GeoAI	Geospatial Artificial Intelligence
GeoTIFF	Geographic Tagged Image File Format
GIS	Geographic Information Systems
GML	Geographic Markup Language
GMO	Genetically Modified Organisms

GNSS	Global Navigation Satellite System
GRD	Ground Range Detected
GWEM	GeoCoverTM Water bodies Extraction Method
HICO	Hyperspectral Imager for Coastal Ocean
HRWI	High Resolution Water Index
HYP	Hyperion
IaaS	Infrastructure as a service
ICPDR	International Commission for the Protection of the Danube River
INSPIRE	Infrastructure for Spatial Information in the European Community
IoT	Internet of Things
ISO	International Standards Organization
IT	Information technologies
IW	Interferometric Wide swath
k-NN	k-nearest neighbor
K-T	K-T transformation
LAI	Leaf Area Index
LiDAR	Light Detection and Ranging
LMM	Linear Mixed Model
LR	Linear regression
LSWI	Land Surface Water Index
MARE	Mean Averaged Relative Error
MARPOL	International Convention for the Prevention of Pollution from Ships
MESMA	Multiple Endmember Spectral Mixture Analysis
MLA	Machine Learning Algorithms
MLC	Maximum Likelihood Classifier
MLP	MultiLayer Perceptron
MLR	Multiple Linear Regression
MNDWI	Modification of Normalized Difference Water Index
MODIS	Moderate-resolution Imaging Spectroradiometer
MRSB	Most Related Single Band
MSI	Multispectral Instrument
MWEN	Multi-scale Water extraction convolutional neural network
NASA	U.S. National Aeronautics and Space Administration
NDTI	Normalized Difference Turbidity Index
NDVI	Normalized Difference Vegetation Index
NDWI	Normalized Difference Water Index
NGI	Normalized Green Index
NIR	Near-infrared
NOAA	National Oceanic and Atmospheric Administration
NRMSE	Normalized Root Mean Square Error
OBIA	Object Based Image Analysis
OGC	Open Geospatial Consortium,
OPS	Oriented Polystyrene
OSM	OpenStreetMap

OSPAR	Oslo and Paris Conventions
OWCEM	Orthogonal subspace projection Weighted CEM
PaaS	Platform as a service
PCA	Principal Component Analysis
PET	Polyethylene terephthalate
PSPNet	Pyramid Scene Parsing Net
QDA	Quadratic Discriminant Analysis
R	Red band
RANSCAN	RANdom SAmple Consensus
RBD	River Basin District
RBMP	River Basin Management Plans
ReLU	Rectified Linear Activation Function
RF	Random Forest
RMSE	Root Mean Square Error
RT	Regression Tree
SaaS	Software as a service
SAPCNN	Self-Adaptive Pooling Convolutional Neural Network
SAR	Synthetic Aperture Radar
SAV	Submerged Aquatic Vegetation
SC	Specific Conductance
SCL	Scene Classification Layer
SDG	Sustainable Development Goals
SDI	Spatial Data Infrastructure
SEIS	Shared European Environment System
SPM	Suspended Particulate Matter
SRTM	Shuttle Radar Topography Mission
SS	Suspended Solid
SST	Sea Surface Temperature
SVM	Supported Vector Machine
SVR	Supported Vector Machine Regression
SWIR	Short Wave Infrared
TB	Tree Bagger
TBM	phytoplankton total biomass
TCW	Tasseled Cap Wetness
TDS	Total Dissolved Solids
TIRS	Thermal InfraRed Sensor
TM	Multispectral Scanner and Thematic Mapper
TN	Total Nitrogen
TNMN	TransNational Monitoring Network
TOC	Total Organic Carbon
TP	Total Phosphorus
TRWE	Total Renewable Water Resources
UAV	Unmanned Aerial Vehicles
UIQI	Universal Image Quality Index

UN GGIM	United Nations Committee of Experts on Global Geospatial Information Management
UNEP/IOC	United Nations Environment Programme /Intergovernmental Oceanographic Commission
UWEM	automated Urban Water Extraction Method
UWWTD	Urban Wastewater Treatment Directive
VGI	Volunteered Geographic Information
VHR	Very High Resolution
WFD	Water Framework Directive
WGS 84	World Geodetic System
WISE	Water Information System for Europe
WQP	Water Quality Parameters
WRI	Water Ratio Index
ZY-3	Ziyuan 3

I Introduction

Water is vital for the life of humans, animals, plants, and ecosystems. Human health, food security, economic growth, energy production, and ecosystems are all water-dependent. Growing population and urbanization, intensive industrial development, agriculture, increasing demand, and misuse of water have increased water stress, making water a scarce and expensive resource, especially in undeveloped countries.

In 2017, only 71 percent of the global population used safely managed drinking water, and just 45 percent used safely managed sanitation services, leaving 2.2 billion persons without safely managed drinking water, including 785 million without even basic drinking water and 4.2 billion without safely managed sanitation (UNESC 2020).

On 28 July 2010, thought Resolution 64/292, the United Nations General Assembly, recognized the access to safe drinking water and sanitaria as basic human rights since it is essential to the realization of all other human rights (UNGA 2010). The 2030 Agenda for Sustainable Development emphasizes the importance of water for sustainable development and the importance of sustainable management to prevent further decrease in water quality and quantity. In particular, the prevention of pollution by west materials and plastic should be provided. In Europe, the Water Framework Directive 2000/60/EC (WFD) establishes the framework for the prevention of further deterioration and protection of the aquatic environment (E. P. EPC 2000), providing comprehensive guidelines for efficient and complete monitoring and classification of water body status. Moreover, both documents stress the need to transform the way water resources are managed and the importance of monitoring for the detection of priority polluters and characterization of the impact on overall water status.

Geospatial technology, geosensor, and remote sensing systems have become an integral part of daily life. The benefits of those technologies in addressing and solving environmental problems are recognized at a global level through the Integrated Geospatial Information Framework, which "*provides a basis and guide for developing, integrating, strengthening and maximizing geospatial information management and related resources in all countries*" (IGIF 2020). Moreover, the importance and increasing role of geospatial technologies in achieving 2030 SDG are highlighted by SDG Goal 17 (UN 2015) and United Nations Committee of Experts on Global Geospatial Information Management (UN-GGIM) documents (UN GGIM 2020).

The (UN GGIM 2020) focuses on the change of the trends in geospatial information management. Location-based services, Global Navigation Satellite System (GNSS), satellite images, updated digital maps need to be available in real-time to a wide range of users and a ubiquitous part of everyday services instead of being used only in the domain of specialized users. To satisfy those demands, the new processing procedures need to provide the analysis of a large amount of data in real-time with high efficient. (UN GGIM 2020) emphasize the potential of Artificial Intelligence (AI) in geospatial production and management, defining the automated feature extraction as initial steps in implementing AI solutions.

Despite the petabytes of freely available Earth observation and insight gained from previous studies showing that remote sensing can be effectively used in water management, the practical application in monitoring and decision making is still limited. This is mostly due to lack of the technical expertise and knowledge to understand the possibilities and limitations of remote sensing technology, understanding the uncertainties of results and their application, lack of established methodologies and complex processing needs. Water resource managers are more interested in actionable information to support the decision-making process than for a deeper understanding of how those data were created. The currently used procedures for processing remote sensing data in the field of water management treats only one aspect of water bodies i.e. geometry, topology, or attributes. In addition to the lack of completeness, the generalization ability is low. They are mostly developed to fit specific areas reducing the ability of model

application over different regions. Moreover, the performance is strongly influenced by the technical expertise of operators.

The primary aim of this dissertation is defined to overcome the listed challenges taking into account the requirements and recommendations of relevant standards in the field.

1.1. Objectives

The main objective of this dissertation is the development of an AI-based model of processing and distribution of data on water resources, which are collected by remote sensing and modern geospatial techniques, in real and near real-time. The term 'data on water resources', in this dissertation, cover the geometric, topological, and attributive characteristics of the water body. The water bodies are represented as geospatial objects allowing storage of additional attributes, better presentation, improved manipulation of data, and water resource management in a more efficient way. In order to enable the usage of produced data in water management and implementation of WFD, the attributes are defined by WFD requirements, while the data are prepared in line with INSPIRE directive and WISE implementation guidelines.

To achieve this main objective, the following sub-objectives are defined:

- Development of the model based on the comprehensive application of the standards in the field, covering all processes from acquisition to distribution, taking into account the current state-of-the-art in the geospatial technologies, geosensors systems for data collection, and technologies,
- Development of AI model for identification of geometrical characteristics of water resources from optical, SAR, and LiDAR data,
- Development of AI model for identification of attributive characteristics of water bodies from optical and UAV data, and
- Development of a model for identification of topological characteristics of water resources.

Defined sub-objectives are detailed documented in the following chapters.

1.2. Hypothesis

According to the objectives, the null and alternative hypotheses were defined.

Null hypothesis: Data on water resources required by INSPIRE and WFD specifications can be collected, processed, and distributed by modern geoformation technologies, geo sensor systems, and IT technologies.

Alternative hypothesis:

- Actual and historical remote sensing data can provide a comprehensive overview of water bodies characteristics at the regional level with the high spatial and temporal resolution,
- Models based on AI provide automated processing of remote sensing data in real and near-real-time,
- The definition of water resources as geospatial features provides integrated and automated water management, and
- Modern IT technologies, cloud systems, and open data support changes in the traditional and development of new procedures for the processing of remote sensing data.

1.3. Dissertation outline

This dissertation consists of five chapters following the objectives.

In Chapter 2., a comprehensive overview of international laws and the standards in the field is presented. Special attention is dedicated to the analysis of required defined by the UN SDG Agenda, WFD, and INSPIRE directive. The transposition between EU acquis in the field of water and Serbian laws were analyzed. Moreover, the current status of water bodies in the World and Serbia are presented.

Chapter 3. provides an analysis of related studies in extracting geometrical, topological, and attributive characteristics of water bodies from remote sensing data. For each characteristic, the type of remote sensing data (optical, SAR, LiDAR, UAV), used methods, and accuracy of produced results are investigated. Moreover, the recent technical developments such as cloud computing systems, big data, and AI are analyzed with the aspects of their application in the improvement of current models used in water management.

In Chapter 4. The developed models and results are presented. The chapter begins with a definition of multidimensional models and their components. After that, the model for automatic detection of water body geometry from optical, SAR, and LiDAR data, the model for automatic water body quality monitoring based on optical data and UAV data, and the model for automatic extraction of river network was presented in details. The proposed models were tested on real data on the country level (Republic of Serbia). The results of the accuracy assessment and visual inspection were presented and discussed.

In Chapter 5. Concluding remarks and prospective related to this dissertation are described. It provides the main conclusions, implications, and recommendations for future research.

II Status of water bodies in World

The water covers 71 percent of the Earth's surface. Only 3% of the water on the Earth is freshwater, of which more than two-thirds is frozen in glaciers and polar ice. The total renewable water resources (TRWR), defined as the long-term average annual flow of surface and groundwater, shows high spatial and temporal variability. At the country level, the TRWE varies from 5 m^3 in Kuwait per capita to more than 100000 m^3 per capita in Greenland, French Guinea, Iceland, etc. (Figure 1.) (WDI 2014). The 45 countries have less than 1000 m^3 per capita, from which 27 of them have less than 500 m^3 (WDI 2014).
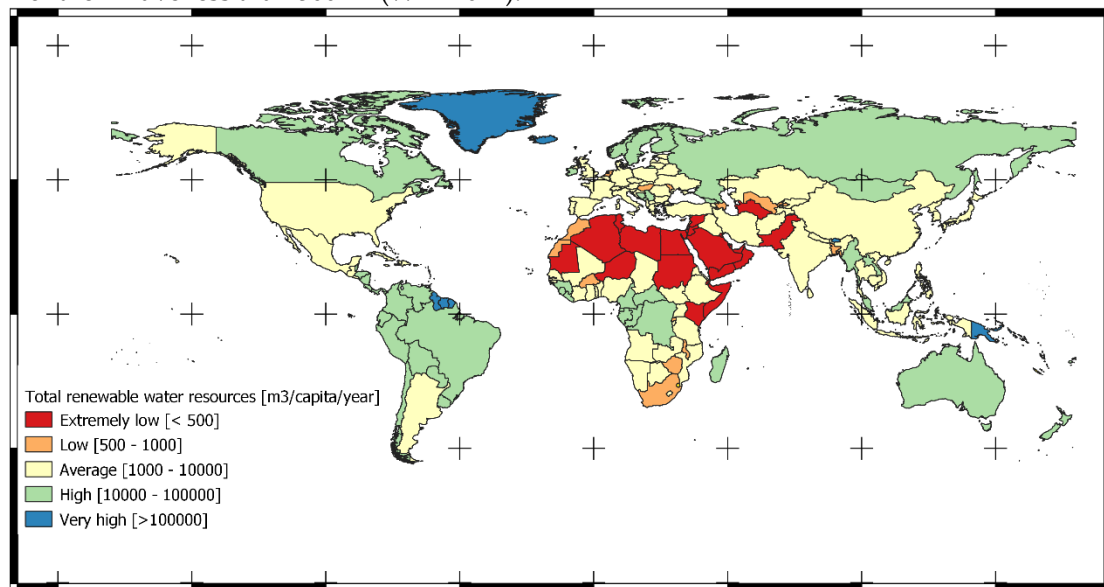
Figure 1. Total renewable water resources per country [m^3/capita/year]

Water is a vital element to overall human existence. On 28 July 2010, thought Resolution 64/292, the United Nations General Assembly, recognized the access to safe drinking water and sanitaria's as fundamental human rights since it is essential to the realization of all human rights (UNGA 2010). Human health, food security, industrial and agricultural development, economic growth, energy production, and ecosystems are all water-dependent. According to the World Health Organization (WHO), between 50 and 100 liters of water per person per day is needed to ensure the most basic needs (Howard and Bartram 2003). Access to basic drinking water service (piped water) is vital for reducing illness and death, especially among children. In 2017, only 71 percent of the global population used safely managed to drink water, and just 45 percent used safely managed sanitation services, leaving 2.2 billion persons without safely managed drinking water, including 785 million without even basic drinking water and 4.2 billion without safely managed sanitation. Of those, 673 million persons still practiced open defecation (UNESC 2020). The proportion of the population that has access to basic water services per country is presented in Figure 2. (UNICEF 2019)
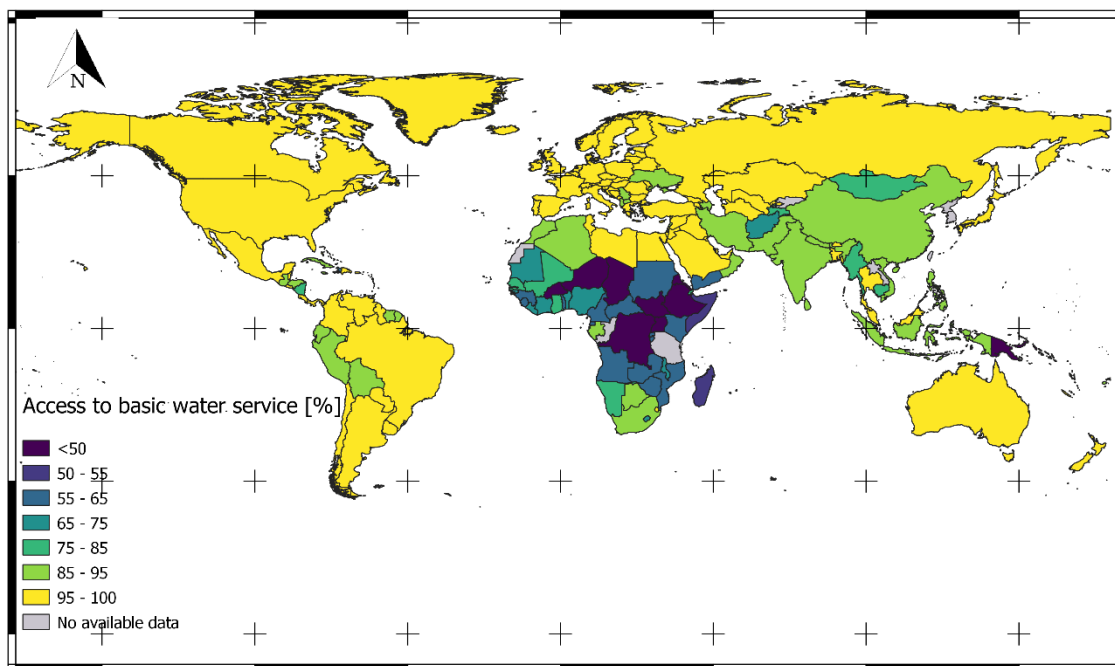
Figure 2. Percent of population per country that has access to basic water services

Global water use has increased by a factor of six over the past 100 years and continues to grow at a rate of about 1% per year (UN-Water 2020). Increasing demands for freshwater resources are largely influenced by population and economic growth, climate changes, urbanization, mitigation, and industrialization, along with an increase in production and consumption. It is projected that the world will face a 40% global water deficit under the business-as-usual climate scenario by 2030 (2030 WRG 2009) while by 2050, the global water demands will increase by 55% (WWAP 2015). In addition to physical scarcity, the degradation of water quality reduces the quantity of water that is safe to use. The increasing pollution of freshwater caused by the disposal of untreated or insufficiently treated wastewater's surface water bodies, pesticides used in agriculture, plastic pollution, etc. represents a global challenge that has increased in both developed and developing countries. In 2012, 842,000 deaths in low- and middle-income countries were linked to contaminated water and inadequate sanitation services (UNESCO 2017). The results of water quality assessment in rivers in Latin America, Africa, and Asia shows that: severe pathogen pollution (fecal coliform bacteria) already affected around one-third of all river stretches, severe organic pollution (biochemical oxygen demand, (BOD)) already affected one out of every seven kilometers of all river stretches, and intense and moderate salinity pollution (total dissolved solids (TDS)) already affected around one-tenth of all river stretches (UNEP 2016). On a European scale, around 40 % of the surface water bodies are in good or high ecological status or potential, with lakes and coastal waters having better quality than rivers and transitional waters, and only 38% are in good chemical status (EEA 2018). In the EU groundwater have the best status with 74% of them achieving good chemical while 89 % achieved good quantitative status (EEA 2018).

2.1. UN sustainable development goals

The 2030 Agenda for Sustainable development, adopted by United Nation Member stats, provide a framework to build a better and more sustainable future for all. The agenda defines 17 Sustainable Development Goals (SDG) and 169 targets that integrated and balanced the three dimensions of sustainable development: the economic, social, and environmental (UN 2015). The Agenda emphasizes the water-related issues by setting SDG 6 aims to "ensure availability and sustainable management of water and sanitation for all." SDG 6 has eight targets addressing:

drinking water, sanitation, and hygiene, water quality, water-use efficiency, integrated water resource management, water-related ecosystems, and means of implementation (Table 1.). Besides, water quality is addressed under other SDGs (Table 1.), recognizing the link between water and poverty reduction, health, ecosystems, and sustainable consumption and production.

Table 1. SDG, targets, and indicators related to water challenges (UN 2015)

Goal	Target	Relevant indicators
SDG 1: No Poverty	**Target 1.4:** By 2030, ensure that all men and women, in particular the poor and the vulnerable, have equal rights to economic resources, as well as access to basic services, ownership and control over land and other forms of property, inheritance, natural resources, appropriate new technology, and financial services, including microfinance	**Indicator 1.4.1:** Proportion of population living in households with access to basic services
SDG 3: Good health and well-being	**Target 3.3:** By 2030, end the epidemics of AIDS, tuberculosis, malaria, and neglected tropical diseases and combat hepatitis, water-borne diseases, and other communicable diseases	
	Target 3.9: By 2030, substantially reduce the number of deaths and illnesses from hazardous chemicals and air, water, and soil pollution and contamination	**Indicator 3.9.2:** Mortality rate attributed to unsafe water, unsafe sanitation, and lack of hygiene (exposure to unsafe Water, Sanitation and Hygiene for All (WASH) services)
SDG 6: Clean water and sanitary	**Target 6.1:** By 2030, achieve universal and equitable access to safe and affordable drinking water for all	**Indicator 6.1.1:** Proportion of population using safely managed drinking water services
	Target 6.2: By 2030, achieve access to adequate and equitable sanitation and hygiene for all and end open defecation, paying special attention to the needs of women and girls and those in vulnerable situations	**Indicator 6.2.1:** Proportion of population using safely managed sanitation services, including a hand-washing facility with soap and water
	Target 6.3: By 2030, improve water quality by reducing pollution, eliminating dumping and minimizing release of hazardous chemicals and materials, halving the proportion of untreated wastewater, and substantially increasing recycling and safe reuse globally	**Indicator 6.3.1:** Proportion of wastewater safely treated **Indicator 6.3.2:** Proportion of bodies of water with good ambient water quality
	Target 6.4: By 2030, substantially increase water-use efficiency across all sectors and ensure sustainable withdrawals and supply of freshwater to address water scarcity and substantially reduce the number of people suffering from water scarcity	**Indicator 6.4.1:** Change in water-use efficiency over time **Indicator 6.4.2:** Level of water stress: freshwater withdrawal as a proportion of available freshwater resources

	Target 6.5: By 2030, implement integrated water resources management at all levels, including through transboundary cooperation as appropriate	**Indicator 6.5.1:** Degree of integrated water resources management implementation (0-100) **Indicator 6.5.2:** Proportion of transboundary basin area with an operational arrangement for water cooperation
	Target 6.6: By 2020, protect and restore water-related ecosystems, including mountains, forests, wetlands, rivers, aquifers and lakes	**Indicator 6.6.1:** <u>Change in the extent of water-related ecosystems over time</u>
SDG 12: Responsible consumption and production	**Target 12.4:** By 2020, achieve the environmentally sound management of chemicals and all wastes throughout their life cycle, in accordance with agreed international frameworks, and significantly reduce their release to air, water and soil in order to minimize their adverse impacts on human health and the environment	**Indicator 12.4.2:** Hazardous waste generated per capita and proportion of hazardous waste treated, by type of treatment
SDG 14: Life below water	**Target 14.1:** By 2025, prevent and significantly reduce marine pollution of all kinds, in particular from land-based activities, including marine debris and nutrient pollution	**Indicator 14.1.1:** <u>Index of coastal eutrophication and floating plastic debris density</u>
SDG 15: Life on Land	**Target 15.1:** By 2020, ensure the conservation, restoration, and sustainable use of terrestrial and inland freshwater ecosystems and their services, in particular forests, wetlands, mountains, and drylands, in line with obligations under international agreements	**Indicator 15.1.2:** Proportion of important sites for terrestrial and freshwater biodiversity that are covered by protected areas, by ecosystem type

Different data types are required to track progress towards Targets and Indicators. Article 273. of the Future That We Want (Futere We Want 2012) document recognizes the importance of "*space-technology-based data, in situ monitoring and reliable geospatial information for sustainable development policymaking, programming and project operations*." The EO and spatial information with their continuous spatial and temporal resolution are essential for monitoring the effectiveness of the SDG framework at local, national, regional, and global levels. Additionally, the use of EO and spatial information significantly reduce the cost of monitoring, providing a framework for sustainable monitoring with limited resources.

2.2. European Union Water Framework Directive

The Water Framework Directive 2000/60/EC (WFD), adopted in 2000, establishes the framework for the prevention of further deterioration and protection of the aquatic environment across Europe (E. P. EPC 2000). In the context of WFD, the aquatic environment includes rivers, lakes, transitional waters, groundwaters, and coastal waters out of 1 nautic mile (12 nautic miles for chemical status). A process of surface water body identification, categorization, and typification is described in Annex II of Directive.

The primary aim of the WFD is to achieve 'good status' in all bodies of surface water and groundwaters. The 'good status' means that water shows a slight change from those normally associated with the surface water body type under undisturbed conditions (reference conditions). It is achieved when both ecological and chemical status are at least good (E. P. EPC 2000). Ecological status is an expression of the quality of the structure and functioning of the aquatic

ecosystem while concentrations of pollutants express chemical status. For each type of water body, reference conditions are identified and compared to monitoring results to assess ecological status (classified in five classes from "poor "to "high ") and chemical status (classified in two classes) (Figure 3.) (E. P. EPC 2000).
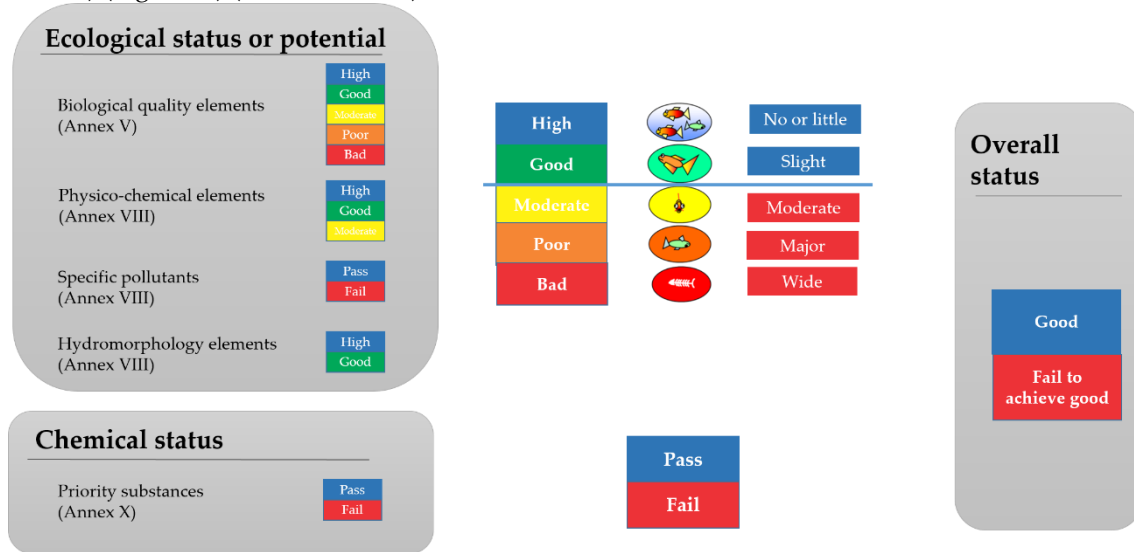
Figure 3. Assessment of the status of water bodies according to WFD

The success of the Directive in achieving the aim and its related objectives is mainly measured by the status of "water bodies" (Guidance document no 7, 2003).   To assess the status of the water body, monitoring of biological, hydro morphological, and physicochemical quality elements that are most sensitive to the identified pressures need to be made. According to (EEA 2018) the main pressures on surface water bodies in the EU are hydro morphological (affecting 40% of water bodies), diffuse sources (38%), atmospheric deposition, particularly of mercury (18%), and water abstraction (7%).

Monitoring programs must establish a coherent and comprehensive overview of water status within each River Basin District (RBD). Three types of monitoring programs that provide the best representation of pressures for quality elements are described in Annex V (surveillance, operational, and investigative monitoring). Article V requires RBD to be characterized and the environmental impact of human activities to be reviewed under Annex II (E. P. EPC 2000). Therefore, the Member States are obligated for each River Basin Management Plans (RBMP) reporting cycle to establish surveillance monitoring for one year which will provide confidant and precise overview of ecological and chemical status (E. P. EPC 2000).

The relevant quality elements for classification of ecological status for the river, lakes, transitional and coastal waters have been primarily selected in Annex V of the WFD. At the same time, a list of priority substances is defined in Annex X. Additional, Member State should use specific sub-elements that are vulnerable to defined pressures on the water body. Figure 4. and Figure 5. shows the quality elements specified in Annex V and additional recommended quality parameters which have been identified by the Member States for the particular water body (EC 2003)
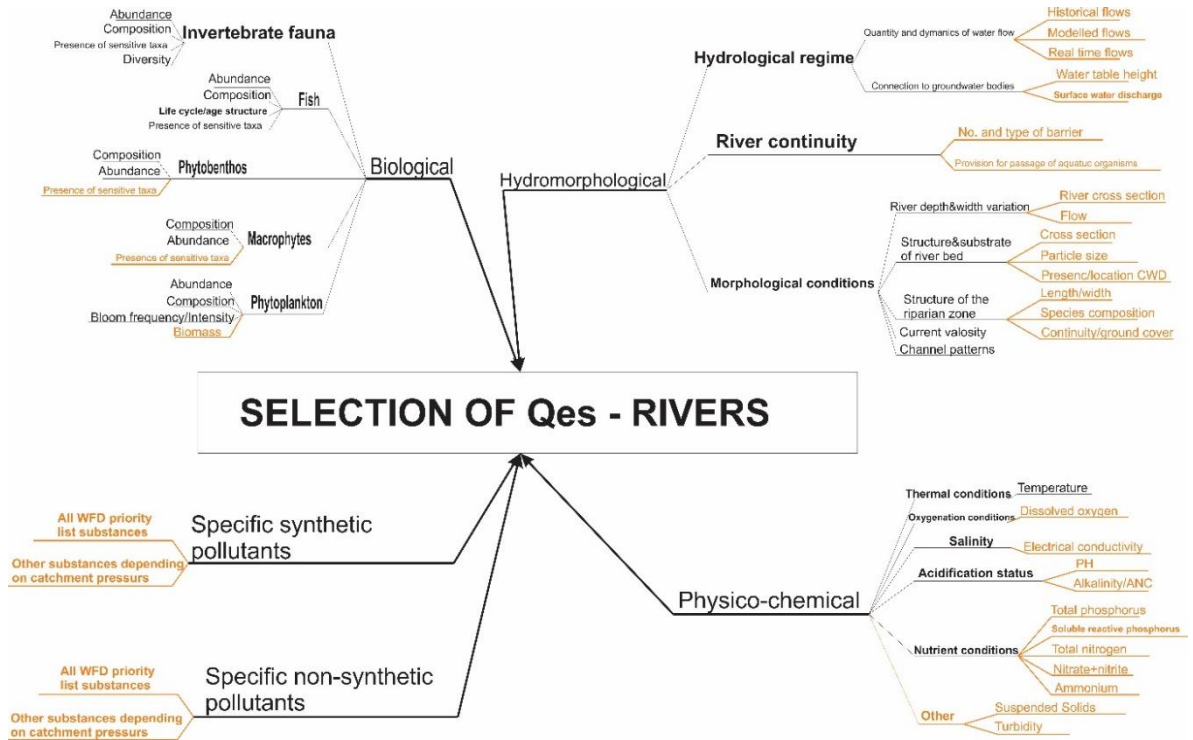
Figure 4. Quality elements for rivers (EC 2003)
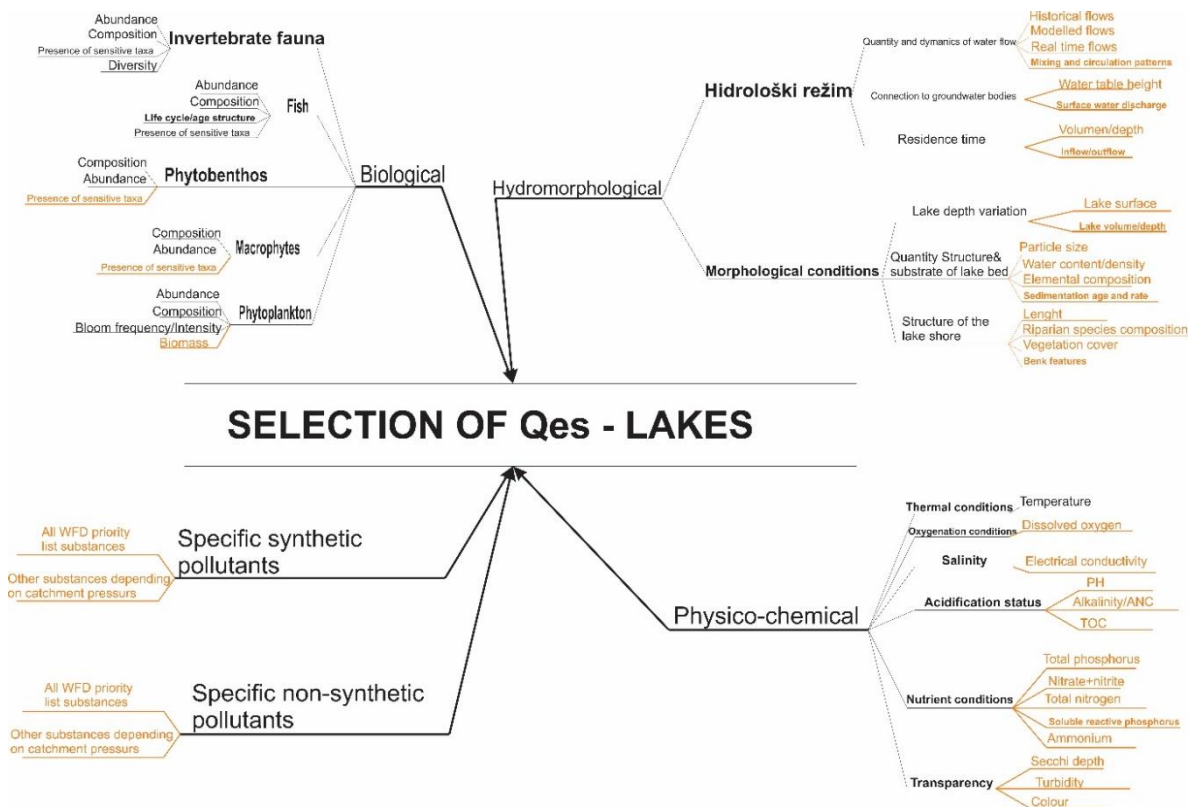
Figure 5. Quality parameters for lakes (EC 2003)

Classification of ecological status is based on the Ecological Quality Ratio (EQR) and assessment ecological quality of physicochemical elements. EQR is defined as the ratio of observed biological value and references biological value (Guidance document no 10, 2003). Monitoring of biological quality elements such as an abundance of fish is a very onerous task,

therefore, the Directive specifies quality elements for the classification of ecological status that include hydro morphological, chemical, and physicochemical elements supporting (indicative) the biological elements (EC 2003). Additionally, the operational monitoring (or in some cases investigative monitoring) is created for the water bodies that are, based on impact assessment following Annex II or surveillance monitoring, are identified as being at risk of failing to meet their environmental objectives (E. P. EPC 2000).

The level of confidence and precision of the results provided by the monitoring programmes is a function of the number of water bodies included in the monitoring, a number of stations that are required to assess the status of each water body, and the frequency at which parameters have to be monitored (EC 2003). The lower risk of misclassification of water body status requires more monitoring and therefore the higher costs of implementation. The Directive requires that sufficient water bodies with a sufficient number of monitoring stations, at the frequency that provides the required precision, should be included in the surveillance monitoring. However, Directive and Guidance documents have not specified the levels of precision and confidence required from monitoring programs. Therefore the sufficient number of water bodies and monitoring stations are not exactly defined.

The WFD implies that rivers with catchment areas greater than 10 km² and lakes greater than 0.5 km² in surface area and all of water bodies into which priority substances are discharged need to be included within the water status assessment and monitoring (E. P. EPC 2000) but this is a very ambitious goal and requires a major financial. It is recommended that desired precision should be balanced against the cost of implementation. The scale of monitoring programs depends on the extent of, variability in and impacts on the water environment meaning that more water bodies should be monitored in a heterogeneous RBD in terms of types of the water body and anthropogenic pressures than in a more homogenous catchment. Besides, the water bodies with similar critical characteristics can be grouped and assessment of group status can be made by using just representative water bodies selected from the group.

Table 2. The minimum frequency of monitoring per quality parameter recommended by WFD (E. P. EPC 2000) and Guidance Document No 7. (EC 2003)

Quality element	Annex V		Guidance document No 7	
	Rivers	Lakes	River	Lakes
Biological				
Phytoplankton	6 months	6 months	1-3 months	1-3 months
Macro invertebrates,	3 years	3 years	6-12 months	12 months
Other aquatic flora,	3 years	3 years	3-6 months	12 months
Fish	3 years	3 years	12 months	12 months
Hydromorphological				
Hydrology	Continuous	1 month	Continuous	Weekly/monthly
Continuity	6 years	6 years	5-6 years	6 years
Morphology	6 years	6 years	12 mounts	6 years
Physico-chemical				
Thermal conditions	3 months	3 months	1-2 months	1-3 months
Oxygenation	3 months	3 months	1-2 months	Daily/monthly
Salinity	3 months	3 months	1-2 months	1-3 months
Nutrient status	3 months	3 months	1-2 months	1-3 months
Acidification status	3 months	3 months	1-2 months	1-3 months
Priority substances	1 month	1 month	1 month	1 month

Quantifying temporal and spatial variability of quality elements is an important aspect in the process of designing the monitoring programs (EC 2003). The frequency of monitoring is flexible since some quality parameters are more variable than others. The parameters that show

the high level of variability requires mora sampling (and cost). The minimum frequency of monitoring per quality elements is defined in Annex V of Directive (E. P. EPC 2000) (Table 2.).

In addition to the high temporal variability of quality parameters such as phytoplanktons, oxygenation, nutrients, etc., the water isn't usually well mixed within the waterbody, and concentration of parameters can vary greatly between locations, therefore, the higher number of monitoring station is needed to quantify spatial variability properly. This implies the considerable increase of resources needed for such monitoring since it would need at least 20 or 30 samples (EC 2003). This is in contrast with the minimum frequency defined in Annex V (Table 2). The compromise between those cases was made in frequency recommendation suggested in Guidance Document No. 7 (EC 2003).

2.3. Geographic Information System recommendation for implementation of WFD

The implementation of the WFD requires a large amount of spatial data that should be used for the preparation and reporting of the RBMP. That information should be reported in the form of maps (list of required maps is defined in Annex I of (Guidance Document No 9 2003)). Also, it is necessary to share information between many parties that are involved in the implementation of WFD, ranging from local authorities to the European Commission.

The WFD uses Water Information System for Europe (WISE) for data collection and reporting, providing a simplified reporting process and a clearer distinction between the needs of different parties and different levels (Guidance Document No: 22 2009). WISE is based on an open and distributed service-oriented architecture, applying appropriated standards and specifications for Open Geospatial Consortium (OGC), the International Standards Organization (ISO) European Committee for Standards (CEN), and guidelines from the INSPIRE directive. Interoperability and transparency are important aspects of WISE since they provide information discovery, sharing, and exchange between different levels. The WISE provides hosting of spatial and non-spatial data and visualization of data. There are two main types of spatial datasets involved: spatial data submitted according to Directives and WISE Reference GIS dataset. Most of the data (except reference) are decentralized and maintained at the most appropriated level therefore the link between the national water information system and WISE needs to be established.

The spatial data are reported in the form of individual GIS layers that enables aggregation of data and the production of the requested map on the EU level. The GIS layer is vector data (point, line, or polygon dataset) whit associated attribute information. The data must be submitted as Geographic Markup Language (GML) file (data may be prepared as shapefile and converted to GML using available conversion tool). Metadata must be provided for each spatial data file, according to the INSPIRE metadata profile. The data should be reported at the ETRS89-GRS80 geodetic coordinate system (EPSG: 4258) with positional accuracy acceptable for cartographic representation at the 1:100 000 scales or larger (spatial accuracy 50 m or larger) (Guidance Document No: 22 2009). Table 3. summarized the GIS layer requested for the surface water body by WFD.

The surface water body for which reference geometry is a polygon should be reported in SurfaceWaterBody dataset. In contrast, bodies that have linear reference geometry must be reported in the SurfaceWaterBodyLine data set. In addition, a representation of the centerlines of surface water bodies is requested. The centerline, reported in the SurfaceWaterBodyCentreline, must be split into segments, such that each segment belongs to one and only one hydrographic feature (WISE GIS Guidance 2016).

Table 3. Reference geometry for different types of water body (WISE GIS Guidance 2016)

Surface water body	Feature type	Related data sets
River Basin District	Polygon	RiverBasinDistric
River	polyline/polygon	SurfaceWaterBody SurfaceWaterBodyLine SurfaceWaterBodyCentreline
Lake	polygon	SurfaceWaterBody SurfaceWaterBodyLine SurfaceWaterBodyCentreline
Transitional waters	polygon	SurfaceWaterBody
Coastal water	polygon	SurfaceWaterBody
Territorial waters	polygon	SurfaceWaterBody
Monitoring Sites	Point	MonitoringSites
Protected area	Polygon Line Point	ProtectedArea ProtectedAreaLine ProtectedAreaPoint

2.4. Spatial Data Infrastructure and INSPIRE

The information on the state of the environment, pressures, and their impacts is essential for the development of effective policy, implementation, and monitor of their success. Agenda 21 (UNSD)(UNSD 1992) emphasize the importance of spatial data to support decision-making process and understanding and integrating social, economic and environmental perspectives at local, regional, and global level. The Agenda demanded to bring the gap in the '*availability, quality, coherence, standardization, and accessibility of data'*, particularly between developed and developing countries (UNSD). Many countries employed the Spatial Data Infrastructure (SDI) as a framework for addressing those gaps for geospatial data. The SDI is defined as a collection of technologies, policies and institutional agreements that provide data discovery, evaluation and application for users and providers within all levels of government, the private sector, non-profit sector, academia and citizens (GSDI Association). The general rules for establishing the SDI in the European Union to support environmental policies are defined in the Infrastructure for Spatial Information in the European Community (INSPIRE) Directive (EPC). INSPIRE specify common data models, code lists, map layers and additional metadata on the interoperability to be used when exchanging spatial datasets (TWG-HY). The data harmonization part of the INSPIRE directive consists of data specifications and guidance documents that are organized in three annexes and 34 spatial data themes.

The WISE represents the water-related component of INSPIRE and Shared European Environment System (SEIS) and it is developed in close relationship to the INSPIRE initiative to ensure the sheared, interoperable and transparent system. In addition to data reported according to WFD the WISE contains the data reported in line with other water-related directives such as Urban Waste Water Treatment Directive, Bathing Waters Directive, Nitrates Directive, Drinking Water Directive, Flood Directive and Marine Strategy Directive. The description of inter-relationship between objects in each WISE dataset and their associated attributes provide through data models and data dictionaries. The WISE data model is developed following INSPIRE recommendation and it is modeled against a common conceptual model for ESDI. Therefore the WISE conceptual model doesn't create a single data model with each theme within WISE rather it puts data in the context of WISE enabling interoperability and harmonization (Guidance Document No: 22).

The harmonized data specification for hydrographic elements including surface water bodies and related phenomena is provided in the theme Hydrology as defined in Annex I of the

INSPIRE Directive. Geographically the Hydrology theme covers all surface water body areas covered by RBD as defined by WFD (TWG-HY). In addition to Hydrology, the WFD spatial data objects are related to:

1. Annex I
   o Geographic Names
   o Administrative Units
2. Annex II
   o Elevation
   o Geology
3. Annex III
   o Environmental monitoring facilities
   o Area management/restriction/regulation zones and reporting units
   o Statistical Units

The WISE metadata profile represents extended INSPIRE metadata developed in line with INSPIRE Metadata Implementing Rules: Technical Guidelines based on EN ISO 19115 and EN ISO 19119. In the WISE, the spatial objects are uniquely identified using the INSPIRE identifier which consists of 3 separate elements: inspireIdLocalId, inspireIdNamespace, and inspireIdVersionId. The given WISE spatial object can be used for the reporting obligation under different thematic context. To address those requirements, INSPIRE Annex II/III data specifications introduced the ThematicIdentifier. The ThematicalIdentifier consists of thematicalIdIdentifier and thematicalIdIdentifierScheme. The thematicalId is very important in the context of reporting since it is required to join the non-spatial data (reported under various directives) and related spatial objects.

2.5. Current status and legal framework for water body protection in Serbia

Preservation of water quality is one of the priority areas of environmental protection in the European Union. In September 2013 a Stabilization and Association Agreement between the EU and Serbia entered into force. The focus of the negotiation process is on the harmonization of current Serbian legal regulation with the EU acquis communautaire within 35 thematic chapters (Ministry of Foreign Affairs of the Republic Serbia). Chapter 27 contains the EU environment policy. Environmental acquis comprises over 200 major legal acts covering both horizontal issues and legal arrangements on water and air quality, waste management, nature protection and biodiversity, industrial pollution control and risk management, chemicals and genetically modified organisms (GMOs), noise, and forestry. The introduction of the WFD and its daughter directives aimed to bring a new era for European water management, focusing on understanding and integrating all aspect of the water environment to be effective and sustainable ((Ministry of Foreign Affairs of the Republic Serbia). The main objective of the Directive is to maintain the "good" to "high" ecological status of inland surface waters, transitional, coastal and groundwater and react whenever the status is not achieved.

In addition to the Water Framework Directive, the water management area is regulated by a series of EU legal acts (Directive on environmental quality standards in the field of water policy 2008/105/EC, Drinking Water Directive 2007/6/ EC, Urban Wastewater Treatment Directive 91/271/EEC (UWWTD), the Floods Directive 2007/60/EC, etc.), with which national laws must be harmonized. Water management in Serbia is the responsibility of the Water Directorate and is defined by the Law on Water 30/2010, 93/2012, Law on Environmental Protection 135/04, 36/09, Regulation on water classification 5/68, and Regulation on limit values for pollutants in surface and ground waters and sediments. Review of EU acquis in the area of water management and the period needed for full transposition is presented in Table 4.

Strengthening of the existing administrative and institutional capacity in the water sector is a

prerequisite for successful transposition and implementation of the Directive and most aid projects are focused on this issue (Transposition and implementation of environmental and climate change acquis-chapter 27: status and plans).

The cost of implementation in the water sector is extremely high and requires financing planning from the national, EU, and other sources. It is particularly related to the large investment needs especially in the implementation of UWWTD, the presence of arsenic in groundwater on the territory of Autonomous Province of Vojvodina, and other problems for the implementation of the Drinking Water Directive, implementation of environmental quality standards as well as the time required for the implementation of water management plans. Costs of implementation of the UWWTD, Drinking water directive, and Nitrates directive are estimate to 2000, 4962, and 819 million euros respectively. Moreover, costs for the implementation of the Floods directive are not currently assessed (MAEP).

Table 4. Transposition between EU acquis in the field of water and Serbian laws

EU Legislation	Serbia Legislation	Current status	Transition period
2000/60/EC Water Framework	Law on Water 30/2010, 93/12 Decision on the Designation of Water District Boundaries (75/10), Rulebook on Reference Conditions for the Types of Surface Waters (67/11), Rulebook on the Designation of Surface Water and Groundwater Bodies (96/10), Regulation on limit values of pollutants in surface waters, groundwaters and sediment and timelines for reaching of the values (50/12) and Rulebook on parameters of Ecological and Chemical Status of Surface Waters, and Quantitative and Chemical Status of Groundwaters (74/11), The Regulation on the Establishment of the Water Status Monitoring Programme (100/12, 43/13 and 85/14).	Partially implemented (47%)	2041
2008/105/EC Water Quality Standards	Law on Water, Regulation on limit values of the priority and priority hazardous substances polluting surface water and deadlines for their achievement (24/14).	Partially implemented (8%)	2033
2006/118/EC Groundwater	Law on Water (30/10 and 93/15), Regulation on limit values of pollutants in surface waters, groundwaters and sediment and timelines for reaching of the values (Official Gazette RS no. 50/12) and Rulebook on Parameters of Ecological and Chemical Status of Surface Waters, and Quantitative and Chemical Status of Groundwaters (Official Gazette RS No. 74/11).	In progress (25%)	2032
91/676/EEC Nitrates	Law on Water 30/2010, 93/12	In progress (15%)	2020
91/271/EEC UWWT	Law on Water 30/2010, 93/12	In progress (32%)	2041

98/83/EC Drinking Water	Law on Food Safety 41/09, Law on Water 30/10 and 93/12, Law on Public Health (OG RS 107/05), Law on Communal Activities (OG RS 88/11)	Partially implemented (59%)	2034
2007/6/EC Bathing Water	Regulation on water classification 5/68 and Regulation on limit values for pollutants in surface and ground waters and sediments, and the deadlines for their achievement 50/12.	In progress (23%)	2020
2007/60/EC Floods	Law on Water 30/2010, 93/12, Regulation on the establishment of the methodology for Flood risk assessment (1/12)	Partially implemented (71%)	2021

The current connection rate to wastewater treatment is around 13.6% (in 2010) while about 3% receive adequate tertiary treatment. Approximately 75% of the population in towns and only 9% of the population in rural areas is connected to the public sewerage system, so 35.8% of households in central Serbia and 23.4% in Vojvodina use the public sewerage system. Only 5% of industrial wastewater is treated in three phases (Đereg / Marković) and (IVJČ). Water quality monitoring is in the jurisdiction of the Agency for Environmental Protection and the Republican Hydrometeorological Institute. The first Programme of surface water body monitoring harmonized with WFD requirements was carried out in 2012. A total of 498 surface water bodies need to be monitored from which only 30 % are included in surveillance and operational monitoring (AEP). Monitoring stations are mainly located at large rivers and artificial water bodies while the smallest amount of data refers to small and medium waterways (altitude over 500 m) and small watercourses outside the Pannonia basin (IVJČ). Water quality is classified into five classes. The results of monitoring show continuous improvement of the ecological status/potential of all water bodies. In 2016, 14 % of the water bodies belong to the II quality class, 65% in the II, and 21 % to III quality class (Figure 6).
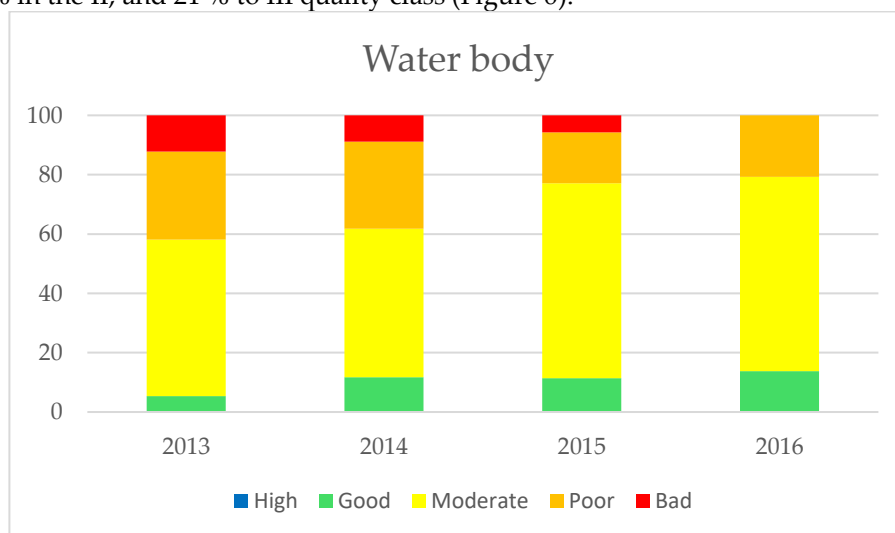
(a)
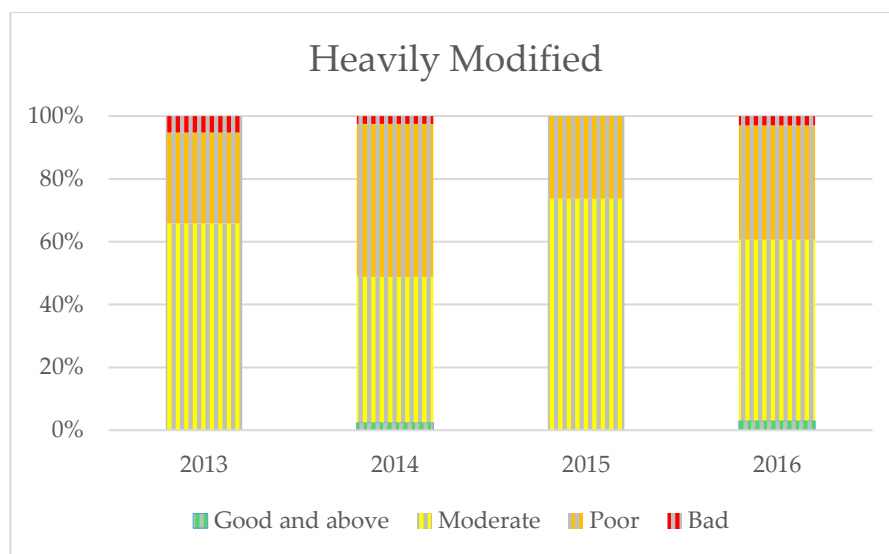
(b)
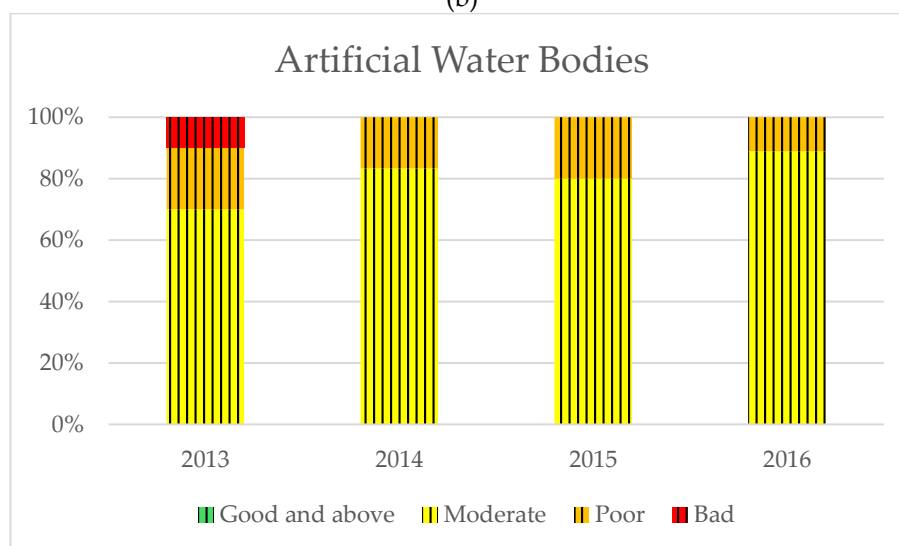
(c)

Figure 6. Ecological status/potential of water bodies in Serbia (a) ecological status of water bodies, (b) ecological potential of heavily modified water bodies, and (c) ecological potential of artificial water bodies
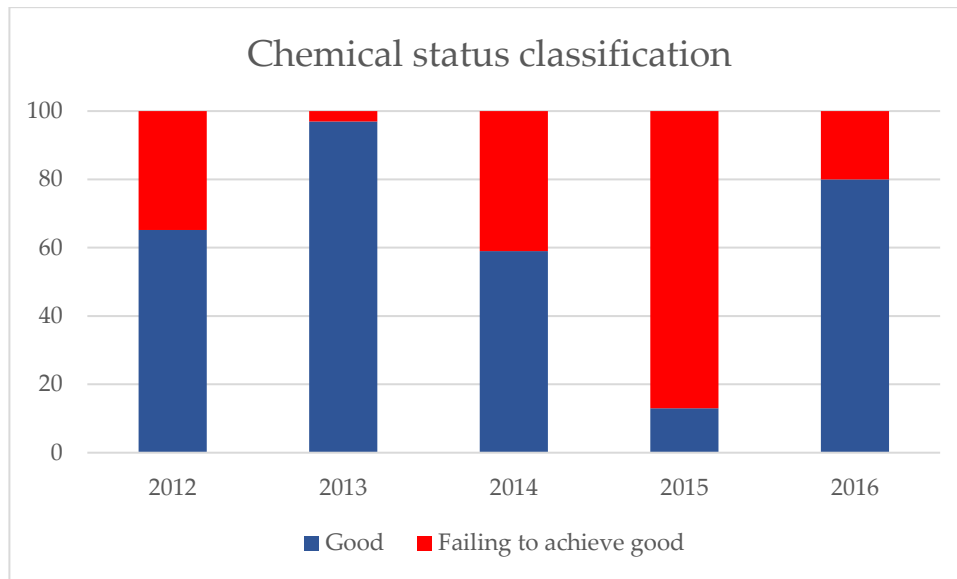
Figure 7. Chemical status of water bodies in Serbia

The deviation from good ecological status (middle ecological potential) and chemical status (Figure 6. and Figure 7) is due to various anthropogenic pressures, of which, according to data, the dominant wastewater of settlements and industry, farms, mines, and agriculture. The major derivation of physicalchemical parameter is noted for ortophosphor. Among the priority and specific pollutants, mercury and arsenic are distinguished in certain samples.

III Trends in IT and GIS

3.1. Spatial data

Spatial data are defined as *"any data with a direct or indirect reference to a specific location or geographical area"* (EPC). The real-world is a series of entities located in space. A spatial object is a digital representation of an entity. Spatial object *"means an abstract representation of a real-world phenomenon related to a specific location or geographical area"* (EPC).

To represent the real-world phenomena in the data model, it is necessary to understand the structure of geospatial phenomena. There are two types of spatial geospatial phenomena: discreet and continuous. The discreet phenomena are discontinuous and can be delineated from other phenomena. It has a clearly defined border and it easy to detect object beginning and ends. For example, rivers and lakes are discreet objects since the border between water and land can be definitively established. Continuous phenomena vary continuously, therefore it is not possible to delineate it as an individual object. The elevation is a continuous phenomenon. It is not possible to measure it everywhere, no matter how closely spaced, the elevation measurements are samples. The storing records of location and value for simple points are not enough since users need to derive useful information about properties of the surface such as slope, aspect, height at any point. Based on the characteristic of those geospatial phenomena, two types of data models have been created for digital representation of the real-world: vector (for discreet phenomena) and raster (for continuous phenomena) data model. The Vector data model stores spatial objects like point, line, or polygons. Raster data model stores spatial objects in the grid of equal-sized cells or pixels. Each pixel contains a value (intensity) representing information such as elevation.

In addition to geometry, each spatial object incorporates one or more attributes that describe a qualitative and quantitative characterization of the phenomena. Attribute data are collected and referenced to each object. For example, the lake can be described in terms of its name, depth, water quality, the concentration of chemical substances, fish population, ecological or chemical status, owner, etc. Attributes can be categorized as nominal, ordinal, or interval/ratio attributes. Nominal attributes are simply names or data generated by assigning the objects into unranked categories. Nominal attributes do not contain quantitative information, order, or size. The lake name or owner are examples of nominal attributes. Ordinal attributes represent data that can be ordered and ranked but not measured. The classification of the ecological status of the lake is an example of an ordinal attribute. Interval/ratio attributes are quantitative since, in addition to rank and order, the absolute difference in magnitudes between categories are defined. They are often recorded as real numbers on a linear scale. Examples of interval/ratio attributes for the lake are area, depth, results of water quality monitoring, the concentration of chemical substances, fish population, etc. The most accurate are ratio attributes representing the results of measurements with respect of origin on a continuous scale. In contrast, the least precise are ordinal attributes that describe the qualitative characteristics of a spatial object in text format.

Topological relationships also define spatial objects. Topological relationships have been considered as important as objects themselves (Chen, Chengming and Zhilin). Topology is the mathematical relationship among the points, lines, and polygons in a vector data layer. It describes the geometric characteristics that remain unchanged during transformation, such as translating, scaling, or rotating. Topology is primarily used to ensure data quality of spatial relationships.

Additionally, it can be used to model the integration of geometry from different feature classes, to improve GIS analysis or to increase access speed. The most commonly used mathematical framework for formalizing topological relations is 9-intersection models (9IM) (Egenhofer and Herring). The 9IM can identify eight topological (disjoint, meet, equal, inside, contains, covers, covered-by, and overlap) relationships between two polygons in R^2 (Egenhofer

and Herring). Besides, the relationships between polygon-line, polygon-point, line-line, line-point, and trivial point-point in 2D can be defined (Chen, Chengming and Zhilin).

3.2. Spatial big data

The rapid development of the internet and the Internet of Things (IoT) and mobile technologies produce the exponential growth of data volume. According to (IBM) the 90% of the world's data has been created in the 2 years (2014-2016) which is more than in the entire history of the human race. Also, the number of internet users grew from 2.4 billion in 2014 to 4.4 billion in 2019 (Schultz) producing a rapid flood of data. Although the data has great potential for decision support, they need to be analyzed to create information suitable for decision-makers. The term Big Data was introduced to represent growing volumes of data. Generally, big data refers to the heterogeneous collection of large structured and unstructured datasets that are so large and complex that they cannot be easily captured, stored, analyzed, and presented by traditional hardware, software, and database tools. The big data are characterized by 3 V's (Laney): Volume – represents the exponentially growing amount of data, from datasets with the size of terabytes to zettabyte; Valocity – the amount of data generated concerning time. The time to act based on those data is often very short therefore those data need to be analyzed in real or near-real time; Variety – represents the variety in data formats. Data can come in various data formats such as structured data and fitted in database tables, semi-structured data such as XML, unstructured data such as transaction and log data, text, image, audio, and video, etc. The heterogeneity of unstructured data represents the challenge for storage, analyzing, and visualization. Some authors have been defined as the additional dimension of Veracity to describe data integrity and quality (4 V's) (Marz and Warren).

It is estimated that approximately 80% of the information used by decision-makers is related to a geographical location (Worrall) which indicates the importance of geospatial data. The 4 V's commonly used to describe the big data are also relevant for geospatial data:

- Volume: Earth Observation (EO) satellites, sensor web for real-time monitoring, Unmanned Aerial Vehicles (UAV), Light Detection and Ranging (LiDAR) observation, ground measurements, permanent GNSS networks and Volunteered Geographic Information (VGI) produce the petabytes of data daily. Non-traditional geospatial data acquisition methods such as phone conversation and social media applications produce geospatial data at even faster speeds.
- Variety: geospatial data are available in different data formats from raster and vector data, point clouds, digitalized maps to geotagged text data, imagery data, videos. Many geospatial data has complex structures demanding more efficient models, indexes, and data management strategies and techniques.
- Velocity: The sensors in the sensor web, real-time GNSS trajectory monitoring, IoT cameras for real-time traffic monitoring produce the data in high frequency.
- Veracity: the level of accuracy varies depending on the data source. Much of geospatial big data are from unverified sources with unknown accuracy. For example, the unknown accuracy of VGI data is the main reason for the limited application (Mooney, Corcoran and Winstanley).

3.3. GIS big data acqusition tehniques

The availability of new sensors, new technologies and new ways of collecting spatial data provided the increasing availability of spatial information moving the acquisition of spatial data towards big data paradigm. Until recently, the collection of geospatial data was technically demanding based on the highly accurate, expensive professional devices and complicated measurement procedures. Now, spatial data acquisition is implemented in everyday devices such as smartphones used by many people. Similarly, the collection of topographic data for the digital

elevation model shifted from manual selecting and capturing significant topographic points to the collection of dense point clouds using LiDAR technology or UAV's and structure from motion algorithms. The environment data shifted from point-based monitoring in small regions to continual monitoring on a global level based on EO data.

3.3.1. Satellite images

Remote sensing, covering a large geographic area at different spatial, spectral and temporal resolutions, provides a large amount of data that have been extensively used for monitoring of water bodies geometry, topology, associated attributes and their changes (Verpoorter, Kutser and Seekell), (Feyisa, Meilby and Fensholt), (Rokni, Ahmad and Selamat). Satellite images are especially important for capturing information about water bodies in remote, inaccessible, extremely large or dangerous to access areas (for example, during floods) (Santoro, Wegmüller and Lamarche). The resolution of remote sensing data can be categorized based on four types of resolution: spatial, spectral, radiometric, and temporal. Based on spatial resolution, remote sensing images can be classified into very-high resolution (under 1 meter), high resolution (between 1 and 5 meters), medium resolution (between 5 and 30 meters), and low resolution (larger than 30 m) (DigitalGlobe). Over three decades, multi-resource satellite imagery of different resolutions, such as Landsat, Sentinel-1, Sentinel-2, RADARSAT Synthetic Aperture Radar (SAR), Moderate-resolution Imaging Spectroradiometer (MODIS), Worldview-2, Ziyuan 3 (ZY-3) or RapidEye (Table 5.) provides vital information about water bodies.

3.3.1.1. Monitoring of water body geometry based on optical images

Table 5 summarizes the state of the art of water body extraction using optical remotely sensed imagery, according to the water body type mapped, the classification approach, and the classification accuracy. Until now, several classification algorithms have been used to delineate water bodies, including unsupervised and supervised classifications (single band or multiple bands), single-band thresholding, and spectral indices. The water index and threshold-based approach have been widely used for rapid and automatic water body mapping in large scale regions (Verpoorter, Kutser and Seekell), (Feyisa, Meilby and Fensholt), (Yang and Chen), (Tetteh and M.). According to (Ji, Zhang and Wylie) the main problems when using water indices were that the results obtained using different indices were inconsistent and that the threshold values applied to distinguish water from non-water were unstable, varying with scene and location. The Normalized Difference Water Index (NDWI) and Modification of Normalized Difference Water Index (MNDWI) were not suitable for delineating water bodies from urban high-spatial resolution images since some urban structures (e.g. shadow, roads, and other dark objects) also have similar values for water as they do for the two indices (Li, Zhang and Xu), (Bochow, Heim and Küster). In addition, the use of water indices is limited because most of them use a Short Wave Infrared (SWIR) band (MNDWI, Automated Water Extraction Index (AWEI), Tasseled Cap Wetness (TCW), Land Surface Water Index (LSWI)) while most high resolution images have only visible and Near-infrared (NIR) bands (e.g. RapidEye, Quickbird, WorldView-4, GeoEye-1, IKONOS, SPOT 6-7) (SATIMG) so Normalized Difference Vegetation Index (NDVI) and NDWI (defined as in (McFeeters)) are the only possible choices for the indices.

A wide range of machine learning algorithms (MLA) as Maximum Likelihood Classifier (MLC), Random Forest (RF), Supported Vector Machine (SVM), Decision Tree (DT) and Artificial Neural Network (ANN) has been extensively used for supervised water body extraction (Table 5.). The SVM has been reported to achieve high performance and is suitable for waterbody mapping (Table 5.), especially with high dimension feature spaces and small training sample sets (Huang, Davis and Townshend), (Ji, Geng and Sun), (Doña, Chang and Caselles), (Byun, Han and Chae). Generally, the MLA provides higher classification accuracy than indexes and threshold-based approaches (Table 5.) since they utilize the information from the training data set. However, creating a representative training dataset is challenging due to the high heterogeneity

of land and water classes across different regions (Karpatne, Khandelwal and Chen). Additionally, the training process is computationally intensive and time-consuming. Due to that, the application is mostly limited at a local and regional scale.

In recent years, deep learning, especially Convolution Neural Networks (CNN), has proved to be an effective tool for large-scale image recognition (He, Zhang and Ren), object detection (Girshick, Donahue and Darrell) and semantic segmentation (Isikdogan, Bovik and Passalacqua). Development of methods for training end-to-end learning framework that enabled per-pixel classification increased availability of data and computational resources enable the use of deep learning in remote sensing (Gu, Wnag and Li) (Li, Huang and Gong). The main advantage of CNN is the ability to learn hierarchies of features by multiple convolutional layers, providing a high generalization capability. Several types of research have used different CNN architectures to extract the water bodies on a local, regional and global scale (Table 5.) with higher accuracy (compared to traditional MLA such as SVM, RF, ANN) due to accurately distinguish between water and shadow, snow, and ice (Isikdogan, Bovik and Passalacqua), (Fang, Wang and Chen), (Guo, He and Jiang). When using remotely sensed imagery as a data source for water body mapping, three main factors affect the final accuracy: the presence of low albedo surfaces, the size and shape of the water body, and the chemical composition of the water. On the one hand, the accuracy of water body mapping may be reduced significantly in areas where the background land cover includes low albedo surfaces such as asphalt roads and dark objects in urban areas, snow and shadows from mountains, buildings, and clouds (Feyisa, Meilby and Fensholt), (Kaplan and Avdan).   In these cases, water bodies and shadows cannot be easily separated due to their similar spectral pattern (Dare). The presence of shadows is a primary source of errors, especially in urban water extraction decreasing the accuracy of surface water mapping and change analysis (Huang, Li and Xu), (Donchyts, Schellekens and Winsemius), (Du, Zhang and Ling), (Verpoorter, Kutser and Tranvik). High spatial resolution images are more affected by dark building shadows than medium resolution images (Li, Gong and Sasagawa), and it is, therefore, advisable to design multi-scale mapping strategies for water bodies. Additionally, the integration of multispectral images and LiDAR data such as return dropout can reduce commission error caused by shadows. (Swan and Griffin) reported that usage of LiDAR data has been increased classification accuracy over 10%.

Table 5. Application of different imagery and classification approaches for water body extraction Note: AWEI, MNDWI, NDWI, Water Ratio Index (WRI), NDVI, High Resolution Water Index (HRWI), NDWIs, Normalized Green Index (NGI), Universal Image Quality Index (UIQI) are water indices, MLC, SVM, FPC: First Principal Component, MRSB: Most Related Single Band, RF: Random Forest, ANN: Artificial Neural Network, GWEM: GeoCoverTM Water bodies Extraction Method, RT: Regression Tree, TB: Tree Bagger, FCLS: Fully Constrained Least Squares, MESMA: Multiple Endmember Spectral Mixture Analysis, ASWM: Automatic Subpixel Water Mapping Method, CVA: Change Vector Analysis, K-T: K-T transformation, OWCEM: Orthogonal subspace projection Weighted CEM, UWEM: automated Urban Water Extraction Method, MLP: multilayer perceptron, MWEN: multi-scale water extraction convolutional neural network, GB: Gradient Boosting, SAPCNN: Self-Adaptive Pooling Convolutional Neural Network

	Author	Remotely sensed imagery	Waterbody type	Classification approach	Overall Accuracy (%)	KHAT	F1
Free imagery	(Feyisa, Meilby and Fensholt)	Landsat 5 TM (1984-2013)		AWEI MNDWI MLC		0.98 0.95 0.97	
	(Rokni, Ahmad and Selamat)	Landsat 5 TM (1984-2013)* Landsat 7 (1999-) Landsat 8 (2013-)	Lakes	NDWI WRI NDVI	99.35 98.45 99.06 96.63	0.95 0.93 0.95	
	(Verpoorter, Kutser and Tranvik)	Landsat 7 ETM+ (1999-)	Lakes	GWEM, ISODATA, K-means		0.20 0.31 0.28	
	(Olmanson, Bauer and Brezonik)	Landsat 7 ETM+ (1999-)	Coastline	SVM	72.17 – 97.65		
	(Frezier and Page)	Landsat 5 TM (1984-2013)	Rivers	MLC	97.4		
	(Rokni, Ahmad and Solaimani)	Landsat 7 ETM + (1999-)	Lakes	ANN, SVM, MLC	99.89 99.87 99.13		

(Doña, Chang and Caselles)	Landsat 5, 7, 8		RT	97		
(Chul Ko, Hun Kim and Yeal Nam)	Landsat 7 ETM+ (1999-)	Inland water bodies	WRI NDWI MLC K-T	85.17 64.83 83.78 77.10		
(Johnson and Iizuka)	Landsat 8 OLI (2013-)	Landuse	SMOTE-RF	78		
(Huang, Chen and Zhang)	Landsat	Inland water bodies	IB BI	96.26 94.57	0.87 0.80	
(Ji, Geng and Sun)	Landsat 8 OLI (2013-)	Lakes	OWCEM		0.87	
(Xie, Luo and Xu)	Landsat 8 OLI (2013-)	Lakes	SVM RF		0.98 0.98	
(Byun, Han and Chae)	Landsat 8 OLI (2013-)	Rivers	ASWM, MNDWI, FCLS, MESMA		0.86, 0.79, 0.58, 0.63	
(Du, Zhang and Ling)	Sentinel-2 (2015-)*	Water bodies	$MNDWI_{10m}^{PCA}$ $MNDWI_{10m}^{IHS}$ $MNDWI_{10m}^{ATWT}$	96.37 96.32 96.57	0.89 0.89 0.90	
(Yang, Zhao and Qin)	Sentinel-2 (2015-)*	Inland water bodies	NDWI MNDWI11 AWEInsh	92.9 99.4 99.6	0.41 0.92 0.95	
(Kaplan and Avdan)	Sentinel-2 (2015-)	Rivers	NDWI		0.89	

	(Yang and Chen)	Sentinel-2 (2015-)*	Inland water bodies	NDWI FPC MRSB	99.39 99.46 99.29	0.91 0.92 0.89	
	(Topaloglu, Sertel and Musaoglu)	Sentinel-2 (2015-) Landsat 8 OLI (2013-)		MLC SVM MLC SVM	70.60 81.67 76.40 84.17	0.66 0.79 0.72 0.82	
	(Isikdogan, Bovik and Passalacqua)	Landsat 7 ETM + (1999 -)	Inland water bodies	MNDWI MLP CNN			0.70 0.64 0.90
	(Wang, Li and Zeng)	Landsat 5, 7, 8	Inland water bodies	MNDWI RF Multiscale CNN		0.89 0.91 0.92	0.89 0.91 0.92
	(Yuan, Chi and Cheng)	Landsat 8 OLI (2013-)	Lakes	CNN	99.3		
	(Yu, Wang and Tian)	Landsat 7 ETM+ (1999-)	Inland water bodies	ANN SVM CNN	92.18 93.42 97.32		
	(Fang, Wang and Chen)	Landsat 8 OLI (2013-)	Lakes	SVM RF GB AlexNet VGG-16 ResNet50	83.82 82.76 83.95 90.79 90.53 91.45		0.84 0.83 0.84 0.90 0.90 0.91
Commercial imagery	(Huang, Davis and Townshend)	WorldView-1 (2007-)*	Inland water bodies	Linear-SVM RBF-SVM TB		0.68 0.69 0.68	

(Tetteh and M.)	RapidEye (2008-)		NGI, NDWI	93.9	0.89	
(Xie et al., 2016)	WorldView-2 (2009-)*		NDWI-MSI MLC-MSI SVM-MSI		0.98 0.98 0.98	
(Huang, Xie and Fang)	WorldView-2 (2009-)*	Rivers, Lakes, Canals, Ponds	Linear-SVM, RBF-SVM, TB,		0.68 0.69 0.68	
(Yao, Wang and Dong)	ZY-3 (2012-)		HRWI NDWI UWEM NDWIS		0.89 0.80 0.95 0.81	
(Wang, Wu and Wei)	GF-1 (2013-)	Inland water bodies	DenseNet 79			0.93
(Guo, He and Jiang)	GF-1 (2013-)	Inland water bodies	MWEN FCN UNet DeepLab V3+	98.62 98.52 98.18 91.82		
(Y. Chen, R. Fan and X. Yanf)	ZY-3, GF-2	Rivers	SAP CNN	99.29		

Another issue in water surface mapping is the size of the water body. Water bodies in urban areas are usually small and have a complex morphology, which results in a considerable amount of mixed pixels, the confusion between water and other features, and high spectral variance of the water body (Lu, Wu and Yan), (Donchyts, Schellekens and Winsemius). According to (Verpoorter, Kutser and Tranvik, Automated Mapping of Water Bodies Using Landsat Multispectral Data), the delineation of surface water bodies using moderate spatial resolution imagery is not reliable for detecting small water bodies due to the limited spatial detail. High resolution images can reduce the number of mixed land-water pixels, which increases the accuracy of delineation of water boundaries (Du, Zhang and Ling), (Yang, Zhao and Qin) (Yang and Chen, Evaluation of Automated Urban Surface Water Extraction from Sentinel-2A Imagery Using different water indicies); (Yao, Wang and Dong), (Chul Ko, Hun Kim and Yeal Nam) but also increases the shadow problem (Dare).

Besides, the accuracy of water body mapping is also affected by high levels of suspended solids, chlorophyll, nutrients, and various pollutants which change the spectral signature compared to those of unpolluted areas (Donchyts, Schellekens and Winsemius) making it difficult to use spectral indices with a single threshold to separate water from non-water pixels (Yao, Wang and Dong).

3.2.1.2. Monitoring of water body geometry based on radar images

Synthetic Aperture Radar (SAR), as an active remote sensing sensor operating in a longer wavelength compared with an optical sensor. It can penetrate clouds and collect ground information regardless of atmospheric conditions. Due to its any weather capabilities and image acquisition capacity during day or night or in cloudy conditions, SAR imagery offers an alternative to the optical imagery. The intensity of the returned signal from the surface is influenced by sensor and ground parameters, including the average surface roughness and soil dielectric properties (Brivio, Colombo and Maggi) (Massonnet and Souyris). Horizontal smooth surfaces with high dialectic constant, such as water bodies, acts like mirrors, and almost all backscatter is directed away from the sensor in the specular direction, providing a fragile return signal (Brivio, Colombo and Maggi) (Minchew, Jones and Holt). Due to that, water bodies are represented by dark tonality, making them easily recognizable. For this reason, many approaches for the delineation of a surface water body is based on the application of an image histogram threshold, with low backscatter value attributed to water (Bioresita, Puissant and Stumpf), (Behnamian, Banks and White), (Pierdicca, Pulvirenti and Chini), (Yomwan, Cao and Rakwatin), (Canisius, Brisco and Murnaghan). However, the backscatter varies depending on several mechanisms, such as bad weather conditions or the presence of vegetation. The backscatter coefficient can be increased by the wind-induced surface roughness, especially in VV polarization (Kuenzer, Guo and Hith) (Gstaiger, Gebhardt and Huth). The return signal over vegetated water bodies can be enhanced due to the double-bounce scattering. Besides, the double-bounced effect increases the backscatter values of waters near urban features such as buildings (Liao and Wen). The other flat surfaces, such as roads, can provide similar reflection properties as urban surface water (Stefan, Matgen and Hollaus). Due to that, water body extraction by applying a fixed threshold may give less accurate results.

To address those limitations, different approaches have been used. Hong et al. 2015. proposed water extraction (producer accuracy: 82.66 %; user accuracy 60.21 %) methods using SAR amplitude imagery and terrain information for thresholding method and object-based noise removal. The threshold values are determined based on the maximum-likelihood classifier and a land cover map created using Landsat TM imagery. (Vickers, Malnes and Hogda) used unsupervised K-means clustering algorithm and Sentinel-1, Radarsat-2 and ASAR images to create the maps of surface water cover with 1.4% accuracy. (Bolanos, Stiff and Brisco) presents

the combination of thresholding technique with texture indicators and edge detection algorithm for fully automated water classification of water bodies with high accuracy (88 %) based on Radarsat-2 image. (Benoudjit and Guida), used fusion of pre-flood SAR and optical Sentinel-2 data and Stochastic Gradient Descent for supervised classification of flooded extend with an overall accuracy of 90%. The mask was automatically generated based on Sentinel-2 data. (Bangira, Alfieri and Menenti), applied several MLA (DT, RF, k-nearest neighbor (k-NN) and SVM) to features derived from Sentinel-1 and Sentinel-2 data and compared the outputs with automatic thresholding for the detection of complex water bodies. Although MLA outperforms thresholding results the training data are needed therefore the authors recommend using dual thresholding based on the SAR and optical images for the universal model. (Huang, De Vries and Huang) were delineated water bodies from Sentinel 1 image (Kappa: 0.7) by using RF algorithm and Shuttle Radar Topography Mission (SRTM) water body dataset for mask generation. (Pham-Duc, Prigent and Aires), a used fusion of Sentinel 1 and Landsat-8 imagery as input and NN to determine optimal threshold value producing high accuracy (OA: 99%). (Simon, Tormos and P.-A) used integration of high resolution optical and radar data and OBIA (threshold) to detect the small land reservoir with high accuracy (OA: 98%) while (Mahdianpari, Salehi and Mahammadimanesh) employed OBIA and RF algorithm to extract water from ALOS-2 L-band, RadarSAT-2 C-Band and TerraSAR-X image with OA of 99.74%.

Recently the deep CNN has become state of the art in many fields such as landuse/landcover classification (Carranza-Garcia, Garcia-Gutierrez and Riquelme), water detection from optical images (Table 5.), or change detection in SAR images (Li, Peng and Chen). However, there are still very few studies dedicated to investigating the use of CNN for surface water detection in SAR images.

3.3.1.3. Monitoring of water quality based on optical images

Traditionally, the monitoring of Water Quality Parameters (WQP) is based on collecting samples from the field and laboratory analysis. Although in-situ measurement offers high accuracy, the application in monitoring spatial and temporal variations in water quality is highly limited because of the expensive and time-consuming process. The water quality within water bodies is rarely constant due to unpredictable events such as storms, accidental spillages, or leakages. The automated sensors network makes it possible to study quality variation with a high temporal resolution, but it is restricted to the geographic location of the instrumented stations. The spatial variation of water quality differs between different water body types, and it is highly influenced by hydrodynamic characteristics such as flow direction and discharge. It is more noticeable for the rivers, and variation will be greater near to the sources of pollution. Therefore the analysis of the spatial variability represents the powerful tool for identification and control of those pollutions (Zhao, Xia and Yang). Moreover, in-situ techniques are not suitable for monitoring a large number of water bodies at the regional or global level. Therefore the comprehensive assessment of spatial and temporal variation in water quality is challenging.

To overcome those limits, remote sensing technologies play an important role in monitoring and identifying water bodies over large scale regions more effectively and efficiently. The spectral characteristics of water are functions of the hydrological, biological, and chemical characteristics of water (Seyhan and Dekker). Therefore the amount of radiation at various wavelengths reflected from the water surface can be used directly or indirectly to detect different WQP. Many researchers have demonstrated the application of the optical images for the monitoring of physical and biological constitutes such as turbidity, chlorophyll concentration (Chl-a) (phytoplankton), and the organic matters such as Total Nitrogen (TN) and Total Phosphorus (TP) in different water bodies (Table 6.).

The clear water reflects light with wavelengths < 600 nm, resulting in high reflectance in the blue-green while absorbing radiation at NIR portion of the spectrum and beyond. The estimation of Chl-a based on remote sensing data is well established. Chl-a strongly absorbs blue (B) (first

peak of strong absorption) and red (R) light (second peak of strong absorption) while the reflection peak is located at the green (G) (minimal absorption) part of the spectrum (Ha, Koike and Nhuan). Various spectral bands have been used to quantify chl-a. (Bonansea, Pinotti and Derrero) used the R and G band, (Lim and Choi), (Nas, Ekercin and Karabörk) and (Ekercin) B, G, R, NIR band while (El Din, Zhang and Suliman) used all Landsat 8 bands to develop the algorithm for retrieve chl-a concentration. In additional to spectral bands, bands ratio such as NIR/R, G/R, G/B (Thi Thu Ha, Thien Phuong Thao and Koike), a normalized difference of R and G band (J.A.D, Alonso and Garcia), maximum chlorophyll index (computed based on R, NIR, and, RedEdge) (Elhag, Gits and Othman) have been used for monitoring with higher accuracy.

The remote sensing has been widely used for assessment of spatial and temporal Total Suspended Solids (TSS) patterns (Larsin, Simic Milas and Vincent), (Liu, Li and Shi), (Doji, Ferns and Broomhall). Spectral bands in the B and G spectral regions in combinations of R or NIR bands are used to explore the potential of TSS mapping. (Nas, Ekercin and Karabörk) employed the R band while (Ekercin) used G and R bands to retrieve TSS concentration. (Umar, Rhoads and Greenberg) reported that the R to G ratios with NIR and R bands are the most effective predictors of TSS. They used Landsat 8 and RF algorithm to predict TSS concentration within the range of 19 to 1700 mg/l with a root mean square error (RMSE) of 115 mg/l and mean absolute error (MAE) 68.3 mg/l. (Doji, Ferns and Broomhall) were used R and NIR bands to estimate TSS concentration between 2.4 and 69.6 mg/l with a RMSE and mean averaged relative error (MARE) of 5.75 mg/L and 33.33% respectively. (Vinh Pham, Thi Thu Ha and Phlevan) employed Landsat 8 for mapping TSS, ranged from 6.7 to 90.3 mg/m3) in the Red River with G/R ration reporting normalized RMSE (NRMSE) of 20 % while (Caballero, Steinmetz and Navarro) were used Sentinel 2 bands obtaining NRMSE of 25.06 % for R band and 10.28% for NIR band.

Turbidity is an optical index of water quality that directly impacts the clarity and color of the water column. It can be affected by suspended sediment (such as silt or clay, inorganic materials), Colored Dissolved Organic Matter (CDOM), inorganic or organic materials (chlorophyll, phytoplankton's). Although turbidity and suspended solids are highly correlated, it does not represent an exact measure of TSS concentration but is a good indirect indicator for it. An increase or decrease in water clarity can negatively impact on biological components of the system that may be adapted to specific light-penetrating conditions (Song, Wang and Blackwell), (Carson, Benjamin and Krista). Turbidity refers to the amount of incoming light attenuation, mainly due to particle scattering, increasing water reflectance in the R and NIR domain. In the SWIR part of the spectrum, the pure-water absorption is very high, and at very long SWIR wavelengths ($\lambda > 1600$ nm) even extremely turbid waters are effectively black (Shi and Wang) (the radiation completely absorbed by the water body). Single-band or ratio of two bands can be used to develop a relationship between turbidity and spectral reflectance. (Baughman, Jones and Bartz), (Guo, He and Jiang) reported the highest correlation between turbidity and R band while (Nas, Ekercin and Karabörk) used B, G, R bands. Also, (Baughman, Jones and Bartz), (Elhag, Gits and Othman) were obtained the high correlation between turbidity and Normalized Difference Turbidity Index (NDTI). (Dogliotti, Ruddick and Nechad) was used a single NIR band algorithm for retrieving the turbidity with nRMSE of 20 % for turbidity ranging from 1 to 1000 FNU. (Sakuno, Tajima and Yoshioka) were employed ratio of Sentinel-2's NIR and R band to retrieve turbidity with RMSE of 257 NTU while (Joshi, D'Sa and Osburn) was used Landsat 5 R band to map turbidity with RMSE = 7.78 ± 2.59 NTU. Analyzed studies show that the NIR band could be useful only in highly-turbid waters where particle back-scattering prevails over the water absorption, but it may not provide helpful information about water clarity in low to moderately turbid water (Joshi, D'Sa and Osburn). Therefore it should be noted that NIR band is recommended for high turbidity values while R band should be used for lower concentrations (up to 15 NTU) (Dogliotti, Ruddick and Nechad).

The satellite detection of TP and TN remind challenging since they don't have significant spectral responses therefore, methods used for their monitoring, based on remote sensing, can be divided into indirect and direct. Indirect methods try to find a relationship between TP and TN with optically active substances such as turbidity, TSS, chlorophyll. In contrast, direct method estimates nutrients concentration by establishing the relationship between surface reflectance and their concentration. (Wu, Wu and Qi) used the regression equation based on SDD and Chl-a i.e. R/G and B/R ratio to estimate the TP concentration. (Lim and Choi) used the R and NIR band for TN and G and NIR band for TN monitoring. (Elhag, Gits and Othman) were employed normalized difference of NIR and G band to monitor TN content. (Du, Wang and Li) was investigated the relationship between TP (range from 0.014 to 0.396) and Sentinel-3 surface reflectance by using a machine learning algorithm with RMSE of 0.049 mg/l. (Alparslan, Coskun and Alganci) using B1, B2, B3, B4, B5, and B7 of Landsat 5 obtained the TP concentration.

SDD is an optical property of water, and it represents the measurement of water transparency. The water transparency is determined based on light attenuation principles. Therefore, remote sensing has great potential for the estimation of SDD. It is highly correlated to water turbidity and the amount of TSS present in the water body, and it can be used to determine the concertation of nutrients. The review of the literature shows that SDD can be quantified using visible spectral bands and various band ratios. (Bonansea, Pinotti and Derrero) were used B and NIR band, (Zheng, Ren and Li) NIR/G ratio, (Nas, Ekercin and Karabörk) B/R while (Ekercin) employed B, G, and R band for the development of an algorithm for SDD measurements. Moreover, (Mancino, Nole and Urbano) reported the high correlation between SDD and B, R/G, B/G, G/B ratios.

The direct monitoring of DO by optical images is highly challenging. (Kim, Son and Kim) used multiple regression and MODIS Aqua Level 2 to map the spatial distribution of DO. The concentration of DO is computed as a linear combination of sea surface temperature (SST), SST in one month period, and Chl-a concentration. (Japitana and Burc) developed a regression model based on turbidity and coastal band to monitor DO. At the same time (Mushtaq and Nee Lala) was performed the regression analysis of principal component Axis I and Axis IV to monitor DO and single B band to monitor COD concentration. (El Din, Zhang and Suliman) and (Peterson, Sagan and Sloan) employed B, G, R, NIR, SWIR1, and SWIR 2 bands and NN to determine the DO concertation.

In addition to different band combinations, the various methods have been applied for WQP monitoring. (El Din, Zhang and Suliman) were used seven Landsat bands (B, G, R, NIR, SWIR1 and SWIR 2) and ANN for high accurate mapping of Turbidity, DO, Chemical Oxygen Demand (COD), and Biological Oxygen Demand (BOD). (Nas, Ekercin and Karabörk) were used 28 bands and band combination (B, G, R, NIR) and multiple regression to predict Suspended Sediment (SS), turbidity, chl-a , and Secchi disk depth (SSD) while (Song, Wang and Blackwell) were used ANN and Landsat 7 Band 1-4 and B3/B2 and B3/B1 band ratio for monitoring of chl-a, Turbidity, total dissolved organic matter (TOC), and TP obtaining RMSE of 0.82, 6.12, 1.52 and 0.04 respectively. According to the analysis (Table 6.), ANN outperforms other methods (J. Liu, Y. Zhang and D. Yuan) (El Din, Zhang and Suliman) (Song, Wang and Blackwell), providing accurate monitoring of water quality parameters.

Many studies have been using different platforms such as low resolution (MODIS-Aqua 250 m Data, MERSI), medium resolution (Sentinel-2, Landsat 8), and high-resolution images (IKONOS, QuickBird, RapidEye, Worldview 2) (Table 6.). The monitoring of optical active parameters such as chl-a, CDOM, SDD, TOC, TSM, Turbidity, EC, SPM is well established and can be based on images of different spatial resolution depending on the size of the water body. To monitor the hydro morphological parameters such as depth of water body, riparian zone, species structure in the riparian zone, the high resolution images need to be used (Table 6.). (Johansen, Phinn and Wite) compared the LiDAR, QuickBird, and SPOT data for riparian zone width and bank stability monitoring. The LiDAR produced the highest accuracy with the lowest

costs for a large stream area. Additionally, mapping of species structure in the riparian zone is challenging even with high resolution due to the spatial variability and limited width (Corbane, Lang and Pipkins). For example, (Peerbhay, Mutanga and Lottering) used the same data and methodology to map species at forest margins, open areas and riparian zone. The accuracy for the riparian zone was significantly lower compared to other (riparian zone: 67.8 %; forest margins: 91.3%; and open area: 85.1 %). To address those limitations (Jeong, Mo and Kim) integrated optical and LiDAR data.

The derivation of water body depth from multispectral images (satellite-derived bathymetry) is based on the fact that the amount of reflected radiance over shallow waters is a function of water surface reflectance, scattering and absorption in the water column, the bed reflection, and atmospheric transmittance. In the visible bands that penetrate the water column ($350 - 700$ nm), an exponential attenuation of radiance as a function of both depth and wavelength provides the fundamental principle for depth estimation (Stumpf and Sinclair), (Pushparaj and Hegde). Water clarity determines the penetration of light thought the water column and, therefore, the ability of optical images for bathymetry estimation. The depth of the water body bed can only be estimated to the extent of light penetration i.e. SDD (Pe'eri, Parrish and Azuike) and it is usually used for the coastal area that cannot be accessed by ship or airplane.

Landsat images, due to moderate spatial resolution, open access, and over 40 years long achieve, have been mostly used for monitoring WQP of inland water bodies (Table 6.). However, there is several limitations factor that needs to be considered. Developed models from remote sensing data require adequate calibration and validation using in-situ measurements and can be used only in the absence of clouds. To obtain reliable results, the time gap between gathering in-site and remote sensing data should be as small as possible. The Landsat 8 temporal resolution of 16 days imposes major limitations on inter-seasonal monitoring, especially in an area characterized by frequent cloud cover and haze. Atmospherically interference can be significant over the water body representing a potential source of error. Since the small difference in surface reflectance is significant, an appropriated atmospheric correction needs to be applied. Additionally, a spatial resolution of 30 m is not suitable for the narrow width and small area of urban water bodies, especially urban rivers, and channels.

Table 6. Application of different imagery and methods for water quality monitoring.

LR: Linear regression, MLR: Multiple Linear Regression, SVR: Supported Vector Machine Regression, ELR: Extreme Learning machine Regression, DNN: Deep Neural Network, BOMBER: Bio-Optical Model Based tool for Estimating water quality and bottom properties from Remote sensing images, LMM: Linear Mixed Model, PCA: Principal Component Analysis, CART: Classification and Regression Trees, CRF: Conditional Random Fields,
CDOM: colored dissolved organic matter, SPM: suspended particulate matter, TOC: Total organic carbon, COD: Chemical Oxygen Demand; BOD: Biological Oxygen Demand; TSS: Total Suspended Solid, SS: Suspended Solid, SDD: Secchi disk depth, BGA: Blue-green algae, SC: specific conductance. fDOM: fluorescent dissolved organic matter; SAV: Submerged Aquatic Vegetation; LAI: Leaf Area Index, TDS: Total Dissolved Solids, EC: Electrical Conductivity.
ALI: Earth Observing-1 Advanced Land Imager, HYP: Hyperion, HICO: Hyperspectral Imager for Coastal Ocean, TBM: phytoplankton total biomass

Author	Platform	Parameter	Parameter in WFD	Water body type	Method	RMSE	RE
(J. Liu, Y. Zhang and D. Yuan)	IKONOS	TN TP	PC- Nutrient conditions PC- Nutrient conditions	Inland water body	MLR **ANN**	0.89 mg/l 0.14 mg/l	0,98 0,94
(El Din, Zhang and Suliman)	Landsat 8	Turbidity TSS DO COD BOD	PC-Others PC-Others PC-Oxygen condition PC-Oxygen condition PC-Oxygen condition	River	**ANN** SVM	0.07 NTU 0.23 mg/l 0.18 mg/l 0.16 mg/l 0.04 mg/l	0,98 0.98 0.93 0.94 0.93
(Nas, Ekercin and Karabörk)	Landsat 5	Chl-a Turbidity SDD SS	B- Phytoplankton abundance/biomass PC-Transparency PC-Transparency PC-Others	Lake	MLR		0.47 0.57 0.58 0.67
(Lim and Choi)	Landsat8	SS TN Chl-a TP	PC-Others PC- Nutrient conditions B- Phytoplankton abundance/biomass PC- Nutrient conditions	River	MLR		0.74 0.48 0.73 0.58
(Sun, Li and Wang, A Unified Model for	Hyper spectral data	Chl-a	B- Phytoplankton abundance/biomass	Lake	SVM	2.67 mgm-3	0.90

Remotely Estimating Chlorophyll a in Lake Taihu, China, Based on SVM and In Situ Hyperspectral Data)							
(Mancino, Nole and Urbano)	Landsat 5	SDD Chl-a	PC-Transparence B- Phytoplankton abundance/biomass	Lake	LR	0.54 m 1.3	
(Quang, Sasaki and Higa)	Landsat 8	Turbidity	PC-Transparency	Coastal	Regression		0.84
(Guo, Wu and Bing)	Modis	Chl-a	B- Phytoplankton abundance/biomass	River	LR ANN		0.58 0.75
(Peterson, Sagan and Sloan)	Landsat 8 Sentinel 2	BGA Chla-a DO fDOM SC Turbidity	B-macrophyte B- Phytoplankton abundance/biomass PC-Oxygen condition PC-salinity PC-Transparency	Lake	MLR SVR ELR **DNN**	0.86 μg/l 7.56 mg/l 1.81 mg/l 14.50 QSU 48.46 μS/cm 5.19 NTU	
(Xiong, Lin and Ma)	Modis	TP SPM	PC- Nutrient conditions PC-Others	Lake	LR	0.031 mg/l 15.32 mg/l	
(Hafeez, Wong and Ho)	Landsat 5 Landsat 7 Landsat 8	SS Chl-a Turbidity	PC-Others B- Phytoplankton abundance/biomass PC-Transparency	Inland water body	**ANN** SVR Cubist RF	0.27 mg/l 0.70 mg/l 0.94 FTU	

(Elhag, Gits and Othman)	Sentinel 2	Chl-a TN Turbidity	B- Phytoplankton abundance/biomass PC- Nutrient conditions PC-Transparency	Lake	LR	0.05 0.01 0.16	
(Baughman, Jones and Bartz)	Landsat 7	Turbidity	PC-Transparency	Lake	LR	2.42 NTU	
(Song, Wang and Blackwell)	Landsat 7	Chl-a Turbidity TOC TP	B- Phytoplankton abundance/biomass PC-Transparency PC-Acidification status PC- Nutrient conditions	Lake	MLR ANN	0.82 μg/l 6.12 NTU 1.52 mg/l 0.04 mg/l	
(Ha, Koike and Nhuan)	Modis	Chl-a	B- Phytoplankton abundance/biomass	Coastal	LR	1.13 mg/m³	
(Thi Thu Ha, Thien Phuong Thao and Koike)	Sentinel 2	Chl-a	B- Phytoplankton abundance/biomass	Lake	Exponential regression		0.82
(Liu, Li and Shi)	Sentinel 2	SPM	PC-Others	Lake	Regression	28.14 mg/l	0.91
(Vinh Pham, Thi Thu Ha and Phlevan)	Landsat 8	TSS	PC-Others	River	Exponential regression	16.72 mg/l	
(Caballero, Steinmetz and Navarro)	Sentinel 2	TSS	PC-Others	Coastal	Regression	34.95 mg/l	
(Giardino, Bresciani	MODIS Landsat OLI RapidEye	Chl-a SPM CDOM Depth	B- Phytoplankton PC-Secchi disk depth PC-Color HM-Morphological	Lake	BOMER	$\pm0.1\ mg/m^3$ $\pm0,08\ g/m^3$ $\pm0,004\ m^{-1}$ 0.8 m	

and Cayyaniga)							
(Fricke and Baschek)	Landsat 7	Temperature	PC – Thermal condition	River		$\pm 0.7\,°C$	
(Pu, Bell and Meyer)	Landsat 7 ALI **HYP**	%SAV LAI	B-macrophyte/abundance B-macrophyte/abundance	Coastal	MLR	15.73% 1.12	0.78 0.58
(Ekercin)	IKONOS	SDD Chl-a TSS	PC-Transparency B- Phytoplankton PC-Others	River	MLR	0.15 m 1.13 $\mu g/l$ 0.73 mg/l	
(Koedsin, Intararuang and Ritchie)	WorldView 2	%SAV Species type	B-macrophyte/abundance B-macrophyte/composition	Coastal	MLR	$\pm 10.38\,g$ $* DW/m^2$	73.74 75.00
(Kutsar, Verpoorter and Paavel)	Mersi	CDOM DOC TOC DIC TIC pCO$_2$	PC-Color PC- Acidification status PC- Acidification status PC- Acidification status PC- Acidification status PC- Acidification status	Lake	LR		0.81 0.74 0.71 0.94 0.68 0.56
(Bonansea, Pinotti and Derrero)	Landsat 5 Landsat 7	Chl-a SDD Temperature	B- Phytoplankton PC- Transparency PC – Thermal condition	Lake	LMM		0.88 0.82 0.96
(Wu, Wu and Qi)	Landsat 5	TP	PC- Nutrient conditions	River	Regression		0.77
(Zheng, Ren and Li)	Landsat 8	SDD	PC- Transparency	Lake	LR	0.52 m^{-1}	0.82
(Keith, Lunetta and Schaeffer)	MODIS HICO	CDOM Salinity	PC-Color PC-salinity	Coastal	LR		0.83 0.81

(Cheng, Guo and Dang)	MERSI	N	PC- Nutrient conditions	River	LR		
(Doxani, Papadopou lou and Lafazani)	WorldView-2	Depth	HM – depth variation	Coastal	LR	0.01-1.52 m	
(J.A.D, Alonso and Garcia)	MERSI	Chl-a Phycocyanin	B- Phytoplankton	Lake	MLR	8.6 mgm^{-3} 12.92 mgm^{-3}	
(Garaba, Friedtichs and Vob)	MERSI	Color	PC-Color	Coastal	Regression		0.89
(Sun, Qiu and Li)	HJ1A/HIS	TP	PC- Nutrient conditions	Coastal	SVR		0.77
(Monteys, Harris and Caloca)	Rapideye	Depth	HM-Morphological conditions-Depth variation	Coastal	Log regression	$\pm 1\,m$	
(Heine, Stuve and Kleinschmit)	RapidEye	Water level	HM-Hydrological Regime-Quantity and dynamics	Lake		12 cm	
(Abdelmali k)	ASTER	pH EC Turbidity TDS Salinity Temperature Alkalinity Orthophosphorus	PC-Acidification status PC-Salinity PC-Transparency PC-Others PC-Salinity PC- Thermal conditions PC- Acidification status PC- Nutrient conditions	Lake	Quadratic regression		0.95 0.99 0.99 0.99 0.98 0.53 0.82 0.94

		TOC	PC- Acidification status				0.98
(Philipson, Kratzer and Mustaoha)	MERSI	Chl-a CDOM Turbidity	B- Phytoplankton PC-Transparency PC-Transparency	Lake	LR	0.9 $\mu g/l^{-1}$ 0.17 m^{-1} 0.32 mg/l^{-1}	0.85 0.87 0.90
(Brezonik, Olmanson and Finlay)	Sentinel 2 Landsat 8	CDOM	PC-Color	Lake	Log regression	0.44 0.47	
(Politi, Cutler and Rowan)	MODIS	Chl-a SDD	B- Phytoplankton PC-Transparency	Lake	LR		0.59 0.76
(Zolfaghari and Duguay)	MERSI	Chl-a SDD	B- Phytoplankton PC - Transparency	Lake	Regression	0.31 mg/l 0.19 m	
(Chebud, Naja and Rivero)	Landsat 5	Chl-a Turbidity TP	B- Phytoplankton PC-Others PC- Nutrient conditions	River	ANN	0.03 mg/l 0.5 NTU 0.17 mg/m³	
(Alikas, Kangro and Randoja)	MERSI	Chl-a TBM SDD	B- Phytoplankton B- Phytoplankton PC-Transparency	Lake	LR	9.1 mgm-3 9 gm-3 0.5 m	
(Kanno and Tanaka)	WorldView-2	Depth	HM-Morphological conditions-Depth variation	Coastal	LR	0.50 m	
(Mushtaq and Nee Lala)	Landsat 8	pH COD DO Alkalinity Chloride TDS TSS Turbidity EC P	PC- Acidification status PC - Oxygen condition PC - Oxygen condition PC- Acidification status PC-Others PC-Others PC-Transparency PC- Salinity PC- Nutrient conditions	Lake	Regression		0.61 0.45 0.49 0.43 0.48 0.62 0.66 0.50 0.62 0.73

(Johansen, Phinn and Wite)	QuickBird SPOT	Riparian zone width Bank stability Riparian zone width Bank stability	HM-Morphological conditions – structure of riparian zone	River	OBIA, threshold	25.73 m 1.35 38.66 m 1.51	
(Alaibakhsh, Emelyanova and Barron)	Landsat 5	Riparian vegetation cover	HM-Morphological conditions – structure of riparian zone	River	PCA, thresholding		0.82*
(Yousefi, Mirzaee and Keesstra)	Landsat 8	Riparian vegetation cover	HM-Morphological conditions – structure of riparian zone	River	SVM		0.88*
(Macfarlane, McGinty and Laub)	GeoEye-1 Oblique aerial photography	Riparian vegetation cover	HM-Morphological conditions – structure of riparian zone	River	OBIA		0.77*
(Peerbhay, Mutanga and Lottering)	WorldView 2	Riparian zone species	HM-Morphological conditions – structure of riparian zone	River	RF		0.68*
(Doody, Lewis and Benyon)	WorldView 2	Riparian zone species	HM-Morphological conditions – structure of riparian zone	River	ML		0.89*
(Strasser and Lang)	WorldView 2	Riparian zone species	HM-Morphological conditions – structure of riparian zone	River	OBIA, threshold		0.88*
(Ferndandes, Aguiar and Silva)	WorldView 2	Riparian zone species	HM-Morphological conditions – structure of riparian zone	River	OBIA, CART		0.77*
(Zhang, Pulliainen	Landsat 5	Turbidity SDD SS	PC-Transparency PC-Transparency PC-Others	Coastal	NN	0.35 FTU 0.25 m 0.72 mg/l	

and Koponen)							

3.3.1.4. Monitoring of water quality parameters based on the radar image

Although SARs data are widely used for water pollution detection like oil pollution and regional ice monitoring, their capabilities for monitoring biological and physicochemical water quality parameters, in the context of WFD, are limited. Radar waves do not notably penetrate to the water column. Therefore radar signals only carry information about water surfaces such as water surface geometry (roughness), the material on the water surface, and the dielectric constant of the top water layer. Few studies examine the ability of SAR for water quality monitoring. Most of them are based on the change of the dialectic constant of water. (Sieburth and Conover) reported that during the outbreak of algal bloom the layer of oil-like substance formed on the water surface. Therefore, the SAR data can be used to monitor algal bloom. (G. Wang, J. Li and B. Zhang) were employed the SAR image and SVM for monitoring of cyanobacterial blooms producing the OA of 67.74 %. However, the detection of algal blooms are highly limited due to wind. They reported that the wind speed of 1.3 m/s caused the dark regions leading to the overestimation of the area of the algal bloom. Moreover, the algal bloom does not appear on the water surface when wind speed is greater than 3 m/s. (Zhang, Pulliainen and Koponen) were used the combination of Landsat 5 and ERS-2 SAR C data and NN to improve the monitoring of turbidity, SDD, and SS concentration. The results show that SAR improves less than 5% accuracy (RMSE 0.28 FNU; 0.19 m; 0.65 mg/l respectively). (Bresciani, Adamo and Carolis) were used MERSI and ASAR and linear regression to determine the concentration of chl-a during the cyanobacterial bloom. The results show that the proposed methodology can be used to monitor high values of chl-a (>50 mg/m^3) with wind speed in the range of 2 to 6 m/s.

Although the SAR signal does not penetrate to water, the bathymetric features of shallow waters (<50 m) or even deep water (>500 m) (Li, Yang and Zheng) can be observed indirectly through the interaction of current and the underwater topology. (Wiehle, Pleskachevsky and Gebhardt) explored near-coast bathymetry from about -70 up to -10 m depth with RMSE of 7.1 m by using TerraSar-X data. (Bian, Shao and Tian) were used the Radassat-2 data and fast Fourier transformation to estimate water depth over the near-shore area with an average relative error of 9.73%.

Generally speaking, there are two approaches used to monitor water level by using SAR data: interferometric SAR and approach based on the water surface area fluctuation and related water level alterations. (Vickers, Malnes and Hogda) were used the Sentinel-1, Radarsat-2, ASAR data, and in-situ measurement to model the relationship between water extend and water level and monitor the lake water level with RMSE of 0.4 m. (Simon, Tormos and P.-A) used the COSMO SkyMed, TerraSAR-X images, and threshold method to monitor the water level (RMSE: 0.42 m). (Zaidi, Vignudelli and Khero) used Sentinel 3A data in the SAR mode and in-situ gauge measurement for lake water estimation with RMSE of 0.43 m similarly (Munyazneza, Wali and Uhlenbrook) and (Maillard, Bercher and Clamant) compared the altimetry data obtained from ENVISAR with gauge data reporting the RMSE of 0.25 m (for lake) and 0.6 m (for rivers) respectively. The approaches presented in (Zaidi, Vignudelli and Khero), (Munyazneza, Wali and Uhlenbrook), and (Maillard, Bercher and Clamant) relies partly on knowledge of the location of water bodies therefore the water body masks are used as the ancillary data. (Cao, Lee and Jung). estimated water level changes over wetland by using the ALOS2 images and differential SAR interferometry (dInSAR), producing the RMSE of 0.2 m while (Siles, Trudel and Peters) reported the RMSE of 0.07 m. (Yoon, Kim and Lee) demonstrated approach for highly accurate monitoring of water level (RMSE: -9 cm) in reservoirs from TerraSAR-X and InSAR. (M. Zhang, Z. Li and B. Tian) used L-band ALOS PALSAR InSAR image to study water level changes with RMSE of 0.04 m.

3.3.2. LiDAR

Recent advances in remote sensing techniques have greatly improved our ability to collect high-resolution topographic data at a range of scales. Light Detection And Ranging (LiDAR) remote sensing has become a widely used method to provide high-resolution topographical datasets duo to the advantage of collecting three-dimensional information very effectively over a large area by means of precision and time. LiDAR is an active remote sensing system that operates by emitting laser pulses of light at high frequencies towards the Earth's surface. Every emitted pulse propagates through the atmosphere before hitting a target, where parts of the pulse are reflected, absorbed, and transmitted depending on the characteristics of the illuminated object. A receiver collects the photons which are reflected. The range is computed by the travel time between the pulse and return of a signal.

3.3.2.1. Monitoring of water body geometry

Over the past years, the possibility of detecting water bodies from LiDAR data has been investigated. The LiDAR system mostly operates in the NIR spectrum. The reflection properties of water surfaces for NIR beams are categorized by strong absorption, hence, LiDAR intensity returns are usually lower than the intensity of the land. The point cloud returns of water surface are associated with low signal intensity, dropouts, and a high relative variation of intensity (Hofle, Vetter and Pfeifer), (Smeeckaert, Mallet and David). Of course, this depends on the velocity turbulence and depth of the water (Antonarakis, Richards and Brasington). To date, most of the water body classification methods work on rasterized digital elevation, and intensity models derive from the original point cloud. The overview of used parameters and methods for extraction of water body from LiDAR is presented in Table 7.

Table 7. Parameters used for water extraction from LiDAR data

Author	Method	Used parameters	OA [%]	Kappa
(Brzank, Heipke and Goepfert)	Fuzzy logic concept (Pixel-based)	Height, Intensity, 2D point density	96.50	
(Johansen, Tiede and Blaschke)	Threshold (Object-based)	DTM, Terrain slop, Fractional cover count to PPC		
(Johansen, Arroyo and Armston)	Threshold (Object-based)	DTM, Terrain slop, Fractional cover count, Canopy height model		
(Teo and Huang)	Supervised NN classifier	Lidar: nDSM, Roughness, Intensity, Echo ratio, Entropy, Homogeneity Spectral image: MNF, NDVI, Entropy, Homogeneity Object: Area, Length-to-width ratio	95%	
(Antonarakis, Richards and Brasington)	Threshold (object-based)	Canopy surface, Terrain model Vegetation height model, Intensity model, Identity difference model, Skewness model, Kurtosis model, Percentage canopy model	95-99	

(Smeeckaert, Mallet and David)	SVM (Pixel-based)	Height, Local point density, Local shape of the 3D point neighborhood	90.00	
(Hooshyar, Kim and D)	Thresholds (Pixel-based)	Intensity, Elevation		
(Crasto, Hopkinson and Forbes)	DT (Pixel-based)	Intensity, Scan Angle, Elevation, Point Density, SD Elevation, SD Intensity		0.94
(Morsy, Shaker and El-Rabbany)	Region grow -threshold (Point based)	Hight variation, Height standard deviation, Intensity coefficient of variation, Intensity density, Point density, Number of returns	99.00	
(Prosek, Gdulova and Bartak)	SVM (object-based)	Point density, Intensity, Ratio first/all returns, Elevation of nDSM, Slop, Multispectral reflectance		
(d'Andrimont, Marlies and Defourny)	Threshold (pixel-based)	Height, Intensity		
(Johansen, Phinn and Wite)	Threshold (object-based)	DTM, Slop, Plant fractional cover counts, Conopy height model	99.00	
(Schmidt, Rottensteiner and Sorgel)	ML CRL (point based)	Intensity, Point density, Distance to ground, Average height, Difference of average heights for various radii, Lowest eigenvalue, Gaussian curvature, Mean curvature		
(Hofle, Vetter and Pfeifer)	Region grow - threshold (point-based)	Elevation, roughness, intensity, and intensity density	97.00	

Most of the analyzed papers utilize the threshold method. The threshold values were manually selected to fit tested data, limiting algorithm generalization abilities and application for other study areas.

Water bodies usually occupy the lowest elevation in the scene, so the elevation threshold can be used to define the border between water and land. However, the elevation threshold will not provide accurate classification in elevated water areas since the elevation associate with the water body at hilly and low laying area will not be the same. The intensity of LiDAR return is a function of the aircraft's attitude, laser pulse angle of incidence, and water surface roughness. The water bodies are usually associated with low intensity of the return signal. However, discrimination of water bodies by using a single intensity threshold is challenging due to the high variation of intensity over the water body. The intensity peak can be found near the nadir regions, while the low intensity and dropouts are associated with higher inclination angles on the calm water (Hofle, Vetter and Pfeifer). The environment conditions, such as the wind, increase the water surface roughness causing the change of inclination angle and intensity of the return signal.

Additionally, smooth low albedo surfaces such as asphalt roads also have low intensity producing commission error. The intensity will also increase in shallow areas due to water body bed reflection. Besides, the LiDAR return intensity varies significantly with surface roughness producing high variance of intensity.

One the one hand, the main advantage of using LiDAR data for water body delineation is the ability to map the full extent of water body bed since LiDAR beam can penetrate to vegetation allowing to detect overgrown water surfaces. On the other hand, the accuracy of detected land/water border, in addition to classification accuracy, is influenced by the density of the point cloud since the water-land boundary runs somewhere between classifies water and non-water points (Hofle, Vetter and Pfeifer).

3.3.2.2. Monitoring of water quality elements

The monitoring of several hydro morphological WQP requires the three-dimensional. In addition to the 3D point clouds of the surface, LiDAR technology can penetrate dense vegetation and water providing information on the topography under vegetation, the structure of the vegetation, and bathymetry. Alongside with X, Y, Z coordinates, the intensity and number of returns are recorder for each point within the point cloud. The intensity is defined as a ratio of reflected and emitted light. It is a function of laser wavelength, the laser scanning geometry, and the water surface morphology (waves, roughness) (Yan, Shaker and LaRocque). The LiDAR sensor operates in the optical and infrared wavelengths. The most common is topographic LiDAR operating with NIR wavelength. Since water absorbs most NIR energy, the bathymetry LiDAR operating at 532 nm wavelength is designed to collect depth data. Additionally, ultraviolet fluorescence LiDAR, operating at 355 nm, provides an analysis of physical and biological parameters such as the turbidity or algae bloom. The overview of LiDAR usage for WQP monitoring is presented in Table 8.

Turbidity and bottom reflectivity are major factors that limited penetration depth of green laser pulses and thus the depth range that can be accurately surveyed. The turbidity is more important since it enters as a negative exponential factor, while bottom reflection is a linear factor (Guenther, Cunningham and LaRocque). The maximum reachable depth can vary from 1-2 m in very turbid waters to up to 50 m in very clear waters with highly reflecting bottom (Danson). It is reported that the bathymetric LiDAR can survey from 1.5 (Pratomo, Khomsin and Putranto) to 3 (Guenther, Cunningham and LaRocque) times SDD. However, the target area must be in a flight-capable area, and the cost of ALB is still too high. In addition to an actual reflection of the air-water interface, the first return of ALB contains the energy backscattered from particulate materials in the first water layer (Guenther, Cunningham and LaRocque). Due to that first return does not represent the water surface and topographic LiDAR can determine water level with higher accuracy compared to ALB (Zhao, Zhao and Zhang).

Table 8. WQP monitoring by using different LiDAR data

Author	LiDAR type	Parameter	The parameter in context of WFD	Water body type	Method	RMSE	RE
(Palmer, Pelevin and Goncharenko)	UFL	TSM CDOM Chl-a	PC-Others PC-Color B-phytoplankton	Lake	Regression		0.90 0.82 0.83
(Kinzel, Legleiter and Nelson)	Green LiDAR	Depth	HM-Morphological condition	River		0.15 m	
(Molkov, Fedorov and Pelevin)	UFL	Chl-a TSM	B-phytoplankton PC-Others	Lake	Regression	9.76 mg/m³ 0.66 mg/l	
(Mandlburger, Hauer and Wieser)	Green	Cross-section Riparian zone	HM-Morphological conditions – River depth & width variation HM-Morphological conditions – Structure of riparian zone	River	Manual	2 cm	
(Crasto, Hopkinson and Forbes)	Multispectral	Water Level	HM-Hydrological regime	River	Threshold		
(Wang and Philpot)	Green	Benthic habitat	B – macrophyte	Coastal	Manual		
(Brion, Chone and Buggin-Belanger)	NIR	Slop Width	HM- Morphology - Structure of the riparian zone	River			0.83 0.70

(A. Michez, H. Piegay and F. Toromanoff)	NIR	Riparian zone	HM-Morphological conditions – Structure of riparian zone	River	OBIA Threshold		
(Zhao, Zhao and Zhang)	Green	Water Level Depth	HM-Hydrological regime HM- Morphology	Coastal	Regression	5.03 cm 1.30 cm	
(Webster, McGuigan and Crowell)	Green	Depth seagrass	HM- Morphology B – macrophyte	Coastal	Threshold	10 cm	
(Johansen, Phinn and Wite)	NIR	Riparian zone width Bank stability	HM-Morphological conditions – Structure of riparian zone HM-Morphological conditions – Structure of riparian zone	River	OBIA Threshold	12.79 m 1.06	
(Jeong, Mo and Kim)	NIR	Riparian species	HM-Morphological conditions – Structure of riparian zone-species composition	River	OBIA DT		0.88
(Johansen, Tiede and Blaschke)	NIR	Riparian zone	HM-Morphological conditions – Structure of riparian zone-length/width	River	OBIA Threshold	3.9 m	
(Lasier, Hubert-Moy and Dufour)	Bispectral	Riparian species	HM-Morphological conditions – Structure of riparian zone-species composition	River	RF		0.67
(McKean, Nagel and Tonina)	Green	Depth	HM-Morphological conditions – Structure & substrate od river bed	River	RC/manual	$\pm\, 0.2\ m$	

(Yeu, yee and Yun)	Green and NIR	Depth	HM-Morphological conditions – Structure & substrate od river bed	Coastal	LR	0.2 m	
(Pratomo, Khomsin and Putranto)	Green	Depth	HM-Morphological conditions – Structure & substrate od river bed		Manual	0.24 m	

3.3.3. Unmanned Aerial Vehicle

Unmanned Aerial Vehicle (UAV) has emerged as a low-cost alternative to the conventional photogrammetric system for an image-capturing platform, which has allowed low-cost production of high quality and high-frequency data. In addition to the high spatial and temporal resolutions, UAV technologies bring a substantial improvement to the flexibility of the data acquisition and the design of the monitoring campaigns. Feature more, the development of the Structure from Motion (SfM) algorithm provided a cost-effective alternative method of rapidly acquiring very-high resolution (sub-meter) and hyper resolution (sub-centimeter) topographic data (Westoby, Brasington and Glasser). In that context, the UAV represents a possible solution to overcome certain shortcomings of satellite and aircraft systems. In addition, the development of lightweight sensors, available for integration with UAV platforms, provided acquisition of multispectral, hyperspectral, radar, and LiDAR high-resolution data with high flexibility in terms of cost and acquisition time. Table 9. Summarized current state of the art in water monitoring remote sensing based on UAV, focusing on biological, hydro morphological, and phisico-chemical aspects.

The UAV platform integrates various sensors, providing different data types that can be used for monitoring of different WQP. The main advantage is high resolution, low cost of equipment (for example: the price of UAV ~ $1000 -$20000, multispectral camera ~ $6000, LiDAR ~ $8000, radar ~ $300, PPK/RTK GNSS + IMU ~ $1000-$10000) and flexibility of arranging field campiness. However, there are two main limitations: the UAV is usually used for monitoring at a local scale, and most of the countries have established regulations that restrict the usage of UAV technology, especially in urban areas.

Table 9. Monitoring of water quality parameters based on UAV

Author	UAV type	Parameter	Parameter in the context of WFD	Water body type	Method	RMSE	RE
(Su and Chou)	Multispectral	Chl-a TP SDD	B-phytoplankton PC-nutrient conditions PC-Transparency	Lake	Regression	0.078 mg/l	
(Michey, Piegaz and Lisein)	Hyperspectral	Riparian species	HM-Morphological conditions – Structure of riparian zone	River	OBIA MF		75 %
(A. Michez, H. Piegay and L. Jonathan)	Multispectral	Riparian species	HM-Morphological conditions – Structure of riparian zone	River	OBIA RF		84 %
(Dunford, Michel and Gagnage)	RBG	Riparian species	HM-Morphological conditions – Structure of riparian zone	River	DT		91 %
(T.-C. Su)	Multispectral	Chla-a SDD Turbidity	B-phytoplankton PC-Transparency PC-Transparency	Lake	LR	14.19 $\mu g/l^{-1}$ 0.01 m 3.2 NTU	
(McEliece, Hinz and Guarini)	Multispectral	Chl-a Turbidity	B-phytoplankton PC-Transparency	Coastal	LR		78 % 74 %
(Wang, Yue and Wang)	Multispectral	DO Turbidity	PC-Oxygenation conditions PC-Transparency		MLRM ANN ELM	0.29 mg/l 0.69 NTU	
(Husson, Hagner and Ecke)	Multispectral	Riparian species	HM-Morphological conditions – Structure of riparian zone	Lake River	Manual		95 % 80 %

(Flynn and Chapra)	RBG	Aquatic vegetation	B-macrophytes	River	SAM		90 %
(Chabot, Dillon and Ahmed)	RBG	Aquatic vegetation	B-macrophytes	River	OBIA RF		78 %
(Bandini, Butts and Jacobsen)	Radar	Water level	HM - Hydrological regime	River	Regression	0.07 m	
(Biggs, Nikora and Gibbins)	RBG	Aquatic vegetation	B-macrophytes	River	Manual		
(Bandini, Pheriffere Sunding and Linde)	RBG Radar LiDAR	Water level	HM - Hydrological regime	River	Manual Regression Manual	0.18 m 0.03 m 0.22 m	
(Mandlburger, Pfennifbauer and Wieser)	Green LiDAR	Water level Water depth	HM - Hydrological regime HM-Morphological conditions –Structure & substrate od river bed	River		0.05 m 0.10 m	
(Ridolfi and Manciola)	RBG	Water level	HM - Hydrological regime	Lake	Threshold	0.05 m	

3.3.4. Monitoring of topology of a water body

In addition to the geometry of the surface water body, the spatial patterns (river network) and structure (river network topology) are fundamental characteristics of catchment, which is crucial for the understanding of water, sediments and nutrients transport, ecosystem dynamics, and geomorphological processes. A network is a mathematical representation of a spatial arrangement of a set of objects in the form of links (river channels) and nodes (sources and confluences), while the network topology represents interconnectedness in a network.

Traditionally hydrographic networks have been manually derived from topographical maps of air photos. Although it provides high accuracy, manual extraction is labor-intensive and unusable at a regional or global scale. To address those limitations, a method for automatic extraction from DEM has been developed and reported (Qin, Xu and Tian), (Wu, Li and Li), (Mao, Ye and Xu), (H. Chen, Q. Liang and Y. Liu). The DEM-based methods produce high accuracy in the steep and hilly regions, but accuracy is significantly reduced in low laying areas unless high-resolution DEM isn't used (Jakovljević and Govedarica, Water Body Extraction and Flood Risk Assessment Using Lidar and Open Data). Therefore, the application is limited due to the unavailability of high-resolution DEM. Moreover, the temporal changes in a highly dynamic environment cannot be accurately presented

Remote sensing data, on the other hand, provides global coverage with high spatial and temporal resolution. Recently, several approaches for the extraction of river centerline from river masks have been developed. (Pavelsky and Smith) were introduced RivWidth algorithm for the extraction of centerline and calculation of river width. The algorithm calculates the distance for each water pixel to the nearest non-water pixel and applies Laplacian filters to derive the centerline. (Allen and Pavelsky) were used RivWidth approach to create a Global River Network from Landsat (GRWL) databases. (Isikdogan, Bovik and Passalacqua) were created the RivaMap software for extraction of a river network by applying the singularity index in a fully automatic manner, however, the presented approach breaks the connectivity of the river network. Feature more, the centerlines of tributaries to the centerlines of the main river are not connected. (Monegaglia, Zolezzi and Guneralp) created PyRIS tool for extraction for automatic extraction of channel centerline from Landsat images by applying a skeletonization procedure followed by a pruning algorithm. Although this approach provides connectivity of the river network, it extracts only the main channel avoiding tributaries and spurs. (Schwenk, Khandelwal and Fratkin) developed method for extraction of centerline by using skeletonization and shortest flow path. However, the shortest path does not represent the centerline generally. Similarly, (Fisher, Bookhagen and Amos) and (Yang, Pavelsky and Allen) were applied skeletonization of extracted masks for detection of centerline while (Chen, Liang and Liand) were extracted centerline from Landsat by using best river path searching procedure. It outperformed RiverMap and GRWL in extraction locations of river networks and ensuring river connectivity. However, it is not able to completely extract anbranching rivers. (Obida, Blackburn and Whyatt) were created river centerline from Sentinel-1 images by using thin tools to reduce the number of cells representing the river.

The river network continuity is a common problem for all the presented method. Rivers, extracted from RS imagery, usually appears as a set of disconnected polygons due to natural obstacles (such as shadows, cloud) or man-made objects (bridge, dames). Feature more, the presented methods are based on water surface mask extracted from RS imagery using a single band or index threshold and therefore, the small water bodies are usually omitted, resulting in an incomplete river network. More importantly, all methods treat only links as an element of the river network, while nodes are completely omitted.

3.4. Open data

According to the accessibility to the data, sensors can be divided into two groups: commercial and free data sources (open data). The open data consists of data that is freely available, in reusable formats and under the provision of open licenses (without any restrictions both in terms of access and fee) (Hossain and Chan). The free, full and open data policy adopted by the Copernicus and Landsat programs has granted access to the Sentinel 1-2, Landsat 4-8 data products, via a simple pre-registration. The main advantages of free images are long term continuous data acquisition, global coverage, free and rapid access (especially important in emergency management), while spatial resolution is one of the largest limitations for some applications. Moreover, since the frequency of image observation may vary significantly depending on the location, using multiple satellite missions increases the temporal resolution of the datasets. In addition, (Mandanici and Bitelli) performed a radiometric comparison of Sentinel-2 and Landsat 8 Operational Land Imager (OLI) imagery for land and water monitoring. The results pointed out that in most cases, the data from both sensors can be combined, while some issues arose regarding the NIR bands.

Landsat series of EO satellites have continuously acquired images of the Earth's surface since 1972. Landsat 5 carried the Multispectral Scanner and Thematic Mapper (TM). TM provides seven spectral bands (Figure 8.) with a spatial resolution of 30 m and 16 days of temporal resolution. The Landsat 7 satellite carries the improved version of TM instrument, Enhanced Thematic Mapper Plus (ETM+), which provides eight spectral bands with a spatial resolution of 30 m except for the panchromatic band (spatial resolution 15 m).

Landsat-8 carries an improved OLI sensor and the Thermal InfraRed Sensor (TIRS). The OLI sensor provides nine spectral bands with a spatial resolution of 30 m, except the panchromatic band, which has a spectral resolution of 15 m (Table 2). The approximate scene size is 170 km north-south by 183 km east-west (Chul Ko, Hun Kim and Yeal Nam). The temporal resolution of Landsat 8 OLI images is 16 days.

Sentinel-1 is a C-band SAR satellite system operating at a center frequency of 5.405 GZ during day and night, enables image acquisition regardless of the weather. The C-SAR instrument support operation in dual-polarization (HH+HV, VV+VH) and four acquisition modes. The Interferometric Wide swath (IW) mode is the default acquisition mode over land. In the case of an emergency observation request, the Stripmap (SM) mode can be used. The polarization scheme uses HH+HV polarization for the polar areas while VV+VH polarization is available for all other observation zones (ESA, Sentinel-1 Observation Scenario). For Europe, the revisit time is 6 days. Besides, Sentinel-1 continuous the C-band SAR EO heritage of ESA's ERS-1, ERS-2 and ENVISAT and Canadian Radarsat-1 and Radarsat-2.

Sentinel-2 is a European wide-swath, high-resolution, multi-spectral optical satellite system which provides observations of global terrestrial surfaces with a revisit frequency of approximately 10 days using one satellite i.e. 5 days using two satellites (Sentinel 2B satellite was launched on March 07, 2017, data are still not available). Sentinel-2 carries a Multispectral Instrument (MSI) with 13 spectral bands from the Visible Spectrum (VIS) and NIR to SWIR at different spatial resolutions on the ground (Figure 8.), ranging from 10 m to 60 m with a 290 km field of view (ESA, Sentinel 2).
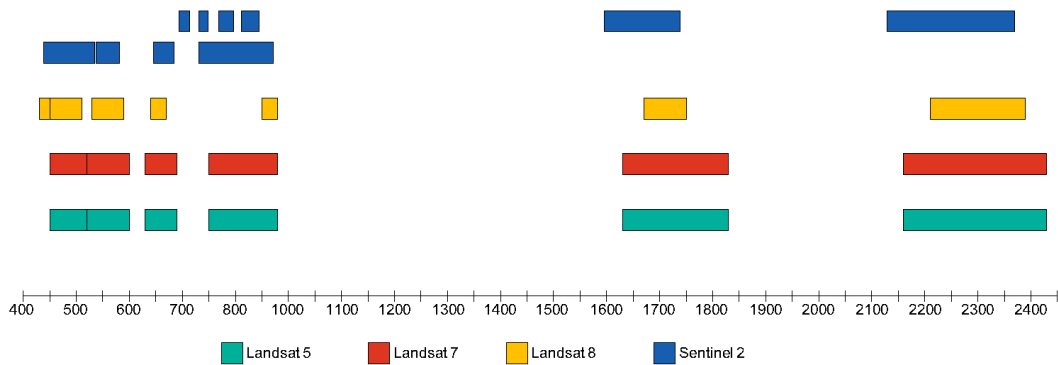
Figure 8. Comparasion of bands of Landsat 5, Landsat 7, Landsat 8 and Sentinel 2

The Advanced Spaceborne Thermal Emission and Reflection Radiometer (ASTER) Global Digital Elevation Model (GDEM) was jointly developed by the U.S. National Aeronautics and Space Administration (NASA) and Japan's Ministry of Economy, Trade and Industry. The ASTER GDEM covers land surfaces between 83°N and 83°S and is comprised of 22,702 tiles.   Tiles that contain at least 0.01% of the land area are included. The ASTER GDEM is distributed as Geographic Tagged Image File Format (GeoTIFF) files with geographic coordinates (latitude, longitude).   The data are posted on a 1 arc-second (approximately 30–m at the equator) grid and referenced to the 1984 World Geodetic System (WGS84)/ 1996 Earth Gravitational Model (EGM96) geoid (DAAC).

Regarding other types of open-source data, OpenStreetMap (OSM) is one of the most popular examples of a VGI project (OSM 2017). Over the years, OSM has turned out to be a serious geodata alternative for different applications and has been used in a wide range of Geographic Information Systems (GIS) and applications, especially in disaster management (Neis) and emergency planning, such as earthquakes (Poinani, Rocha and Degrossi) or floods (Eckel, Herfort and Zipf), (Schelhorn, B. and Leiner).

OSM aims to create, provide and compensate for the lack of free spatial data, since geographic data, even if freely available, are provided with licenses that restrict the use of the information (Girres and Touya). The data generally come from free sources like personal GNSS tracks, satellite imagery, or cadastral data. Additionally, different providers of high-resolution aerial images such as Bing Maps have granted permission to use their images for mapping activities (Goetz and Zipf). OSM data are freely downloadable in vector format (Girres and Touya). The positional accuracy of the OSM data depends on the way the data were collected (GNSS signal preciseness, displaced aerial images, manual digitizing using medium- or high-resolution imagery or bulk movements) and the contributors' freedom within the data collection process (Barron, Neis and Zipf). Due to the data collection method, the expected accuracy of OSM dataset is related to the quality of the GNSS receiver (which can have a positional accuracy of 6-10 m) (Haklay). OSM data quality and coverage also differ between regions. High positional accuracy and a large number of details that surpass what proprietary data vendors have to offer are found around urban areas with a high number of contributors. In contrast, rural areas often show a lower level of OSM data quality (OSM) (Barron, Neis and Zipf). The main advantage of OSM over the local authoritative data sets is that it provides global coverage, although data quality may vary. The OSM data set for Serbia can be downloaded from https://www.geofabrik.de. The dataset is provided as a set of thematic layers (buildings, natural points, railways, roads, waterways, and water), which are classified according to their OSM tags. The information about water bodies are represented in the "water" and "waterway" layers. The rivers, streams, canals, and drains are available as line geometries in the "waterway" layer, while lakes, reservoirs, large rivers, and wetlands are available as polygons in the "water" layer.

The volunteered nature of OSM is the main reason why GIS professionals have not adopted it that much (Mooney, Corcoran and Winstanley). This stresses the need to develop automated methods and tools to validate its quality in comparison to other datasets.

3.5. Geospatial artificial intelligence

Artificial intelligence (AI) is the capability of a functional unit to perform functions that are generally associates with human intelligence, such as reasoning and learning (ISO/IEC). Geospatial Artificial Intelligence (GeoAI) is a sub-disciple of AI that uses machine learning to extract knowledge form spatial data. The GeoAI has been recognized as an essential tool for automation of data processing, particularly image analysis and real-time information extraction (UN GGIM). Since big volume of satellite images, with global coverage and high temporal resolution, are available in the cloud, the neural network algorithms can be used for automatic detection and feature extraction.

3.5.1. Processing of remote sensing data

Over past decades, significant effort has been made in developing automatic water body classification methods using remote sensing data. Different approaches and methods have been developed to eliminate misleading information such as distinguishing water from low albedo surfaces (topographic shadow, cloud shadows, built-up areas) at optical images, increase of signal return due to the wind at radar image, or high variance of intensity and height for LiDAR data. Traditional classification approaches can be divided at pixel-based and object-based methods depending on the basic processing unit, per-pixel or per-object. Pixel-based methods are used widely to classify individual pixels based on spectral reflectance, without considering spatial or contextual information. In this context, pixels lack semantic meaning in the real world. There are two main limitations of the pixel-based approach: the mixed pixels and the 'salt and pepper' effect. The mixed pixel is defined as a single pixel that contains the features from multiple classes. It is usually associated with the classification of coarsely or medium spatial resolution. The second limitation is that contextual information about neighborhood pixels is not used in classification. Whit an increase of spatial resolution, the area represented by a pixel decrease. In a very-high spatial resolution image, the pixel size is significantly smaller than the object of interest, consequently, the interclass variance is higher, comparing to medium or coarse spatial resolution remotely sensed data. Due to that, the traditional pixel-based approach classifies pixels differently than the surrounding areas resulting in the 'salt and pepper' effect. Those limitations can be solved by an increase of spatial resolution (mixed pixel) or employing object-based image analysis (OBIA) ('salt and pepper' effect) (Blaschke, Lang and Lorup). The OBIA approach consists of two main steps: segmentation and classification (Ding). The segmentation algorithm aggregates the pixels into an object according to the one or more criteria of homogeneity and provides building blocks of OBIA. Object-based classification utilizes the properties of the object i.e. additional spectral information compared to pixels (mean band value, median values, minimum and maximum values, mean ratios, variance), geometrical features, spatial relations, and topology relations (Benz, Hofmann and Willhauck). The major limitation of OBIA is that selection of appropriated input variables, and a large number of parameters used in both steps. Determination of appropriate value for parameters is not trivial, and it is usually based on an integrative "trial-and-error" approach. In addition, image segmentation is computationally and time demanding, making it extremely challenging to handle large-scene data. The methods used for the extraction of information of water bodies from different types of remote sensing data are summarized in Table 10.

Table 10. Summary of the state-of-the-art water body classification methods with their input type. The orange color represents the multispectral images, blue LiDAR data, and red SAR images. Numerical values represent the number of papers within the category.

	The spatial resolution of remote sensing data	Pixel-based				Object-based			Cloud point			Manual
		Threshold	Regression	ML	DL	Threshold	Regression	ML	Threshold	Regression	ML	
Geometry	Very-high and high resolution	2		3	3							
		3		3					2		1	
						1						
	Medium resolution	10		5	3							
		6		4		1		1				
Attributes	Very-high and high resolution	1	10	6		4		3				2
		2	4	1		3		1				5
		1	1			1		1				
	Medium resolution		16	8		1						
			3	1				1				
	Low resolution		12	1								
Topology	Very-high and high resolution	1										
		3										
	Medium resolution	5		1								
		2										
	Low resolution											
	Integrated (Geometry, Attributes and Topology)											

The reviewed classification methods for extraction of water bodies from multispectral images start with pixel-based threshold methods, followed by pixel-based machine learning algorithms (MLP, SVM, RF) and reach the existing deep learning methods. The methods based on spectral indexes and thresholds have an accuracy range of (64% -99%), similar to pixel-based SVM (72%-99.6%), MLC (70% – 97%) and pixel-based RF (78% - 82%). In comparison between different MLA the SVM provided the highest accuracy (Table 10.) (Duro, Franklin and Dube) made a comparison of pixel-based and object-based image analysis for land use/land cover classification, including water class-based of medium resolution images. Based on the results, there was no significant advantage to preferring object-based image analysis over pixel-based for water body extraction using medium resolution images.

The mapping water body geometry from SAR image using pixel-based threshold method have an accuracy range of (88% - 98%), pixel-based ML algorithm (70% - 99%) while object-based method have accuracy range of (98% - 99.74%). There is not significant difference in performance of pixel-based (90% - 99%), object-based (95% - 99%) and point-based (97% - 99%) for water mapping based on LiDAR data.

According to the literature review, the methods for the established relationship between in-situ data and surface reflectance could generally be divided into two categories: traditional linear regression and MLA. In the recent studies, MLA such as an ANN (El Din, Zhang and Suliman), (Chebud, Naja and Rivero) and SVM (Sun, Li and Wang, A Unified Model for Remotely Estimating Chlorophyll a in Lake Taihu, China, Based on SVM and In Situ Hyperspectral Data) have been increasingly used in this field producing higher accuracy (Table 6.). The monitoring of

macrophyte, the riparian vegetation, and species structure is mostly based on VRH images and object-based methods.

However, these traditional methods rely on features or rules identified by experts in order to reduce the complexity of the data. Deep learning-based methods can automatically learn high-level features from the data, eliminating the need of expertise and hard feature extraction. Patch-based CNN has an increased accuracy range than other traditional methods (90% - 99.3%) (Table 5.).

3.5.2. Automated processing procedures

With an exponentially increasing volume of remote sensing data, automated processing procedures are crucial for analyzing big data and achieving the goal of real-time data. Overall, many scientists have been focusing on automating the workflow from collection to application. Those workflows include automated functions for detecting an object of interest, vectorization, linking of data sets, and adding attributions. As big volumes of satellite imagery are made available in the cloud, providing global spatial coverage with increasing granularity level (spatial and temporal resolution), both automatic change detection and feature extraction procedures can be performed through deep learning algorithms. Deep learning is the only viable approach to build automated processing procedures that can operate in a real-world environment. (Goodfellow, Bengio and Courville) defined deep learning as *"a particular kind of machine learning that achieves great power and flexibility by learning to represent the world as a nested hierarchy of concepts, with each concept defined in relation to simpler concepts, and more abstract representations computed in terms of less abstract ones."* The main advantage of deep learning is the way it represents an object of interest. Traditional ML (such as MLC, RF, SVM) do not examine the object directly, instead, the object is defined as a set of relative information created by experts. Each piece of information included in representation is known as a feature (Goodfellow, Bengio and Courville). For example, the expert will represent water bodies on multispectral images as reflectance in a specific band and spectral indexes. The traditional ML classifies water bodies based on the learned correlation between those features and outcomes and it cannot influence how features are created. Deep learning learns from the knowledge experience how to extract useful abstract features that are not contained in the input data avoiding the need for human operators. Each detected feature is described by different hidden layers. Therefore in deep learning first layer detect water body edges by comparing the brightness of neighboring pixels, the second layer extract corners and contours as a collection of edges, the third layer detect parts of the water body by finding the specific collections of contours and edges and finally the description of parts is used to recognize the water body presented at the picture.

3.5.2.1. CNN

In recent years, deep CNN has been achieved stat-of-the-art accuracy in a variety of computer vision tasks including image classification (K. He, X. Zhang and S. Ren), object detection (Ren, He and Girshick), (Gray, Fleishman and Klein) and semantic segmentation (Boonpook, Tan and Ye), (Ronneberger, Fischer and Brox). CNN is a type of NN that use convolution instead of general matrix multiplication, and it is specialized for processing image (gridded topology) data. The fundamental data structure in NN is a layer. A typical convolution layer consists of three operations convolution, detector, and pooling. Firstly layer preform convolutions on feature maps with two spatial axes (height and width of the image) and depth (number of channels). The convolution layer extracts the patches by sliding window of fixed size (usually 3x3 or 5x5) and preformed the transformation for all patches, via dot product with a weight matrix followed by adding bias to produce a set of linear activation (Goodfellow, Bengio and Courville), (Chollet, Deep Learning with Python). After that, each linear activation is run through a nonlinear activation function such as a rectified linear activation function (ReLU). In the end the output feature map is produced by pooling operation. The depth of the output feature

maps is defined by the number of filters which encode specific aspects of the input data allowing CNN to learn spatial hierarchical patterns. The batch normalization (BN) layer is placed after each convolution to speed up the training process and reduce the internal covariance of each batch of features maps.

The important aspect of the design of deep neural networks is a choice of a loss function. The loss function measures the performance of the network by computing the disagreement between network output (prediction) and expected (true) value. During the training, the loss should be minimized. Back-propagation is usually employed to train deep NN. It's work by propagating a feedback signal from output loss down to earlier layers, applying chain rule to compute the gradient of each network parameters with respect to the loss. The network parameters are then moved by the magnitude of the learning rate in the opposite direction from the gradient to minimize loss function (Chollet, Deep Learning with Python).

3.5.2.2. CNN for Semantic Segmentation

CNN has been quickly adopted for semantic segmentation of remote sensing images (Fang, Wang and Chen), (Guo, He and Jiang). Semantic segmentation aims to assign the set of predefined class labels to each pixel in the image. (Long, Shelhamer and Darrell) were first developed the end-to-end model for image segmentation called Fully Convolutional Neural Network. According to the structure, the state-of-the-art models for semantic segmentation can be divided into encoder-decoder and spatial pyramid pooling. The encoder-decoder consists of encoder function that converts the input data into feature maps by using convolution, activation, and pooling layer and decoder function that up sample the encoder features maps and convert them to segmentation results. SegNet and U-Net are typical architecture with encoder-decoder structure. The architectures are presented in Figure 9.

SegNet uses a flat architecture i.e. the number of features is the same in all layers (Figure 9. (a)) (Kendall, Badrinarayanan and Cipolla). The reduced spatial resolution in the encoder due to the pooling process is upsampled in the decoder by using the memorized pooling indices from the encoder sequence and convolution layers (Figure 9. (b)). This retains the high frequency of details in the segmented image, reduces training time, and provides high memory efficiency (Badrinarayanan, Handa and Cipolla). The final result of the decoder is classified by using soft-max algorithm. The output of soft-max is n channel image where n represents the number of classes.

The U-Net architecture (Figure 9. (c)) consists of an encoder that captures contextual information and a symmetrical decoder which restore spatial resolution. The encoder followed the typical architecture of CNN (convolution, activation, max-pooling), progressively decreasing feature maps resolution, and increasing the number of feature channels per each encoder at the same time. The skip connection is used to connect high resolution features maps from the encoder with corresponding upsampled output of the decoder, which allows the network to learn back relevant features that are lost after pooling operations and to predict more precise outputs based on that information (Ronneberger, Fischer and Brox). Due to that U-Net produces more precise maps than SegNet, but is more computationally demanding (Boonpook, Tan and Ye). However, the main advantage of U-Net is the ability to produce more precise segmentation with few training images (Ronneberger, Fischer and Brox). Several research have successfully adopted the U-Net architecture to remote sensing imagery. (Prathap and Afanasyev) won SpaceNet challenge by using U-Net for building segmentation. (Wieldand, Martinis and Li) were tested the performance of U-Net for water segmentation over 358 test image tiles of Landsat 5, 7, 8, and Sentinel 2, achieving the OA: 93% and F-1 score: 0.93. (Schuegraf and Bittner) were adapted the U-Net architecture for accurate building footprint extraction from VHR images (F1-score: 0.90). (Li, Liu and Yang) detected the sea-land boundary from VHR image with high accuracy (F1:0.98). The success of U-Net is mostly attributed to the several skip connection between layers that

reduce the length of the shortest path from lower layer parameters to outputs making it easier to gradient to flow and thus reduce the vanishing gradient problem.

(a)

(b)

(c)
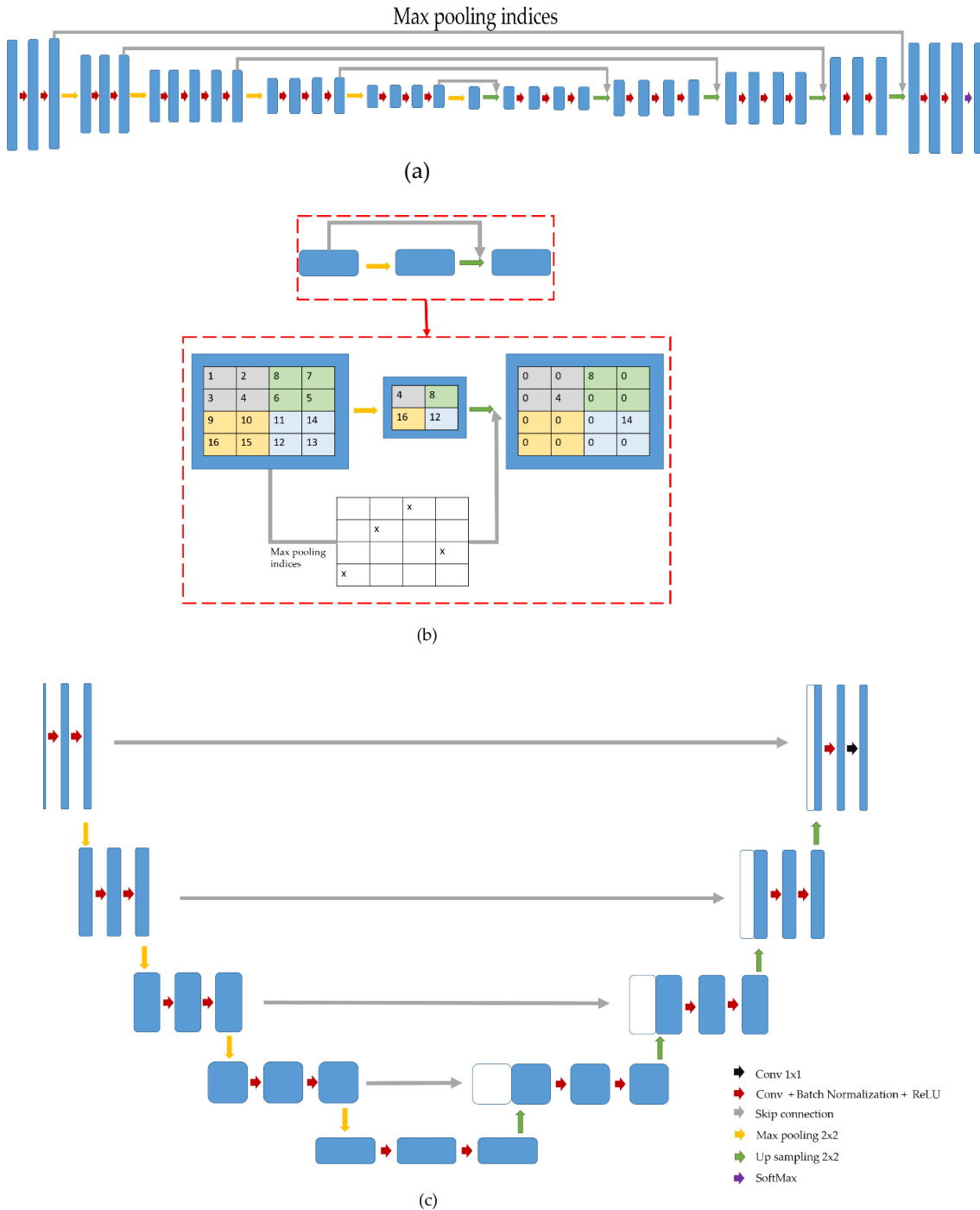
Figure 9. Encoder-decoder architecture for semantic segmentation (a) SegNet, (b) SegNet max pooling, (c) U-Net

Recently, Pyramid Scene Parsing Net (PSPNet) demonstrated outstanding performance on several semantic segmentation tasks such as urban scene classification (Cordts, Omran and Ramos) or ImageNet recognition challenge (Russakovsky, Deng and Su). PSPNet (Figure 10.) uses CNN to create a feature map. Then the spatial pyramid pooling model applies max pooling operation with four different windows sizes and strides to extract the multi-scale information (covering whole, half of and small portions of the image) from the feature map. Feature maps in different levels are fused as global pair and concatenated with the original output of CNN to

create final feature representation which contains global and local context information (Zhao, Shi and Qi). The final representation is then fed to a fully connected layer to get a per-pixel classification.

Figure 10. Architecture of PSPNet

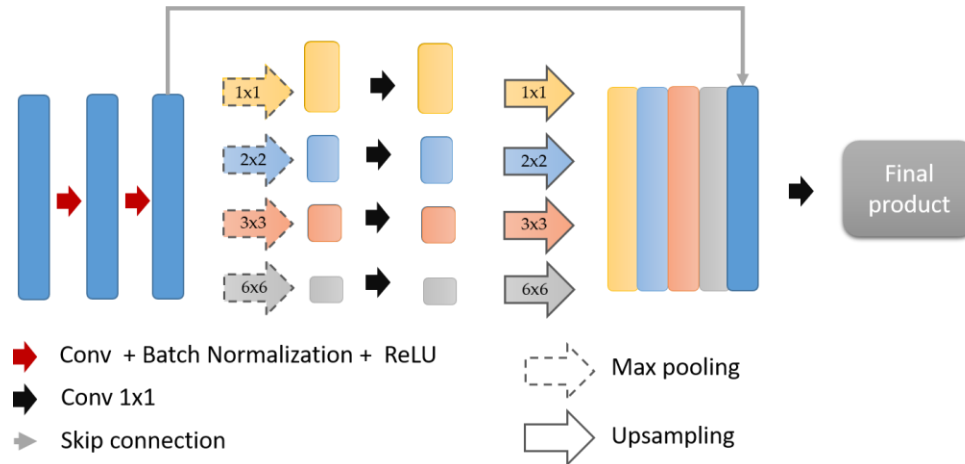(Y. Zhang, W. Li and W. Gong) compared performance of different network architectures such as SegNet, PSPNet and U-Net for building extraction. The highest accuracy was obtained for U-Net architecture. (Hu, Li and Lin) were obtained the same results. (Pashaei, Kamangir and Starek) evaluate the performance of U-Net, DeepLabV3+, PSPNet, SegNet, FCN for land cover mapping. U-Net produced the most accurate classification results.

3.5.2.3. Training of deeper neural network

Empirical studies show that the deeper models tend to perform better (Simonyan and Zisserman), (Goodfellow, Bulatov and J.) therefore the most common way to improve the performance of the network is increasing the depth. However, the deeper neural network is more difficult to train. A deeper network is more prone to the notorious problem of the vanish gradient. The vanishing gradient problem refers to a dramatic gradient decrease as it back propagates trough network, and by the time they reach close to the shallower layers, the updates for the weights nearly vanish.

To address the vanish gradient problem in very deep CNN (K. He, X. Zhang and S. Ren) introduced residual blocks. The residual block (Figure 11.(a)) uses a skip connection to perform the identity mapping. The untransformed input of the convolution layer is directly added to the output of the same layer therefore, the convolutional layer only has to learn to output a residual that changes the output of the previous layer. The output of the residual unit is defined as (K. He, X. Zhang and S. Ren):

$$x_{l+1} = x_l + F(x_l, W_l) \tag{1}$$

Where x_l is the input feature of the l-th residual block and W_l is a set of the weights associated with l-th residual block. Based on equation (1) the activation of any deeper unit can be written as the summation of the activation of shallower units and a residual function. This also implies that gradient consists of two additive terms: term that propagates information directly without concerns of any wright layers and another term that propagates through the weight layer (K. He, X. Zhang and S. Ren). This ensures that information can be directly propagated to any shallower unit x_l. Due to that the deep ResNet networks are much easier to optimize and more efficient to train deep networks. Additionally, the skip connection does not increase the number of parameters or computational complexity. The ResNets consists of residual blocks. The residual block has two 3x3 convolutional layers followed by batch normalization and ReLU activation function (Figure 11. (b)). The deeper ResNet with 50, 101 and 152-layer uses the bottleneck design

for the residual block to reduce training time. The block consists of 1x1, 3x3 and 1x1 convolution, where 1x1 reduce and restores dimensionality (K. He, X. Zhang and S. Ren). In addition, 1x1 convolution can be added to transform the input into the desired shape for adding operation.
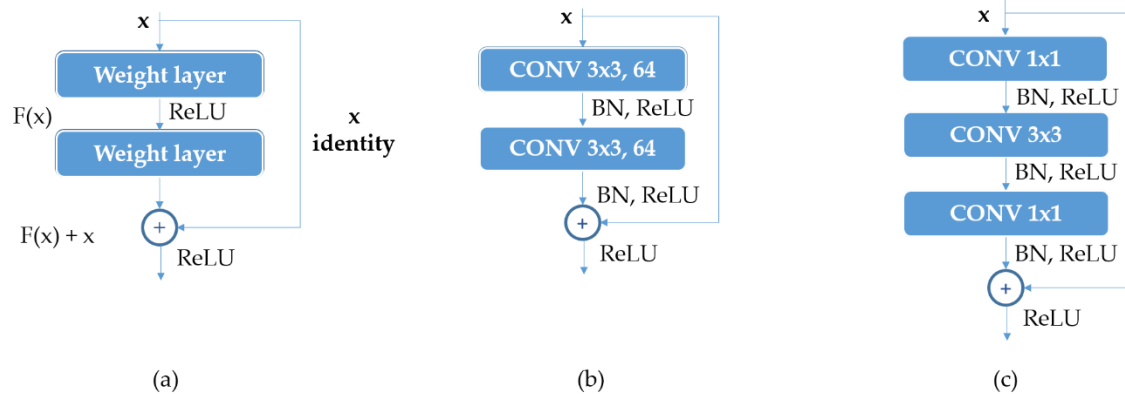

Figure 11. Residual learning (a) building block, (b) building block for ResNet 18/34, (c) building block for ResNet 50/101/152

3.5.3. Cloud computing

Management of the big remote sensing, including multi-resolution, multi-temporal, and multi-spectral datasets in different formats distributed across data centers, poses a significant challenge for traditional information systems. Moreover, the need for real-time processing at a global level is demanding even though the high-performance computing resources. Recently the Cloud computing has been used for addressing those challenges. According to (NIST) definition cloud computing represents "*a model for enabling ubiquitous, convenient, on-demand network access to a shared pool of configurable computing resources (e.g., networks, servers, storage, applications, and services) that can be rapidly provisioned and released with minimal management effort or service provider interaction*". Services on the cloud can be grouped into three categories: infrastructure as a service (IaaS), platform as a service (PaaS), and software as a service (SaaS) (Hwang and Chen), (Rittinghouse and Ransome).

IaaS provides customers on-permision virtualized infrastructure resources such as servers, storage, computational resources, or network on pay per use basis. Therefore customers can adjust the infrastructure resources to their needs and only pay for what they use, avoiding expense and complexity of buying and managing physical servers. Customers can use IaaS to build PaaS and SaaS for their customers.

PaaS delivers the computing resources needed for the development and management of cloud applications. The PaaS include components like middleware models, database management system, operational systems, programming languages, libraries, and web services providing the environment that enables users to develop, test, and implement of application through the internet.

SaaS provides and delivers the entire software to the users on pay per use basis. The software is accessed via the internet by any device. The software can be used instantly without any installation and shared between different users more efficiently.

Remote sensing data storage and processing have large requirements for computer performance. In order to provide data services for large scale applications and personalized products for water resource management, the remote sensing cloud-oriented infrastructure is developed in this study. The infrastructure consists of tree cloud infrastructure components IaaS, PaaS, and SaaS (Figure 12). At the bottom, the IaaS layer integrates the computing (Google Colab and GEE), storage (GEE and Google Drive), and network resources into a virtual environment that meets computing and storage needs. Google Earth Engine (GEE) (Gorelick, Hancher and Dixon) is a cloud-based platform for planetary-scale environment data access, analysis, and

visualization. It uses Google's computational infrastructure optimized for parallel processing of geospatial data. GEE provides access to a continually growing, petabyte-scale archive of publicly available, remotely sensed imagery such as Landsat 8, Sentinel 1, Sentinel 2, etc. The custom programs can be written by using client libraries that are available in Python and JavaScript language. The Earth Engine Python API can be deployed in a Google Colaboratory notebook.

Colab (Colab) allows anybody to write and execute arbitrary python code through the browser and is especially well suited to machine learning, data analysis, and education. Google Colab is a hosted Jupyter notebook service that requires no setup to use while providing free access to computing resources, including GPUs. However, the resources are limited to the single 12 GB NVIDIA Tesla K80 GPU that can be used up to 12 hours continuously. In addition to the free version, Colab pro is available. Colab pro offers access to T4 or P100 GPU up to 24 hours. The notebooks are stored at Google Drive. Data can be loaded/stored from Google Drive or Google Cloud Storage.
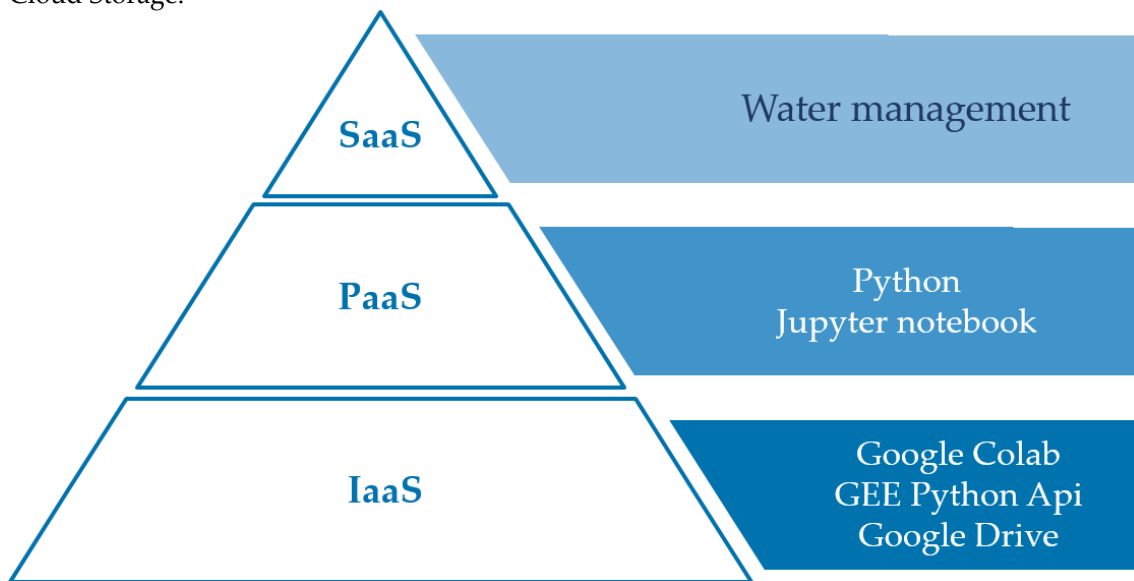

Figure 12. Implementation framework used in this thesis

The middle layer is implemented through Jupyter notebook and Python. The Python allows the development of cloud software for processing remote sensing data while the Jupyter notebook provides a platform for running developed software. The Jupyter Notebook (Jupyter) is an open-source web application that allows researchers to create and share documents that contain live code, equations, computational outputs, text, multimedia resources providing a flexible environment for performing end to end data science workflows – data cleaning, statistical modeling, building and training machine learning models, visualizing data, etc.

Python (Python) is an interpreted, object-oriented, high-level programming language with dynamic semantics. It is a general-purpose language specifically designed to simplify read and write. Python is developed under an OSI-approved open source license, making it freely usable and distributable, even for commercial use. Python supports modules and packages, which encourages program modularity and code reuse. Python is one of the most used programming languages for the development of deep learning algorithms. The TensorFlow, PyTorch, and FastAI are popular deep learning libraries.

The top layer is SaaS, which provides remote sensing water management services for automatic data processing through a unified interface, including computing, storage, and other services.

IV Multidimensional model

The application of geospatial and IT technologies in water resources management has not yet come to life at full capacity. As illustrated in Table 10, the application of new technologies is still limited to solutions and support for individual and specific activities in data collection, data processing, and data distribution. Most commonly, the result of such processing is a limited set of attributes and/or geometry or topology information. The water resources management systems is often restricted to only one aspect of application i.e. on a one dimension of the system.

The approach used in this thesis is primarily based on a comprehensive overview of the processes that are executed in the system form the moment of acquisition through processing to distribution of data, respecting the standards and related works, automating processes and observing the system from different aspects or dimensions.

A multidimensional model of the use of geospatial technologies in water resource management (Figure 13.) provides an overview of the system from the aspects of:
1. Comprehensive application of relevant standards in each phase from acquisition to distribution and usage (ISO, OGC, INSPIRE, WFD…),
2. Location-based characteristics of water resources (water resource is geospatial objects with elements of geometry, topology, and attributes),
3. Currently available geospatial technologies (GNSS, RS, LiDAR, Photogrammetry),
4. Currently available geosensor system for data acquisition (RADAR, SAR, Optical, MS, HS),
5. Currently available IT platforms and technologies (Big Data, Cloud, IaaS, SaaS, DaaS, AI, Python, Colab...),
6. Processing and data distribution(real-time, near-real-time and post-processing), and
7. Quantities of collected data per unit time (one data, thousands of data, millions of data).

The central place in the model is observation of the water resource as a geospatial object with geometry, topology, and attributes. The analysis and management of water bodies in the whole model are based on that definition. The attributive, geometrical and topological characteristics of such object are defined through the dimension of requirements determined by standards in water resources management and experiences from existing implemented systems in this filed. In this model, these characteristics are determined by automated procedures primarily based on AI and sensor systems. In this way, it is possible to process, distribute, and use data acquired by geo sensor systems in real-time or near real-time, which represents a significant step forward in processing concepts.

The primary aim of the proposed model is to reduce the time from data acquisition and to the moment of obtaining information suitable for the decision making process. A modern system for the acquisition of geospatial data in real-time, can be used as primary and recommended, but not only sources of data in this model providing real-time management of water bodies. The models primarily used for processing of geospatial data (processing of satellite images, photogrammetry images, point clouds collected by laser scanning) is still based on post-processing systems with significant usage of system resources (equipment, people, finances) in which specialist knowledge plays a key role. AI solutions used in this model enable automated procedures for the processing of geospatial data. Therefore, the influence of people on data processing is reduced to a minimum. This is crucially important for applying remote sensing technologies in water management since people with lower technical knowledge can extract useful information for the decision making process. Implementation of developed solutions in SaaS and cloud infrastructure additionally facilitates the application of this model.

A multidimensional model of use remote sensing data in water management consists of 7 fully automatized algorithms. The geometry of the water body is detected by using 3 algorithms based on optical images and CNN, SAR images and CNN and LiDAR data, ANN, and threshold

method. Attributes of the water body are extracted by using 2 algorithms for the detection of floating plastic based on UAV image and CNN and for monitoring of WQP based on optical images and ANN. Finally, an algorithm for automatic extraction of river network form optical and SAR images was developed.
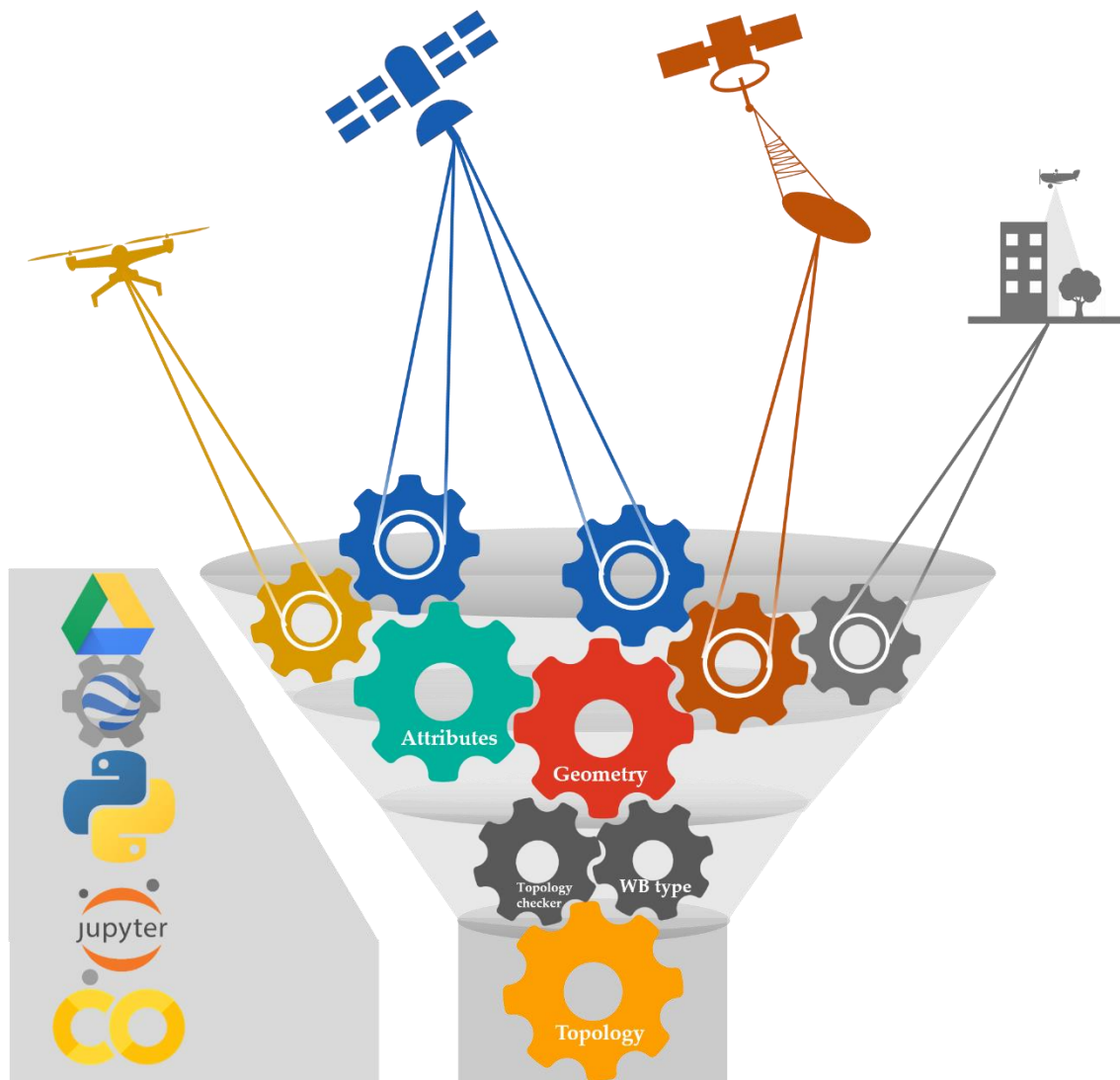
Figure 13. A multidimensional model of using remote sensing data in water management

4.1. Water body as a geospatial object

The WFD data model is proposed in (E. P. EPC). The data model aims to satisfy the requirements defined by Directive and extends the basic distinctions between "Surface Water" and "Groundwater" and "Protected Areas" adding the "Monitoirng Network", Management/Administration" and "Ecological Status" (Guidance Document No 9). Within the model, logically related features are grouped into four packages: Water Bodies, Monitoring Status, Administration and Status. Package Water Bodies define the classification of water bodies and all information relative to them. According to the type, WFD distinguishes Surface and groundwater bodies. Thus, the abstract class SurfaceWaterBody is classified into FreshWater and Saline Water. Package Management Units contain classes related to management and administration. These units are river basin district, river basin, sub-basin, ecoregion, and protected area. River basin district means the area of land and sea, made up of one or more

neighboring river basins together with their associated groundwaters and coastal waters, and represents the main unit for management of river basins. A WaterBody or a Monitoring station may belong to a single RiverBasineDistric. Monitoring stations are defined in Monitoring Station packages. According to water body type WFD distinguish monitoring of surface water and groundwater therefore class Monitoring station is divided into two subclasses: SurfaceMonitoirngStations and GroundwaterMonitoringStations. The status parameters are stored in Status package. For SurfaceWater bodies, four classes are defined: FreshWaterEchologicalStatus, PhysicoChemicalClassification, SalineWaterEcologicalStatus and SWStatus. The GWStatus class provides status reports for a given date for a given Groundwater Body. The UML diagram of WFD data model is shown in Figure 14.
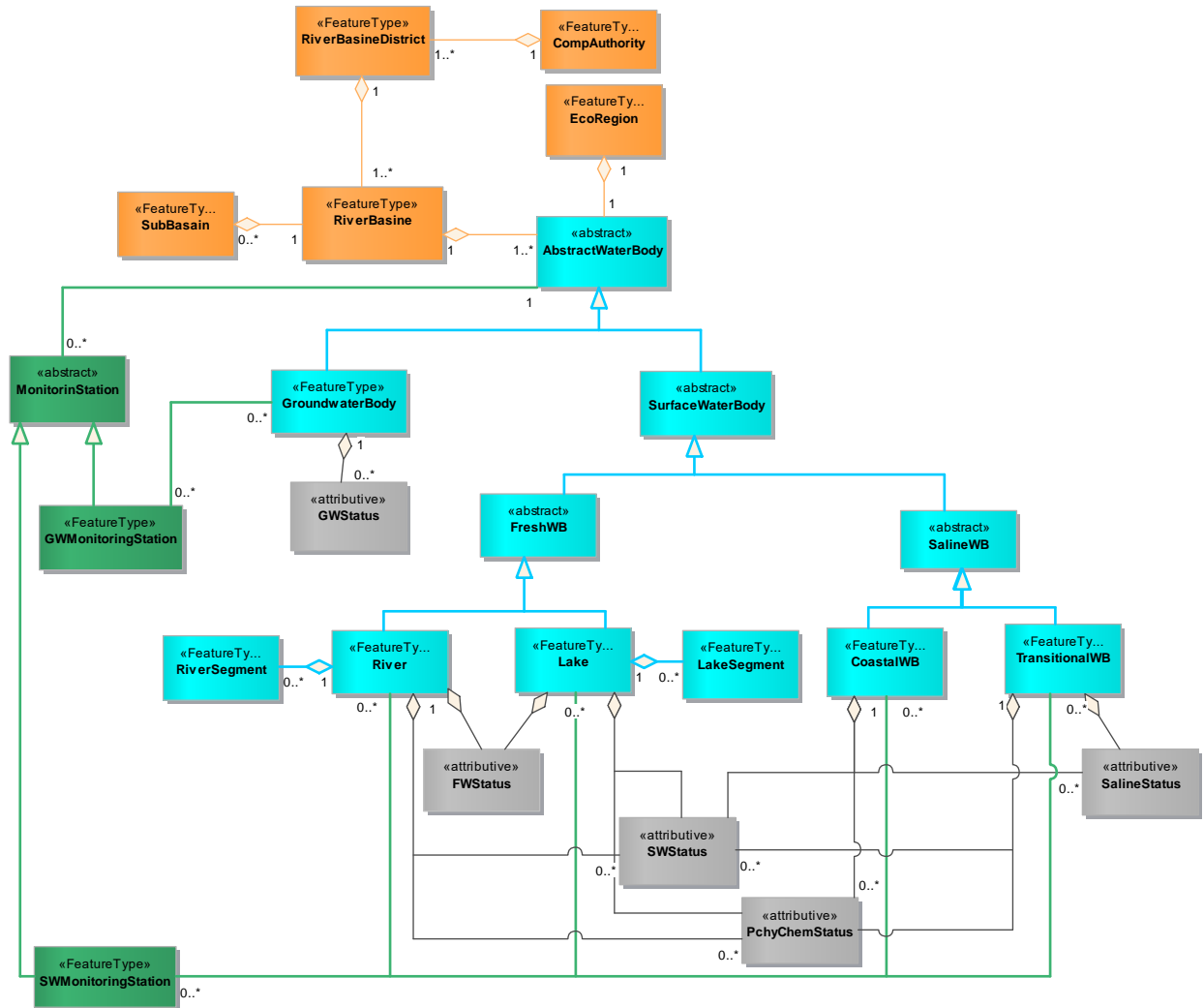
Figure 14. WFD data model

INSPIRE DIRECTIVE (2007/2/EC) serves to establish the necessary infrastructure for spatial information within the EU to ensure the better integration of environmental policy. The INSPIRE Directive responds to the need for quality geo-referenced information to support understanding of the complexity of, and interactions between, human activities and environmental pressures and impacts (EC-Sector 2).

INSPIRE data specification to specify common data models, code lists, map layers and additional metadata on the interoperability to be used when exchanging spatial datasets. Datasets in the scope of INSPIRE are organized in three annexes and 34 spatial data themes.

Data required by WFD should be collected once and shared among public sector organizations across boundaries therefore WFD data should be created and maintained compatible with the INSPIRE dataset and should be available in INSPIRE model.

Associations have been defined between WFD spatial object types within INSPIRE themes to represent the explicit relationship between the themes:

•WFD Surface Water Body is related to one or more HydroObject (Annex I INSPIRE theme Hydrography (INSPIRE HY))

• WFD Ground Water Body is related to one or more GroundWater Body and/or Hydrogeological Units (Annex I INSPIRE theme Geology)

•WFD Monitoring stations are related to Environmental Monitoring Facilities Objects (Annex III INSPIRE theme Environmental Monitoring Facilities)

•WFD subunits and RiverDistricBasin are related to Management Regulation or Restrict zone (Annex III INSPIRE theme Area Management/Restriction/Regulation Zones and Reporting) Also, surface water bodies defined according to WFD are represented as Reporting units.

•Elevation data are part of Annex II INSPIRE theme Elevation.

The Annex I theme Hydrography is involved with a description of the sea, lakes, rivers and other waters, with their phenomena and all hydrographic-related elements (INSPIRE HY). Geographically, the theme —Hydrography covers all inland water and marine areas covered by river basin districts as defined by WFD. The INSPIRE HY theme is based on physical water objects that form part of the hydrological network (watercourses, standing water, wetlands). Altho, WFD water bodies, follow the geometry of the surface waters, the nodes can differ from the nodes of the physical watercourse segment. Also, the number of watercourses forme a single waterbody for the WFD. Since Inspire HY doesn't specify how a watercourse should be broken into smaller pieces it is possible to build a reporting unit e.g. from sections of the watercourse and/or standing water, through a common identification in the base HydroObject (INSPIRE HY). A number of these sections would then form e.g. a WFDRiver or WFDLake (Annex III Area Management/Restriction/Regulation Zones and Reporting – Reporting Units)

The drainage basin and river basin in HY pertain to the physical catchment area and not to the RiverBasinDistrict (RBD) or SubUnit as defined in the Water Framework Directive. These last two are administrative units that have no direct relation to the physical catchment and basin therefore RBD more a reporting unit then a physical feature and there are not modeled by Annex I theme but is deemed to be part of Annex III theme management and reporting units.

INSPIRE has adopted the use of ISO 19156:2011 standard on Observations and Measurements for the reporting of observation and measurements, which includes the process of taking samples and measurements taken directly on some feature of interest or indirectly on a specimen taken at a feature of interest.

Additionally, a menage of information on the temporal variability of non-hydrological features, including the identification of predecessors and successors, needs to be provided (Guidance Document No: 22). The predecessor identifies the object that the current object replaces while successors specify the object that replaces the current object. The concept of predecessors and successors does not exist in the INSPIRE AM theme. Therefore the INSPIRE Annex III – Statistical Units date specification was integrated, providing the concepts and data elements to represent changes.

The integration of the INSPIRE and WFD model is shown in Figure 15.
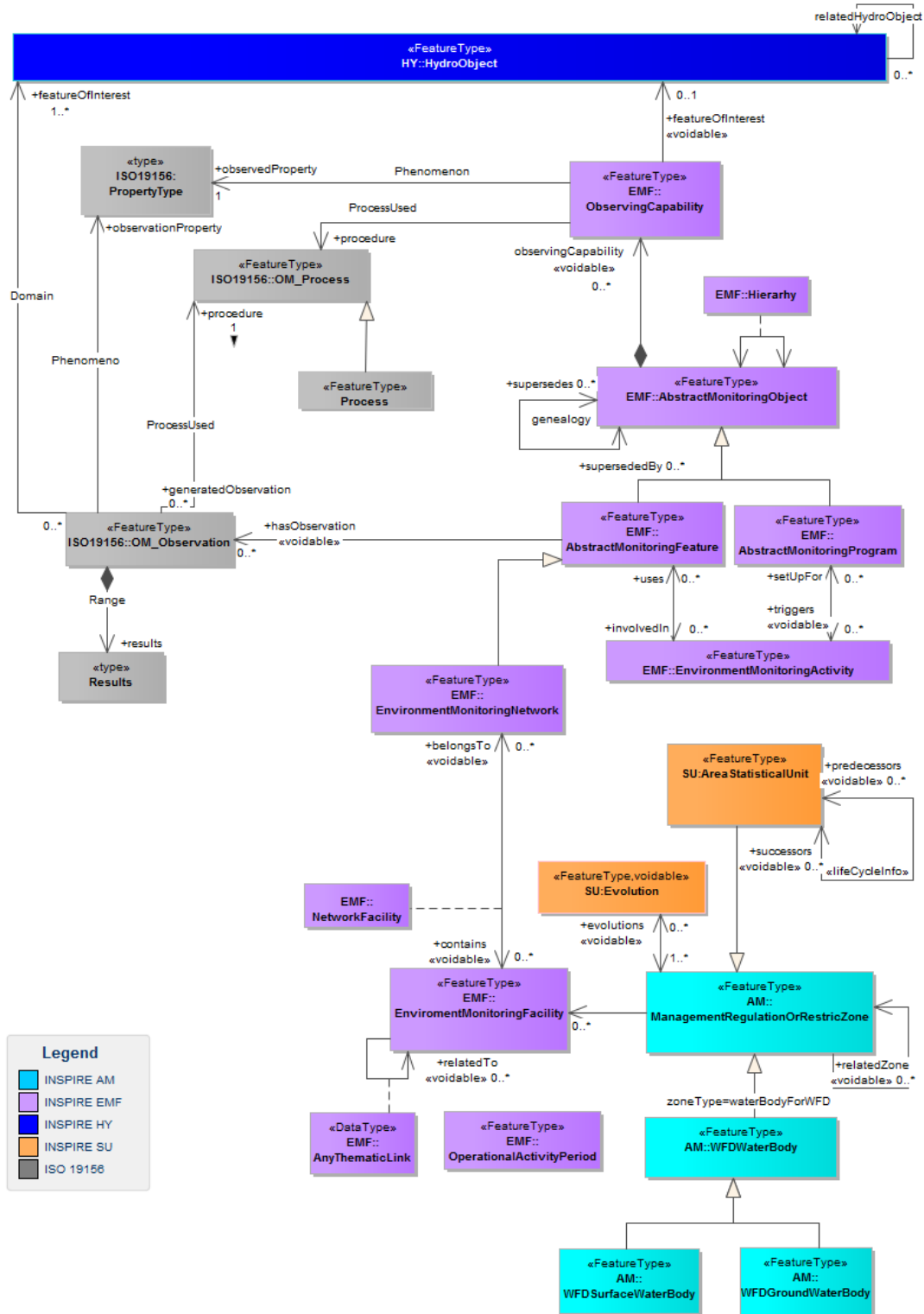
Figure 15. Integration of INSPIRE and WFD data model

Conceptually mapping between INSPIRE AM and WFD data mode for River Water body is presented in Figure 16. River, as defined in the WFD can be described using the generic ManagementRestrictionOrRegulationZone spatial object with the value *waterBody ForWFD* as the *zoneTypeCode*. The *EnvironmentalDomains* has value *water*. River, as a specific type of water, is defined using the *specialisedZoneTypeCode*. Additionally, several attributes in WFD reporting schema can be conceptually mapped as INSPIRE attribute. WFD data specification, *EUCode* and

MSCode identifier are assigned to a River. Those code properties should be encoded as a thematicIds. The thematicId is encoded using the *euSurfaceWaterBodyCode* for *thematicIdIdentifierScheme* attribute. A thematic identifier may form part of the *inspireId*.
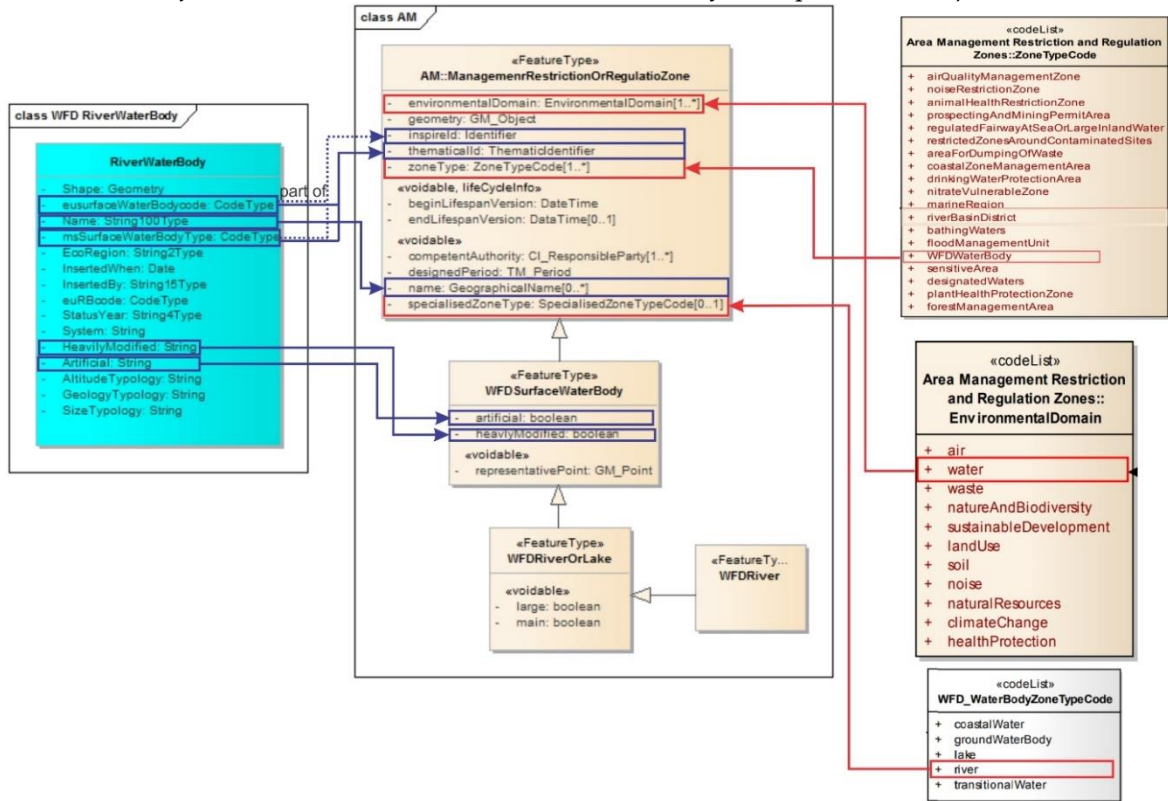
Figure 16. The conceptual mapping between INSPIRE and WFD

INSPIRE specify the geometry of the water body in addition to generic attributes. The actual value as WFD status that needs to be reported on is not included therefore INSPIRE base model must be extended in such a way that the information to be reported on is included. An extension of INSPIRE AM with WFD Status package is presented in Figure 17. All status parameters are linked to the relevant water body via the euSurfaceWaterBodycode.
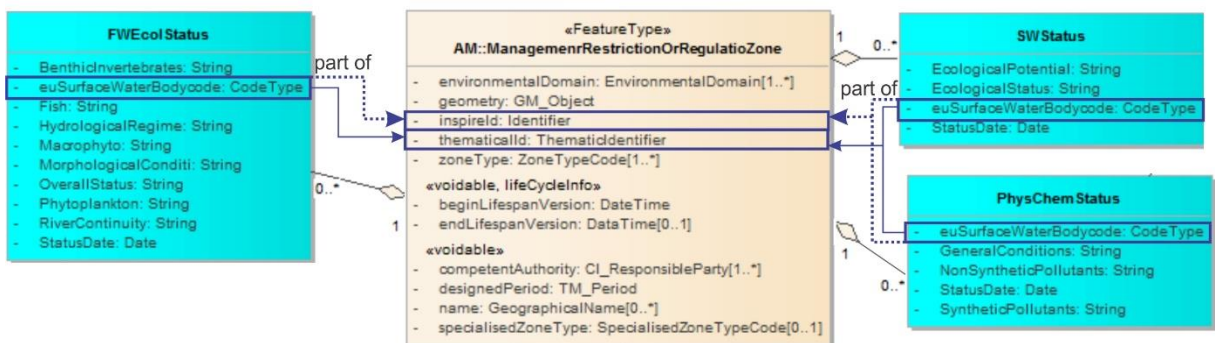
Figure 17. Extension of INSPIRE AM with WFD status

Moreover, data models need to include not only spatial objects but also attributes. The numerical concentrations of WQP are important for interpretation and understanding of WFD categorical status class e.g. identification of WQP which concentration excide defined limits causing that water body fail to good status or showing improvement of WQP within and across WFD status classes. Linking of water quality data reported to WISE-SoE to water bodies reported through WFD and WISE Spatial reporting need to be provided. Association between WFD water quality parameters and INSPIRE object are presented in Table 11.

Table 11. Association between WFD water quality parameters and INSPIRE object

INSPIRE THEME			AM			HY		EM	EL
Type of Quality element	Quality element	Consistency	WFDRiver	WFDLake	WFDTranistional	Physical Water	Nodes	MonitoringStations	
Biological	Invertebrate fauna	Point	+	+	+			+	
	Fish	Point	+	+	+			+	
	Macrophytes	Point	+	+				+	
	Phytobenthos	Point	+	+				+	
	Phytoplankton	Point	+	+	+			+	
	Macroalgae	Point			+			+	
	Angiosperms	Point			+			+	
Hidromorphological	Historical Flow	Point	+	+				+	
	Modeled Flow	Point	+	+				+	
	Real time Flows	Point	+	+				+	
	Water Table height	Point	+	+				+	+
	River continuity	Point, Line, Polygon	+			+	+		
	Cross-section	Point	+						+
	Structure and substrate of the river bed	Point	+					+	
	Structure of the riparian zone	Line	+			+			+
	Surface water Discharges	Point	+	+					
	Residence Time			+					+
	Lake surface	Polygon		+		+			
	Lake depth	Point		+					+
	Lake volumen			+					+
	Structure of lake shore	Line		+		+			
	Quantity, structure and substrate of lake bed	Point		+				+	
	Quantity, structure and substrate of the bed	Point			+			+	

	Structure of the transitional zone	Line			+	+				
	Tidal regime	Point			+		+	+		
	Depth variation	Point			+					+
Physico-chemical	Temperature	Point	+	+	+			+		
	Dissolved Oxygen	Point	+	+	+			+		
	Electrical conductivity	Point	+	+	+			+		
	PH	Point	+	+				+		
	Alkalinity	Point	+	+				+		
	TOC	Point		+				+		
	TP	Point	+	+	+			+		
	TN	Point	+	+	+			+		
	Nitrite+nitrate	Point	+	+	+			+		
	Soluble reactive phosphorus	Point	+	+	+			+		
	Ammonium	Point	+	+	+			+		
	Suspendet solid	Point	+					+		
	Turbidity	Point	+	+	+			+		
	Colour	Point		+	+			+		
	Secchi depth	Point		+	+			+		
Specific sintetic pollutant		Point	+	+	+			+		
Specific non-sintetic pollutant		Point	+	+	+			+		

Additionally, spatial data must be completed, reliable, and should include information on selected data quality elements. These are completeness (commission, omission), logical consistency (conceptual, domain, topological, format), positional (absolut or external), and thematic accuracy (Guidance Document No 9). According to (Guidance Document No: 22) two forms of analysis should be undertaken: exploratory (visual checks for verifying spatial reference, scale, resolution, positional accuracy, the existence of metadata, completeness of the metadata, etc.) and confirmatory (automated checks to discover geometry/topology/attribute errors supported by the use of GIS tools). The need to harmonize the geometry is strictly related to the topological consistency within and between different feature classes (date quality issues) (Guidance Document No: 22). Topological consistency describes the trustworthiness of the topological and logical relationships between the dataset segments and is usually assumed to refer to the lack of topological errors (Joksić and Bajat). Topological errors exist due to violations of predefined topology rules (Sehira, Singh and Singh Rai). Different algorithms can be used for the detection of topological errors like OpenJump (Sehira, Singh and Singh Rai), ArcGIS (Servigne, Ubeda and Puricelli), The correctness of errors should be reported as part of the data quality element topological consistency. Topological rules for water bodies are presented in Table 12.

Table 12. Spatial relationship between water bodies (DE-9IM matrix)

	WFD River	WFD Lake	WFD Transitional	WFD Coastal	RiverSubBasain	RiverBasain	RiverBasainDistrict	Watercourse	ManMade	Competent authority	GroundWater	HydroNode	EnvironmentMonitoing Facility
WFD River	Not overlap Not intersect		Not overlap	Not overlap	Not intersect	Within		Contains				Touches	Contains
WFD Lake		Not overlap	Not overlap	Not overlap			Covered by			Covered by		Touches	Contains
WFD Transitional	Not overlap	Not overlap	Not overlap	Not overlap		Not overlap	Covered by	Not overlap		Covered by		Touches	Contains
WFD Coastal	Not overlap	Not overlap	Touches Not overlap			Touches	Covered by	Not overlap		Covered by		Touches	Contains
River sub-basins	Contains		Not overlap	Not overlap	Not overlap		Covered by	Not intersect				Touches	
RiverBasain	Contains		Not overlape	Not overlape	Cover	Not overlap	Within		Contains				
RiverBasain District	Cover	Cover	Cover	Cover		Cover	Not overlap				Cover		Cover

Watercourse	Within		Not overlap	Not overlap	Not intersect			Not overlap Not intersect				Touches	
ManMade	Overlaps					Within							
Competent authority		Cover	Cover	Cover			Cover			Not overlap			Cover
GroundWater							Within			Within			
HydroNode	Touches	Touches	Touches	Touches	Touches		Touches						
EnvironmentMonitoing Facility	Within	Within	Within	Within			Covered by			Covered by	Within		

4.2. Study area

The Republic of Serbia is located in Southeast Europe, covering part of the Pannonian Plain and Central and Western Balkan Peninsula (Figure 18). Serbia covers 88.361 km² from which 56.8 % is cropland, and 36.6 % is covered by forest (OECD). The almost entire territory of Serbia belongs to Danube (Black Sea) basin. The part of Kosovo (White Drin basin) belongs to the Adriatic draining basin while the Vardar basin belongs to the Aegean. The Danube is the lagers river in Serbia and the second largest river basin in Europe, covering 801.463 km² over 19 countries and more than 81 million people (ICPDR, Countries of the Danube River Basin). The length of the Danube River is 2850 km from which 588 km passes through the Republic of Serbia (Ministry of Construction). The tributes of the Danube in Serbia are Sava, Tisa, Drina, and Great Morava (Morava). The Great Morava is formed by the confluence of West Morava and South Morava. Great Morava (including West and South Morava) flows nearly entirely through Serbia and covers 40% of its territory.

Figure 18. Study area

The presented study area was used to verify the model for water body extraction based on optical and SAR image, monitoring of water quality based on optical image, and extraction of river network topology. The model for classification of LiDAR and UAV point cloud, detection of water body geometry from LiDAR data, and monitoring of visible waste material based on UAV were verified on different study areas due to lack of data.

4.3. Water body geometry

The automatic detection of water bodies from remote sensing images is challenging due to high inter-class variability and low inter-class distance, especially for small water bodies. The

water bodies appear at different scales and orientations. Moreover, objects with similar spectral signatures are present in the images belonging to different classes.

On the one hand, automatic water body delineation is most often performed by using water indices and threshold-based approaches (Table 3). However, the threshold values varying significantly with scene and location. On the other hand, classification approaches using a MLA require significant training data that are traditionally labor-intensive to collect. Therefore, the application is mostly limited at a local and regional scale.

4.3.1. Water body detection based on optical and radar images

4.3.1.1. Methodology

In this chapter, the new approach for automatic water body detection based on optical and radar images is presented. Automatically derived training data are used to train CNN for fully automatic water body detection. Figure 19. summarized the proposed approach. It consists of an algorithm for automatic water body mask detection (Figure 20.), preprocessing, classification, accuracy assessment, and validation phase.

Preprocessing: The Sentinel 2 Level 2A satellite images were used to create the water body mask for both Sentinel 1 and Sentinel 2 images. Level 2A was atmospherically corrected by using Sentinel 2 Atmospherically Correction, which is based on (Richter and Schläpfer) and (Mayer and Kylling). The Level 2A image also contains the Scene Classification Layer (SCL), which provides a pixel classification map with four different classes for clouds and six different classes for shadows, cloud shadows, vegetation, soil, water, and snow (ESA, Level-2A Algorithm overview). Visual inspection showed that water pixels are mostly classified as water or dark pixels. Waterbody masks were created by using the region grow algorithm (Figure 19.) where water pixels are used as seeds, and neighbored pixels that are classified as dark pixels and have reflection lower than 800 in SWIR 2 band are added to the region.

Dual polarized VV and VH Sentinel-1 Level 1 Ground Range Detected (GRD) images were acquired from GEE. GRD product was created by using the following preprocessing steps: apply orbit file, GRD border noise removal, thermal noise removal, radiometric calibration and terrain correction (GEE), (ESA, Sentinel-1 Toolbox). In addition, to VV and VH, the VV/VH ratio was calculated. For each band, a 7x7 Refined Lee filter (J. Lee) was applied to reduce speckle noise using Local Linear Minimum Mean Square Error estimation with edge-aligned windows providing better preservation of image details. The mask is created by using Sentinel 2 data and algorithm for automatic water body mask detection. The maximum time gap between observation of Sentinel 1 and Sentinel 2 data is five days.
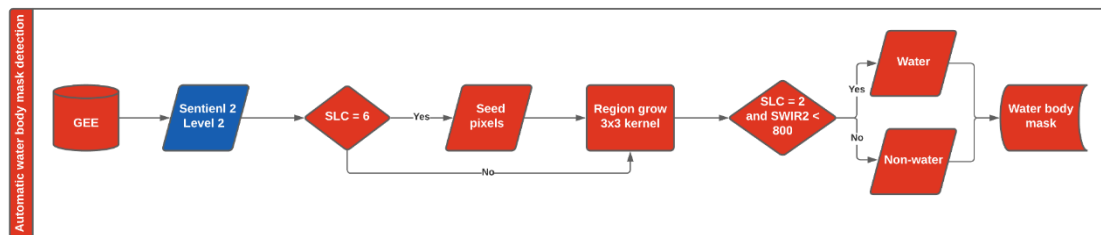

Figure 19. Algorithm for automatic water body mask generation

Classification: The end-to-end semantic segmentation model based on U-Net architecture was proposed for water body delineation. To achieve consistent training as the depth of the network increase, the ResNet 50 was used as an encoder part of the network. The architecture of ResNet 50 has four stages. The network performs the initial convolution and max-pooling using 7x7 and 3x3 kernel sizes, respectively. Afterward, stages 1, 2, 3, and 4 consists of 3, 4, 6, 3 resnet building blocks (Figure 9. (c)). As the network progress from one stage to another, the feature

map resolution is reduced by 2 in terms of height and width while the number of feature channels is doubled. The decoder is fully symmetrical to the encoder, and it is used to restore feature map resolution enabling precise localization. Each step in the decoder consists of 2x2 upsampling that halves the number of feature channels concatenation with the corresponding feature map from the encoder path, followed by two 3x3 convolutions, BN and ReLU activation function. In the final layer, a 1 × 1 convolution with the Sigmoid activation function is used to predict the probability of a pixel being assigned to water or non-water class.

The performance of a deep learning network is strongly dependent on a large amount of training data, which is needed to understand hidden patterns of data. Data dependence is the most serious problem in deep learning since it is time and labor-intensive to build a large-scale high-quality annotated dataset. Transfer learning has been widely used for solving an insufficient data problem. It relaxes the hypothesis that the training data must be identically distributed with test data. This assumption is possible due to the fact that deep learning represents the complex concepts by combining simpler ones such as edges, corners, and contours. Therefore the deep transfer learning refers to the reusing the shallow layers of the network trained on the larger collection and its connection weights while the last layers (more task-specific layers) are unfrozen and fine-tuned on available training data to recognize targets with the higher accuracy. Fine-tuning of existing networks that are trained on large datasets such as ImageNet is most commonly used in practice. ImageNet is a large and diverse dataset with more than 14 million images labeled into 1000 classes. ImageNet consists of natural images which are different from remote sensing images in term of spatial and spectral information. All remote sensing images are captured from a top-down view while natural images are obtained from different perspectives therefore the visual representation of the object is different in scale and direction.

Additionally, the multispectral information captured in a different part of the electromagnetic spectrum, such as visible, NIR, and SWIR is crucial for water body detection, while natural images include only RGB color space. However, several research applied pre-trained large networks to remote sensing fields. (Castelluccio, Poggi and Sansone) were tested performance fine-tuning of CNN trained on ImageNet for two remote sensing datasets UC-Merced (airborne RGB color space) and Brasilin Coffee scenes (SPOT satellite images), providing state of the art accuracy. (Penatti, Nogueira and dos Santos) also conclude that pre-trained CNN generalizes well in remote sensing and areal image domains, which are considerably different from the ones they were trained. (de Lima and Marfurt) were showed that the transfer learning from natural to remote sensing images is a powerful tool for classification despite the relatively large difference between the source and target dataset. Taking that into account, the encoder was pretrained on ImageNet dataset.

In addition to limited size, datasets for the classification of inland water bodies are highly imbalanced since most pixels represent non-water class. To prevent imbalance learning, enlarge dataset, and reduce over-fitting the data augmentation was used. Data augmentation generated additional and most diversified data samples thought the transformation of the original image improving model performance. In satellite image classification domain clipping, rotating, flipping, and translating are mostly used transformation (Ghaffar, McKinstry and Maul), (Yu, Wu and Luo).

Accuracy assessment: To compare the results of the classifications using the different satellite imagery, the confusion matrix, recall, precision, F1-score, and an estimate of KHAT were calculated, as showed in Foody (2008). The KHAT was used as a measure of classification accuracy and interpreted using the method described by Congalton and Mead (1986).

The use of the confusion matrix, and therefore the previous statistics, is based on the assumption that each pixel can be allocated to a single class in both the ground and map data sets, and that these two data sets have the same spatial resolution and are perfectly registered (Stahler et al. 2006). Failure to meet these conditions may lead to significant classification errors

in a very fragmented area where mixed pixels are common. In general, the proportion of mixed pixels increases with a coarsening of the spatial resolution of the imagery (Stahler et al. 2006).

Furthermore, the spatial resolution has been found to have more influence on the spatial distribution of the classification errors than on the overall classification accuracy (Chen, Stow, and Gong 2004). Also, if the aim is to map at a finer scale than the data source, the problems derived from the spatial misregistration are likely to be large in conventional approaches to accuracy assessment (Stahler et al. 2006). The relationship between pixel size and map scale is shown in Table 13.

Table 13. Relationship between pixel size and map scale

Map scale	Resolution [m]
1:1000	0.5
1:5000	2.5
1:10000	5
1:50000	25
1:100000	50
1:300000	150
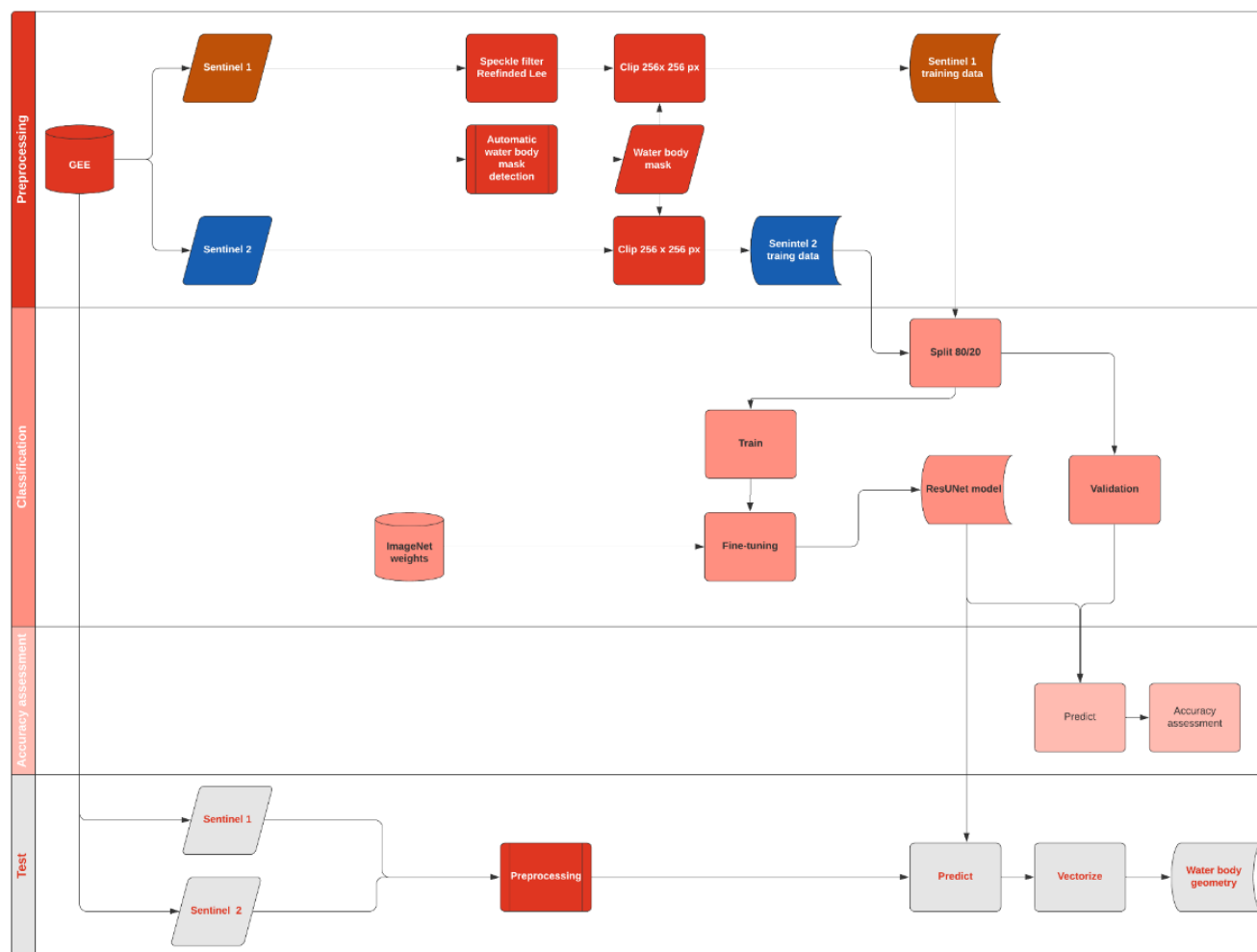
1

2   Figure 20. Workflow for automatic water body detection

4.3.1.2. Implementation

Due to limited processing power, the original images are decomposed to 256x256 px patches. The model was based on U-Net architecture, which uses ResNet 50 as an encoder. The first layer and weights learned during training on the ImageNet dataset were modified to allow the 6 band images (R, G, B, NIR, SWIR 1 and SWIR 2) as input. Dataset was split into 80% for training and 20% for validation. The network is fine-tuned on the dataset created during preprocessing. The cross-entropy and Stochastic Gradient Descent were selected as loss function and optimization algorithm. The GPU limited the batch size and it was chosen as big as possible for each network. The models were implemented in the Python 3 programming language by using artificial intelligence libraries such as PyTorch, TensorFlow, Keras, and Matplotlib. The training of the networks was done using the publicly available cloud platform Colaboratory (Google Colab). The hyperparameters used for the model training are presented in Table 14.

Table 14. Parameters that were used for training the models.

Image	Architecture	Dataset size	Batch Size	Learning Rate	Training time
Sentinel 2	ResUNet 50	4304	8	3×10^{-5}	11 min
Sentinel 1	ResUNet 50	4680	8	9×10^{-5}	12 min

4.3.1.3. Results and discussion

Accuracy assessment of the proposed model for Sentinel 2 is based on 861 and 13600 image patches for validation and test phases, respectively, while 922 (validation) and 13824 (test) image patches were used for Sentinel 1. The accuracy assessment for surface waterbody mapping using the two sensors is shown in Table 15. As the results show, the precision above 0.8 and recall above 0.95, indicating that the proposed model detects water class well but also includes points of other classes in it. As a measure of agreement or accuracy, KHAT is considered to show strong agreement when it is greater than 0.75 (Jones and Vaughan 2010). Therefore, both satellite imagery (Sentinel 1 and Sentinel 2) provided waterbody maps with a strong agreement with reality.) Those results are confirmed by visual inspection of results (Figure 21.) The detected water bodies in the Republic of Serbia are presented in Appendix B.

Table 15. Results of accuracy assessment for water body detection from Sentinel 1 and Sentinel 2 satellite images

Phase	Image	Precision	Recall	F1-score	Kappa
Validation	Sentinel 1	0.85	0.96	0.90	0.90
	Sentinel 2	0.90	0.95	0.92	0.92
Test	Sentinel 1	0.80	0.98	0.88	0.88
	Sentinel 2	0.81	0.99	0.89	0.89

As presented results indicated, the proposed approach provides water body detection in the complex environment from optical and SAR images with consistently high F1-score and kappa coefficient despite varying topology, land-use/land cover, and atmospherical conditions. The maximum difference between F1 score during the validation and test phase was 3% indicating the algorithm high generalization ability. Therefore it can be used for automatic water body detection from different areas without manual intervention. It is observed that during the test phase recall value increases while the precision decrease meaning that on the one hand algorithm is more secure that pixel labeled as water represents the water body in the real-world but on the other hand, it includes more non-water pixels in water class. The visual inspection shows (Figure 21.) that detected wetlands and channels are more completed comparing to masks, which also decrease the precision.
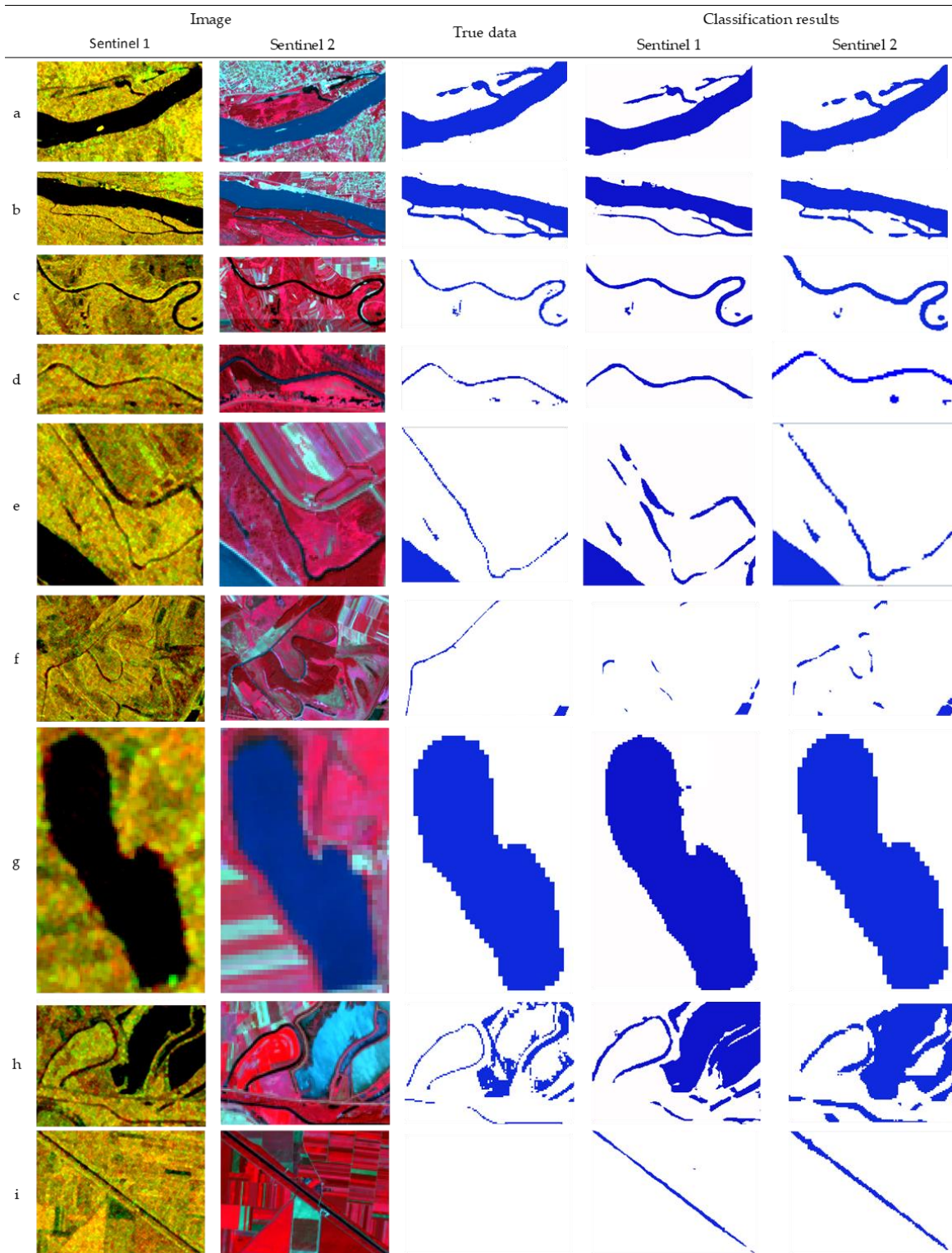
Figure 21. Visual comparasion of extracted water bodies for different water body types (a), (b) large river (> 400 m width), (c) medium river (width around 100 m), (d), (e), (f) small rivers (width between 10-35 m), (g) lake, (h) wetland, (i) artificial channels

Moreover, visual inspection indicates that most of the errors are related to the river banks. Figure 21 (f) shows that the algorithm has difficulties in detecting narrow rivers with a width of ~20 m from Sentinel 1 data, although there are detected on Sentinel 2 images. This is probably due to complex interactions of

SAR reflection with terrain and vegetation along small river banks, causing the increase of backscattering and the omission of water body (Pham-Duc, Prigent and Aires). The several small river segments which width don't exceed 50 m (Figure 21 (e), (f)) are omitted. Detection of these sections is difficult due to trees and shrub along river banks. On the other hand, the overestimation of the water surface is visible around small river banks (Figure 21 (d), (e)). Also, some agriculture fields are misclassified as water bodies producing lower precision. This is due to the higher sensitivity of SAR to water content. With the increase of water content, the dialectic constant of bare soil also increases, reducing backscattering making it difficult to separate from water bodies (Baghdadi, M. and M.), (Peng, Loew and Merlin). Additionally, precision was affected by misclassification of roads near water bodies (Figure 21 (e)). Roads are characterized as flat surfaces with low roughness, reflecting most incoming radar energy causing the low backscatter return and, therefore similar characteristics as water bodies. However, the algorithm generalized well between roads (and other impervious surfaces) and water in urban areas (Figure 21 (a), (b)). This can be explained by high building density, which causes double bounce and increase of backscattering.

As a comparison between two sensors, Sentinel 2 provided slightly better results. The recall value was the same, while Sentinel 2 produced higher precision and the slightly higher F1-score and KHAT. The visual comparison of the delineation of different water body types, including rivers, channels, ponds, wetlands, and lakes on the test images (Figure 21.), shows that the water bodies extracted from the satellite images followed a similar pattern. As can be seen from the figure, the algorithm can predict lakes, large rivers, and even small ponds or reservoirs with high accuracy (Figure 21 (a), (b), (g)). As expected, the lowest accuracy is obtained for small and narrow streams. The small water bodies were overestimated (Figure 21 (d), (e), (f)) due to mixed pixels producing lower precision. The overestimation is larger for Sentinel 2 since it has a lower spatial resolution producing a higher number of mixed pixels. The high recall, as well as visual inspection, confirmed that the algorithm accurately delineated water bodies from low albedo surfaces with similar spectral patterns such as built-up areas, roads, and shadows, which are one of the main sources of errors when indexes or MLA are used (Huang, Li and Xu), (Donchyts, Schellekens and Winsemius), (Du, Zhang and Ling), (Verpoorter, Kutser and Tranvik, Automated Mapping of Water Bodies Using Landsat Multispectral Data).

The F1 score and KHAT for water classes are the same and were 0.92 and 0.89 during the validation and test phase, respectively. (Du, Zhang and Ling) were detected water bodies from Sentinel 2 image by using MNDWI producing KHAT coefficient of 0.90. (Yang and Chen, Evaluation of Automated Urban Surface Water Extraction from Sentinel-2A Imagery Using different water indicies) used the MNDWI from Sentinel 2 images for automatic water body mapping achieving the kappa coefficient of 0.90. (Yang, Zhao and Qin) evaluated the performance of OBIA and MNDWI for water body mapping from Sentinel 2 image reporting kappa coefficient of 0.92. Similarly, (Kaplan and Avdan) used NDWI and OBIA for river detection with kappa of 0.89. While (Topaloglu, Sertel and Musaoglu) and (Jakovljević , Govedarica and Álvarez-Taboada) reported kappa of 0.79 and 0.89 respectively for water body by using SVM. Therefore the proposed approach achieves state-of-the-art accuracy. Moreover, the accuracy assessment is based on complete segmentation at the pixel level, resulting in lower accuracy values than a comparison against point samples.

Similarly to Sentinel 2, the algorithm produces high classification accuracy for SAR images. The F1 value is 0.90 and 0.88 for the validation and test phase, respectively. (Pham-Duc, Prigent and Aires) were used Sentinel 1 images and NN achieving kappa coefficient of 0.83 for the detection of water bodies in the environment with the same complexity as in the study area. (Bolanos, Stiff and Brisco) used RADARSAT-2 C-band data and threshold-based approach for automatic detection of water bodies producing kappa of 0.84. (Bangira, Alfieri / Menenti) compared the performance of threshold-based approaches and various MLA for detection of small reservoirs from Sentinel 1 images. They reported the kappa coefficient of 0.71 and 0.83 for threshold and SVM, respectively.

4.3.2. Water body detection based on LiDAR data

The LiDAR data are frequently used for flood modeling (Yan, Di Baldassarre and Solomatine), flood risk mapping (Bodoque, Guardiola-Albert and Aroca-Jimenez), (T. Webster) and surface water body extraction (Smeeckaert, Mallet and David), (Brzank, Heipke and Goepfert), (Hofle, Vetter and Pfeifer). All these applications are built around the generation of DEM using raw point clouds. Recent advances in remote sensing techniques have greatly improved the ability to collect high-resolution topographic data at various scales. LiDAR remote sensing has become a widely used method to provide high-resolution topographical datasets duo to the advantage of collecting three-dimensional information very effectively over a large area. A major limitation of LiDAR is the high instrument and survey costs, especially for small study areas (Smith, Carrivick and Quincey).

UAV has emerged as a low-cost alternative to the conventional photogrammetric system for an image-capturing platform, which has allowed low-cost production of high quality and high-frequency data. In addition to the high levels of spatial and temporal resolutions, UAV technologies bring a substantial improvement to the flexibility of the data acquisition and the design of the monitoring campaigns. Feature more, the development of Structure from Motion (SfM) algorithm provided a cost-effective alternative method of rapidly acquiring very-high resolution (sub-meter) and hyper resolution (sub-centimeter) topographic data (Westoby, Brasington and Glasser)

4.3.2.1. Point cloud classification

As stated before, that applications of point cloud in flood modeling are built around the generation of a DEM. The DEM refers to a bare-earth surface created through the interpolation of ground points. The accuracy of produced DEM is affected by (i) accuracy and density of original point cloud, (ii) performance of algorithm for ground point classification, (iii) the algorithm for interpolation, and the (iv) DEM resolution (X. Liu, Z. Zhang and J. Peterson). Although high point cloud densities of LiDAR and UAV SfM data provide more detailed topographic information, a massive amount of information is demanding for processing and storing. Reduction of point cloud density decreases the data acquisition and data processing costs but can affect the accuracy of the generated model. Also, the author of (Asal) reported a 50% reduction of LiDAR point density without big deterioration in the visual and statistical characteristics of the generated DEMs. The results in (X. Liu, Z. Zhang and J. Peterson) showed that data with 50% reduction provided compatible surface estimation, but significantly reduced half of the processing time and storage space. In addition, (Thomas, Jordan and Shine) obtained 0.02 m mean absolute difference in elevation between the 1 m LiDAR DEM generated based on point cloud with an average point density of 40.2 and the DEM obtained from a 2 points per m^2 point cloud. On another hand, accurate DEM can only be obtained if the raw point cloud is classified in order to distinguish between objects on the ground and the ground itself. The point cloud is represented as a set of 3D points, where each point P_i is a vector of its coordinates (x_i, y_i, z_i). Depending on the device used for data acquisition, additional features are available such as intensity, return number, number of returns, or color. Several filtering algorithms have been proposed. They are based on geometrical features of 3D ground points that differ them from non-ground, such as lowest elevation in local neighborhoods, surface slope is generally lower between ground points, the elevation difference between neighboring ground points is lower than the difference to non-ground points, and the ground surfaces are locally smooth and homogeneous. (Rashidi and Rastiveis) utilized the slope between points and the elevation information in a local window to detect non ground points. (Axelsson) used the progressive TIN (triangulated irregular network) method, starting from the lowest points in the neighborhoods with a predetermined size. The progressive TIN and physical simulation methods tested provided the highest accuracy for the forested area and flat area, respectively. Although filtering provided satisfactory results, they needed a lot of human involvement in the process. With the rapid emergence of deep learning techniques, different types of frameworks have been developed and applied to classification tasks. Generally, point clouds can be classified using voxel-based, point-based, or projection-based approaches. (Hu and Yuan) proposed a ground point extraction from an Airborne Laser Scanning (ALS)

point cloud using deep convolution networks. In their research, for every point with spatial context, the neighboring points within a window are extracted and transformed into an image. After that, the point classification is treated as the image classification. The model, trained with 17 million labeled points, provided high accuracy. (Rizaldy, Persello and Gevaert) used a fully convolutional network based approach to classify an ALS point cloud into the ground, building, and vegetation with an average error of 5.21%. The original point cloud was converted into images by calculating each pixel value based on the features of the lowest point. In addition, the difference between the lowest point in the corresponding pixel and the lowest point in a 20 x 20 m horizontal window centered on the point. (Sofman, Bagnell and Stentz) classified the environment into four classes: roads, grass, trees, and buildings, using an artificial neural network (ANN). They fed the network with projected data points that contained the point position, color measurement, and laser reflectance power measurements to a grid cell size of 0.3 m^2. The highest and lowest accuracy obtained was for buildings (93.87%) and grass class, respectively (66.73%). Although the projection based methods provide high accuracy, they require large computational power to train the classifier, and the prediction time can also be restrictive. (Qi, Su and Mo) showed the potential of a convolutional neural network (CNN) fed by raw point coordinates, corresponding color information, and normalized positions for indoor point cloud classification. (Hackel, Wegner and Schindler) described the point-based semantic classification of a Terrestrial Laser Scanning (TLS) point cloud based on downsampling of the point cloud with a voxel-gridded filter, and then computed 3D features based on eigenvalues and corresponding eigenvectors of the covariance tensor from fixed set of k nearest neighbors. (Becker, Hano and Rosonskaya) combined the geometrical feature introduced in the work of (Hackel, Wegner and Schindler) and color features to feed a machine learning algorithm.

The objectives of this chapter are as follows: (1) to determine the suitability of the presented approach of raw point cloud classification and ground point filtering based on deep learning and NN; (2) to test the convenience of using rebalanced datasets for point cloud classification; (3) to evaluate the effect of the land cover class on the algorithm performance and the elevation accuracy; and (4) to access usability of the LiDAR and UAV SfM DEM in flood risk mapping.

4.3.2.1.1. Study area and data

Four study areas were defined, two for calibration and two for validation. They are located in the Srem and Kolubara District, western Serbia. The validation area (Figure 22 A and B) was located at the confluence of the Bosut and Sava Rivers, Municipality of Sremska Mitrovica, Republic of Serbia. Validation area (A) is located at river banks and has high terrain discontinuity. It is covered by water bodies (4.3%), buildings (2.5%), low vegetation (70.4%), medium vegetation (2.3%), high vegetation (7.6%), roads (2.1%), and embankment (2.7%). Validation area (B) is covered by high mixed vegetation (4.3%), agricultural fields and grassland (65.1%), urban areas (8.1%), roads (2.3%), embankment (1%), and bushes (1.4%). Both validation areas are mainly flat, because the highest DEM accuracy for flood modeling needs to be provided in flat areas. On the other hand, different land cover classes were chosen to compare the algorithm performance in different environmental scenarios.

This study used LiDAR and UAV data, which were collected over the areas shown in Figure 1. LIDAR data was collected over the areas A, B, C, and D, (Figure 1) and UAV data over the areas A and B. LiDAR data were used to calibrate the algorithm to obtain the DEM, as well as to test the influence of using balanced/imbalanced data when calibrating it. Once the algorithm was tested and validated, it was applied to the UAV data. The following paragraphs describe both LiDAR and UAV data sets.

Calibration (training) sample points were selected from a large number of point clouds with different terrain complexities. The training area in Figure 1C represents the steep terrain covered by dense vegetation, while area (D) represents the flat terrain covered by mostly agricultural fields and built up areas. Table 16. summarizes the data used in this study.

Table 16. Light detection and ranging (LiDAR) data used in the study.

Area	Type	Number of Points	Ground [%]	Non Ground [%]

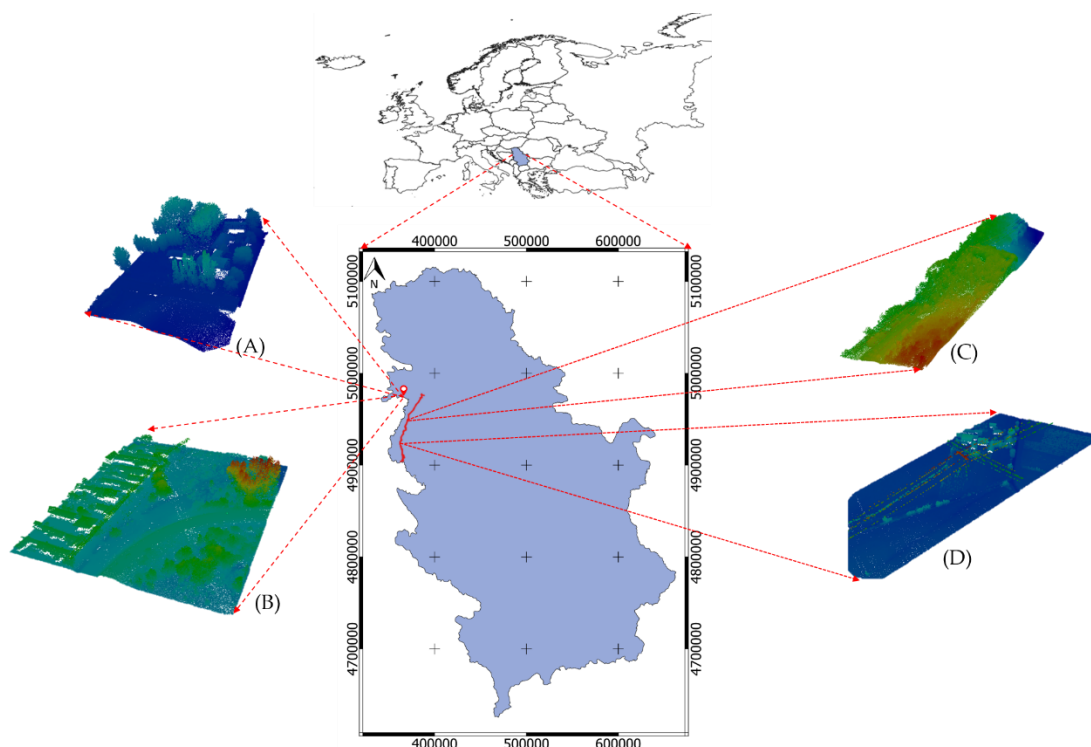| A	Validation	2,804,726	23.2	76.7
B	Validation	4,419,520	17.8	82.2
C	Algorithm calibration	3,801,412	8.1	91.9
D	Algorithm calibration	1,811,545	23.6	76.4

Figure 22. Study area location. Four study sites (A, B, C, D). The coordinate reference system is WGS84/UTM34 34N EPSG 32634.

The LiDAR data were captured on 1 December 2017 with an average point spacing of 5.4 cm. The flying height, during the capturing of the LiDAR data, was approximately 200 m above ground level. The aircraft speed was 45 kn. Maximum scan angle was set to 60°. The list of instruments used for LiDAR data acquisition is presented in Table 17.

Table 17. Instrument mapping list used for LiDAR point cloud acquisition.

Type	Title 2
LiDAR	LMS-Q680i-Full Waveform Analysis with settable frequency up to 400,000 Hz, with field of view of 60°, and a divergence of 0.5 mrad beam; Class 3R
Navigation system	IGI CCNS5 Aerocontrol (positioning and navigation unit data storage); Inertial Measurement Unit (IMU) IIf (inertial unit - 400 HZ); GPS a 2 HZ (Novatel antenna 12-channel L1/L2).
Camera	n.1 Metric Camera Digicam-H39 (39 Mpixels)
Thermal Camera	Variocam thermal sensor system with a detector of 1024 x 768 pixels and the spectral range from 7.5 to 14 μm.

The UAV survey was conducted in April 2018 using a WingtraOne drone fitted with a 42 MP Sony RX1RII camera (Table 18). The GCPs are required in order to register the results into a reference coordinate

system (WGS84/UTM34, EPSG: 32634). Thirteen GCPs were distributed over the study area. The GCP consists of visible targets (1 m x 1 m red crosses). The GCPs were surveyed using a RTK GPS receiver and GNNS permanent network of Serbia (AGROS). The average point density of UAV point cloud is 160 points per square meter.

Table 18. Unmanned aerial vehicle (UAV) data survey details.

Image Resolution [MP]	Number of GCP	Attitude of Image Capture [m]	Forward Overlap [%]	Side Overlap [%]	Ground Resolution [cm pix^{-1}]
42	13	150	70	70	2.7

4.3.2.1.2. Methodology

LiDAR data were used to calibrate the algorithm to obtain the DEM, as well as to test the influence of using balanced/imbalanced data when calibrating it. Once the algorithm was tested, it was applied to the UAV data. Therefore, the following workflow was applied (Figure 23.):

(1) LiDAR point cloud: calculation of the contextual information for each point by considering the spatial arrangement of all points inside the local neighborhood,

(2) LiDAR point cloud: feature extraction,

(3) LiDAR point cloud: calibration and supervised classification (ground and non-ground points) using the deep back propagation neural network (BPNN)

(4) Accuracy assessment of the LiDAR point cloud classification

(5) Application to the UAV data

1. Create the UAV point clouds (from overlapping images and using the SfM algorithm)
2. UAV point cloud: feature extraction (the same as (2))
3. UAV point cloud: calibration and supervised classification (ground and non-ground points) using the deep back propagation neural network (BPNN) (the same as (3))
4. Accuracy assessment of the UAV point cloud classification (the same as (4))

(6) Accuracy assessment of the LiDAR and UAV derived DEMs

(7) Flood risk assessment using the created DEM.
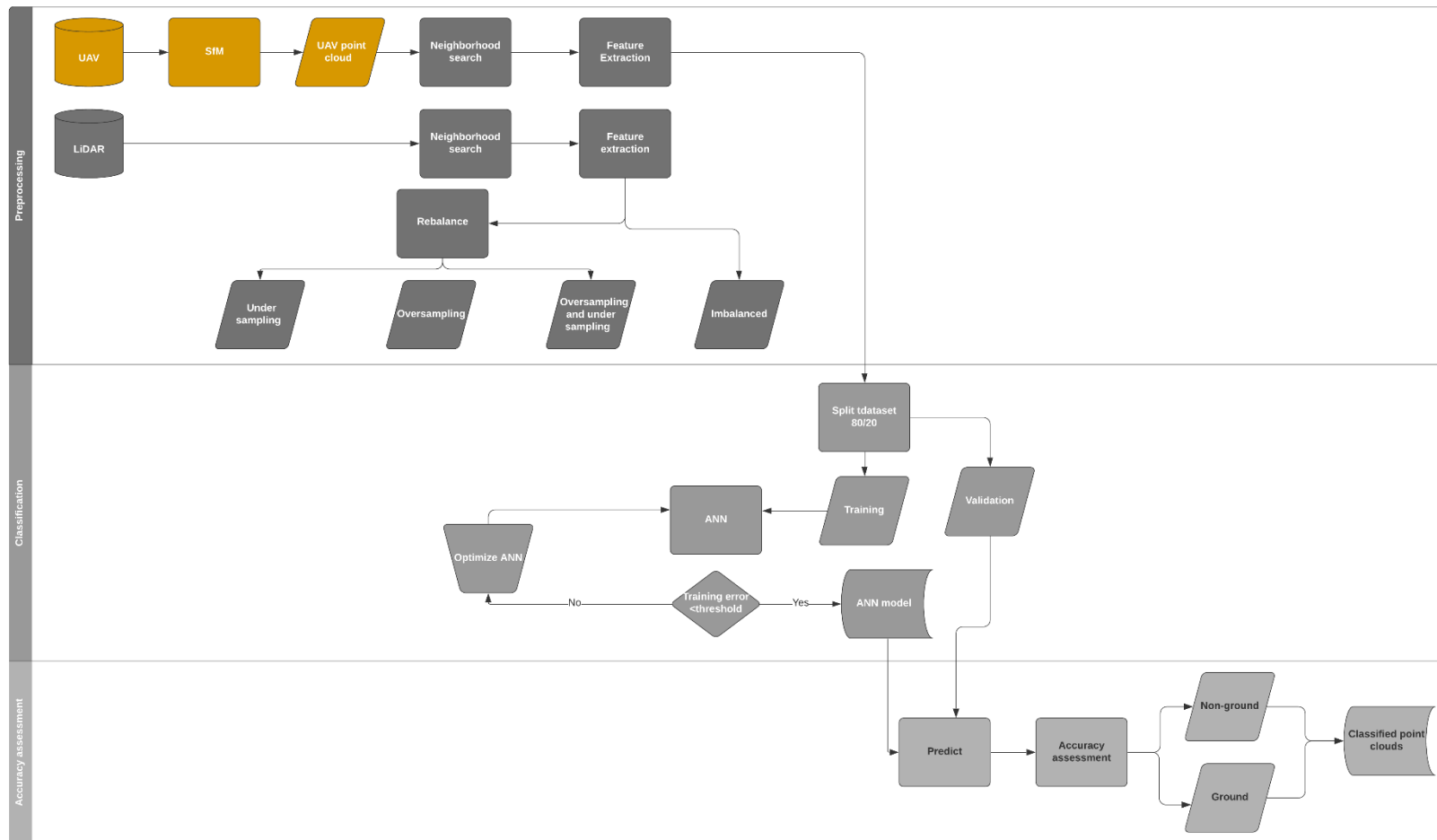
The next paragraphs explain each step in more detail.

Figure 23. Workflow for automatic point cloud classification

Preprocessing: The SfM algorithm was applied to the set of UAV images acquired from multiple viewpoints to reconstruct the 3D geometry of objects and surfaces, and to transform them into a point cloud. The workflow consisted of three main steps, described below.

In the first step, SfM used scale-invariant feature transforms (SIFT) to detect and describe local features (key points) that are invariant to image scaling, orientation, affine distortion, and changes in illumination conditions, and can be matched across multiple images using the RANdom SAmple Consensus (RANSAC) method (Westoby, Brasington and Glasser). Because we used the customer grade digital camera, which does not carry a GPS and IMU sensor that can collect data with sufficient accuracy, the intrinsic orientation parameters are neither known nor stable. To overcome these problems, the bundle block adjustment of matching key points was applied to compute the extrinsic camera (position and orientation) of each camera exposure station [30]. Also, the bundle adjustment simultaneously estimated the 3D coordinates for a sparse, unscaled point cloud and intrinsic camera parameters (focal length and two radial distortion parameters).

In the second step, the initial value of camera parameters and 3D point cloud were optimized by minimizing of a non-linear cost function that reflects the measurement and re-projection errors (Smith, Carrickk and Quincey). The GCP points, established before the survey, were used to georeference the SfM derived from the point cloud using the seven parameters Helmert transformation. For the seven parameter transformation, a minimum of three GCP needs to be used. In this case, 13 GCP were used. As a third and final step, the multi-view stereo (MVS) image matching algorithm used the output of the bundle adjustment to build a dense 3D point cloud.

After that, neighboard search and feature extraction for points within LiDAR and UAV point cloud was preformed. Two approaches can be used to define the local 3D neighborhood of a given 3D point $X \in R^3$: geometric search and k-nearest-neighbor search. The most commonly used method is the spherical neighbored definition, where the local neighborhood is formed by all points in a sphere defined by a fixed radius. Geometric search can be based on a cylindrical neighborhood definition, where the local neighborhood is formed by all 3D points whose 2D projection onto the ground plane is within a fixed radius circle (Filin and Pfeofer). In the k-nearest neighbor search, the local neighbors are the fixed k nearest neighbors from the query point. All those methods are defined by one parameter, which is represented by either a radius or several nearest neighbors and can be derived based on prior knowledge about data. Because of a significant impact on local neighborhood and feature extraction, it is expected that the different neighborhood types and different parameters can have a significant influence on the classification result. (Weinmann, Mallet and Jutzi) analyzed the behavior of standard 2D and 3D geometric features for different neighborhood types. Derived features were used to evaluate three classifiers for a different classification task. In that work, the results showed that the spherical neighborhood with a radius of 1 m provided high classification accuracy for each classifier. Therefore, in this research, we utilized the spherical neighborhood. After that, the neighborhood search, performed for each 3D point, was described as follows: for a given point cloud $P = \{X_1, \ldots, X_n\}$ in a three-dimensional Euclidean vector space, those points $X \in P$ that are located in the sphere defined with a center in query point X_i and fixed radius represent local neighborhood of point X_i. A kd-tree, binary tree based on a hierarchical subdivision of space by splitting hyperplanes that are orthogonal to the coordinate axes (Friedman, Bentley and Finkel), is widely used for nearest neighbor search in computer sciences. The ckd-tree, defined as in the work of (Maneewongvatana and Mount), finds 3D neighbors for 15,000 points 20% faster than kd-tree, and thus is used in this study.

Thus, in this work, the neighborhood search was performed using ckd-tree implemented in the Python programing language. The spherical neighborhood definition with radius of 1 m was set, and for each query point X_i, minimum, maximum, and mean height in the local neighborhood was extracted. Then, difference values between the height of query point z_i and z_{max}, z_{mean} and z_{min}, as well as the height range, were calculated for each point. In addition to geometric features, the intensity value was also used. The intensity for LiDAR data was defined as the return strength of the laser pulse, while the intensity of UAV data is calculated from red green blue (RGB) colors of the point according to the following expression: $Intensity_{UAV} = 0.21 \times Red\ 0.72 \times Green\ 0.07 \times Blue$.

Classification: Each point of the point cloud was classified as ground or non-ground using the back propagation neural network algorithm. For the main characteristics of BPNN, see the work of (Alsmadi, Omar and Noah). The task of classification was to predict label y for a given input x. The input consisted of eight layers (obtained in step 3.2.): three global geometric features (X_i, Y_i, Z_i), four extracted features from local neighbored (Z_i-Z_{min}, Z_i-Z_{max}, Z_i-Z_{mean}, Z_{max}-Z_{min}), and intensity. During the forward-passing, given input features x and a network with weights W, bias b and hyperbolic tangent (tanh)activation function the output of each layer h are defined as in Equation (2).

$$h = \sum_{d=1}^{D} W_d^T \times x_d \, b \tag{2}$$

Next, a loss was calculated as the negative log-likelihood between the prediction and the true label. The closer the prediction to the true label for each sample, the smaller the loss would be. The loss function was minimized by adjusting all of the parameters in the network using back-propagation. The learning was performed by adam, a stochastic gradient-based optimizer proposed by the authors of (Kingma and Ba). The selected activation function and optimizer provided the highest accuracy among tested combination, that is, sigmoid, rectified linear unit (relu), tanh, adam and stochastic gradient descent (sgd). The maximum number of epochs was set to 400, the learning ratio was 0.0001. The output consisted of labeled points, with the labels corresponding to the classes defined in training set (i.e., ground and non-ground).

The calibration data sets (C and D) were split into 70% for training and 30% for testing. A total of 5,612,957 labeled points were used to train the neural network in this study. The validation, training, and testing ground truths were labeled using automatic filtering implemented in TerraScan software and post manual editing.

Although point clouds offer large point counts in absolute terms, they contain large class imbalance. A dataset is imbalanced if the classes are not approximately equally represented. This is because of the natural ground and non-ground imbalance presented in both urban and rural environments, as well as in steep and flat terrain. The largest imbalance was noticed in area C covered by dense vegetation and objects (Table 1). The class imbalance can compromise the process of NN learning, because the model tends to focus on the prevalent class and ignore the rare events (Kubat and Matwin). Therefore, and in order to compare the results of using imbalanced and balanced data sets to obtain ground points and DEM, in addition to the initially imbalanced C and D point clouds, three balanced data sets per point cloud were created using different re-balancing methods. The first data set (BU) was balanced by randomly removing data from the non-ground class (i.e., under sampling the non-ground class), so that its ratio approaches the ground class ratio; this strategy reduced the original data set by 75%, so that the final BU data set consisted of 1,403,696 points. The second balanced data set was obtained by oversampling (BO), where the representatives of the least represented class were replicated, creating additional 4,209,261 points (reaching a total number of 9,822,218 points in the BO dataset). As the data are just replicated, oversampling can lead to over-fit to small data samples; therefore, the combination of undersampling and oversampling was also tested (BOU). This third method was applied to balance the dataset, and in this case, the number points of ground class increased by 300% (4,211,088 points created), while the non-ground class was reduced by 50%. In all the balanced datasets, the class ratio (ground, non-ground) was 50%. Once the three balanced datasets were created, all four data sets were standardized using the StandardScaler function (sklearn. preprocessing. StandardScaler.).

The proposed approach was implemented in the Jupyter Notebook environment and Python programming language by using numpy, laspy, scipy, and sklearn libraries.

Accuracy assessment: To determine the accuracy of the point cloud classification, overall accuracy, the most common metric for classifier evaluation, can be used to assess the overall effectiveness of the algorithm by estimating the probability of the true value of the class label. However, imbalance validation datasets can lead to wrong conclusions because one class is overrepresented and the other underrepresented, and thus the omission and commission errors (and the overall accuracy (OA)) are affected. Thus, precision, recall, and *F1*-score were calculated to provide a comprehensive assessment of the proposed approach. Precision (3) computes the percent of points classified as ground that are really ground, while recall

represents the fraction of correctly labeled ground points. In a perfect model, the precision and recall (4) will be equal to one. The F1-score represents the harmonic mean of precision and recall in Equation (5) (Fawcett).

$$precision = \frac{tp}{tp + fp}, \tag{3}$$

$$recall = \frac{tp}{tp + fn}, \tag{4}$$

where *tp*, *fp*, and *fn* are true positive, false positive, and false negative, respectively.

$$F1 = \frac{2 \times recall \times precision}{recall \times precision} \tag{5}$$

According to Equation 4, the *F1*-score will be null whenever the precision or recall is equal to null, while the value of the *F1*-score will increase proportionally to the increase of precision and recall. The higher value of *F1*-score indicates that the model performs better on the positive class (Bekkar, Kheliouane Djemaa and Akrouf Alitouche).

In this chapter, the overall accuracy, precision, recall, and F1-score were calculated for the two validation sets (A and B) (Table 1); for the imbalanced (original) dataset; and for the three rebalanced datasets (BU, BO, BOU), obtained in an analogous way to the BU, BO, and BOU datasets described for training and testing in Section 3.3.

Additionally, the accuracy of point clouds and DEM were evaluated. The accuracy of UAV and LiDAR based point cloud was assessed by comparing the results with the true data (datasets A and B). Two methods were applied: DEM of difference (DoD) and cloud-to-cloud (C2C) method

DEM of difference (DoD) is the most common method of point cloud comparison. The classified LiDAR and UAV ground points were gridded to generate DEMs with a spatial resolution of 0.25 m and then differenced on a pixel-by-pixel basis, allowing the estimation of vertical uncertainty and the detection of change. Also, the root mean square error (RMSE) and the mean average error (MAE) of elevation measurements were computed by extracting the DoDs in 36,600 randomly created check points across the entire A and B study areas. The number of check points was defined in order to provide density of 1 point per m².

As gridding a point cloud and generating a DEM involves an interpolation error, direct cloud to cloud differences were calculated using the C2C tool implemented in open source CloudComparer software (CloudCompare). This method also allows for assessing the spatial variability of cloud accuracy. For each point of the second point cloud, the closest point can be defined in the first point cloud based on different performing algorithms (Lague, Brodu and Leroux). The output of applying this method is a point cloud that contains information about the absolute distance for each point along the three axes (X, Y, Z). On the basis of the absolute distance, mean absolute distance (MAD) and standard deviation (SD) were calculated.

4.3.2.1.3. Results and discussion

Point Cloud Classification: The results of the accuracy assessment for ground class extraction from the LiDAR point clouds using deep learning based on backpropagation neural network are displayed in Table 19. The algorithm showed a stable performance among the different data sets. As a measure of classification accuracy, the F1-score is considered to show strong agreement when it is close to 1, while values close to 0 indicate a poor agreement. Therefore, all data sets (original, BU, BO, BOU) provided ground point classifications with a strong agreement with the true data, as indicated by the low number of false positives and false negatives. The lowest F1-score in the testing phase was obtained for the ground class in the imbalanced data set, as only 71% of the ground points were correctly classified by the algorithm (recall: 0.71), while for the balanced datasets, the recall values were between 0.86 and 0.93.

For the validation, all the balanced datasets showed low precision (<0.4) and high recall (>0.8) for the ground point class, and high precision (>0.9) and low recall (<0.5) for the non-ground points. According to these values, in the balanced data sets, the algorithm produced a low number of false negatives, but a high number of false positives. As a result, the balanced data sets produced a significantly lower F1-score for the ground class in the validation phase, compared with the testing phase (0.90 vs. 0.53). The imbalanced data

set provided stable metrics values between the validation and testing phase (0.78 vs. 0.79 F1-score for the ground class).

Table 19. Results of the accuracy assessment for the LiDAR datasets and the proposed classification method. BU (data set balanced by undersampling of non-ground class), BO (data set balanced by oversampling of ground class), BOU (data set balanced by oversampli

			Precision	Recall	F1-score	OA [%]
Test	BU	Non-ground	0.90	0.89	0.89	89.53
		Ground	0.89	0.90	0.90	
	BO	Non-ground	0.92	0.86	0.89	89.77
		Ground	0.88	0.93	0.90	
	BOU	Non-ground	0.90	0.92	0.91	89.68
		Ground	0.88	0.86	0.87	
	Imbalanced	Non-ground	0.92	0.98	0.96	93.37
		Ground	0.89	0.71	0.79	
Validation	BU	Non-ground	0.99	0.56	0.72	64.80
		Ground	0.37	0.97	0.52	
	BO	Non-ground	0.95	0.51	0.66	60.81
		Ground	0.36	0.93	0.52	
	BOU	Non-ground	0.93	0.58	0.71	64.52
		Ground	0.38	0.85	0.53	
	Imbalanced	Non-ground	0.93	0.97	0.95	92.20
		Ground	0.86	0.72	0.78	

Regarding the convenience of using balanced or imbalanced point could datasets for ground/non ground classifications, the comparison among the four LiDAR data set (Table 19.) showed that the imbalanced data set was more accurate for ground point classification than the balanced ones in the validation phase.

On one hand, the results of the classification of the balanced data sets showed a strong agreement with true data for both classes in the testing phase (Table 19.). In addition, the results showed that the method used for balancing the dataset (BU, BO, BOU) does not have significant influence in the algorithm accuracy (i.e., all the F1-scores were between 0.87 and 0.90). On the other hand, taking the BU dataset as an example of the three balancing methods, the F1-score strongly decreased in the validation phase when using the balanced data sets (ground: 0.90 vs 0.52; non ground: 0.89 vs 0.72). The values of recall and precision showed that the model is capable to detect ground points almost perfectly (recall: 0.97), but it also tends to misclassify the non-ground class as ground (precision: 0.37), producing a moderate F1 score (0.52).

To explain those results, it should be noted that during the test phase, for the balanced data sets, the artificially rebalanced training and test sets were used, producing high accuracies in the classification. Nevertheless, during the validation phase, the balanced training set was used for training the classifier, while the imbalanced (the real point cloud) validation set was used to test the classifier. Therefore, the training and validation sets had different distributions because of the bias introduced during rebalancing. It is well known that rebalancing modifies the prior training set and, consequently, biases the posteriori probability of a classifier (Dal Pozzolo, Caelen and Bontempi, When is undersampling effective in unbalanced classification tasks?). The classifier trained this way tends to move the optimal separation boundary toward the majority class (Dal Pozzolo, Caelen and Johnson), so that more non ground points are classified into the ground class. This produced high recall and low precision for the balanced data set in the validation phase (Table 19.). Additionally, oversampling can lead to over-fit to small data samples, while downsampling due to information loss (Dal Pozzolo, Caelen and Bontempi, When is undersampling effective in unbalanced classification tasks?) could reduce the classifier performance.

For the imbalanced data set, the performance of developed approach remained stable in both the testing and validation phase (Table 19.). The high value of precision, recall, and F1-score indicated an almost

perfect classification of the non-ground class. As a result of imbalance distribution and highly overlapping classes, the number of ground points correctly classified decreased (Sun, Wong and Kamel), producing a lower F1-score (non ground: 0.95 vs ground: 0.78). The recall and precision value indicated that the model is highly trustable (precision: 0.86), correctly detecting 72% of the ground points. The values attained for the ground class were similar to the ones reported by (Rizaldy, Persello and Gevaert), who reached an average total error of 5.21%, with low type I (4.28%) and type II (14.28%) errors, meaning that more non-ground points were mislabeled. The higher type II error was explained by the number of non-ground data points in both samples being considerably lower than the number of ground points. Therefore, the validation recall value in the imbalanced data set could be explained in this case by the lower number of ground points. (Hackel, Wegner and Schindler) reached an overall classification accuracy of 95–98% and a mean F1-score of 0.70–0.74, which is similar to the results obtained in this study. However, the algorithm presented in this paper provided an almost complete ground classification (recall: 0.99, precision: 0.98, F1: 0.98), probably because of the low class overlapping, as linear separable classes are not sensitive to any amount of imbalance (Sun, Wong and Kamel), (Japkowicz and Stephen). Because of the high degree of complexity of our data, the approach presented in this paper is more sensitive to imbalanced data sets then the approach shown in the work of (Hackel, Wegner and Schindler). The benefit of rebalancing is strongly dependent on the nature of the classification task and should be used only if the distribution of the generated and real data set will remain same.

Taking into account the results presented in Table 19, the classified imbalanced LiDAR and UAV point clouds gathered on the validation areas (Figure 22 A and B) were used for the next sections (production of DEM and accuracy assessment).

Spatial Variability of UAV and LiDAR DEM Accuracy: The DoD method was used to calculate total elevation discrepancies between the ground truth and LiDAR and UAV DEM. We used the residuals to estimate the MAE and RMSE. As MAE is a measure of DEM accuracy and is used to identify the overall bias in the data, the results showed that the classified LiDAR data tended to underestimate the elevation by an average of 5 cm (Table 5.), while the UAV data overestimated the elevation by an average of 28 cm (Table 20.).

Table 20. Accuracy of LiDAR and UAV digital elevation model (DEM) per land cover/land use classes (root mean square error (RMSE) and mean average error (MAE)) using the DEM of difference (DoD) method.

	LiDAR		UAV	
	RMSE [m]	MAE [m]	RMSE [m]	MAE [m]
All classes	0.25	0.05	0.59	-0.28
Water	0.37	0.09	1.70	-1.11
High vegetation	0.20	0.03	1.00	-0.39
Medium vegetation	0.19	0.04	0.51	-0.26
Low vegetation	0.19	0.04	0.23	-0.21
Bare land	0.20	0.03	0.25	-0.18
Built up areas	0.27	0.06	0.28	-0.27

In addition, the examination of individual cross sections at different locations across the study area was done in order to better understand the influence of land use/land cover classes in DEM accuracy. The results of the comparison are presented in Figure 24. In the case of the LiDAR DEM, the profiles were coincident or within a few centimeters of the true data (Figure 24. (a), (b), and (d)). The largest distance was noticed in the river bed (Figure 24 (c)). For the UAV DEM, elevation differences in the river bed and area covered by dense vegetation (Figure 24 (b) and (c)) were the largest, while the smallest elevation difference was obtained for bare land (Figure 3d) . In relation to the accuracy in elevation, the LiDAR DEM had an RMSE of 0.25 m and an MAE of 0.05 m, while the UAV DEM had values of 0.59 m and –0.28 m, respectively (Table 20). In the work of (Hu and Yuan), total classification error of LiDAR ground class was 2.9% over 40 various complex terrains, while RMSE ranged from 0.05 to 0.28 m. When the effect of the land cover/land use class in the accuracy of the DEM was analyzed (Table 20.), it showed that the largest differences between both DEMs were obtained in the area covered by water bodies (RMSE of 0.37 m and 1.70 m for LiDAR and

UAV DEM, respectively). The errors associated with this land cover were probably because of the fact that the training data did not include water bodies.

The second largest error for the UAV DEM was obtained for the high vegetation class (RMSE 1.00 m), with an average underestimation of 0.39 m, while the smallest ones were, in both cases, obtained for the low vegetation class (RMSE of 0.19 m and 0.23 m for LiDAR and UAV DEM, respectively). The RMSE for the vegetation classes was not significantly different in the LiDAR DEM, while for UAV DEM, the RMSE increased with the height of the vegetation class (Table 20.). Along the same lines, the DoD examination of cross sections (Figure 24.) and the results of the C2C comparison (Figure 25.) also showed the increase of RMSE and MAE for UAV DEM with the increase of vegetation height. Those findings are in line with results presented in the work of (Salach, Bakula and Pilarska). In general, and for all land cover classes, the UAV DEM overestimated the elevation (MAE < 0), while the LIDAR DEM tended to underestimate it (MAE > 0).
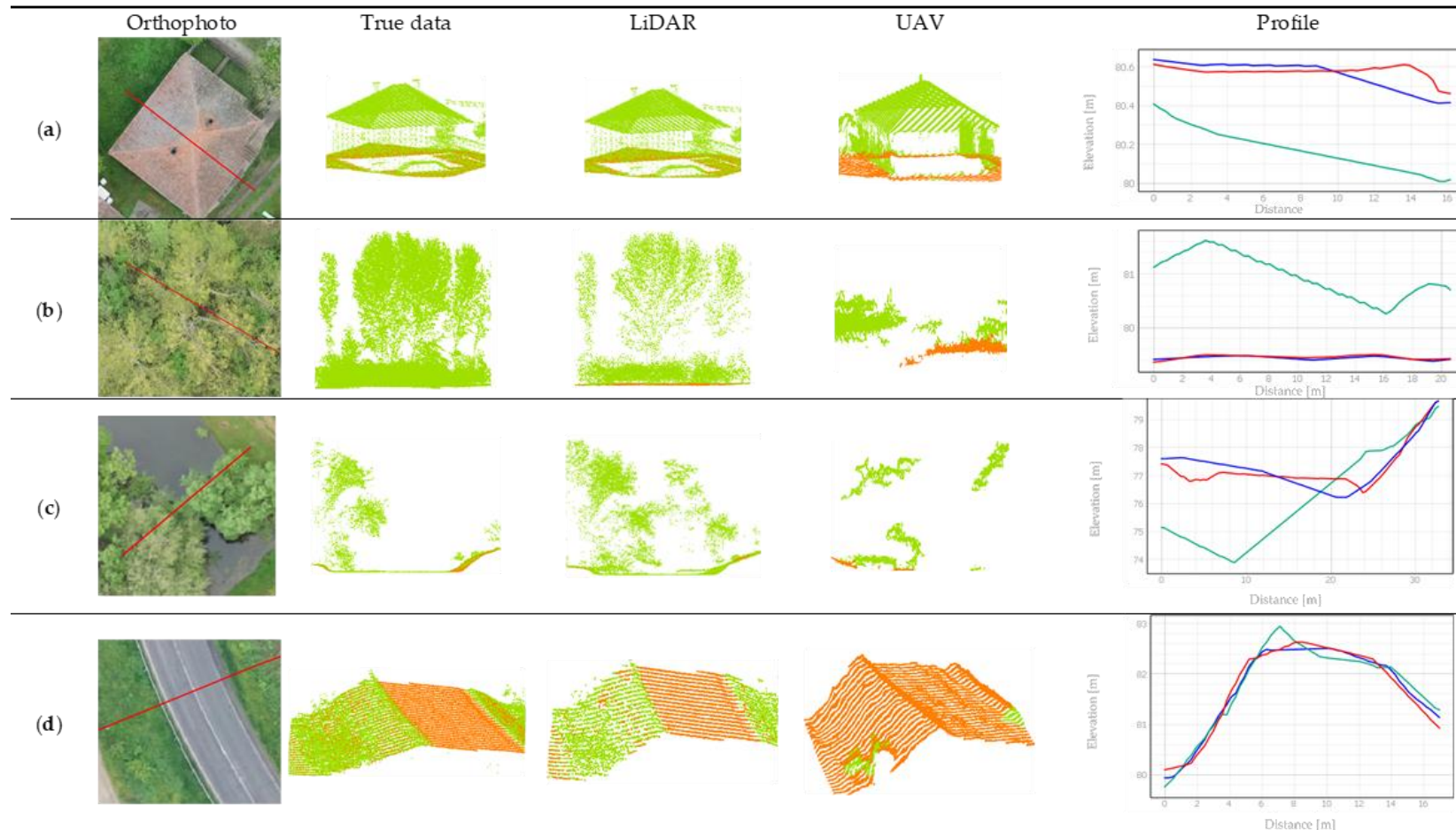
Figure 24.   Comparison true data and LiDAR and UAV data using the proposed classification method. The green points represent the non-ground class, while the orange points represent the ground class. Profiles were created over different land cover classes ((a) built up areas; (b) dense vegetation; (c) water; (d) bare earth) based on DEM with a spatial resolution of 25 cm. The red, blue, and green lines represent the true, LiDAR, and UAV data, respectively.

Accuracy of UAV and LiDAR Point Clouds (C2C Method): The distance between the reference (true point cloud) and target (LiDAR and UAV) point clouds was calculated using the C2C tool. The spatial distribution of the results of the C2C comparison along the Z axis for the LiDAR and UAV point clouds are shown in Figure 4. The MAD and the SD along the Z axis between the true point cloud and the LiDAR point cloud were significantly lower than when the UAV point cloud was compared (i.e., 0.002 m vs. 0.113 m, and 0.03 m vs. 0.392 m, respectively). The range of absolute distances for LIDAR was –1.28 to 4.18 m, smaller than for the UAV point cloud (–5.12 to 3.87 m).
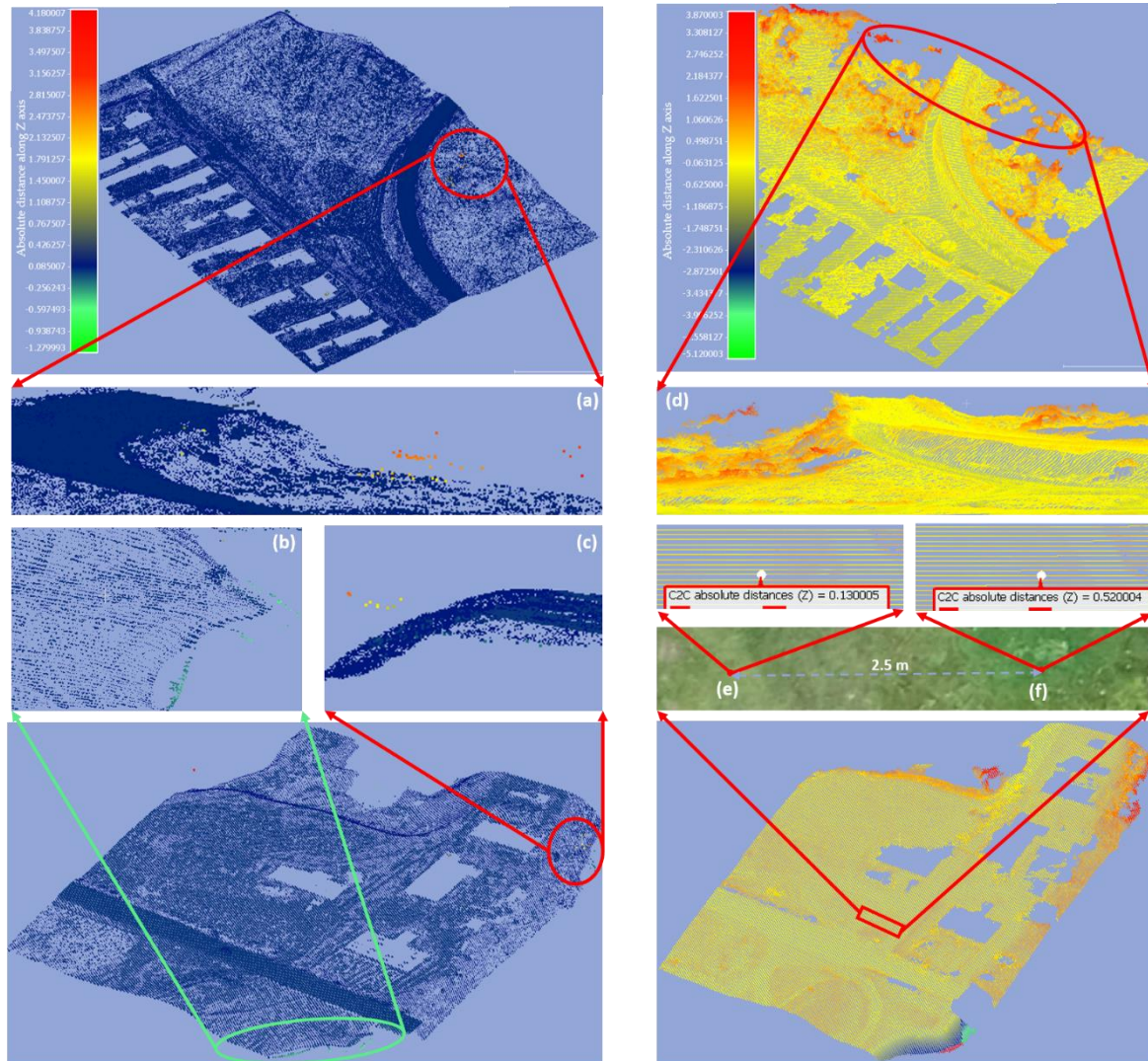
Figure 25. Visual comparison of cloud-to-cloud (C2C) absolute distance along the Z axis. Left column represents the distance between LiDAR and true data ((a) and (c) represents the maximum positive difference, (b) maximum negative distance), while the right column represents the distance between UAV and true data ((d) maximum positive distance, (e) and (f) illustrate the relationship between spatial variability of distance and land cover class i.e. grass and shrubs respectively).

In order to better understand those results, the number of points in different ranges of absolute error along the Z axis were computed (Table 21.). Although the distance between true and LiDAR point clouds varied significantly, the C2C distance for 99.72% of the points was smaller than 5 cm, while for the UAV point clouds, the C2C distance was between 0.5 and –0.5 m for 87.21% of the points (Table 21.).

Table 21. Distribution of points based on cloud-to-cloud (C2C) distance for LiDAR and UAV point clouds.

Absolute Distance along Z axis [m]	Number of Points Lidar	Percent Lidar [%]	Number of Points UAV	Percent UAV [%]
−5.12 to −4	0	0	2129	0.0282
−4 to −3	0	0	1610	0.0213
−3 to −2	0	0	11,462	0.1517
−2 to −1	8	0.0005	19,712	0.2608
−1 to −0.5	52	0.0036	275,648	3.6471
−0.25 to −0.5	292	0.0203	680,829	9.0079
−0.1 to −0.25	600	0.0418	789,888	10.4509
−0.1 to −0.05	1330	0.0925	440,820	5.8324
−0.05 to −0.01	14,105	0.9816	242,428	3.2075
−0.01 to 0	1,303,374	90.7021	0	0
0 to 0.01	67,085	4.6685	360,129	4.7648
0.01 to 0.05	43,076	2.9976	274,241	3.6284
0.05 to 0.1	5367	0.3735	400,257	5.2957
0.1 to 0.25	1056	0.0734	2,119,942	28.0486
0.25 to 0.5	279	0.0194	1,283,580	16.9828
0.5 to 1	176	0.0122	580,283	6.9696
1 to 2	47	0.0032	128,656	1.5211
2 to 3	109	0.0076	12,980	0.1585
3 to 4	26	0.0018	1778	0.0226
4 to 4.18	1	0.0002	0	0

In addition to the aspects discussed in the previous sections, and in order to determine the overall suitability of the proposed method to produce DEM for UAV and LiDAR data, the advantages and the shortcomings of this classification method are discussed below, taking into account the DEM accuracy.

The MAD and SD for the UAV point cloud (0.11 m and 0.39 m, respectively) were significantly higher than for the LiDAR data (0.002 m and 0.03 m, respectively). Those results are in line with the findings presented in the work of (Asal) and with results obtained comparing both point clouds using the DoD method (previous section).

Regarding the spatial variability of UAV and LiDAR DEM accuracy (Table 21.), on the one hand, the large positive absolute distance along the Z axis between the LIDAR DEM and the true data (Table 21.) was the result of the misclassification between the ground class and the points representing vegetation. The misclassification of some parts of the trees that were located near to the elevated embankment and the terrain break lines at the river banks produced the highest C2C distance (Figure 25. (a) and (c)). (Rizaldy, Persello and Gevaert) reported a similar problem with the misclassification of non-ground points in the area where the ground surface is connected to the elevated bridge, because the boundary between the ground and the bridge is fuzzy owing to the gradual inclination of the road surface. As tree parts classified as ground were located at the same height as embankment, a similar explanation could be applied. On the other hand, large negative distances were noticed at the terrain brake lines near to water bodies (Table 19., Figure 25 (b)). This is not surprising because the training data set did not include this type of terrain and water bodies. Also, water absorbs most often the laser pulse causing dropouts, which could influence algorithm performance.

For the case of the UAV point cloud, the distances between true and compared data along the Z axis were between −5.12 and 4 m (Table 21.). The location of the largest negative values (errors) in the UAV point cloud was the same as for those obtained for the LiDAR point cloud, although the distance values were much larger for the UAV points (Table 21.). The same happened for the large positive

values (Figure 4d). Nevertheless, the number of points with a distance larger than ±1 m accounted for just 2.16% of the total amount of points, which did not have a significant effect on the MAD and SD values. UAV equipped with a passive sensor (like in this case) does not have the ability to penetrate vegetation and, therefore, the accuracy of the UAV DEM is strongly affected by the land cover class (Table 6, Figure 4e and f). As the survey was conducted in April, when the vegetation was already in the growing season, most UAV points were within a distance of 0.25 m from the true data (Table 6), which could be close to the height of the vegetation at that time. Additionally, the 3D model creation using SfM is based on static scenes, and as trees and water are prone to movement, it represents a problem for the key point matching algorithm, causing dropouts, inaccurate elevation representation, and lack of data (Figure 25 (d)).

The main advantage of the proposed method (raw point cloud classification and ground point filtering based on deep learning and NN) is the ability to classify raw point clouds without parameter settings and point to image conversion. Therefore, it is more efficient regarding computational cost, and it is easier to use. The quality and size of training samples are crucially important for successful classification (Kavzgoul). The algorithm will label the ground points of different terrain complexity with high accuracy if training data contain sufficient representatives of various terrain types and include all land covers. In the future, the geometric features based on the local structure tensor and more efficient neighbor finding algorithm should be tested.

4.3.2.2. Water body delineation from LiDAR data

The review of stata-of-arte approaches used for water body delineation from LiDAR data is presented in section 3.3.2.1. Due to the highly limited data set, the deep learning algorithms were not considered for classification. The aims of this section are: (1) to research the utility of a high-resolution airborne LiDAR dataset and object-based classification for water surface extraction (2) to compare classification LiDAR results with those from Sentinel 2 multispectral satellite images.

4.3.2.2.1. Study area and data

The study area is located at the confluence of the river Bosut and Sava, Municipality of Sremska Mitrovica, Republic of Serbia (Figure 26.). The study area is part of Pannonian basin with a dominant flat topography, mostly covered by agricultural fields and built up areas. River Bosut is a "flatland river" with the height difference between the source and confluence of only 15 meters. Such a small slope causes great river meandering and frequent natural pollution (transparency, mud) (Wikipedia). Bosut pumping station is located at the confluence of Bosut and Sava. When the water level of Sava is higher than Bosut, water needs to be pumped back to the Sava, therefore Bosut pumping station has an influence on Sava water level and, during the floods in May 2014 it had a significant role in the flood protection of Sremska Mitrovica and its surroundings.
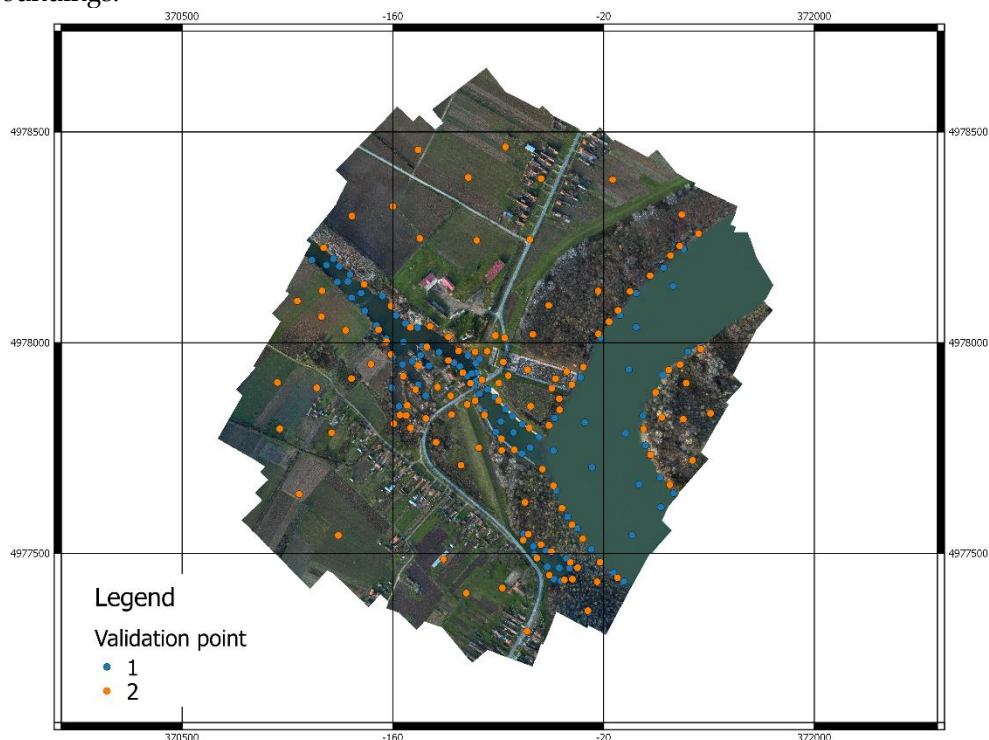

Figure 26. Study area [Validation points: 1 water, 2 non-water]

LiDAR: The airborne LiDAR data and digital aerial photographs used in this study were captured using Litemapper 6800 on December 01, 2017. Instrument mapping list is provided in Table 17.

The LiDAR data were captured with an average point spacing of 5.4 cm. The LiDAR returns were classified into eight classes: unassigned, ground, low vegetation, medium vegetation, high vegetation, buildings, noise and model key by the data provider using proprietary software. The flying height when capturing the LiDAR data was approximately 200 m above ground level. The aircraft speed was 45 in. Maximum scan angle was set to 60°.

Ortophoto: Digital orthophotos were captured by a digital aerial photogrammetric camera and GNSS/INS systems on board (in the plane). The assessment of XY coordinates was conducted by using control points. The location of these control points was three times more accurate than the defined accuracy of digital orthophoto coordinates. Additional GNSS data were obtained from the GNSS station of AGROS (Active Geodetic Network of Serbia) network. Also, data were gathered by using the signal from at least 5 GNSS satellites properly distributed (PDOP ≤ 4).

Sentinel-2: The feature space for the Sentinel-2A image comprised of four 10 m Sentinel-2A Level 2A bands (R, G, B, NIR) and two bands 20 m bands (SWIR 1, SWIR 2) pan-sharpened to 10 m resolution. According to (Du, Zhang and Ling) 10 m NIR band had the greatest correlation with SWIR band, therefore, it is used as a pan like band-since Sentinel-2 mission doesn't have a pan band.

4.3.2.2.2. Methodology

The approach followed in this paper is showed in Figure 27. and it consists of three main parts: preprocessing, classification, and accuracy assessment. It consists of three phases: preprocessing, classification and accuracy assessment.

Preprocessing: The LiDAR point cloud was firstly classified to the ground and non-ground points by using the approach presented at section 4.4.1. Based on classification results the three raster dataset were created: DTM, DSM, and Slope. Additionally, the LiDAR point cloud was processed into Intensity and point density (Figure 28). The digital terrain model was produced at a pixel size of 10 cm using an inverse distance weighted interpolation of returns classified as ground hits. From this DTM, the rate of change in horizontal and vertical direction terrain slope layer measured in degrees was calculated. Digital Surface Model was produced from the first return points, which samples' elevation of the first object encountered by the laser beam on its path to the ground, by using the maximal height. Normalized DSM was produced by subtracting DTM from DSM. nDSM represents vegetation height above ground. According to (Hooshyar, Kim and D) to classify water body, it is essential to use the return of the intensity from the ground surface. Therefore, the intensity layer used in this study was created as the minimum intensity of ground returns. Point density was created as a ratio of a number of registered points and number of pixels.

Classification: Object-based image analysis was carried out in order to identify two classes (water and non-water), using a threshold-based method. According to (Smeeckaert, Mallet and David) surface water body is defined as a discrete and significant element of surface water such as a lake, a reservoir, a stream, a river or a canal, part of a stream, river or canal, a transitional water or a stretch of coastal water.

LiDAR-derived data: Streambed is continuous flat low-lying areas surrounded by steep stream banks. First, lowest-lying areas, that represent potential water bodies, were identified based on low absolute height. However, mapping the water body cannot be simply done by setting an elevation threshold from a DTM, as upstream areas will have different elevations to downstream areas (Johansen, Tiede and Blaschke), therefore, additional information is used. Water surfaces are assumed to be very horizontal (Smeeckaert, Mallet and David), (Hofle, Vetter and Pfeifer) therefore slope layer was generated based on DTM in order to identify flat surfaces. Intensity information from near-infrared topographical LiDAR system, that is a relative strength measurement of the return pulse by the LiDAR sensor, is lower from water surface compared with land cover since water highly absorb NIR range of spectra (Brezonik, Olmanson and Finlay), (Hooshyar, Kim and D).
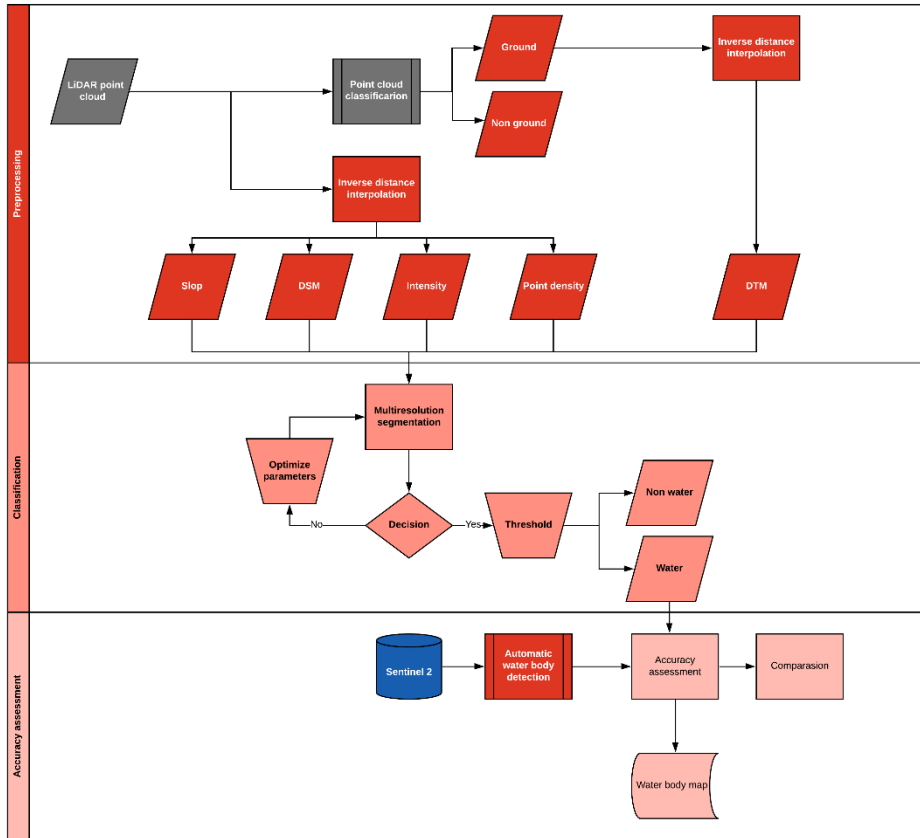
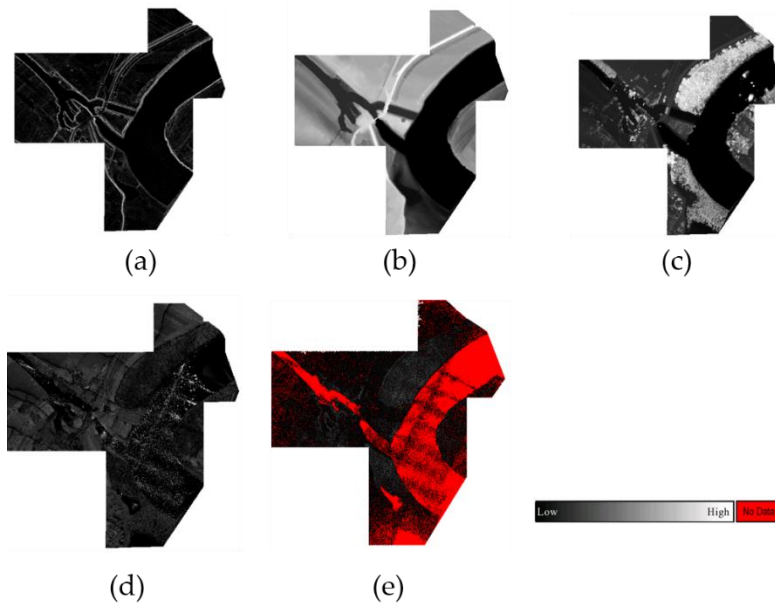Figure 27. Workfloe for extraction of water bodeis from LiDAR data

Figure 28. LiDAR-derived raster data set (a) slope, (b)DTM, (c)nDSM, (d) intensity (e)point density

Since water is low albedo surface part of the emitted radiation returning significantly varies and may not be distinguished from the background noise (Smeeckaert, Mallet and David). Also, the intensity of LiDAR return can be too small to be detected therefore, dropouts are frequent,

producing much lower point density in the water bodies comparing to inland areas (Smeeckaert, Mallet and David). DSM was used to mask vegetation, which is frequent in the riparian zone. In reality, the ground surface objects are composed of a number of pixels. The segmentation algorithm aggregates the pixels into an object according to the one or more criteria of homogeneity and provides building blocks of object-based image analysis. Object-based classification considers the properties of the object i.e. additional spectral information compared to pixels (mean band value, median values, minimum and maximum values, mean ratios, variance). Still, spatial dimension like shape, size, distance, neighborhood, topologies etc. are crucial to OBIA method (Ke, Quackenbush and Im), (Teo and Huang), (Du, Zhang and Ling). The OBIA was based on LiDAR-derived raster products (DTM, DSM, Slope, Intensity and point density). The OBIA was performed in recognition 8.7 where Cognition Network Language was used for the development of a rule set which provides a time-efficient mapping of water bodies. The multi-resolution segmentation was used. Weights for each layer were determined based on their ability to delineate the water body. The higher weights were established for DTM, Slope, and DSM. Threshold values are determined in eCognition using update range function.

Accuracy assessment: In order to estimate the accuracy of the classification pixel-by-pixel approach was used. The OA, omission error, commission errora and KHAT statistics are calculated based on confusion matrix. The validation points were verified using a digital RGB orthophoto (spatial resolution of 5 cm) and their spatial distribution is displayed in Figure 1.

4.3.2.2.3. Results and discussion

The experiments in this study analyzed two different aspects: accuracy assessment of water body extraction, and comparison of results obtained from LiDAR-derived data and Sentinel 2 images. Visual inspection of Figure 29. indicated that the proposed method successfully extracted water bodies with complete shapes, while the extracted results for Sentinel-2 were incomplete due to ommition of shallow parts of river body producing large omission errors.
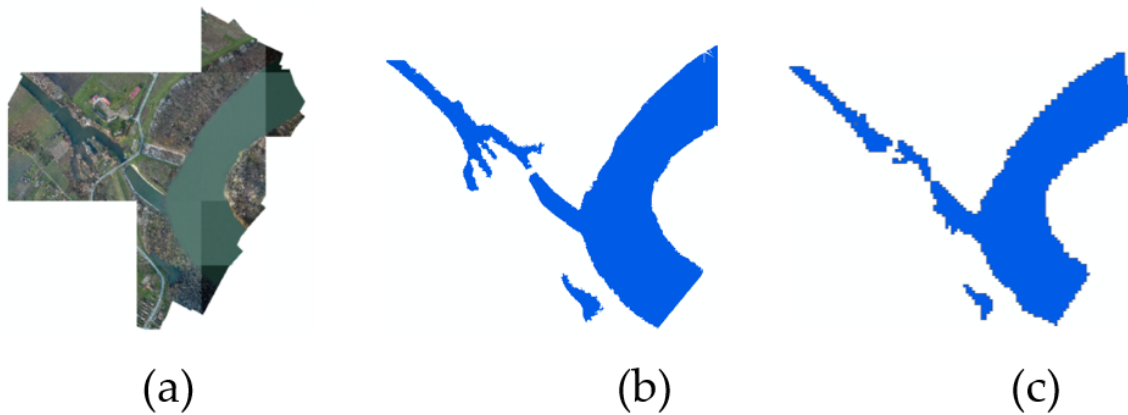

Figure 29. (a) digital orthophoto, (b) water bodies extracted from LiDAR-derived data, (c) water bodies extracted from Sentinel 2

The results of the accuracy assessment for surface water body mapping using the LiDAR-derived data and Sentinel-2 are shown in Table 22.

Table 22. Accuracy assessment for a surface water body

	Kappa	OA	Commission		Omission	
			Water	Else	Water	Else
LiDAR	0,82 (0,75-0,90)	91,19	12,26	5,79	7	10,24

Sentinel-2	0,43 (0,31-0,55)	73,69	26,25	27,89	41	16,54

As a measure of agreement or accuracy, KHAT is considered to show strong agreement when it is greater than 0.75 (Jones and R.A.), while values lower than 0.40 indicate poor agreement (Chen, Stow and Gong). Therefore waterbody extraction from LiDAR-derived data shows a perfect, while Sentinel 2 provide moderate agreement with reality. The classification using LiDAR-derived data had a significantly higher according to all parameters (OA, Kappa. CE, OE) than Sentinel 2 which is expected to the significantly higher resolution.

Although the classification of LiDAR data uses the additional features intensity, point density, the height, and the slope represent the most important feature because the additional features are often noisier due to the unstable emitted pulse, changing surface reflectance etc. Also, waves within water cause often larger height variations and in case of white crests inhomogeneous reflectance behavior (Brzank, Heipke and Goepfert). Based on accuracy assessment and visual validation proposed algorithm tends to overestimate water bodies. Trees over water bodies which were classified as water produce higher commission error and overestimation in LiDAR dataset. One of the advantages of LiDAR as an active remote sensing technology over passive optical images is that LiDAR-derived data are not affected by shadows that significantly affect the accuracy of water body extraction.

The algorithm used for Sentinel 2 images strongly underestimated water area and produced high omission error. The main reasons for high omission error of Sentinel -2 are low spatial resolution and mixing pixels that produce confusion between water and other features. Moreover, haze, shadow, seasonal, and the daily difference in the sun angle, the change in water quality parameter can produce lower accuracy. Considering a month gap between the acquisition of Sentinel 2 and digital orthophoto used for determining the location of validation points, the change of water level can produce a significant error. The possible limitations of the presented approach are: presented methods are based on the segmentation parameter and classification rule sets which may need to be modified for another area of research, and ground truth points used for classification accuracy assessment were determined by visual inspection of digital orthophoto images.

4.4. Water Body Attributes

The review of the application of remote sensing technologies in the monitoring of WQP and assessment of their status is presented in sections 3.3.1.3., 3.3.1.4., 3.3.2.2., and 3.3.3. In this thesis, the monitoring of biological and phisico-chemical parameters is based on the integration of optical remote sensing and in situ data. Additionally, the potential of UAV data for the detection of visible waste materials was presented.

4.4.1. Water Quality Parameters

In this study, optical remote sensing data are used to monitor WQP, an indicator of biological status, general condition, oxygen regime, and nutrients. Totally concentration of six WQP, including chl-a (biological parameters) and SS, Turbidity, TN, TP, and DO (phisico-chemical parameters) were estimated.

Chl-a is considered as an indicator of phytoplankton abundance and biomass in waters and can be used to determine the water quality, biophysical status, and eutrophication level of a water body. It is used in oxygenic photosynthesis and is found in plants, algae, and cyanobacteria.

Suspended sediments are one of the most common pollutions in the freshwater system. Several factors control TSS concentration, including relief, channel slope, basin size, weather, and human intervention (Chakrapani). Increased TSS concentration inhibits the proper function of the aquatic ecosystem and changes water quality (increase temperature, reduce dissolved oxygen).

Nitrogen (N), needed for protein synthesis, and Phosphorus (P), required for DNA, RNA, and energy transfer, are the key limiting nutrients for plant growth in most aquatic and terrestrial ecosystems (J. Liu, Y. Zhang and D. Yuan). TP studies consist of the measurement of all inorganic, organic, and dissolved forms of phosphorus. The concentration of TP is directly related to chl-a and indirectly for turbidity i.e., SDD. The increase of chl-a concentration increases the TP concentration while the increase of TP decreases the SDD.

DO is one of the critical parameters that represents the amount of oxygen that is available at the water body. The water temperature highly influences the amount of DO, and it can be used to estimate its concentration. The amount of DO and water quality are directly related i.e., a higher concentration of DO indicating the better water quality.

The overview of the state-of-the-art method used for monitoring WQP from optical images is presented in Table 6.

4.4.1.1. Data

Optical remote sensing monitoring of WQP is based on the comparison between surface reflectance and correspondent in situ measurement.

In-situ data are provided by the International Commission for the Protection of the Danube River (ICPDR). To provide an overall status of pollution and long-term trends in water quality and pollution in the major rivers of the Danube River Basin ICPDR established the TransNational Monitoring Network (TNMN). The network consists of 101 monitoring stations with up to 3 sampling points across the Danube. The minimum sampling frequency is 12 per year for chemical and twice a year for biological parameters (ICPDR, TNMN - TransNational Monitoiring Network). The location of monitoring stations is presented in Figure 18.   Landsat 5, Landsat 7, and Landsat 8 Surface reflectance products from 1996 to 2017 over Danube River Basin were used. Landsat Surface reflectance is atmospherically corrected, containing 6 bands processed to orthorectified surface reflectance using LEDAPS (USGS, Landsat 4-7 Collection 1 Surface Reflectance Code LEDAPS Product Guide). The Google Earth Engine API integrated into Google Colab was used as an access point to the images. The bands used in the study are shown in Figure 8.

4.4.1.2. Methodology

Figure 32. summarizes the approach followed in this paper. It consists of four main steps: preprocessing, classification, accuracy assessment, and monitoring of WQP concentration.

Preprocessing: The coordinates of the monitoring station are reprojected from WGS84 to WGS84/UTM 34 N projection to match the Landsat coordinate system. Since each monitoring station consists of multiple sampling points for which the exact location and concentration of WQP have not known, the profiles across rivers were created. Along profiles, on each 30 m, the point was created (Figure 30). For each point, the values of surface reflectance were extracted from available Landsat 5, Landsat 7, and Landsat 8 Surface Reflectance Level 2A image. The extracted surface reflectance values along profiles are averaged and paired with the appropriate monitoring station. The resulting table contains the id of monitoring stations, the corresponding value of surface reflectance, and the sensing data. The surface reflectance is filtered by date to match the in situ data. The maximum time gap between in situ sampling and satellite overpass is 3 days. Final training data contain the surface reflectance of B, G, R, NIR, SWIR1, SWIR 2 band, band ratios B/R, G/SWIR2, spectral indices NDWI and NDTU, and the corresponding concentration of WQP. Pearson correlation analysis was used to investigate the association between two variables with a correlation coefficient (r). The data are standardized to fit normal distribution with mean 0 and standard deviation 1 and split to training and test set.
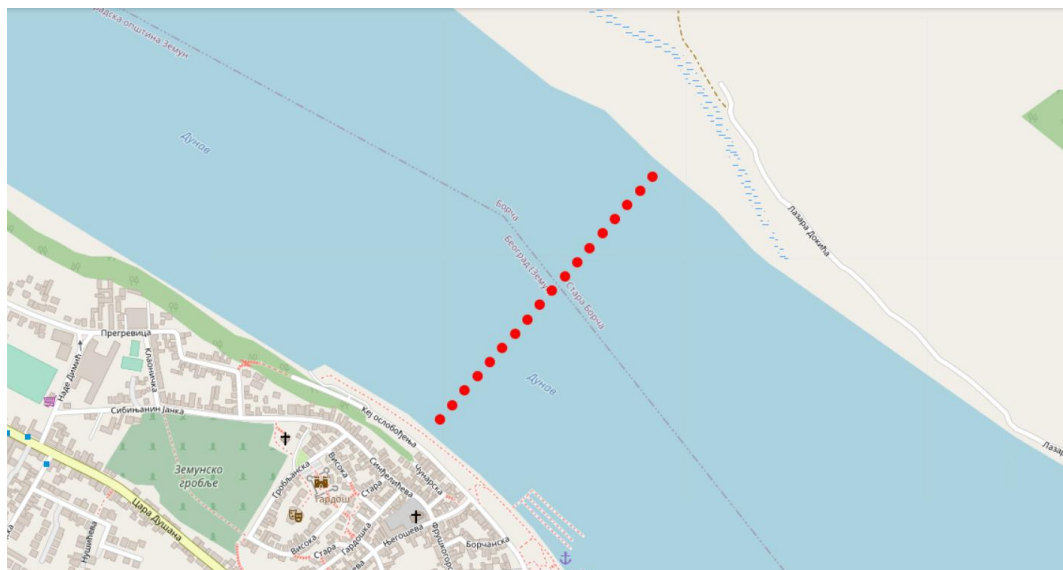
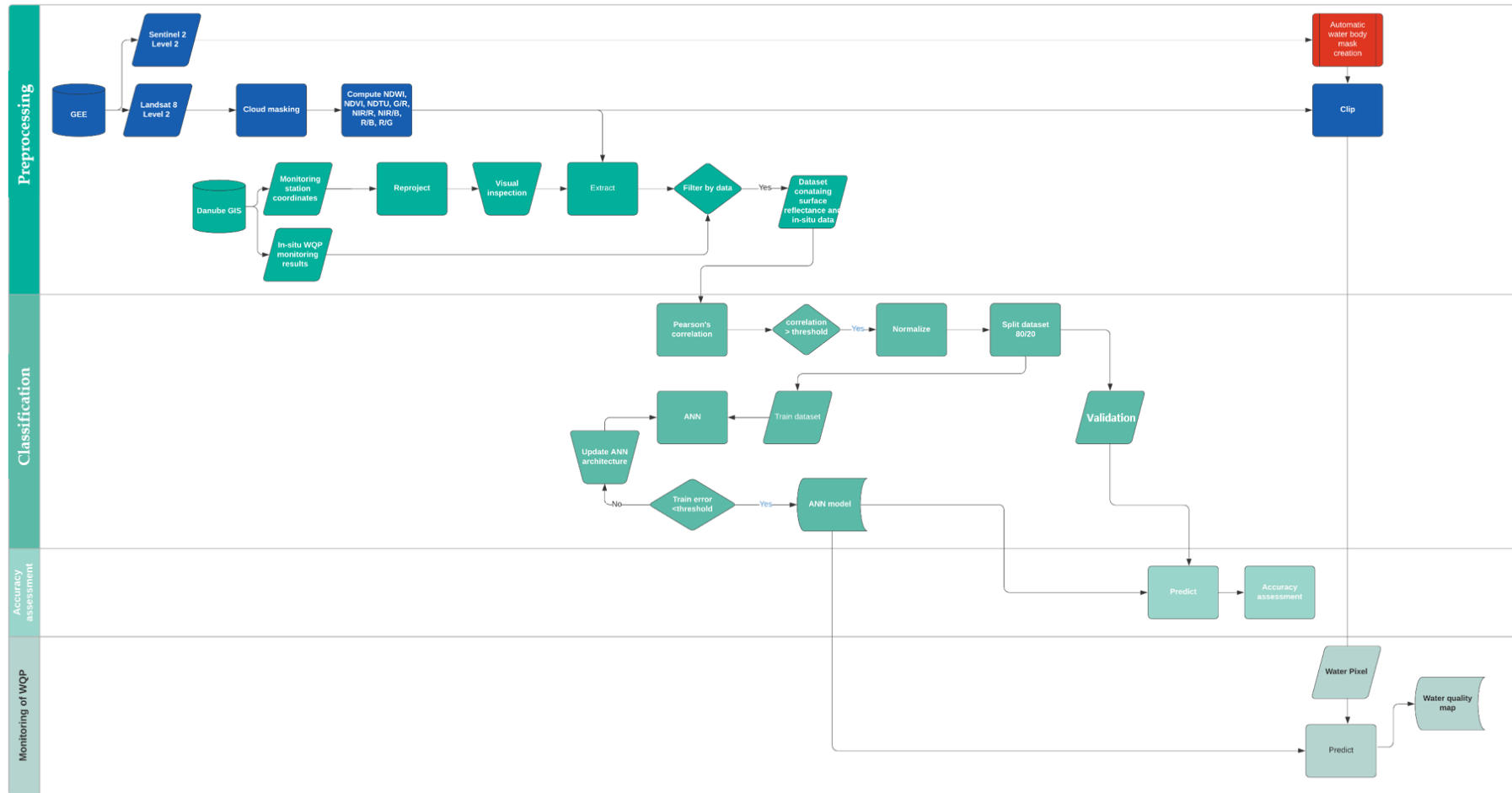Figure 30. Points used for extraction of surface reflectance

Figure 31. Proposed workflow for water quality monitoring based on optical images

Classification: The relationship between WQP concentration and surface reflectance was modeled by using ANN. ANNs are pattern-recognition algorithms that consist of an interconnected group of artificial neurons, and it processes information using a connection approach to computation (Fausset). The organization of the connection between the neurons represents the architecture of the network (feedforward or backpropagation) and network topology (fully connected, partially connected). In this study, a fully connected back-propagation neural network was applied. The network has three layers: input, hidden, and output (Figure 32.). The input layer represents predictor or independent variables (in this case radiance measurement of different wavelengths). Hidden layers contain a varying number of neurons. Each neuron consists of two parts, a linear summation function where the input parameters are multiplied by the connection's weight parameters, added to the bias, and summed together and an activation function that modulates the output of the neuron. An activation function is nonlinear, usually ReLU or sigmoid, enabling the NN to learn patterns that are not linearly separable (Anthony and Bartlett). The number of nodes in the hidden layer depends on the complexity of the approximated function and sample numbers. If the network is too small, the self-learning ability and precision of the network will decrease, causing under-fitting. Under-fitting can be resolved by adding more hidden neurons. Meanwhile, if network is too large, training time will increase, and the generalization capability of the network will decrease, producing over-fitting (Krasnopolsky, Gemmill and Breaker). Generalization represents the ability to predict data that it has not seen before correctly. ANN that generalizes well will provide a correct prediction of unseen data, which can be slightly different from the training data. Each hidden neurons act as a feature detector discovering the different characteristics of input data by performing nonlinear transformation into new space (feature space) where classes can be easily separated. Therefore the more hidden nodes mean more salient features are used to determine the boundary between classes. However, if the network is too large, its ends up memorize input data such as features that are present in training data, but not true of the underlying function that is modeled disabling the generalization between similar input-output patterns (Haykin). There is not a theoretical formula that can be used for the selection of optimum NN architecture. The architecture is fixed by using a trial-and-error approach. The trial-and-error approach starts with simple architecture, and the model is calibrated by adding one by one hidden neurons until there is no significant improvement in the performance of the NN. The output values of the hidden layer are input values of the output layer, which also performs the summation and activation functions. The output of this layer is the target of water quality parameters. To derive the correct output, the network learns by training on subsets of in situ data. In the back-propagated network, outputs are then compared with actual values from the training data set, the error is calculated, and results are transferred to the output layer. As data pass through the network many times, weights are adjusted and errors are reduced (Figure 32.).
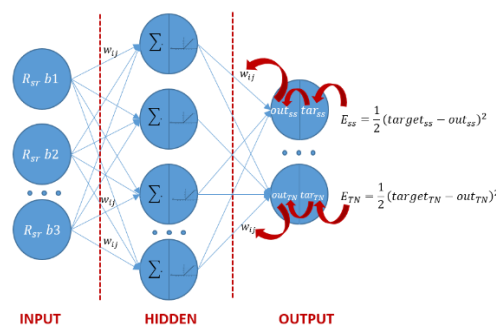

Figure 32. Architecture of ANN

Accuracy assessment: The performance of the developed workflow was evaluated using RMSE (6) and normalized RMSE (7). A RMSE measures the quality of the model fit. The 0 indicates perfect fit for the data, while large values will be obtained if the estimated concentration of WQP and true concentration differed substantially. NRMSE is used to compare results between models with different scales.

$$RMSE = \sqrt{\frac{1}{n}\sum_{i=1}^{n}\left(x_i^{estimated} - x_i^{measured}\right)^2} \tag{6}$$

$$NRMSE = \frac{RMSE}{x_{max}^{measured} - x_{min}^{measured}} \tag{7}$$

4.4.1.3. Implementation

The developed workflow was implemented in the Python programming language. The workflow consists of four modules for the creation of training data, classification, accuracy assessment, and monitoring of WQP, and it is fully automatic. Manual input is only used for the selection of optimal NN architecture. The remote sensing data are accessed and preprocessed by using GEE Python API. The data set and NN architecture were defined for each WQP. All data set were split at 80% for training and 20% for validation. To avoid overfitting, the early stopping is used. Early stopping is a commonly used form of regularization which interrupts the training process when there is not the improvement of validation loss for a predefined number of epochs. Each time when validation loss has improved, the copy of model parameters is stored. After training of the algorithm termites, those parameters are used instead of the last parameters.

The training of the networks was done using the publicly available cloud platform Colaboratory (Google Colab), which is based on Jupyter Notebooks. The parameters used in the model training are presented in Table 23.

Table 23. Parameters used to train the model for water quality monitoring

Parameter	Dataset size	ANN architecture	Epoch	Optimizer	Loss	Min	Max
Chla	1405	15-15-15-15-6-1	834	RMSprop	Mse	0	99.5
DO	2372	20-20-20-20-6-1	842			3.2	19.5
SS	2773	20-20-20-20-6-1	1500			0.5	871
TN	1063	15-15-15-15-6-1	447			0.3	15.21
TP	2220	20-20-20-20-6-1	214			0.007	1.64

4.4.1.4. Results and discussion

Remote sensing monitoring of water quality is based on the understanding of how the variation of WQP influences the optical properties of the water column. Although in large water bodies, with a homogenous concentration of WQP, the strong correlation between WQP concentration and surface reflectance tend to be derived, the water quality monitoring of small to medium-sized river is challenging due to the coarsely spatial resolution of the sensor, spatially heterogeneity of concentration and more temporally dynamic changes. The correlation matrix and scatter plot are shown at Appendex A. The resulting r values were significantly lower compared with previous studies. For example, (Bonansea, Pinotti and Derrero) reported the higher correlation between chl-a concentration in a reservoir and Landsat 8's B and G bands with r values of 0.64 and 0.68, respectively,

while in this study, the r values where -0.1 and -0.063. Similarly, (Lim and Choi) obtained maximum r value between TN in rivers and R and NIR bands of 0.41 and 0.45 respectively, compared with 0.11 and 0.059 in this study while the correlation between TP and B, G and R band were similar and around -0.5 (compared with -0.42 in this study). As stated before, the correlation is influenced by the high complexity of the environment with a large number of small water bodies, the high number of pollutants increasing the spatial variability water quality parameter, and the quality of atmospherical correction. Additionally, the methodology used for in-situ data collection also reduces correlation since the exact sampling location wasn't known. The results show that r values increase when the surface reflection is averaged along with profiles compared with using only available coordinates of monitoring stations. As expected, the highest correlation was obtained between Landsat 8 and optical active parameters SS and chl-a ranged from -0.53 (G/SWIR2) to 0.22 (rR) and -0.26 (G/SWIR2 ration) to 0.08 (NDTU) respectively, while the lowest values are acquired for TN (-0.08 (G/SWIR2) to 0.11 (B, R)). The lower r values and shapes of scatter plots in this study indicated the relationship between the in-situ data and surface reflectance is non-linear. Due to that ANN with non-linear ReLU activation function was used for WQP concentration estimation. Totally 5 models were developed. The results of the accuracy assessment are presented at Table 24.

Table 24. Accuracy assessment of WQP monitoring

Parameter	Train			Validation			RMSE	NRMSE [%]
Chl-a [µg/l]	9.440	1.581	9.440	14.365	1.896	14.365	3.66	3.68
DO [mg/l]	0.012	0.073	0.012	0.032	0.143	0.032	0.09	0.57
SS [mg/l]	177.971	3.480	179.510	472.253	5.000	502.481	8.50	0.97
TN [mg/l]	0.054	0.139	0.054	0.119	0.204	0.119	0.43	2.89
TP [mg/l]	0.0008	0.0107	0.00082	0.0043	0.0176	0.0043	0.04	2.73

According to the results, the highest accuracy was obtained for DO and SS (Table 24.). The applied approach provides a more accurate estimation of DO comparing with studies based on NN (El Din, Zhang and Suliman), (Peterson and Sloan), (Jakovljević, Govedarica and Álvarez-Taboada, Assessment of biological and physic chemical water quality parameters using Landsat 8 time series), where nRMSE were 2.63%, 9.1%, 10% respectively. Similar results are obtained by comparing results of SS with studies based on linear regression (Nazeer, Bilal and Alsahli) with nRMSE 4.68%, machine learning (Govedarica and Jakovljević, Monitoring spatial and temporal variation of water quality parameters using time series of open multispectral data) with nRMSE 6.65%, and ANN (Matthews, Bernard and Winter), (Nazeer, Bilal and Alsahli), with nRMSE 14.1%, 8.27%.

The NN model was produced nRMSE of 2.89% and 2.73% for nitrate and phosphor concentration. The (Wang, Wang and Zhou) were obtained the nRMSE 18.2 % for TN and 17.2% for TP by using backpropagate NN and GOCI images in coastal waters. (Govedarica and Jakovljević, Monitoring spatial and temporal variation of water quality parameters using time series of open multispectral data) were achieved nRMSE of 12.56% and 12.76% for TN and TP by using ANN and 6.88% and 9.72 by using SVM algorithm. Based on Table 23. and Table 24. it can be concluded that the accuracy of prediction is directly influenced by the number of samples used for NN training. Due to that, the highest accuracy was obtained for DO and SS since they have the largest number of samples. Also, this study confirms findings from (Govedarica and Jakovljević, Monitoring spatial and temporal variation of water quality parameters using time series of open multispectral data) since NN trained on a larger dataset (219 vs. ~2000) outperformed SVM.

The lowest accuracy was reported for chl-a (nRMSE 3.68 %). However developed model significantly outperforms regression models presented in (Bonansea, Pinotti and Derrero) (nRMSE

7.25%) as well as NN models presented in (Matthews, Bernard and Winter), (Peterson and Sloan), (Nazeer, Bilal and Alsahli) with nRMSE of 9.8 %, 10.24 % and 7.56 % respectively.

The trained models were used to predict the concentration of WQP for each pixel. Results of prediction were classified into five classes. The ranges of each class were defined in line with (Sl.glasnik SRS), (Sl.glasnik RS br. 50/2012), (Sl.glasnik RS br. 74/2011)(Table 25.).

Table 25. Ranges for classification of water body status

Class/Parameter	Chl-a	DO [mg/l]	SS	TN	TP
I	0-25	8.5>	0-10	<1	0-0.05
II	25-50	7-8.5	10-30	1-2	0.05-0.30
III	50-100	5-7	30-40	2-8	0.30-0.40
IV	100-250	4-5	40-80	8-15	0.40-1
V	>250	<4	>80	>15	>1

The spatial distribution of WQP in the Belgrade is shown in Figure 33., while results for the study area are available in Appendix C.
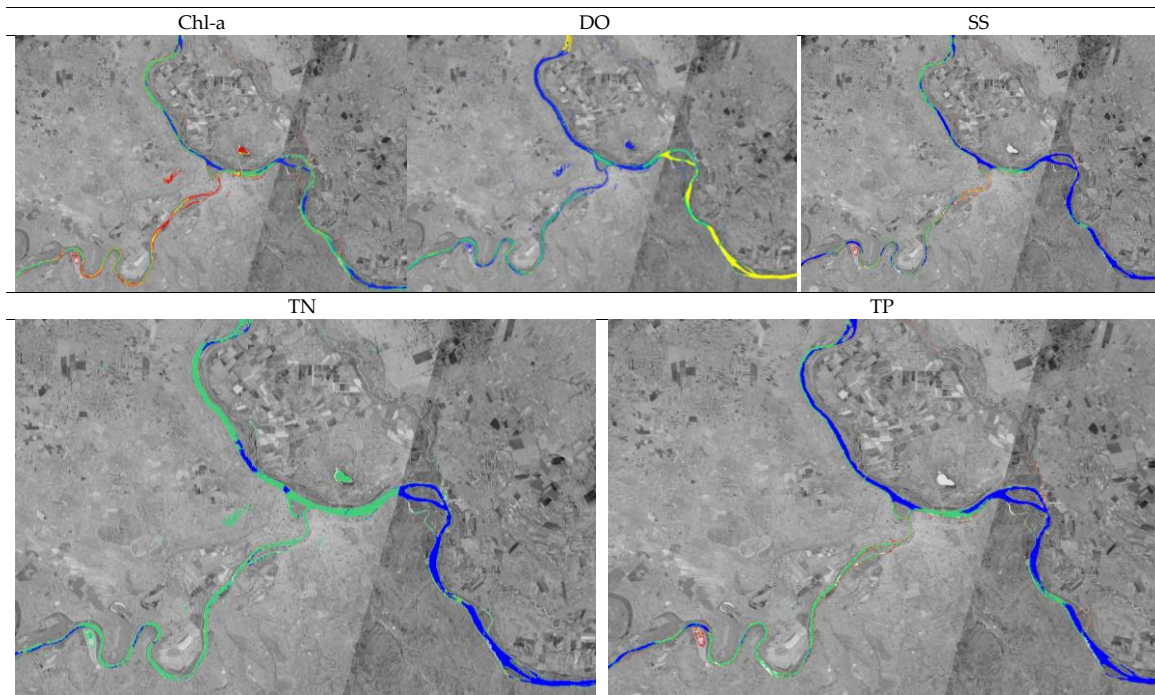
Figure 33. Visual inspection of water quality monitoring results

Based on visual inspection (Figure 33.) it can be concluded that cities are larger polluters. This is expected since less than 10 % of wastewater is treated in Serbia (IVJČ). The spatial distribution of values of DO is moderated, indicating that aquatic life is under stress. The DO concentration in Danube decrease along it flows across Serbia. The highest SS concentration was at small rivers, wetlands, and lakes. Additionally, several hotspots with a high concentration of SS in the Danube were observed at the location of gravel exploitation. The visual inspection and statistical results show a high correlation between TP and SS. This is expected since SS acts as a carrier for TP in streams, and

it can be used as a basis for monitoring TP concentration by remote sensing (Villa, Folster and Kyllmar). It has been observed that increase of TP concentration results in a global tendency of increasing and chl-a concentration. Those findings are in line with results presented in (McQueen, Post and Mills) and (Y. Chen, C. Fan and K. Teubner). Additionally, chl-a significantly increases when TN concentration is reduced at high TP concentration, which is consistent with the conclusion presented in (Filstrup and Downing). Moreover, the visual inspection shows that chl-a concentration is highest at river banks and decreases in the center of the river, which is in the line either the physical process of sedimentation along river banks and algae encroachment (Sabater, Artigas and Duran).

Limitations of remote sensing for WQP monitoring: Remote sensing penetrate to water column up to SDD therefore, it cannot provide complete information about the vertical variation of water quality in deeper water bodies. The sensitivity of multispectral sensors to clouds and haze is one of the main shortcomings for satellite observation of water quality. Additionally, monitoring of small water bodies, often represented in satellite images with a few clear and number of mixed pixels, is highly challenged.

The current methodology used for collecting in-situ data in the Danube river basin is not suitable for integration with remote sensing data due to its spatial and temporal limitation. First of all, the exact location and number of sampling points are not known. For each monitoring station (which coordinates are available) up to three sampling points across the main rivers are used, and the average concentration of WQP is assigned to that station. Consequently, it is not possible to pair surface reflectance with the appropriated concentration of WQP. Secondly, the low frequency of sampling (12 times per year for physico-chemical and twice per year for biological parameters) without optimizing field campaigns with satellite overpass increases the time gap between in-situ and remote sensing measurements, significantly reduce the size of the dataset. Additionally, the sensitivity of multispectral sensors to clouds and haze has the same effect. Due to that, in this study, less than 10 % of available in situ data were used for model calibration.

The optimization of in-situ field campaigns can be done by planning the time of sampling in accordance with satellite overpass over the area of interest. Several online tools provide information about satellites acquire data and paths such as Landsat Acquisition Tool (USGS, Landsat Acquisition Tool). However, the clouds cause significant and unpredictable data gaps making it difficult to plan in-situ measurement.

In recent years, the sensors for automatic monitoring of physico-chemical WQP, such as DO, pH, turbidity, temperature, CDOM, have been widely used. Sensors provide real or near-real-time monitoring in a cost-effective manner since they reduce the number of field visits and cost of laboratory analysis. The high frequent measurements provide a better understanding of the temporal variation of water quality. Since measurements are made at least once per day, all cloud-free satellite images can be integrated with in-situ data, significantly increasing the size of the dataset available for algorithm calibration and provides data for the test of its performance. Feature more, the time gap between in-situ and remote sensing data is reduced to a minimum while correlation is increased.

Moreover, the atmospheric correction is extremely critical for the reliability of WQP monitoring by using remote sensing data. In many cases, less than 10 % of spectral reflectance obtained by sensor carry information about water bodies while the rest (more than 90%) is contributed by atmospheric scattering (Shen and Verhoef). Compared to a clear atmosphere, atmospherical haze increases reflectance, which may lead to less accurate retrieval of WQP in the case of optically complex waters. The performance of atmospheric correction algorithms is limited by the accuracy of used atmospherical parameters (aerosol type and visibility). The atmospheric effects on remote sensing data can be minimized thought the usage of in-situ water leaving reflectance measurement, which are collected over study area.

Beside the atmospheric sckatering, the bottom effect can increase the water reflectance. The effect of the bottom is a function of water depth, water clarity, and type of water body bed (Lee, Carder and Arnone). Therefore the detection of optical shallow waters is important for understanding the uncertainties of developed products and future improvements.

4.4.2. Detection of visible waste materials

In addition to WQP defined by WFD, the Regulation of Water Classification of the Republic of Serbia (Sl.glasnik SRS) demands the monitoring of organoleptic properties of water, i.e., the smell, the color, and visible waste materials. According to Regulation, the water bodies that contains visible waste materials are classified at 5th class. Due to that, the algorithm for the detection of floating plastic was developed.

Plastic pollution has become one of the most significant environmental issues of our age. Since the 1950s, when it was invented, as sanitary and cheap material, plastic took the place of paper and glass in food packaging, wood in furniture, and metal in car production. Global plastic production has increased annually, reaching almost 360 million tons in 2018 (Plastics Europe). Only nine percent of the nine billion tons of plastic that has ever been produced has been recycled (Program). Subsequently, more than 8 million tons of plastic end up in the ocean each year (U. UNEP). Plastic is not biodegradable, and over time, macro plastic pieces degrade into smaller and smaller pieces called microplastic (less than five millimeters long (Lebreton, van der Zwet and Damsteeg)). Microplastic can be swallowed by a wide variety of marine organisms and then rise through the food chain, ending up on our dinner tables. Marine plastic litter is a global environmental problem with significant economic, ecological, public health, and aesthetic impacts. Effective measures to prevent negative effects of marine plastics require an understanding of its origin, pathways, and trends.

Land-based litter, transported by rivers to oceans, is estimated to be a major contributor to this problem (Lebreton, van der Zwet and Damsteeg), (Jambeck, Hardesty and Brooks). The research presented by (The guardian) estimates that just 10 river systems transport more than 90% of the global input. The global estimations of plastic debris entering oceans annually, although numerous, are typically based on local or regional scale surveys, and they vary from 250,000 tons (Eriksen, Lebreton and Carson) to 4.8–12.7 million tons of plastic (Jambeck, Geyer and Wilcox). Therefore, the amount of plastic in the global oceans remains poorly understood with a knowledge gap in terms of the temporal and spatial distribution of plastics, degradation, and beach processes. This information is vital for the development of activity plans for reducing land-based litter impact in oceans. Several efforts have been made to establish a standardized monitoring methodology, such as Oslo and Paris Conventions (OSPAR) (OSPAR), Commonwealth Scientific and Industrial Research Organization (CSIRO) (Hardesty, Lawson and van der Velde), National Oceanic and Atmospheric Administration (NOAA) (Opfer, Arthur and Lippiatt), and United Nations Environment Programme /Intergovernmental Oceanographic Commission (UNEP/IOC) (Cheshire, Adler and Barbière). Those methodologies are based on traditional beach monitoring by visual counting of plastic pieces along transects. Many guidelines on survey and monitoring of marine litter, such as OSPAR (OSPAR), NOAA (Opfer, Arthur and Lippiatt), and UNEP/IOC (Cheshire, Adler and Barbière) record the counts of all items larger than 2.5 cm x 2.5 cm, since this is the minimum disposal size permitted under the International Convention for the Prevention of Pollution from Ships (MARPOL) for ground shipping waste (Ribic, Dixon and Vining). According to (Cheshire, Adler and Barbière), each person is responsible for noticing or collecting all litter in the 2 m wide zone along a transect and, as a consequence, traditional beach surveys involve a large number of people. As an example, CSIRO engaged thousands of students, teachers, and employees in order to survey coastal debris in 175 sites in Australia, surveying 575 two-meter wide transects over a period of 18 months (Hardesty, Lawson

and van der Velde). Visual surveys are, therefore, time and labor consuming, and usually only a sub-sample of the target study area is covered. In addition, the surveyors can be in unsafe situations due to heavy wind, slippery rocks, hazards such as rain and snow, or exposed to dangerous substances (such as chemical substances, medical waste, etc.). Plastic litter is mostly concentrated on banks, coastlines and in the upper layer of surface water bodies, mostly within the first 0.5 m (Kooi, Reisser and Slat). Taking that into account, remote sensing technologies with a high spatial, temporal and spectral resolution have the potential to become reliable sources of information on floating plastics. Two examples of using these techniques have been provided by (Jakovljevic, Govedarica and Alvarez Taboada) and (Aoyama). (Jakovljevic, Govedarica and Alvarez Taboada) developed an algorithm for the detection of floating plastic in freshwater, based on Artificial Neural Networks and high-resolution multispectral WorldView-2 images, reporting a RMSE of 0.03 during the test phases. (Aoyama) used high-resolution WordView-3 satellite images and the Spectral Angle Mapper algorithm for the extraction of marine debris in the Sea of Japan.

In recent years, UAVs have been recognized as an effective low-cost image-capturing platform, suitable for monitoring aquatic environments with high accuracy (Gray, Fleishman and Klein), (Hong, Han and Kim). Customizable flight routes at low-level altitudes in combination with new algorithms for photogrammetric processing, such as the Structure from Motion (SfM) algorithm, provide a cost-effective acquisition of geospatial data with high spatial and temporal resolution, suitable for qualitative and quantitative analysis of natural and artificial structures of streams and floodplains. In addition to infrared and standard sensors, UAV can be equipped with multispectral cameras enabling its data to be combined with satellite imagery. (Martin, Parkes and Zhang) used high-resolution (<1 cm) UAV images and the Random Forest algorithm for the detection of plastic on the beaches, obtaining detection rates of 44%, 5%, and 3.7% for drinking containers, bottle caps, and plastic bags, respectively. (Topouzelis, Papakonstantinou and Garaba) compared the spectral response of Sentinel 2 and high-resolution UAV images over a large plastic floating target (100 m^2). (Geraeds, van Emmeric and de Vries) used images obtained by UAV at different flight heights to manually label the riverbank and floating plastic. (Moy, Neilson and Chung) created a hot spot map of debris on Hawaii Island beaches by visually interpreting orthorectified imagery mosaics with a ground sample distance of 2 cm. Although UAVs can provide appropriate spatial and temporal resolution to produce suitable data for mapping floating plastic, most of the methods developed so far are based on visual interpretation and manual labeling of plastic pieces, which is time-consuming and labor-intensive.

Recently, the deep CNN has been widely used in image classification tasks such as automatic classification, object detection (Gray, Fleishman and Klein), (Hong, Han and Kim), and semantic segmentation (Boonpook, Tan and Ye), (Ronneberger, Fischer and Brox), (Schmidt, Krauth and Wagner). With the rapid improvement of Graphics Processing Unit (GPU) computing and the increase of open training datasets, CNN models, such as AlexNet (Krizhevsky, Sutskever and Hinton), VGGNet (Simonyan and Zisserman), ResNet (K. He, X. Zhang and S. Ren), DenseNet (Huang, Xie and Fang), and Inception (Szegedy, Ioffe and Vanhoucke), used for image classification or for semantic segmentation in combination with Fully Convolutional Network (FCN), U-Net or DeepLab architecture, have achieved state-of-art accuracy in this topic. However, they completely discard the spatial information in the top layer, thus, producing a lack of accurate positioning and class boundary characterization.

Semantic segmentation aims to assign the set of predefined class labels to each pixel in the image. In early research, deep semantic segmentation used the patch-based CNN method (Song, Kim and Kim), (Lagkvist, Kiselev and Alirezaie), where images are first divided into patches and then fed into CNN networks. The network predicts the central pixel label based on the surrounding image patches. This process is repeated for each pixel, producing a high computational cost, especially in

overlapping patches. To solve this problem (Long, Shelhamer and Darrell) proposed to use a FCN. The FCN is an end-to-end model that maintains a two-dimensional structure of a feature map and uses contextual and location information to predict class labels, reducing the computational cost significantly. Semantic segmentation models based on FCN can be divided into four categories: encoder-decoder structure (Boonpook, Tan and Ye), (Ronneberger, Fischer and Brox), dilated convolutions (Yu and Koltun), and spatial pyramid pooling (Chen, Papandreou and Kokkinos), which are described below.

The encoder-decoder structure is widely applied to semantic segmentation. Firstly, the encoder generates feature maps with high-level semantic but low resolution by using convolutions, pooling and an activation layer. Finally, the decoder upsamples the low-resolution encoder feature maps, retrieving the location information and obtaining fine-scaled segmentation results. SegNet (Boonpook, Tan and Ye) and U-Net (Ronneberger, Fischer and Brox) are typical architectures with encoder-decoder structures. On the one hand, SegNet (Boonpook, Tan and Ye) stores the index of each max pooling window in the encoder, which then stores the indices of the maximum pixel, so the decoders upsample the input using the indices coming from the encoder stage. On the other hand, U-Net (Ronneberger, Fischer and Brox) is a highly symmetric U-shaped architecture where the skip connection is used to directly link the output of each level from encoder to the corresponding level of the decoder. Therefore, comparing U-Net to SegNet, the first does not reuse indices but instead it transfers the entire feature map to the corresponding decoders and consonant them to the upsampled decoder feature maps. This process produces more accurate maps than using SegNet, but it consumes more memory (Boonpook, Tan and Ye). Also, U-Net can produce a precise segmentation with very few training images (Ronneberger, Fischer and Brox). (Zhao, Yuan and Song) used UAV RGB and multispectral images and U-Net architecture to extract rice lodging, obtaining the dice coefficients of 0.94 and 0.92, respectively. (Xu, Wu and Xie) used ResUNet for building extraction from Very High Resolution (VHR) multispectral satellite images reporting an *F1* score of 0.98. In that case, the ResUNet adopted the U-Net as basic architecture but the U-Net learning units were replaced with residual learning units. Similarly, (Yi, Zhang and Zhang) used DeepResUNet and aerial VHR to map urban buildings, reaching high accuracies (*F1* score: 0.93).

(Chen, Papandreou and Kokkinos) introduced DeepLab architecture, which uses a parallel atrous convolution design instead of deconvolution for upsampling, performing similarly to other state-of-the-art models. Recent studies show that U-Net architecture outperforms DeepLab in cases with complex water environments (Guo, He and Jiang), (Pashaei, Kamangir and Starek). Furthermore, U-Net architecture is preferred to DeepLab architecture because due to a higher number of hyperparameters the DeepLab architecture is more computationally intensive (processing time is increased by 58%) (Guo, He and Jiang) and it needs more training steps to reach a performance comparable to U-Net (Pashaei, Kamangir and Starek).

The first step in addressing the ocean's plastic problem is to do an estimation of the amount of plastic, where it is accumulating and its pathways. However, the differences in the protocols which attempt to monitor the temporal and spatial distribution of plastic pollution (OSPAR (OSPAR), NOAA (Opfer, Arthur and Lippiatt), and the fact that the accuracy of the collected data varies depending on the observer's skill, make the integration and comparison of the estimations challenging. The research presented in this paper aims to fulfill the need for an efficient and rapid estimation of floating plastic. The main goals of this paper are to: (1) examine the performance of different deep learning algorithms for mapping floating plastic using high-resolution UAV images, (2) to examine the relationship between the spatial resolution of the UAV imagery and the size of the detected plastic, (3) to test the possibility of mapping different plastic materials such as Oriented Polystyrene (OPS), Polyethylene terephthalate (PET), and Nylon, and (4) to define a methodology for UAV surveying to map floating plastic.

4.5.2.1. Study area and data

Two study areas near Mrkonjić Grad (Bosnia and Herzegovina) were defined (Figure 34.): (i) the artificial Lake Balkana, with clear water, and (ii) the confluence of the Crna Rijeka and the Vrbas Rivers.

For the study area in the artificial Lake Balkana, targets were designed to examine the possibility of mapping plastics of different sizes using UAV imagery. The targets consisted of (i) a wooden frame (100 cm × 80 cm) with thin and transparent gauze and plastic squares, with side lengths from 1 to 10 cm (Figure 35. (b)), (ii) a wooden frame (100 cm × 80 cm) with thin and transparent gauze and plastic squares, with sides from 11 to 16 cm long, (iii) a wooden frame (100 cm × 80 cm) attached to a metal frame located 20 cm below it, with thin and transparent gauze and plastic squares, with sides from 1 to 10 cm long (Figure 35. (a)), and (iv) plastic bottles of different sizes and colors connected by ropes (Figure 2d).

A rope with a diameter of 4 mm was used to keep the frames in the area of interest during the surveys (Figure 35. (c)), while the wood made them floatable. The targets were released in the water in the deepest part of the lake, to exclude the reflection of the lake bottom. Besides, three different plastic materials were used: OPS (used for the plastic squares (Figure 2. (a) and 2 (b)), PET (plastic bottles Figure 35. (d)), and Nylon (rope Figure 35. (c)).
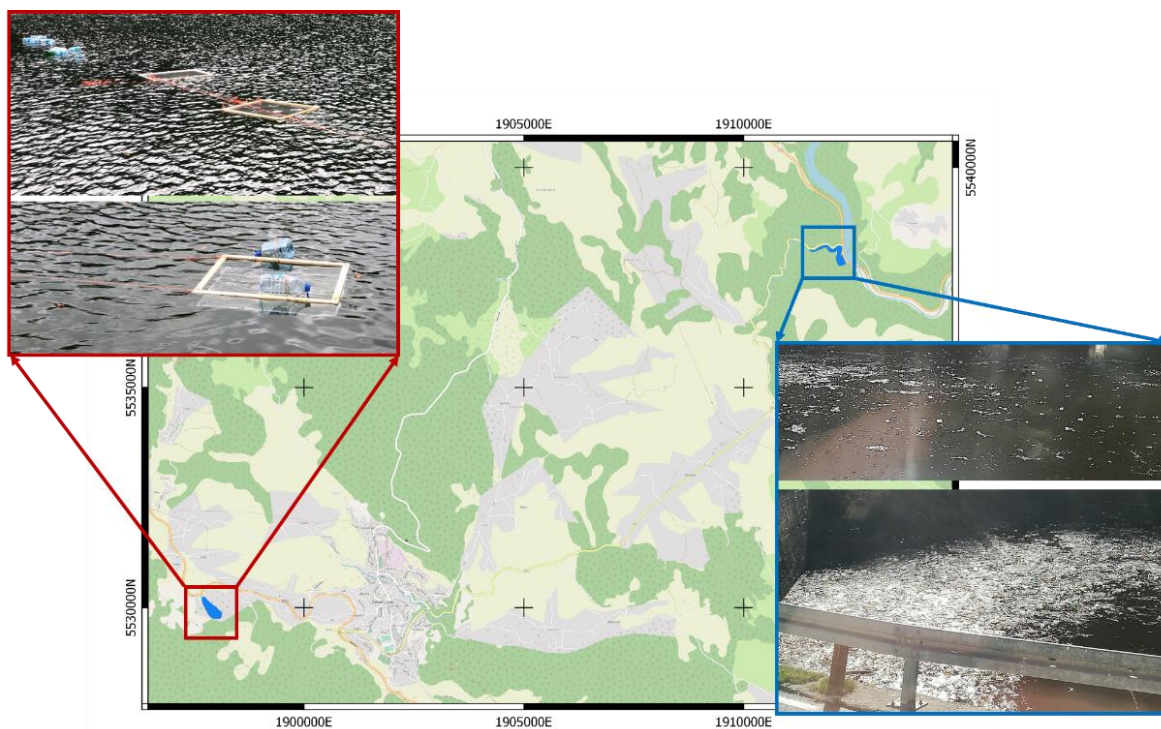
Figure 34. Study areas: Lake Balkana (left) and Crna Rijeka River (right). EPSG:3857.

Figure 35. Targets used in the study area located in Lake Balkana (a) frame with metal construction for the underwater survey, (b) frame for the on the water surface survey, (c) nylon rope, (d) plastic bottles.

For the second study area, upstream of the confluence of the Crna Rijeka and the Vrbas Rivers a net for collecting floating garbage was installed. Floating waste is the major source of litter in this area, due to the disposal of the garbage in illegal landfills and picnic sites along the river or directly in the river. The net collects about 10,000 m³ of material annually, from which 60% is wood, 35% plastic packaging, and 5% other (Bočac). The plastic packaging consists of 55% PET, while 45% consists of Polyethylene, and Polypropylene (Bočac). The amount of litter depends mostly on the weather conditions. The largest quantity is captured during the rainy periods (spring and autumn) when water level increases and washes away the garbage from the river banks. In May 2019, due to heavy rains, the net broke and 10,000 tons of floating garbage ended up in the head pond of the hydroelectric power plant. In order to detect and map the plastic (the self-built targets and the plastic stopped by the net), 6 UAV surveys were conducted, using a DJI Mavic pro equipped with an RGB camera. Five surveys with different flight heights (12-90 m) took place over the Balkana Lake area, and one (at a 90 m flight height) over the Crna Rijeka River. The flight heights and spatial resolutions of the surveys are presented in Table 28.

Table 26. Flight heights and spatial resolutions of the conducted surveys.

Flight Height (m)	Spatial Resolution (mm)	
	Balkana	Crna Rijeka
12	4	-
40	13	-
55	18	-

70	23	-
90	30	30

4.5.2.2. Methodology

In this paper, a pixel classification method to extract floating plastic pieces from water bodies within VHR remote sensing images based on deep learning algorithms is proposed. Semantic segmentation of floating plastic is highly challenging due to several limitations: low amount of training data, highly imbalanced data sets, limited accuracy of ground truth data, and frequent scene changes due to constant plastic movement. To address those limitations, we propose the workflow showed in Figure 36, which summarizes the approach followed in this paper and consists of three main steps: preprocessing, classification, and accuracy assessment.

Figure 36. Workflow used in this study where "B*" and "CR**" correspond with the Balkana and Crna Rijeka dataset respectively. UAV = Unmanned Aerial Vehicles; SfM = Structure from Motion

Preprocessing : For each flight, the acquired images and the SfM algorithm were used to generate a high-resolution orthophoto. The SfM algorithm comprises of three main steps (Govedarica, Jakovljević and Taboada, Flood risk assessment based on LiDAR and UAV points clouds and DEM): (1) the SIFT algorithm detects and describes key points while the RANdom

SAmple Consensus (RANSCAN) method matches key points across multiple images. The bundle block adjustment of matching key points was used to compute the extrinsic and intrinsic camera parameters and three-dimensional (3D) coordinates for a sparse unscaled point cloud; (2) point cloud densification; and (3) digital terrain model and orthophoto generation.

To train the deep learning classifier ground truth data are necessary. Since this study represents the first attempt to map floating plastic based on UAV images, previous ground truth data was not available. Therefore, we created our labels, which was challenging and time consuming, due to the small size, the different colors, the different spectral signatures, the different level of submersion and the constant moving of the floating plastic items.

To reduce the errors caused by the manual delineation of classes, the multiresolution segmentation algorithm implemented in eCognition was used (Trimble). This algorithm merges pixels to obtain meaningful non-overlapping objects/polygons. The algorithm results are controlled by three factors: (1) scale parameter, i.e., the maximum allowed heterogeneity for the resulting object; (2) shape, i.e., the weight of the object's shape in comparison to the spectral characteristics of the object (color); and (3) compactness, i.e., the weight representing the compactness of object (please see (Trimble) for more information). The selection of the optimal value combination was based on the trial-and-error process. Each segment was then manually labeled using QGIS software, based on a visual inspection of the orthophoto. In the Balkana study area, plastics were classified into three classes: PET, OPS, and nylon. In the Crna Rijeka area, plastic was classified in two groups: plastic and maybe plastic. The maybe plastic class was created to reduce the spectral confusion in the plastic class, and it was assigned to the segments where the operators were not able to state whether it was plastic by visual inspection and by analyzing the spectral signature.

The Balkana study area was surveyed five times but we were not able to use the same mask for the orthophotos from the different flights (i.e. different spatial resolutions) due to the movement of the plastic. Therefore, for each orthophoto a new ground truth mask was created. This limited the accuracy of the mask and algorithm performance for the lower spatial resolution images.

Classification: This paper proposes an end-to-end semantic segmentation model for a floating plastic segmentation based on U-net architecture, which has the ability to work with very little training data and provides a precise segmentation (Ronneberger, Fischer and Brox). U-Net has a symmetrical encoder-decoder architecture. The encoder side effectively extracts and abstracts the image pixel information while the decoder aims to extract the plastic from the feature maps. The U–Net architecture has been widely used in the semantic segmentation of remote sensing imagery (Chen, Papandreou and Kokkinos), (Xu, Wu and Xie), (Yi, Zhang and Zhang). Its success is largely attributed to the several skip connections (Ronneberger, Fischer and Brox), (Zhou, Siddiquee and Tajbakhsh) between encoding and decoding parts which are used to combine spatial details from lower layers and semantic ones from higher layers of the network. Due to a combination of contextual information at different scales of the input resolution, spatial information can be better restored, producing sharper boundaries of predicted objects after the decoder (Wang, Liang and Ding).

Encoder: CNN models consist of a series of layers that are combined in the network. They start with a series of convolutions and a pooling layer, called the convolutional base, and end with a densely connected classifier (Chollet, Deep Learning with Python). The convolutions operate on feature maps with two spatial axes (height and width of the image) and depth (number of channels). The convolutions extract the patches by sliding a window of a fixed size (usually 3 × 3 or 5 × 5) and perform the transformation for all patches, via a dot product with a weight matrix followed by adding bias and the application of the activation function, and finally producing output feature maps (Chollet, Deep Learning with Python), (Goodfellow, Bengio and Courville). The depth of the output feature maps is defined by the number of filters which encode specific aspects of the input data allowing CNN to learn spatial hierarchical patterns. The batch normalization (BN) layer is placed

after each convolution to speed up the training process and reduce the internal covariance of each batch of features maps.

The most common way of improving the performance of the deep neural network is increasing the depth (number of layers) and width (number of units within a layer) of the network. However, enlarged networks are more prone to overfitting especially if the size of the training set is limited (Szegedy, Liu and Jia). Besides, an increase in the network size dramatically increases the use of computational resources.

With the increase of the network depth problems like the vanishing gradient start to emerge. The vanishing gradient problem refers to a dramatic gradient decrease as it backpropagates the true network and by the time they reach close to the shallower layers, the updates for the weights nearly vanish. In order to avoid the vanishing gradient problem, a rectified linear unit (ReLU) (Nair and Hinton) was used as a nonlinear activation function. The ReLU significantly accelerates the training phase in comparison with the activation functions with a descent gradient such as a sigmoid or hyperbolic tangent function. The pooling layers are used after the convolutional layer to spatially downsample the image and to reduce the number of coefficients to process. Although the stride factor (the distance between two successive windows) can be used for downsampling, the max-pooling tends to work better since it increases the variance by looking at the maximum values of the extracted features over small patches. Since there is not any information about the performance of available models in the case of plastic detection, the encoder side was based on the state of the art CNN models, pre-trained on ImageNet (Deng, Dong and Socher) datasets, such as ResNet50 (K. He, X. Zhang and S. Ren), ResNeXt50 (Xie, Girshick and Dollar), Inception-ResNet v2 [30], and Xception (Chollet, Xception: Deep Learning with Depthwise Separable Convolutions). These four architectures were used in this work for the semantic segmentation of floating plastics and are described below.

ResNet50: the deep ResNet architecture addresses the vanishing gradient problem by employing identity skip-connections, which add neither extra parameters nor computational complexity but they lead to a more efficient training and optimization of very deep networks (K. He, X. Zhang and S. Ren). ResNet is constructed by stacking multiple bottleneck blocks called residual blocks (Figure 37. (a)), which consist of three layers of 1×1, 3×3, and 1×1 convolutions. The 1×1 convolution is introduced as the bottleneck layer (to reduce and restore dimensionality) before a 3×3 layer to reduce the number of input feature maps and to improve computational efficiency. In this paper, a 50-layer ResNet network was used.

Inception-ResNet v2: this network is constructed by the integration of ResNet (K. He, X. Zhang and S. Ren) and Inception v4 (Boonpook, Tan and Ye), so a residual connection is used to avoid the gradient vanishing problem while the Inception modules increase the network. In the Inception-ResNet v2, the batch normalization is used only on top of the traditional layer enabling the increase of an overall number of Inception blocks (Szegedy, Ioffe and Vanhoucke). In the Inception blocks, the convolutions with the varying size of the same layer were concatenated at the end of block i.e. the convolution blocks were parallel (Figure 37. (b)). Although the Inception-ResNet v2 shows roughly the same recognition performance as Inception v4, the usage of the residual connection leads to a dramatic improvement in the training speed (Szegedy, Ioffe and Vanhoucke). Therefore, in this paper, the Inception-ResNet v2 was used.

Xception: the Extremely Inception (Xception) architecture replaces the Inception modules with stacked depthwise separable convolution layers followed by a pointwise convolution. It represents the extreme form of the Inception module, where the spatial features and channel-wise features are fully separated (Chollet, Deep Learning with Python). The Xception architecture has 36 layers structured into 14 modules, all of which have linear residual connections around them, except for the first and last modules (Figure 37. (c)) (Chollet, Xception: Deep Learning with Depthwise Separable

Convolutions). The residual connection helps with the vanishing gradient problem both in terms of speed and accuracy.

ResNeXt50: this model is similar to the Inception model since they both follow the split-transform-merge paradigm. However, in the ResNeXt all paths share the same topology and the outputs of different paths are merged by adding them together i.e. ResNeXt consists of a stack of residual blocks that have the same topology (Figure 37. (d)). This architecture introduced the new dimension called cardinality (C) (the number of paths) in addition to depth and width. The results presented in (Xie, Girshick and Dollar) show that an increase in cardinality reduces the error rate while keeping the complexity. In this work a cardinality of 32 was used (Figure 37. (d)).
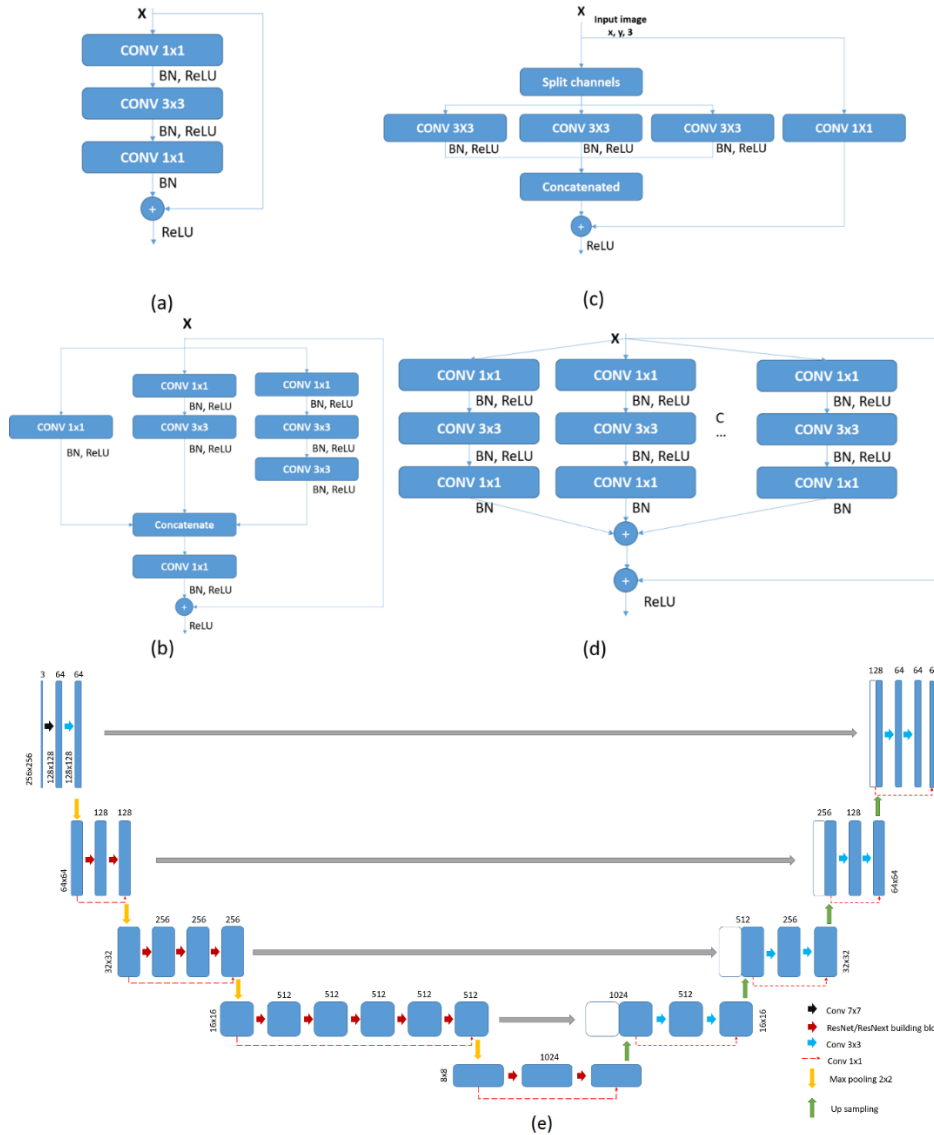
Figure 37. Building blocks of (a) ResNet, (b) Inception-ResNet v2, (c) Xception, and (d) ResNeXt (C = 32) (e) architecture of ResUNet50/ResUNext50. Where: ReLu is Rectified Linear Unit, BN is Batch Normalization, and CONV is convolution.

Decoder: The decoder block aims to upsample the densified encoder (low resolution) feature map to assign a classification result to each pixel of the input image (Boonpook, Tan and Ye). The encoder

and decoder architecture are fully symmetrical i.e. for each encoder there is a corresponding decoder. The decoder gradually recovers the resolution of the original input image by replacing the pooling operation (in the encoder) with 2 × 2 up-sampling operators followed by 3 × 3 convolutions, BN, and the ReLU activation function. The upsampled outputs are combined with contextual information derived from the corresponding encoder via skip connection. In the final layer, a 1 × 1 convolution with the Sigmoid activation function is used to predict the probability of being assigned to one of the pre-defined classes.

Data Augmentation and Transfer Learning: The performance of deep neural networks is highly limited by the low number of training data. The size of the dataset needed for network training is a function of the size of the network (width and depth) and the complexity of the problem. If a model with a large learning capacity is trained on very few data, it can memorize the training sets producing a low generalization power of the model, i.e., overfitting. This overfitting can be reduced by using data augmentation, which artificially enlarges the training set by a random transformation of the existing training samples (Krizhevsky, Sutskever and Hinton). Although the produced images are intercorrelated they are not the same, contributing to a better generalization of the network. In addition to reducing overfitting, data augmentation improves the performance when there are imbalanced class problems (Hasini, Shokri and Dehghan).

Transfer learning is another efficient approach when a limited number of training samples are available. It is based on the idea of fine-tuning (adapting) the models that are already pre-trained on large datasets, such as ImageNet, for completely new classification problems. Transfer learning between different tasks is possible due to the property of deep networks that the first layers are general (i.e., in CNN, first layers tend to learn standard features such as edges, patterns, textures, corners, etc.) while the last layer computes specific features that greatly depend on the chosen dataset and task (such as object parts and objects) (Yosinski, Clune and Bengio). The usual transfer learning approach is based on a fine-tuning which unfreezes (updating weights during the training phase) and adjusts to the parameters of the few top layers in the pre-trained network, while the first layers, representing the general features remain frozen.

Accuracy Assessment: To test the accuracy of the classification results three standard parameters were calculated: precision, recall, and F-score. Precision computes the percent of detected pixels in each class that actually belong to the assigned class, while recall represents the fraction of correctly labeled pixels of each class. In a perfect model, the precision and recall are equal to 1. *F1*-score is a quantitative metric useful for imbalanced training data, and it represents the balance between precision and recall (Fawcett)

The higher the value of the *F1*-score, the better the model performance regarding the positive class (Bekkar, Kheliouane Djemaa and Akrouf Alitouche).

4.5.2.3. Implementation

Due to the limited processing power, the original images were decomposed to 256 × 256 px patches. The models were based on U-Net architecture, which uses ResNet 50, ResNeXt50, Xception, and Inception-ResNet v2 as encoders. The parameters of the original deep architecture pre-training to the ImageNet datasets were maintained during the fine-tuning. The six different models were trained on three different datasets, as follows. ResNet50, ResNeXt50, Xception, and Inception-ResNet v2 were trained on Dataset 1 (Balkana 4 mm), ResUNet50 was trained on Dataset 2 (which consisted of Balkana 4 mm, 13 mm, 18 mm, 23 mm, and 30 mm resolution orthophotos), and ResUNet was trained on Dataset 3 (Crna Rijeka 30 mm resolution orthophoto) (Figure 36). Dataset 1, Dataset 2, and Dataset 3 contained 328, 434, and 1846 images respectively. All datasets were split into 80% of the data for training and 20% for validation. The batch size was limited by the GPU and it was chosen as

big as possible for each network. Different loss functions, such as cross entropy, cross entropy weighted, and focal loss were tested. Since the highest accuracy was obtained using cross entropy, this loss function was used for all the models. The models were implemented in the Python 3 programming language by using artificial intelligence libraries such as PyTorch, TensorFlow, Keras, and Matplotlib. The training of the networks was done using the publicly available cloud platform Colaboratory (Google Colab), which is based on Jupyter Notebooks. The hyperparameters used for the model training are presented in Table 27.

Table 27. Hyperparameters used for training the models.

Study Area	Dataset	Architecture	Batch Size	Learning Rate	Training Time
Balkana	Dataset 1	ResUNet50	8	8×10^{-5}	31 min
Balkana	Dataset 1	ResUNext50	8	1×10^{-6}	44 min
Balkana	Dataset 1	XceptionUNet	8	2×10^{-5}	21 min
Balkana	Dataset 1	InceptionUResNet v2	8	1×10^{-5}	33 min
Balkana	Dataset 2	ResUNet50	8	3×10^{-5}	40 min
Crna Rijeka	Dataset 3	ResUNet50	8	4×10^{-6}	3 h

4.5.2.4. Results and discussion

In this paper, U-Net networks were used for semantic segmentation of floating plastics. Table 28. shows the performance of the four different encoder architectures tested for the extraction of different kinds of plastic materials. Each architecture was pre-trained on the ImageNet datasets and the performance was tested on Dataset 1. Due to simplicity, the results are shown only for the classes that represent plastic.

Table 28. Comparison of different encoder architectures for floating plastic detection (where P, R, F1, are precision, recall, and F1-score respectively) (Dataset 1).

	ResUNet50			ResUNext50			XceptionUNet			InceptionResUNet v2		
	P	R	F1	P	R	F1	P	R	F1	P	R	F1
OPS	0.86	0.86	0.86	0.99	0.19	0.31	0.81	0.39	0.53	0.01	0.00	0.00
Nylon	0.92	0.85	0.88	0.77	0.96	0.85	0.76	0.87	0.81	0.76	0.74	0.75
PET	0.92	0.92	0.92	0.82	0.96	0.88	0.78	0.75	0.77	0.60	0.72	0.65

As shown, ResUNet50 has the highest accuracy (*F1*-score > 0.86) for detecting any of the three plastic classes, while the InceptionResUNet v2 has the lowest (Table 28.). Ground truth data and the results of the classification using the four algorithms are shown in Figure 38. for visual inspection (Data set 1). On the one hand, the results show that the ResUNet50 model detected and classified all plastic types with almost no commission or omission errors, matching the ground truth data very accurately (Figure 38 (ResUNet50)). On the other hand, the high recall and low precision obtained by ResUNext50 and XceptionUNet (Table 28.) indicated an overestimation of floating plastic, due to misclassification of water pixels (Figure 38. (ResUNext50, XceptionUNet)). In addition to the misclassification of water pixels, the low accuracy obtained with the InceptionResUNet v2 model (*F1*: 0; 0.75; 0.65 for each plastic type) was caused by the misclassification between nylon (rope) and PET (bottles), and PET and wood (Figure 38. (InceptionResUNet v2)). The plastic squares were completely omitted by the InceptionResUNet v2, while ResUNext50 strongly misclassified them as wood. On the one hand, the XceptionUNet was capable of detecting small variations in the reflection of different plastic materials (squares *F1*: 0.53) while, on the other hand, it showed the highest sensitivity to the edge-effect, misclassifying them and decreasing the *F1* score. (Innamorati, Ritschel and Weyrich)

showed that segmentation errors are higher for pixels near the edges and even worse at corners (Cui, Zhang and Liu), due to the lack of the contextual information.

For the underwater squares (Figure 38 a), all algorithms, except ResUNet50, misclassified OPS as PET. It should be noted that the total reflection of transparent floating plastic on the water surface is defined as the sum of water reflection, plastic reflection, and the reflection of the light transmitted through the plastic (Jakovljevic, Govedarica and Alvarez Taboada), (Goddijn-Murphy, Peters and van Sebille). In this study, the presence of plastic bottles (PET) increased, on average, the amount of reflected energy from water by 19%, while OPS increased the reflection by only 3.5% (Figure 39), making it challenging to differentiate between these two classes. This difference is even lower in the case of underwater plastic, due to water absorption, and it can explain the low accuracy of the OPS class for three of the tested models. The quantitative accuracy assessment and the visual inspection confirmed that, among the tested models and for the Lake Balkana study area, ResUNet50 was the most sensitive to detect small differences in the amount of reflected energy, which is crucially important for plastic detection and for identifying different types of plastic. Therefore, all the tests used to achieve the remaining goals of this paper (2, 3, 4) were performed using the ResUNet50 model.
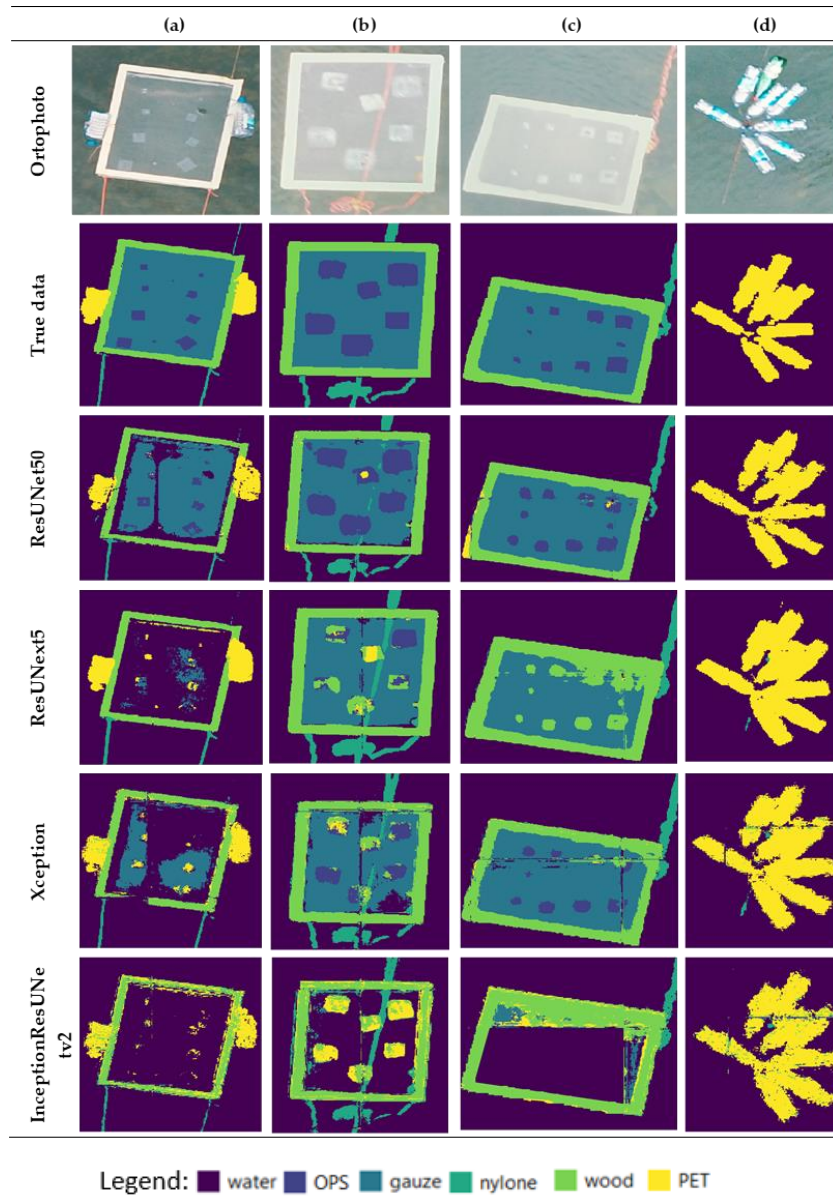
Figure 38. Ground truth data and results of the classification using the four tested models for detecting different plastic materials, located underwater (a) and overwater (b, c, d) (Dataset 1). Where OPS is Oriented Polystyrene and PET is Polyethylene terephthal
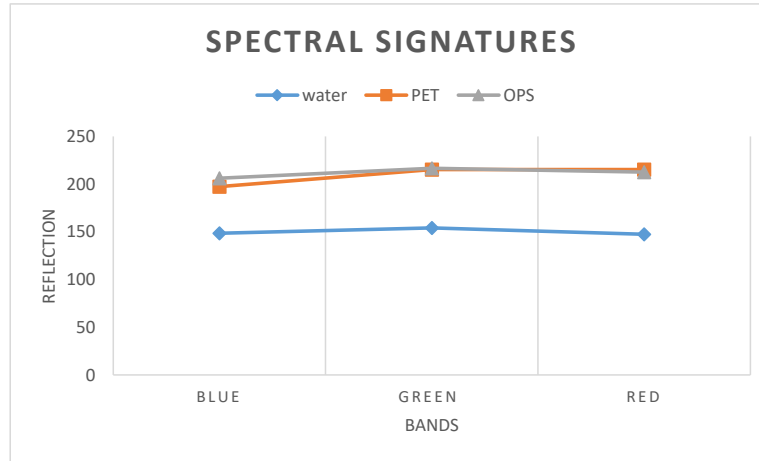
Figure 39. Spectral signatures of water, PET and OPS.

The relationship between the image spatial resolution and the size of the detected plastic was evaluated by using the ResUNet50 model and the ground truth data from Dataset 2. The results of the accuracy assessment are shown in Table 29.

Table 29. The effect of spatial resolution (mm) on ResUNet50 performance (where P, R, F1 are precision, recall, and F1-score respectively) (Dataset 2).

	13 mm			18 mm			23 mm			30 mm		
	P	**R**	*F1*	**P**	**R**	*F1*	**P**	**R**	*F1*	**P**	**R**	*F1*
OPS	0.88	0.77	0.82	0.69	0.71	0.70	0.79	0.31	0.44	0.75	0.45	0.56
Nylon	0.89	0.75	0.82	0.91	0.52	0.66	0.76	0.26	0.39	0.87	0.20	0.33
PET	0.92	0.83	0.87	0.78	0.84	0.81	0.83	0.68	0.75	0.77	0.70	0.73

The results showed that the spatial resolution of the image and the accuracy of the model were directly related, i.e. the accuracy decreased with the decrease in spatial resolution. Those findings are in line with the results presented by (Kannoji and Jaiswal). As expected, ResUNet50 performed the best on the 4 mm resolution images for all kinds of plastics and the lowest accuracy was obtained for the 30 mm spatial resolution image (Table 29.). The exception was the OPS class, which was mostly omitted in the 23 mm classified orthophoto. Due to changes in of weather conditions (sunny intervals) between the flights, sun glint appeared in the 23 mm orthophoto and increased the reflection (Kay, Hedley and Lavender), in comparison with other images, which led to the misclassification between OPS and gauze (Figure 40 (23 mm), a, b, c), causing the low *F1* value. In addition, the amount of reflected energy decreased with the decrease in spatial resolution, due to the larger amount of mixed pixels, resulting in a lower classification accuracy. Visual inspection showed that the algorithm tended to classify mixed pixels as water when the plastic fraction of the target area was larger than the water fraction (e.g. Figure 40d). This result agrees with (Ji, Gong and Geng) who reported that in the case of imbalanced training datasets, mixed pixels tend to be classified as the majority class, even when most of the mixed pixel represents a minority class.
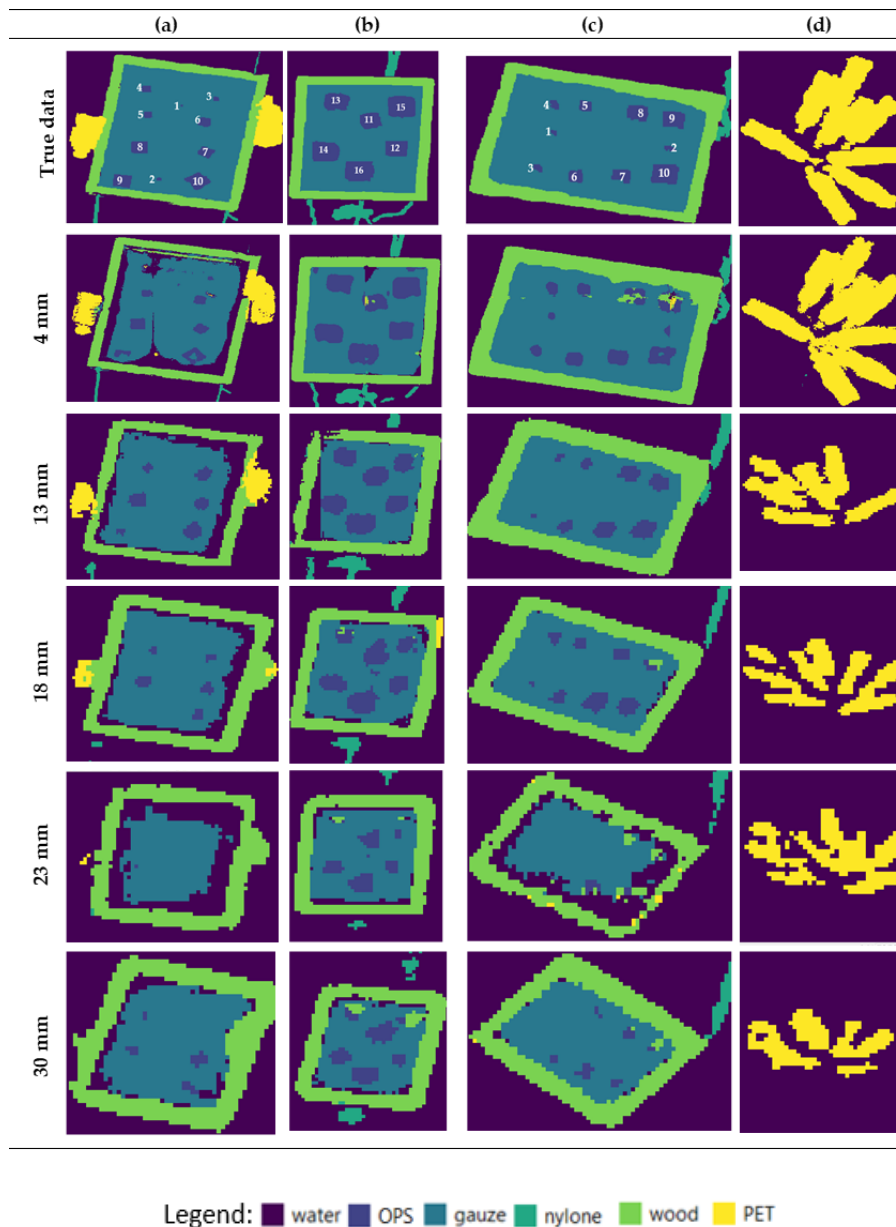
Figure 40. Ground truth data and results of the classification using the ResUNet50 algorithm for visual comparison, at different spatial resolutions and for different plastic materials, located underwater (a) and overwater (b, c, d) (Dataset 2).

In general, for all the tested spatial resolutions, the algorithm achieved high precision and lower recall values indicating that the model cannot detect all plastic pixels, but that it can be trusted when it does. Taking as a reference value the classification obtained from the 4 mm orthophoto, the largest difference in the extension of the area classified as plastic was obtained from the 23 mm orthophoto (OPS: −16.1%; Nylon: −33.2%; PET: −22.3 %) (Figure 41). The smallest difference for the OPS and Nylon classes was obtained from the 18 mm orthophoto (OPS: −1.8%; Nylon: −4.2%), while the 30 mm orthophoto provided the closest area to the reference for PET plastic (PET: −8.9%) (Figure 41).
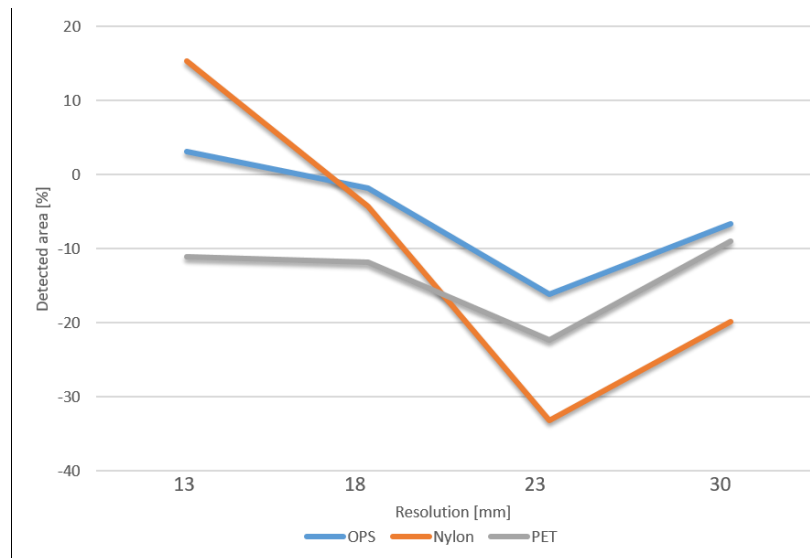
Figure 41. Differences in the extension of the detected area covered by plastic (using the classification of the 4 mm orthophoto as a reference value).

The visual inspection showed that with the 4 mm orthophoto the algorithm detected all the OPS squares, while with the 13 mm and 18 mm orthophotos the algorithm omitted the 1 and 2 cm squares on the water surface, and the 1 to 4 cm squares that were underwater. For the 23 mm image, it omitted all the OPS squares smaller than 11 cm, while for 30 mm image, the 1 to 4 cm squares, which were on the water surface, and the 1 to 6 cm squares located underwater, were misclassified as water (Figure 40). Based on these results it can be concluded that the algorithm needs at least one pure pixel (a pixel that includes a single surface material) for detecting plastics on the water surface, and two pure pixels for the detection of underwater plastics. According to the presented results, orthophotos with of 18 mm spatial resolution can be used for litter surveys which follow OSPAR (OSPAR), NOAA (Opfer, Arthur and Lippiatt) or UNEP/IOC (Cheshire, Adler and Barbière) guidelines, while 4 mm orthophotos should be used for CSIRO (Hardesty, Lawson and van der Velde) surveys, since according to CSIRO guidelines, the minimum size of detected plastic should be 1 cm².

On the one hand, floating plastic is more accurately extracted from images with higher spatial resolution. On the other hand, the higher the spatial resolution of the image, the smaller the extension of the area covered by the image, as showed in Figure 42. Therefore, a compromise between spatial resolution and the covered area needs to be found.
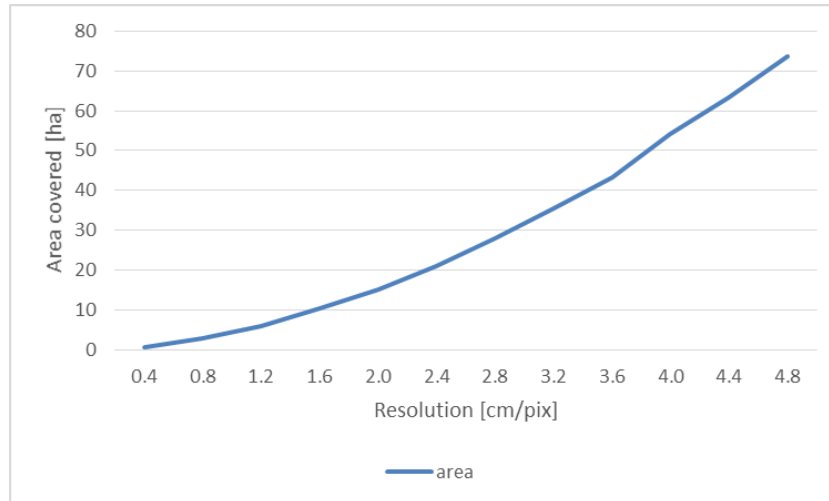
Figure 42. Relationship between the spatial resolution (cm/pixel) and the area covered by an image gathered by the DJI Mavic ProCamera (grid mission with an 80 % overlap).

To test the model performance in an independent scenario, the Crna Rijeka study area was surveyed. Based on the size of the study area and the size of the majority of the plastic items (bottles) that were present, a 30 mm orthophoto was used (Dataset 3), as well as the ResUNet50 model. The results of the accuracy assessment are presented in Table 30.

Table 30. Precision, Recall, and F1-score of plastic classes in the Crna Rijeka study area.

	Precision	Recall	*F1*
Plastic	0.82	0.75	0.78
Maybe Plastic	0.62	0.34	0.43

The ResUNet50 showed a stable performance to classify plastic in the different datasets (Dataset 2 (PET class) and Dataset 3 (plastic class)) when comparing the same spatial resolution (*F1*: 0.73 vs.0.78, respectively) (Table 29 and Table 30). The highest confusion was obtained for the "maybe plastic" class, which was misclassified as water or plastic. For that class the precision was high, while recall was low, indicating the underestimation of the area covered by the maybe plastic class. Although precision, recall, and *F1* score provide a deeper insight into the performance of the algorithm, the area and volume of the detected plastics are more useful for stakeholders. From an operational point of view, when planning a cleaning campaign, that information is the basis for site selection, and for estimating the number of people required and the approximate time needed. In the Crna Rijeka case study, the algorithm only underestimated the plastic area by 3.4%, proving the great potential of its application to optimize cleaning campaigns.

The visual inspection shows (Figure 43) that the locations of the plastic pieces were accurately detected, but some plastic pixels on the border were misclassified as the surrounding class. No differences were observed in the performance of the model between grouped (Figure 43a) or single plastic items (Figure 43b).
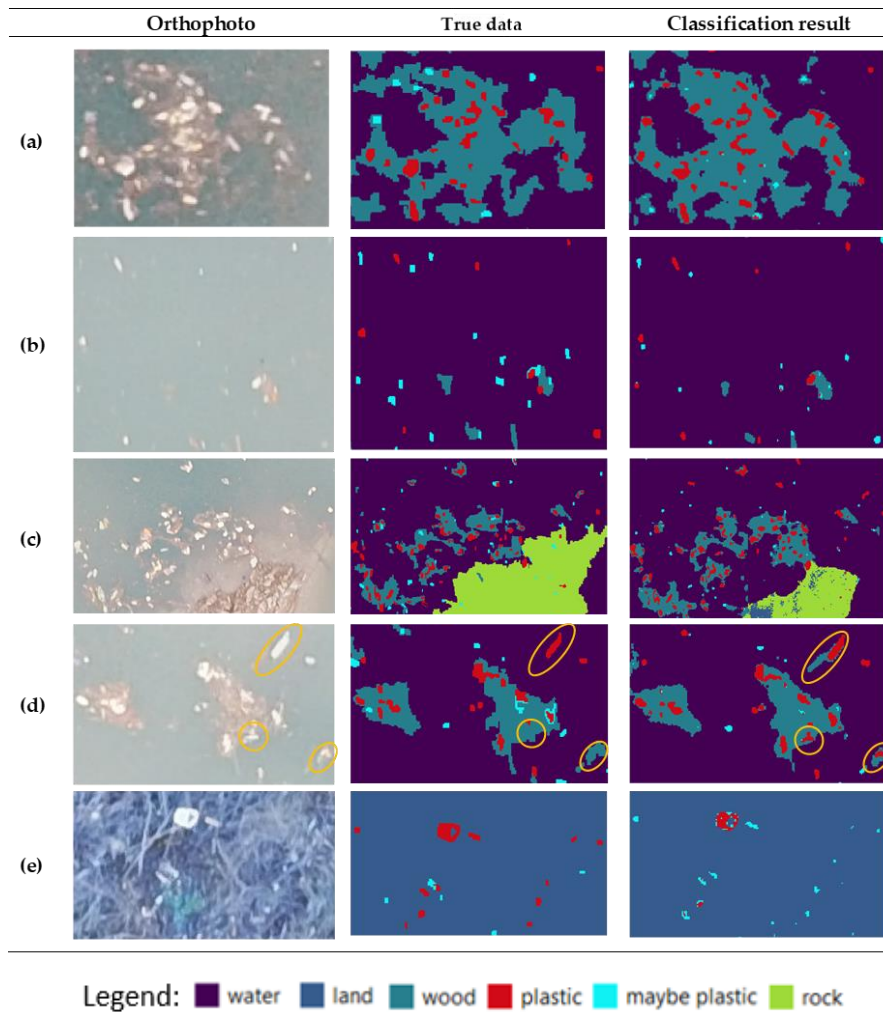
Figure 43. Visual comparison between the orthophoto, true data (ground truth) and classification results for the five different scenarios: (a) group of plastics, (b) single plastic items, (c) plastic in shallow waters, (d) training data errors (orange lines), which were misclassified by the operator and correctly classified by the algorithm (e) plastic on the ground.

Unexpectedly, the algorithm detected plastic accurately in shallow water (Figure 43. (c)). Shallow water is highly challenging for mapping plastic because the presence of the river bed increases water reflectance (same as plastic does) (Jakovljevic, Govedarica and Alvarez Taboada). In this study case, the algorithm accurately extracted the plastic pieces that were omitted from the training data (Figure 43d), showing good generalization abilities, Moreover, the model showed its potential for plastic detection not just in water but also on land, with lower accuracy compared with the floating plastics (Figure 43e).

It should be also taken into account that the results are also affected by the accuracy of the training data. The creation of training data was time consuming and a tedious task. Just in the case of the Crna Rijeka orthophoto (Dataset 3), the 418,542 segments were manually labeled, assigning 5519 to the plastic class and 4014 to the maybe plastic one. Visual labeling of plastic pieces is a difficult task which involves errors due to the limited ability to exactly determine the boundary between plastic and maybe plastic. Therefore, in the case of misclassifications between those two classes, it

cannot be stated if it was an error in the algorithms or if it was due to a misclassification during the manual labeling stage. To address this limitation, we suggest that during the collection of training data, two UAVs with the same flight pattern should be used (Figure 44). The first UAV would fly at a higher altitude while the second UAV would fly lower to provide higher resolution images which can be used for precise delineation and labeling of the plastic class and other classes, to therefore obtain an accurate data mask. Since floating plastic moves continuously, especially on windy days, the speed of the second UAV should be lower than the first one, to synchronize their flight missions and reduce time overlap between surveys.
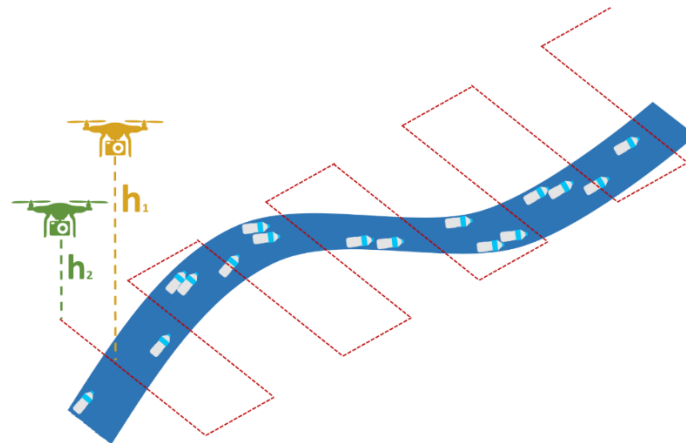
Figure 44. Proposed flight planning methodology to obtain accurate datasets for algorithm calibration

Moreover, the UAV surveys should be carried out during cloudy weather to reduce the sunglint effect, since it limits the quality and accuracy of remote sensing data from water bodies (Kay, Hedley and Lavender). (Anggoro, Siregar and Agus) reported that the reduction of the sunglint effect increased the overall accuracy by 7%. The same accuracy degradation of was noted in the classification of the 23 mm orthophoto (Table 29.; Figure 40 (23 mm)). Also, the wind speed should be as low as possible, especially in the case of small UAVs. The stability of the camera is affected by the wind and it can cause blurred imagery. In addition, the SfM reconstructs a 3D point cloud based on the matching of multiple views, so if the plastic pieces shift their relative position from image-to-image due to wind-induced movements, the reliability of the point cloud and the accuracy of the produced orthophoto is compromised.

4.6. The topology of the water body

While the application of remote sensing data for detection and monitoring of water body geometry is under intensive investigation, less attention has been paid to extraction the extraction of river network topology. The detected water bodies are represented as polygons, while under the WFD, the reference geometry for the river is polyline (or polygons in the case of heavily modified rivers such as damming rivers) (Table 3.) Also, in the scope of the WFD reporting, representation of the central line for surface water bodies is requested (WISE GIS Guidance). Therefore the river network needs to be created to satisfy the WFD requirements.

4.6.1. Methodology

The proposed framework for river network extraction is shown in Figure 45. It consists of topological checker, waterbody type classification, and river network extraction.

Topology checker: The result of the algorithm for automatic water body extraction is water body mask in raster data format. To use those results in the implementation of WFD and water management, it is necessary to convert raster to vector data. The created vector data need to be geometry accurate, and the spatial relationship between water bodies need to be preserved (Table 12.). Since raster is defined as a set of the nonoverlaying grid, the intersection between resulting polygons is not possible however, they can share the same edges (overlap) or same vertexes (touch). Taking that into account, the topological relationship between all polygons was chacked, and in the case of touching or overlapping the polygons were merged.
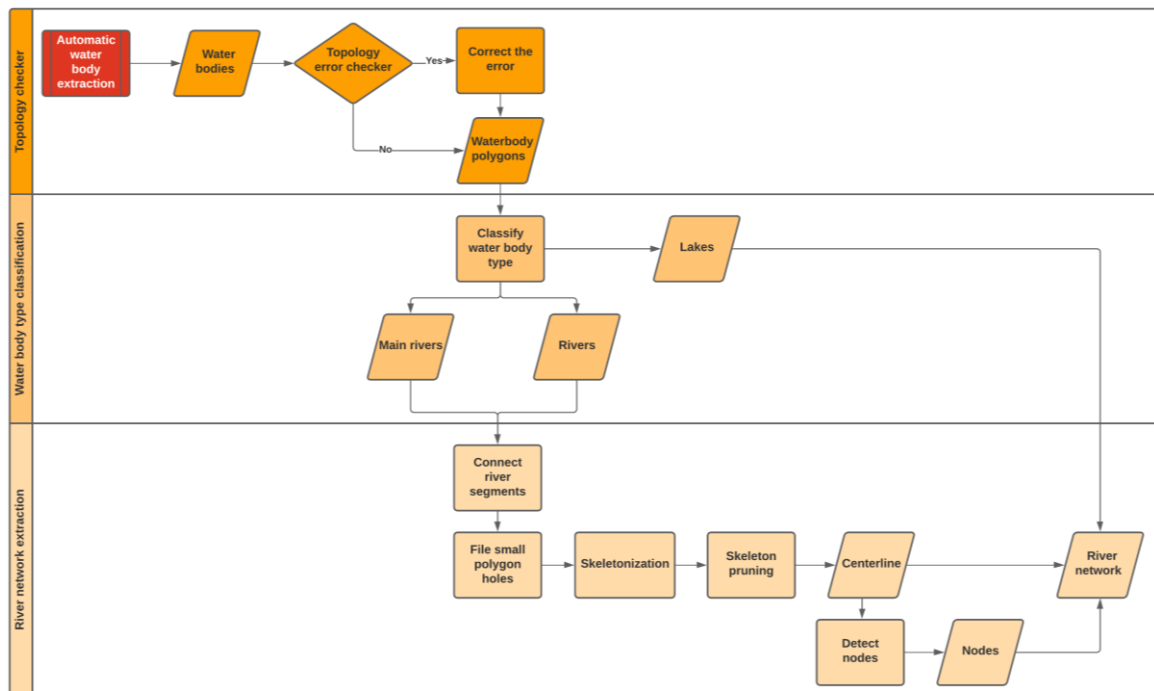
Figure 45. Proposed workflow for extraction of a river network

Water body type classification: Due to natural and man-made obstacles, rivers appear as a set of disconnected segments. The connection between those segments is vital for providing the continuity and topological correctness of the river network. Therefore, the neighboring river segments were connected at polygon level if the distance between them is lower then 40 m (2 pixels), and the flow direction is consistent. The resulting water bodies were classified into rivers and lakes based on shape characteristics. Therefore, the water body type was determined by applying a manually derived threshold for elongation and compactness. Elongation and compactness were calculated by using the following expression:

$$Elongation = \frac{average\ w}{average\ l} \tag{8}$$

$$Compactness = \frac{4\pi \cdot a}{p^2} \tag{9}$$

Where l, w, a, p represents the length, width, area, and perimeter respectively. The elongation is equal to 1 for objects that are circularly or square-shaped while it decreases as the object becomes more elongated. The compactness is defined as a ration of object area to the area of a circle with the same perimeter. Therefore the rivers will be characterized by low elongation and compactness while lakes will produce values close to 1. Additionally, the rivers with average width larger than 500 m were classified as main rivers.

River network extraction: The river polygons contain holes caused by river islands but also small holes caused by ships or other objects present on rivers. The presence of those small holes produces non-existing links causing the errors in the river network topology. To prevent that, all holes in which area is smaller than 10 pixels were removed. The creation of the centerline of rivers was based on the skeletonization of polygons by using the Voronoi diagram. In the first step, the original polygon perimeter was densified by creating vertexes at every 200 m for main rivers and 40 m for rivers. Based on the densified vertices the Voronoi polygons were created. In the third step, the polygon of interest was overlapped with each polygon in the Voronoi diagrams. The river centerline was retrieved by the selection of edges of Voronoi polygons, which do not touch the boundaries of the target polygons. The resulting centerline contains a large number of short lines (side edges of Voronoi polygons) that need to be removed. In this study, the cleaning methods were based on removing all lines whose last point does not represent the start point of the new line. Finally, the nodes were created at the end and intersection between lines.

4.6.2. Results and discussion

The performance of the proposed approach was tested on the extraction of the river network in the Republic of Serbia. The type and the size of river water bodies vary significantly across the study area. The north part (Vojvodina) is characterized by plain terrain, meandering and anbranching rivers, and a high number of spurs. In addition to natural rivers, artificial water bodies such as the channel network Danube-Tisa-Danube are present. At the same time on the south, in the hilly region, the river water bodies are characterized by the large variation in channel geometry and low width. The visual inspection of results is shown in Figure 46., while the extracted river network for the whole study area is presented in Appendix D.

The proposed approach extracts the river network from remote sensing data in a fully automatic manner. The visual inspection of results shows stabile performance over regions with different characteristics and scales (from width to narrow rivers). The algorithm automatically extracts the centerlines of all water bodies, including the main channel, tributaries, spurs, and chute cutoffs (Figure 46 (a), (b)). In addition, the extracted centerlines of tributaries are connected to the centerlines of the rivers they flow, producing the fully-connected river network (Figure 46 (a), (b)). Therefore this tool overcoming the previous limitation founded in (Isikdogan, Bovik and Passalacqua) (Chen, Liang and Liand) (Obida, Blackburn and Whyatt) providing more complete results.

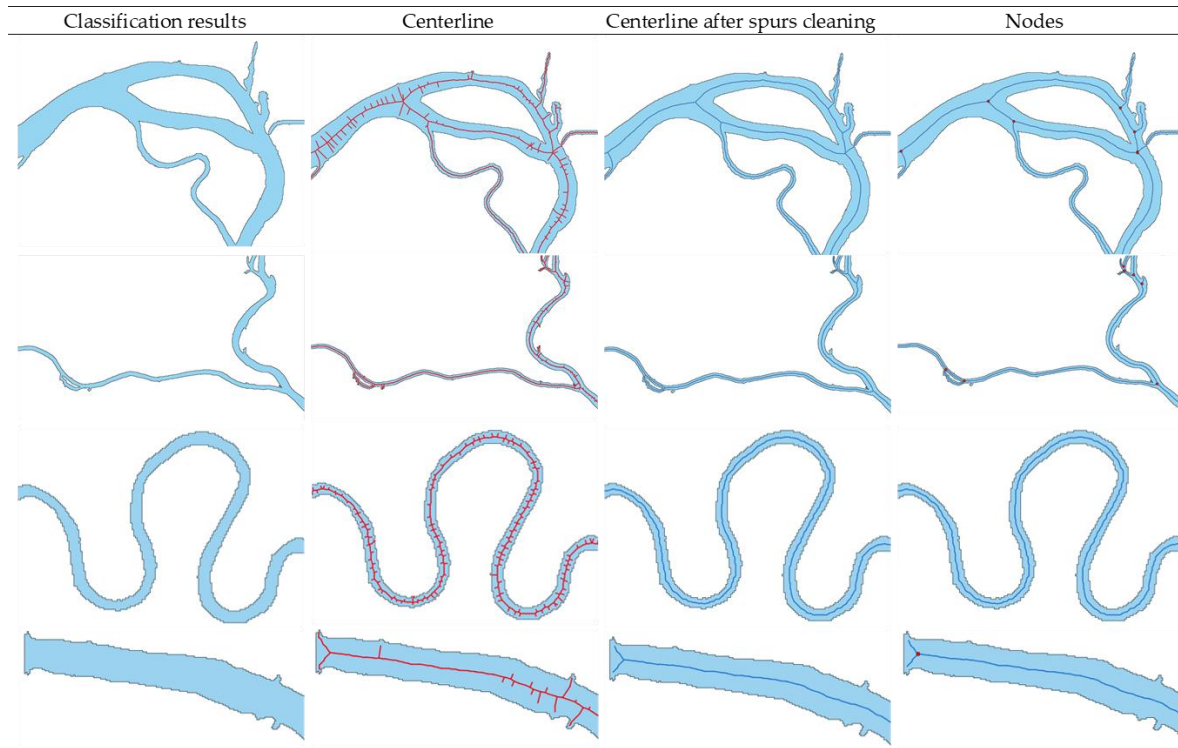| Classification results	Centerline	Centerline after spurs cleaning	Nodes

Figure 46. The visual inspection of the extracted river network

Figure 46 (c) highlights the ability of the algorithm to capturing the abrupt changes of main channels and extracted centerline in complex meandering patterns. Similar results were presented in (Monegaglia, Zolezzi and Guneralp) however, they were limited to the extraction of main channels only. Although the skeletonization provides accurate extraction of the river network, there are two main limitations. The first one is the presence of spurs (Figure 46. (Centerline)) however, this problem was automatically resolved by applying the cleaning method (Figure 46.). Secondly, at the end of the river mask, the resulting line no longer follows the center of the polygon intersecting the channel corners (Figure 46 (c)). This can be resolved by removing the lines that don't have a similar direction as the centerline and extending the centerline in the same direction. The detected nodes accurately represent the location of the river branching and confluences.

The errors in network topology caused by the small holes in river polygons (due to the presence of ships or other man-made structures at rivers during the acquisition of data) are corrected by removing holes that do not represent the river islands (Figure 47 (a)). Moreover, the influence of presented man-made obstacles over the water body on river network continuity is minimized by connecting separate river segments at the polygon level (Figure 47 (b)).
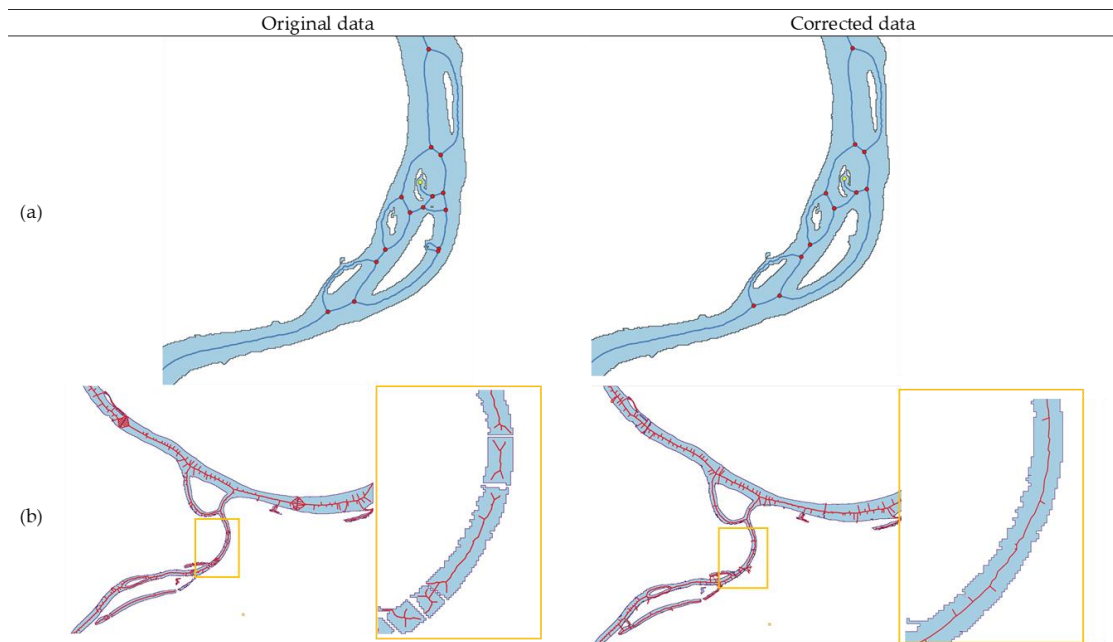
Figure 47. Influence of (a) removing small holes, (b) connection of disjoined river segments on river network compactness and correctness

The accuracy and completeness of the extracted river network are mostly limited by the spatial resolution of satellite images. The rivers with a width equal or narrower then spatial resolution are not completely detected. The presence of gaps courses the river network discontinuity and topological errors.

4.7. Benefits of the multidimensional model

The developed multidimensional model represents the integrated approach covering all phases from acquisition to distribution of data, by providing clearly defined methodologies for automatic extraction of water body geometry, topology, and attributes. The comparison between the traditional approach and the multidimensional model is presented in Figure 48.

The model is based on modern IT and geospatial technologies, including cloud storage, cloud computing, AI, and big data (Figure 12.). The multidimensional model uses data stored in the cloud enabling access and distribution of results more efficiently. In that way, it is possible to extract necessary data from petabytes large EO datasets, significantly reducing time-consuming and resource-intensive task. The access to the 40 years long historical and actual remote sensing data with global spatial coverage is crucial for creating large training data sets needed for successful AI algorithm performance and near-real-time monitoring of water resources by using calibrated AI algorithms. The implementation framework based on Google Colab, Python, and Jupyter enabled the development of a ready-to-use solution which don't demand any usage of user's hardware or installation of software. Moreover, the implementation framework is completely based on open-source libraries and platforms and, therefore free of cost. The only condition for usage of this model is the internet connection. This is especially important for enabling monitoring in undeveloped countries.

The AI provides full automation of processing procedures, avoiding the need for human operators. Due to that, water managers with low technical knowledge can monitor water resources at the state level in near-real-time. The development of the model in line with standards and

requirements of WFD and INSPIRE directive, added use-value and interoperability to data allowing exchange between different stockholders and support of the decision-making process.

Moreover, multidimensional mode improves several aspects of monitoring results. From the geometrical point of view, the multidimensional model significantly increases the frequency of monitoring, providing a better understanding of flow dynamics. In addition to increased temporal resolution, the primary advantage of water resource attribute monitoring based on remote sensing data is the monitoring of spatial variations. On the contrary to the traditional approach where the status of water bodies is represented by using only a few points, the remote sensing data and proposed methodology determine the WQP concentration for each pixel, providing the identification of polluters and understanding of they impact on overall water body status.

Figure 48. Comparison between the traditional approach and multidimensional model

V Conclusion

Considering the defined hypotheses and presented results, it can be concluded that the hypothesis has been confirmed. The proposed multidimensional model confirms that data on water resources required by the WFD and INSPIRE directive can be collected, processed, and distributed by currently available geospatial technologies. The experiments results indicate that: actual and historical remote sensing data can provide a comprehensive overview of water bodies characteristics at the regional level with the high spatial and temporal resolution, AI enables the development of automated processing of remote sensing data in real and near-real time, representation of water resources as geospatial object enables integrated and automated water management, and modern IT technologies, cloud systems and open data enable the change of the traditional and the definition of new data processing procedures.

The remote sensing data, with an improved spatial and temporal resolution, have great potential for water body extraction and monitoring of its dynamics. In this thesis, the ResUNet 50 was used for fully automated detection of water bodies from Sentinel 1 and Sentinel 2 images providing state-of-the-art accuracy (F1: 0.87 and 0.89 respectively) comparing to other studies with the same level of environmental complexity. Comparison of validation and test accuracy for Sentinel 1 (F1: 0.87 vs 0.90) and Sentinel 2 (F1: 0.89 vs 0.92) shows great generalization ability and the possibility to apply the algorithm for automatic water body detection over different areas. Moreover, the algorithm performed similarly on radar and optical images proving that transfer learning can be effectively used when the source and target data sets differ significantly. Regarding the performance of Sentinel 1 and Sentinel 2 for mapping water bodies, Sentinel 2 provided slightly better results. The recall value was the same (S1: 0.95 vs S2: 0.96), while Sentinel 2 produced higher precision (S1: 0.90 vs S2: 0.95) and, therefore, the slightly higher F1-score and KHAT. Extremely high recall value (0.95-0.99) and visual inspection shows that ResUNet 50 is not sensitive to low albedo surfaces such as built-up areas, roads, or shadows, which is one of the primary sources of errors during water body extraction from remote sensing data. The main drawbacks of water body detection from optical images in this study are mixed pixels, which can be reduced by pan sharping SWIR bands or using the higher resolution satellite images. In contrast, the accuracy of water body mapping from radar images is reduced due to high vegetation and shrubs along river banks, especially for small rivers, the high sensitivity of SAR on water content, and similar backscattering characteristics between water and impervious surfaces in rural areas. The visual inspection of results shows that the proposed approach accurately extracts the complete boundaries of water bodies with a width larger than 40 m despite varying topology, land-use/land cover, and atmospherical conditions. The smaller water bodies are difficult to extract, resulting in missing sections or complete omission of those water bodies. Based on the presented results, it can conclude the proposed approach can be used for accurately and free of charge automatic, near-real time water body extraction, and change monitoring with high frequency over large areas. Moreover, radar and optical images can supplement each other's effectively, providing water body extraction in all weather conditions.

In addition to optical and radar images, the possibilities of LiDAR data for water resource mapping were investigated. The first step in the proposed methodology is the classification of ground points and DEM generation. In this thesis, the point cloud classification and ground point filtering based on deep learning was presented and verified. Defined methodology rapidly improved the process of ground classification of LiDAR and UAV data, producing DEM with the required accuracy for water body detection and flood mapping according to European Flood Directive standards. The main advantage of the proposed methodology is the classification of raw point clouds, avoiding data pre-processing, and therefore reducing the computational time and computer power, which is one of

the biggest limitations when dealing with dense point clouds. Another advantage is the full automation of processing procedures so that it is straightforward for users to input the raw point cloud and create the digital elevation model. The accuracy assessment of algorithm performance on balanced and imbalanced data sets showed that the effectiveness of the rebalancing method depends heavily on the nature of the classification task. Therefore rebalancing methods can be used only if it the artificially generated data will have the same distribution as real data. The accuracy assessment of the classified LiDAR point cloud showed that 99.72% of the points had differences smaller than 5 cm with the true data. The created DEM, in addition to DSM, nDSM, Intensity, and point density are used as input to provide efficient land/water discrimination in terms of both accuracy and computing time. For Sentinel-2 water indices (NDWI, MNDWI) and spatial features are used for automatic water bodies extraction. The presented results show the following (1) water bodies extracted from LiDAR-derived data shows a perfect agreement with reality (2) LiDAR data provide significantly higher accuracy, compared with Sentinel 2, which was expected due to higher resolution, (3) The accurate LiDAR data and generate DTM has great potential in term of water body extraction. However, the availability and high cost limit their application. In future work, the performance of deep learning algorithms for the classification of water body points within point cloud should be investigated.

The remote sensing data in conjunction with in-situ measurements can be successfully used for monitoring of water quality parameters, such as chl-a, DO, SS, TN, and TP, with high spatial and temporal resolution decreasing the cost of implementation. The presented approach is based on 20 years of historical in-situ and remote sensing open data and open source solutions. The relationship between surface reflectance and insitu data was model by using ANN providing state-of-the-art accuracy. The accuracy of the produced results was evaluated by using two metrics: RMSE and nRMSE. The highest accuracy was obtained for DO and SS (nRMSE: 0.57 % and 0.97 % respectively), while the lowest accuracy was reported for chl-a (nRMSE: 3.68 %). The analysis of training dataset size and produced accuracy indicated that the accuracy of NN and the number of used samples are directly related. The SVM is less sensitive to small data samples and mixed pixels (Jakovljević , Govedarica and Álvarez-Taboada). Due to that SVM outperform NN (Govedarica and Jakovljević, Monitoring spatial and temporal variation of water quality parameters using time series of open multispectral data) when only a few samples are available for training and should be used for monitoring of water quality in those cases. The accuracy assessments show that Landsat data are suitable for monitoring of water quality. Although the 40 years long Landsat mission allows usage of historical data and enlarges datasets available for training, the temporal resolution of 16 days limits application of Landsat data for measuring water quality, especially in the area with frequent cloud clover. Due to that, less than 10 % of available insitu data can be paired with Landsat surface reflectance when the maximum time gap is set to 3 days. Additionally, monitoring of narrow rivers is limited due to moderate spatial resolution (30 m). The higher spatial and temporal resolution the Sentinel 2 represents better alternative for monitoring water quality since it provide higher accuracy and 25 % larger data set for 50 % less time comparing with Landsat 8 (Govedarica and Jakovljević, Monitoring spatial and temporal variation of water quality parameters using time series of open multispectral data). The main drawback for application of optical images in water quality monitoring is the sensitivity of sensors to clouds and haze. The clouds cause significant and unpredictable data gaps making it difficult to plan in-situ measurement. Additionally, the current methodology for the collection of in situ data limits the application of remote sensing for water quality monitoring. It order to address those limitations it is recommended to use the sensors for automatic monitoring for integration with remote sensing data. Unless water body is instrumented with high number of sensors, remote sensing technology coupled with optimized insitu measurement and advanced processing methods is only satisfactory method for monitoring of remote and large water bodies and overall water quality assessment at regional and global scale. The main advantage of remote sensing

technologies compared to traditional and automatic insitu monitoring is monitoring of spatial variation. The information on spatial variation of water quality is crucial for the identification and control of polluters. Therefore it represents the bases for the development of activation plans to prevent pollution, future degradation of the aquatic environment, and protect public health.

Automatic detection of visible waste material from high-resolution UAV orthophotos can be accurately achieved using the end-to-end semantic segmentation ResUNet50 algorithm. Among the other tested algorithms, ResUNet50 showed a stable performance to detect and classify floating plastic in the different datasets and for different spatial resolutions, for underwater and floating targets (*F1* score > 0.73). The ResUNext50 and XceptionUNet models led to an overestimation of the floating plastic due to misclassification of water pixels. The model also showed its suitability for plastic detection on water, shallow water and also on land, with lower accuracy compared with the floating plastics. An underestimation of the plastic area of only 3.4% showed its utility to monitor plastic pollution effectively and makes it possible to use it to optimize cleaning campaigns, as well as the integration and comparison of the estimations. It was possible to accurately detect and classify the three different plastic types located in the study area (OPS, PET, Nylon) using the ResUNet50 model (*F1*: OPS: 0.86; Nylon: 0.88; PET: 0.92), which was the most sensitive to detect small differences in the amount of reflected energy. Regarding the relationship between spatial resolution and detectable plastic size, the classification accuracy decreased with the decrease in spatial resolution, performing best on 4 mm resolution images for all the different kinds of plastic. The model cannot detect all plastic pixels, but it can be trusted when it does, for all the tested spatial resolutions. Moreover, the algorithm needs at least one pure plastic pixel (a pixel that only contains that material) to detect plastics on the water surface, and two pure pixels for the detection of underwater plastics. The results obtained with the 18 mm spatial resolution orthophotos and the proposed method meet the requirements described in OSPAR (OSPAR), NOAA (Opfer, Arthur and Lippiatt) or UNEP/IOC (Cheshire, Adler and Barbière) guidelines, while CSIRO (Hardesty, Lawson and van der Velde) surveys will require the use of 4 mm orthophotos. Taking as a reference value the classification obtained for the 4 mm orthophoto, the largest difference in the extension of the area classified as plastic was obtained using the 23 mm orthophoto (OPS: 16.1%; Nylon: 33.2%; PET: 22.3 %) (Figure 8). The smallest difference for the OPS and Nylon classes was obtained using the 18 mm orthophoto (OPS: 1.8%; Nylon: 4.2%), while the 30 mm orthophoto provided the closest area to the reference for PET plastic (PET: 8.9%) (Figure 8). When planning a UAV survey to map floating plastic, the following issues should be taking into account: (i) reaching a compromise between the spatial resolution and the area covered by each image, (ii) two UAVs with the same flight pattern should be used, one to collect the imagery to obtain the maps and a second one flying lower than the other, so it can capture very high spatial resolution data to delineate an accurate training dataset, (iii) synchronizing the two flight missions and reduce time overlap between surveys, (iv) flying during cloudy weather to reduce the sun glint effect, and (v) wind speed should be as low as possible, so the quality of the orthophoto is not compromised.

The detected water bodies are further processed to create a river network and analyses the topological relationship between its elements. The designed tool for automated river analysis is capable to create large scale river networks. The visual inspection shows that algorithm performance is stabile over different types and different water body scales. There weren't noticed a difference in algorithm performance over continuous or anbranching rivers, main or tributaries, meandering or strata, width, or narrow. Also, the algorithm successfully extracts the centerlines of spurs and chute cutoffs. The resulting river network is fully connected since the centerlines of tributaries and main channels are connected. This provides detection of the exact position of nodes that are components of the river network. The completeness and correctness of the extracted network are provided by high classification accuracy, a connection between separated river segments at polygon levels, and

removing the holes at river polygons that don't present river islands. The presented approach for river network extraction addresses the main limitations of previous studies. Moreover, it detects both components of river networks (links and nodes) while all previous studies deal only with the extraction of links. The accuracy and completeness of the extracted river network are mostly limited by the spatial resolution of satellite images. The rivers with a width equal or narrower then spatial resolution are not completely detected. The presence of gaps courses the river network discontinuity and topological errors.

Remote sensing technologies with continuous data acquisition and data available in real and near real-time have greater potential to support water resource management and decision-making process. However, the practical application of remote sensing data is still limited. This is mostly due to a lack of technical expertise and knowledge to understand the possibilities and limitations of remote sensing technology, lack of established methodologies, and complex processing needs. The results presented in the previous chapter shows that the proposed multidimensional mode address all those limitations. The main advantage of the model is a clearly defined methodology for monitoring of water resource geometry, topology, and attribute based on remote sensing data, fully automated processing procedures, free of charge and ready to use implementation. This model is completely developed in line with the requirement of WFD, WISE, and INSPIRE directive and recommendation of state-of-the-art research in the field. Consequently, the model produces highly accurate and actionable information to support the decision-making process. More importantly, created information, with appropriated WISE and INSPIRE data structure, provides a classification of water body status and should be used to fulfill the WFD reporting obligations. Additionally, resulting information can be used as the for monitoring of process towards the achievement of SDG, including Indicator 6.3.2., Indicator 6.4.2., Indicator 6.6.1., and Indicator 14.1.1.

References

2030 WRG, 2030 Water Resources Group. "Charting our water future: Economic frameworks to inform decision-making." 2009.

Abdelmalik, K.W. "Role of statistical remote sensing for Inland water quality parameters prediction." *The Egyptian Journal of Remote Sensing and Space Sciences* (2016).

AEP, Agencija za zaštitu životne sredine. *Status površinskih voda Srbije, Analize i elementi za projektovanje monitoirnga*. Beograd: AEP, 2015.

Alaibakhsh, M., et al. "Delineation of riparian vegetation from Landsat multi-temporal imagery using PCA." *Hydrol. Process.* (2017): 800–810.

Alikas, K, et al. "Satellite-based products for monitoring optically complex inland waters in support of EU Water Framework Directive." *International Journal of Remote Sensing* (2015): 4446-4468.

Allen, G. H. and T. M. Pavelsky. "Global extent of rivers and stemas." *Science* (2018): 585-588.

Alparslan, E., H.G. Coskun and U. Alganci. "Water quality determination of Küçükçekmece Lake, Turkey by using multispectral satellite data. ." *Sci. World J.* (2009): 1215–1229.

Alsmadi, M., K. Omar and S. Noah. "Back Propagation Algorithm: The Best Algorithm among the Multi-layer Perceptron Algorithm." *Int. J. Comput. Sci. Netw. Secur* (2009): 378–383.

Anggoro, A., V. Siregar and S. Agus. "The effect of sunglint on benthic habitats mapping in Pari Island using worldview-2 imagery." *Procedia Environ. Sci.* (2016): 487–495.

Anthony, M. and P.L. Bartlett. *Neural Network Learning: Theoretical Foundations*. Cambridge: Cambridge University Press, 2009.

Antonarakis, A.S, K.S Richards and J Brasington. "Object-based land cover classification using airborne LiDAR." *Remote Sensing of Environment* (2008): 2988–2998.

Aoyama, T. "Extraction of marine debris in the Sea of Japan using high-spatial resolution satellite images." *SPIE Remote Sensing of the Oceans and Inland Waters: Techniques, Applications, and Challenges*. SPIE, 2016.

Asal, F.F. "Evaluating the effects of reduction in LiDAR data on the visual and statistical characteristics of the created Digital Elevation Models." *Proceedings of the 2016 XXIII ISPRS Congress, .* Prague: ISPRS, 2016.

Axelsson, P. "DEM generation from laser scanner data using adaptive TIN models." *Int. Arch. Photogramm. Remote Sens* (2000): 110–117.

Badrinarayanan, V., A. Handa and R. Cipolla. "SegNet: A Deep Convolutional Encoder-Decoder Architecture for Robust Semantic Pixel-Wise Labelling." *arXiv: 1511.02680*. arXiV, 2015.

Baghdadi, N., et al. "Calibration of the Water Cloud Model at C-Band for Winter Crop Fields and Grasslands." *Remote Sens.* (2017).

Bandini, F., et al. "Unmanned Aerial System (UAS) observations of water surface elevation in a small stream: Comparison of radar altimetry, LIDAR and photogrammetry techniques." *Remote Sensing of Environment* (2020).

—. "Water level observations from Unmanned Aerial Vehicles for improving estimates of surface water-groundwater interaction." *Hydrological Processes* (2017).

Bangira, T, et al. "Comparing Thresholding with Machine Learning Classifiers for Mapping Complex Water." *Remote Sens.* (2019).

Barron, C., P. Neis and A. A. Zipf. "Comprehensive Framework for Intrinsic OpenStreetMap Quality Analysis." *Transactions in GIS* (2014): 877-895.

Baughman, C, et al. "Reconstructing Turbidity in a Glacially Influenced Lake Using the Landsat TM and ETM+ Surface Reflectance Climate Data Record Archive, Lake Clark, Alaska4. Application of different imagery and methods for water quality monitoring." *Remote Sens.* (2015).

Becker, C., et al. "Classification of Aerial photogrammetric 3D point clouds." *arXiv:1705.08374v1*. arXiv , 2017.

Behnamian, A, et al. "Semi-Automated Surface Water Detection with Synthetic Aperture Radar Data: A Wetland Case Study. ." *Remote Sens.* (2017).

Bekkar, M., H. Kheliouane Djemaa and T. Akrouf Alitouche. "Evaluation Measure for Models Assessment over Imbalanced Data Sets." *J. Inf. Eng. Appl.* (2013): 27–38.

Benoudjit, A and R Guida. "A Novel Fully Automated Mapping of the Flood Extent on SAR Images Using a Supervised Classifier." *Remote Sens.* (2019).

Benz, U.C., et al. "Multi-resolution, object-oriented fuzzy analysis of remote sensing data for GIS-ready information." *ISPRS J. Photogramm. Remote Sens.* (2004): 239–258.

Bian, X., et al. "Underwater Topography Detection in Coastal Areas Using Fully Polarimetric SAR Data." *Remote Sens.* (2017).

Biggs, H.J., et al. "Coupling Unmanned Aerial Vehicle (UAV) and hydraulic surveys to study the geometry and spatial distribution of aquatic macrophytes." *Journal of Ecohydraulics* (2018): 45-48.

Bioresita, F, et al. "A Method for Automatic and Rapid Mapping of Water Surfaces from Sentinel-1 Imagery. ." *Remote Sens.* (2018).

Blaschke, T., et al. "Object-Oriented Image Processing in an Integrated GIS/Remote Sensing Environment and Perspectives for Environmental Applications." *Environ. Inf. Plan. Politics Public* (2000): 555-570.

Bočac, Ekocentar. *Zaustavljanje plutajuceg otpada na mrezi*. n.d. 09 02 2020. <https://ekocentar-bocacjezero.com/zastitna_mreza/zaustavljanje-plutajuceg-otpada-na-mrezi/>.

Bochow, M., et al. "On the Use of Airborne Imaging Spectroscopy Data for the Automatic Detection and Delineation of Surface Water Bodies." *Remote Sensing of Planet Earth* (2012).

Bodoque, J.M., et al. "Flood Damage Analysis: First Floor Elevation Uncertainty Resulting from LiDAR-Derived Digital Surface Models." *Remote Sens.* (2016).

Bolanos, S., et al. "Operational Surface Water Detection and Monitoring Using Radarsat 2." *Remote Sens* (2016).

Bonansea, Ml Rodriguez, M.C, L Pinotti and S Derrero. "Using multi-temporal Landsat imagery and linear mixed models for assessing water quality parameters in Río Tercero reservoir (Argentina)." *Remote Sensing of Environment* (2015): 28-41.

Boonpook, W., et al. "A Deep Learning Approach on Building Detection from Unmanned Aerial Vehicle-Based Images in Riverbank Monitoring." *Sensor* (2018).

Bresciani, M., M.D. Adamo and G. Carolis. "Monitoring blooms and surface accumulation of cyanobacteria in the Curonian Lagoon by combining MERIS and ASAR data." *Remote Sens. Environ* (2014): 124–135.

Brezonik, P.L., et al. "Factors affecting the measurement of CDOM by remote sensing of optically complex inland waters." *Remote Sensing of Environment* (2014).

Brion, P.M, et al. "Improvement of streams hydro-geomorphological assessment using LiDAR DEMs." *Earth surface processes and landforms* (2013): 1808-1821.

Brivio, P.A, et al. "Integration of remote sensing data and GIS for accurate mapping of fooded areas." *Int. j. remote sensing,* (2002): 429–44.

Brzank, A, et al. "Aspects of generating precise digital terrain models in Wadde Sea from Lidat – water classification and structure line extraction." *ISPRS Journal of Photogrammetry & Remote Sensing 63* (2008): 510–528.

Byun, Y., Y. Han and T. Chae. "Image Fusion-Based Change Detection for Flood Extent Extraction Using Bi-Temporal Very High-Resolution Satellite Images." *Remote Sensing* (2015): 10347–10363 .

Byun, Y.,, Y. Han and T. Chae. "Image Fusion-Based Change Detection for Flood Extent Extraction Using Bi-Temporal Very High-Resolution Satellite Images." *Remote Sensing* (2015): 10347–10363.

Caballero, I, F Steinmetz and G Navarro. "Evaluation of the First Year of Operational Sentinel-2A Data for Retrieval of Suspended Solids in Medium- to High-Turbidity Waters." *Remote Sens.* (2018).

Canisius, F., et al. "SAR Backscatter and InSAR Coherence for Monitoring Wetland Extent, Flood Pulse and Vegetation: A Study of the Amazon Lowland." *Remote sens.* (2019).

Cao, N., et al. "Estimation of Water Level Changes of Large-Scale Amazon Wetlands Using ALOS2 ScanSAR Differential Interferometry." *Remote Sens.* (2018).

Carranza-Garcia, M, J Garcia-Gutierrez and J.C Riquelme. "A Framework for Evaluating Land Use and Land Cover Classification Using Convolutional Neural Networks." *Remote Sens.* (2019).

Carson, A.B., et al. "Reconstructing turbidity in a glacially influenced lake using the Landsat TM and ETM+ surface reflectance climate data record archive, Lake Clark, Alaska." *Remote Sens.* (2015): 13692-13710.

Castelluccio, M., et al. "Land Use Classification in Remote Sensing Images by Convolutional Neural Networks." *arXiv:1508.00092v1*. arXiv, 2015.

Chabot, D., et al. "Object-based analysis of UAS imagery to map emergent and submerged invasive aquatic vegetation: a case study." *Journal of Unmanned Vehicle Systems* (2016).

Chakrapani, G.J. "Factors controlling variations in river sediment loads." *Current Science* (2005): 569-575.

Chebud, Y., et al. "Water quality monitoring using remote sensing and an artificial neural network." *Water Air Soil Pollut.* (2012): 4875–4887.

Chen, D., D. Stow and P. Gong. "Examining the effect of spatial resolution and texture window size on classification accuracy: an urban environment case." *Int. J. Remote Sensing* (2004): 2177–2192.

Chen, H, et al. "Hydraulic correction method (HCM) to enhance the efficiency of SRTM DEM in flood modeling." *Journal of Hydrology* (2018): 56-70.

Chen, H., et al. "Extraction of connected river networks from multi-temporal remote sensing imagery using a path tracking technique." *Remote Sensing of Environment* (2020).

Chen, Jun, et al. "A Voronoi-based 9-intersection model for spatial relations." *Int J Geograohical Information Science* (2001): 201-220.

Chen, L.-C., et al. "Deeplab: Semantic image segmentation with deep convolutional nets, Atrous convolution, and fully connected CRFs." *IEEE Trans. Pattern Anal. Mach. Intell.* (2018): 834–848.

Chen, Y, et al. "Extraction of Urban Water Bodies from High-Resolution Remote-Sensing Imagery Using Deep Learning." *Water* (2018).

Chen, Y., et al. "Changes of nutrients and phytoplankton chlorophyll-a in a large shallow lake, Taihu, China: An 8-year investigation." *Hydrobiologia* (2003): 273–279.

Cheng, M, et al. "Assessment of the Evolution of Nitrate Deposition Using Remote Sensing Data Over the Yangtze River Delta, China." *IEEE JOURNAL OF SELECTED TOPICS IN APPLIED EARTH OBSERVATIONS AND REMOTE SENSING* (2016).

Cheshire, A.C., et al. "UNEP/IOC Guidelines on Survey and Monitoring of Marine Litter. UNEP Regional Seas Reports and Studies." 2009.

Chollet, F. *Deep Learning with Python*. Greenwich: Manning publications, 2018.

—. "Xception: Deep Learning with Depthwise Separable Convolutions." *Proceedings of the IEEE Conference on Computer Vision and Pattern Recognition (CVPR)*. Honolulu: IEEE, 2017. 1251-1258.

Chul Ko, B., H. Hun Kim and J. Yeal Nam. "Classification of Potential Water Bodies Using Landsat 8 OLI and a Combination of Two Boosted Random Forest Classifiers." *Sensor* (2015).

CloudCompare. n.d. 5 6 2019. <https://www.cloudcompare.org/ >.

Colab. *Google Colab*. n.d. 15 06 2019. <colab.research.google.com>.

Corbane, C., et al. "Remote Sensing for Mapping Natural Habitats and Their Conservation Status - New Opportunities and Challenges." *International Journal of Applied Earth Observation and Geoinformation* (2015): 7-16.

Cordts, M., et al. "The Cityscapes Dataset for Semantic Urban Scene Understanding." *arXiv:1604.01685v2*. arXiv, 2016.

Crasto, N, et al. "A LiDAR-based decision-tree classification of open water surfaces in an Arctic delta ." *Remote Senisng of Environment* (2015): 90-102.

Cui, Y., et al. "A Deep Learning Algorithm for One-step Contour Aware Nuclei Segmentation of Histopathological Images." *Med. Biol. Eng. Comput.* (2019): 2027–2043.

DAAC, LP. n.d. 22 2 2018. <https://lpdaac.usgs.gov/dataset_discovery/aster/aster_products_table/astgtm>.

Dal Pozzolo, A., et al. "Calibrating probability with under sampling for unbalanced classification." *Proceedings of the IEEE Symposium Series on Computational Intelligence*. Cape Town,: IEEE, 2015.

Dal Pozzolo, A., O. Caelen and G. Bontempi. "When is undersampling effective in unbalanced classification tasks?" *Machine Learning and Knowledge Discovery in Databases*. Berlin: Springer, 2015.

d'Andrimont, R, C Marlies and P Defourny. "Hyperspatial and Multi-Source Water Body Mapping: A Framework to Handle Heterogeneities from Observations and Targets over Large Areas." *Remote Sens.* (2016).

Danson, E. "Understanding lidar bathymetry for shallow waters and coastal mapping. ." *FIG XXIII International Congress*. Munich, 2006.

Dare, P. M. "Shadow Analysis in High-Resolution Satellite Imagery of Urban Areas." *Photogramm Engineering Remote Sensing* (2005): 169–177.

de Lima, R. P. and K. Marfurt. "Convolutional Neural Network for Remote-Sensing Scene Classification: Transfer Learning Analysis." *Remote Sens.* (2019).

Deng, J., et al. "ImageNet: A large-scale hierarchical image database." *Proceedings of the IEEE Conference on Computer Vision and Pattern Recognition*. Miami: IEEE, 2009. 248-255.

Đereg, N. and P. Marković. *Mogućnosti Srbije za dostizanje standarda EU u oblasti upravljanja vodama*. Beograd: Evropski pokret u Srbiji, 2016.

DigitalGlobe. *Remote Sensing Technology Trends and Agriculture*. 2015. 31 07 2020. <https://dg-cms-uploads-production.s3.amazonaws.com/uploads/document/file/31/DG-RemoteSensing-WP.pdf>.

Ding, X.Y. "The Application of eCognition in Land Use Projects." *Geomat. Spat. Inf. Technol* (2005): 116-120.

Dogliotti, A.I, et al. "A single algorithm to retrieve turbidity from remotely-sensed data in all coastal and estuarine waters." *Remote Sensing of Environment* (2015): 157–168.

Doji, P, P Ferns and M Broomhall. "A Semi-Analytic Model for Estimating Total Suspended Sediment Concentration in Turbid Coastal Waters of Northern Western Australia Using MODIS-Aqua 250 m Data." *Remote Sens.* (2016).

Doña, C., et al. "Monitoring Hydrological Patterns of Temporary Lakes Using Remote Sensing and Machine Learning Models: Case Study of La Mancha Humeda Biosphere Reserve in Central Spain." *Remote Sensing* (2016).

Donchyts, G, et al. "A 30 M Resolution SurfaceWater Mask Including Estimation of Positional and Thematic Differences Using Landsat 8, SRTM and OpenStreetMap: A Case Study in the Murray-Darling Basin Australia." *Remote Sensing* (2016).

Doody, T.M., et al. "A method to map riparian exotic vegetation (Salix spp.) area to inform water resource management." *Hydrol. Process.* (2014): 3809–3823.

Doxani, G, et al. "Shallow-water bathymetry over variable bottom type using multispectral WorldView-2 image." *International Archives of the Photogrammetry, Remote Sensing and Spatial Information Sciences,*. Melbourn : ISPRS, 2012.

Du, C, et al. "Estimation of total phosphorus concentration using a water classification method in inland water." *Int J App Earth Obe Geoinformatics* (2018): 29-42.

Du, Y., et al. "Mapping from Sentinel-2 Imagery with Modified Normalized Difference Water Index at 10-M Spatial Resolution Produced by Sharpening the SWIR Band Water Bodies." *Remote Sensing* (2016).

Dunford, R., et al. "Potential and constraints of Unmanned Aerial Vehicle technology for the characterization of Mediterranean riparian forest." *International Journal of Remote Sensing* (2009): 4915-4935.

Duro, D.C., S.E. Franklin and M.G. Dube. "A comparison of pixel-based and object-based image analysis with selected machine learning algorithms for the classification of agricultural landscapes using SPOT-5 HRG imagery." *Remote Sensing of Environment* (2012): 259-272.

EC, European Commission. *Guidance document n.o 7 Monitoring under the Water Framework Directive*. Luxembourg: Office for Official Publications of the European Communities, , 2003.

Eckel, M., et al. "Leveraging OpenStreetMap to support flood risk management in municipalities: A prototype decision support system." *ISCRAM 2016 Conferen*. Rio de Janeiro, 2016.

EC-Sector 2, European Commision. "Handbook on the Implementation of EC Environmental Legislation." 2017.

EEA, European Environment Agency. "European waters Assessment of status and pressures." 2018.

Egenhofer, M. J and J. Herring. *Categorizing binary topological relationships between regions, lines, and points in geographic databases*. Technical Report. Maine: University of Maine, 1991.

Ekercin, S. "Water Quality Retrievals from High Resolution Ikonos Multispectral Imagery: A Case Study in Istanbul, Turkey." *Water Air Soil Pollut* (2007): 239-251.

El Din, E. S, Y Zhang and A Suliman. "Mapping concentrations of surface water quality parameters using a novel remote sensing and artificial intelligence framework." *International Journal of Remote Sensing* (2017): 1023–1042.

Elhag, M, et al. "Assessment of Water Quality Parameters Using Temporal Remote Sensing Spectral Reflectance in Arid Environments, Saudi Arabia." *Water* (2019).

EPC, European Parliament and the Council. "Infrastructure for Spatial Information in the European Community (INSPIRE) Directive." 2007.

EPC, European Parliament and the Councle of the European Union. "Water Framework Directive 2000/60/EC ." 2000.

Eriksen, M., et al. "Plastic pollution in the world's oceans: More than 5 trillion plastic pieces weighing over 250,000 tons afloat at sea." *PLoS ONE* (2014).

ESA. *Level-2A Algorithm overview*. n.d. 15 08 2020. <https://earth.esa.int/web/sentinel/technical-guides/sentinel-2-msi/level-2a/algorithm>.

—. *Sentinel 2*. n.d. 16 06 2017. <https://sentinel.esa.int/web/sentinel/missions/sentinel-2/overview1>.

—. *Sentinel-1 Observation Scenario*. n.d. 29 07 2020. <https://sentinel.esa.int/web/sentinel/missions/sentinel-1/observation-scenario>.

—. *Sentinel-1 Toolbox*. n.d. 15 08 2020. <https://sentinel.esa.int/web/sentinel/toolboxes/sentinel-1>.

Fang, W, et al. "Recognizing Global Reservoirs From Landsat 8 Images: A Deep Learning Approach." *IEEE JOURNAL OF SELECTED TOPICS IN APPLIED EARTH OBSERVATIONS AND REMOTE SENSING* (2019).

Fausset, L. V. *Fundamentals of neural networks: architectures, algorithms and applications,*. New York : Pearson, 1993.

Fawcett, T. "An introduction to ROC analysis." *Pattern Recognit. Lett.* (2006): 861–874.

Ferndandes, M.R., et al. "Optimal attributes for the object based detection of giant reed in riparian habitats: A comparative study between Airborne High Spatial Resolution and WorldView-2 imagery." *International Journal of Applied Earth Observation and Geoinformation* (2014): 79-91.

Feyisa, G., et al. "Automated Water Extraction Index: A New Technique for Surface Water Mapping Using Landsat Imagery." *Remote Sensing of Environment* (2014): 23–35.

Filin, S. and N. Pfeofer. "Neighborhood systems for airborne laser data." *Photogramm. Eng. Remote Sens* (2005): 743–755.

Filstrup, C. T. and J.A. Downing. "Relationship of chlorophyll to phosphorus and nitrogen in nutrient-rich lakes." *Inland Waters* (2017).

Fisher, G. B., B. Bookhagen and C.B. Amos. "Channel planform geometry and slopes from freely available high-spatial resolution imagery and DEM fusion: Implications for channel width scalings, erosion proxies, and fluvial signatures in tectonically active landscapes." *Geomorphology* (2013): 46-56.

Flynn, K.F. and S.C. Chapra. "Remote Sensing of Submerged Aquatic Vegetation in a Shallow Non-Turbid River Using an Unmanned Aerial Vehicle." *Remote sens.* (2014): 12815-12836.

Frezier, P. S. and K. J. Page. "Water Body Detection and Delineation with Landsat TM Data." *Photogrammetric Engineering and Remote Sensing* (2000): 1461–1468.

Fricke, K and B Baschek. "Water surface temperature profiles for the Rhine Ri derived from Landsat ETM+ data." *Remote Sensing for Agricukture, Ecosystems and Hydrology*. SPIE, 2013.

Friedman, J.H., J.L. Bentley and R.A. Finkel. "An algorithm for finding best matches in logarithmic expected time." *ACM Trans. Math. Softw.* (1977): 209–226.

Futere We Want, UN. *Sustainable Developmnet Knowladge platform*. 2012. 17 07 2020. <https://sustainabledevelopment.un.org/futurewewant.html>.

Garaba, S.P, et al. "Classifying Natural Waters with the Forel-Ule Colour Index System: Results, Applications, Correlations and Crowdsourcing." *Int. J. Environ. Res. Public Health* (2015): 16096-16109.

GEE. *Sentinel-1 Algorithms*. n.d. 15 08 2020. <https://developers.google.com/earth-engine/sentinel1>.

Geraeds, M., et al. "Riverine Plastic Litter Monitoring Using Unmanned Aerial Vehicles (UAVs)." *Remote Sens.* (2019).

Ghaffar, M.A.A., et al. "Data augmentation approaches for satellite image super-resolution." *ISPRS Annals of the Photogrammetry, Remote Sensing and Spatial Information Sciences, .* Munich: ISPRS, 2019. 47-54.

Giardino, C, et al. "Evaluation od Multi-Resolution Satellite Sensor for Assessing Water Quality and Bottom Depth of Lake Garda." *Sensor* (2014).

Girres, J.F. and G. Touya. "Elements of quality assessment of French OpenStreetMap data." *Transactions in GIS* (2010).

Girshick, R, et al. "Region-based convolutional networks for accurate object detection and semantic segmentation." *IEEE Transactions on Pattern Analysis and Machine Intelligence* (2016): 142-158.

Goddijn-Murphy, L., et al. "Concept for a hyperspectral remote sensing algorithm for floating marine macro plastics." *Mar. Pollut. Bull.* (2018): 255–262.

Goetz, M. and A. Zipf. "he Evolution of Geo Crowd Sourcing: Bringing Volunteered Geographic Information to the Third Dimension ." *Crowdsourcing Geographic Knowledge* (2012): 139-159.

Goodfellow, I., Y. Bengio and A. Courville. *Deep Learning*. Cambridge: The MIT Press, 2016.

Goodfellow, I.J., et al. "Multi-digit Number Recognition from Street View Imagery using Deep Convolutional Neural Networks." *arXiv:1312.6082v4*. arXiv, 2014.

Gorelick, N., et al. "Google Earth Engine: Planetary-scale geospatial analysis for everyon." *Remote Sensing of Environment* (2017): 18-27.

Govedarica, M. and G. Jakovljević. "Monitoring spatial and temporal variation of water quality parameters using time series of open multispectral data." *Proc. SPIE 11174, Seventh International Conference on Remote Sensing and Geoinformation of the Environment*. Paphos: SPIE, 2019.

Govedarica, M., G. Jakovljević and F.A. Taboada. "Flood risk assessment based on LiDAR and UAV points clouds and DEM." *Proceedings of the SPIE 10783, Remote Sensing for Agriculture, Ecosystems, and Hydrology*. Berlin: SPIE, 2018.

Gray, P.C., et al. " A Convolutional Neural Network for Detecting Sea Turtles in Drone Imagery." *Methods in Ecology and Evolution* (2018).

GSDI Association. "Developing Spatial Data Infrastructures: the SDI CookBook." 2004. *GSDI Association.* 11 7 2020. <http://gsdiassociation.org/images/publications/cookbooks/SDI_Cookbook_GSDI_2004_ver 2.pdf>.

Gstaiger, V, et al. "Multi-sensoral and automated derivation of inundated areas using TerraSAR-X and ENVISAT ASAR data. ." *Int. J. Remote Sens.* (2012): 7291–7304.

Gu, Y, Y Wnag and Y Li. "A Survey on Deep Learning-Driven Remote Sensing Image Scene Understanding: Scene Classification, Scene Retrieval and Scene-Guided Object Detection." *applied sciences* (2019).

Guenther, G.C., et al. " Meeting the accuracy challenge in airborne lidar bathymetry." *EARSeL SIG-Workshop LIDAR*. Dresden, 2000.

Guidance Document No 9, European Commission. "Implementing the Geographical Information System Elements (GIS) of the Water Framework Directive." 2003.

Guidance Document No: 22, European Commission. "Updated Guidance on Implementing the Geographical Information System (GIS) Elements of the EU Water policy." 2009.

Guo, H, et al. "A Multi-Scale Water Extraction Convolutional Neural Network (MWEN) Method for GaoFen-1 Remote Sensing Images." *ISPRS Int. J. Geo-Inf* (2020).

Guo, Q, et al. "Study on Retrieval of Chlorophyll-a Concentration Based on Landsat OLI Imagery in the Haihe River, China,." *Sustainability* (2016).

Ha, N.T.T, K Koike and M.T Nhuan. "Improved Accuracy of Chlorophyll-a Concentration Estimates from MODIS Imagery Using a Two-Band Ratio Algorithm and Geostatistics: As Applied to the Monitoring of Eutrophication Processes over Tien Yen Bay (Norther Vietnam)." *Remote Sens.* (2013): 421-442.

Hackel, T., J.D. Wegner and K. Schindler. "Fast semantic segmentation of the 3D point clouds with strongly varying density." *Proceedings of the 2016 XXIII ISPRS Congress*. Prague: ISPRS, 2016.

Hafeez, S, et al. "Comparison of Machine Learning Algorithms for Retrieval of Water Quality Indicators in Case-II Waters: A Case Study of Hong Kong." *Remote Sens.* (2019).

Haklay, M. "How good is Volunteered Geographical Information? A comparative study of OpenStreetMap and Ordnance Survey datasets." *Environment and Planning B: Planning and Design* (2008).

Hardesty, B.D., et al. "Estimating quantities and sources of marine debris at a continental scale." *Front. Ecol. Environ.* (2016): 18–25.

Hasini, R., M. Shokri and M. Dehghan. "Augmentation Scheme for Dealing with Imbalanced Network Traffic Classification Using Deep Learning." *arXiv:1901.00204* . arXiv , 2019.

Haykin, S. *Neural Networks: A Comprehensive Foundation* . New Jersey: Prentice Hall PTR, 1998.

He, K, et al. "Deep Residual Learning for Image Recognition." *IEEE International Conference on Computer Vision and Pattern Recognition (CVPR)*. 2016.

He, K., et al. "Identity Mappings in Deep Residual Networks." *arXiv:1603.05027v3*. arXiv, 2016.

Heine, I, et al. "Reconstruction of Lake Level Changes of Groundwater-Fed Lakes in Northeastern Germany Using RapidEye Time Series." *Water* (2015): 4175-4199.

Hofle, B, et al. "Water surface mapping from airborne laser scanning using signal intensity and elevation data." *Earth Surf. Process. Landforms* (2009): 1635-1649.

Hong, S.-J., et al. "Application of Deep-Learning Methods to Bird Detection Using Unmanned Aerial Vehicle Imagery." *Sensors* (2019).

Hooshyar, M, et al. "Wet channel network extraction by integrating LiDAR intensity and elevation data." *Water Resour. Res.* (2015): 10029–10046.

Hossain, M.A. and C. Chan. "Open data adoption in Australian government agencies: an exploratory study." *Australasian Conference on Information Systems*. Adelaode, 2015.

Howard, Guy and Jamie Bartram. *Domestic water quantity, service level and health*. World Health Organization, 2003.

Hu, J., et al. "A Comparison and Strategy of Semantic Segmentation on Remote Sensing Images." *arXiv: 1905.10231v1*. arXiv, 2019.

Hu, X. and Y. Yuan. "Deep-Learning-Based Classification for DTM Extraction from ALS Point Cloud." *Remote Sens.* (2016).

Huang, C., et al. "Surface Water Mapping from Suomi NPP-VIIRS Imagery at 30 M Resolution via Blending with Landsat Data." *Remote Sensing* (2016).

Huang, C., L. S. Davis and R. G. J. Townshend. "An Assessment of Support Vector Machines for Land Cover Classification." *International Journal Remote Sensing* (2002): 725–749.

Huang, S., J. Li and M Xu. "Water Surface Variations Monitoring and Flood Hazard Analysis in Dongting Lake Area Using Long-Term Terra/MODIS Data Time Series." *Natural Hazards* (2012): 93– 100.

Huang, W., et al. "Automated Extraction of Surface Water Extent from Sentinel-1 Data." *Remote Sens.* (2018).

Huang, X., et al. "Combining Pixel- and Object-Based Machine Learning for Identification of Water-Body Types from Urban High-Resolution Remote-Sensing Imagery." *IEEE Journal of Selected Topics* (2015).

Husson, E., O. Hagner and F. Ecke. "Unmanned aircraft systems help to map aquatic vegetatio." *Applied Vegetation Science* (2014): 567-577.

Hwang, K. and M. Chen. *Big-Data Analytics for Cloud, IoT and Cognitive Learning*. Chichester, UK: John Willey and Sons, 2017.

IBM. *Big data: Big challenge or Big opportunity*. 2016. 14 7 2020. <https://www.ibm.com/watson/infographic/discovery/big-data-challenge-opportunity/>.

ICPDR. *Countries of the Danube River Basin*. n.d. 5 06 2019. <https://www.icpdr.org/main/danube-basin/countries-danube-river-basin>.

—. *TNMN - TransNational Monitoiring Network*. n.d. 01 06 2019. <http://www.icpdr.org/main/activities-projects/tnmn-transnational-monitoring-network>.

IGIF. *Integrated Geospatial Information Framework: A strategic guid to develop and strengthen national geospatial inforamtion management*. 10 1 2020. 15 7 2020. <https://ggim.un.org/meetings/GGIM-committee/8th-Session/documents/Part%201-IGIF-Overarching-Strategic-Framework-24July2018.pdf>.

Innamorati, C., et al. "Learning on the Edge: Explicit Boundary Handling in CNNs." *arXic:180503106.2018* . arXic, 2018.

INSPIRE HY. "Data Specification on Hydrography-Technical Guidelines." 2013. *INSPIRE.* 25 8 2017. <http://inspire.ec.europa.eu/documents/Data_Specifications/INSPIRE_DataSpecification_HY_v3.1.pdf>.

Isikdogan, F, J C Bovik and P Passalacqua. "Surface Water Mapping by Deep Learning." *IEEE JOURNAL OF SELECTED TOPICS IN APPLIED EARTH OBSERVATIONS AND REMOTE SENSING* (2017).

Isikdogan, F., A. Bovik and P. Passalacqua. "RivaMap: An automated river analysus and mapping engine." *Remote Sensing of Environment* (2017): 88-97.

ISO. "ISO 19100." n.d.

ISO/IEC, 2382:2015. *Information technology - vocabulary*. 2015. 30 7 2020. <https://www.iso.org/obp/ui/#iso:std:iso-iec:2382:ed-1:v1:en>.

IVJČ, Institut za vodoprivredu „Jaroslav Černi". *Strategija upravljanja vodama na teritoriji Republike Srbije*. Beograd: Institut za vodoprivredu „Jaroslav Černi", 2016.

J.A.D, Gomez., C, A Alonso and A.A Garcia. "Remote sensing as a tool for monitoring water quality parameters for Mediterranean Lakes of European Union water framework directive (WFD) and as a system of surveillance of cyanobacterial harmful algae blooms (SCyanoHABs)." *Environ Monit Assess* (2011).

Jakovljević , Gordana, Miro Govedarica and Flor Álvarez-Taboada. "Waterbody mapping: a comparison of remotly sensed and GIS open data sources." *Internationa Journal of Remote Sensing* (2018).

Jakovljević, G. and M. Govedarica. "Water Body Extraction and Flood Risk Assessment Using Lidar and Open Data." *Climate Change Adaptation in Eastern Europe*. Springer, Cham, 2019. 93-111.

Jakovljevic, G., M. Govedarica and F. Alvarez Taboada. "Remote Sensing Data in Mapping Plastic at Surface Water Bodies." *FIG Working Week 2019 Geospatial Information for A Smarter Life and Environmental Resilience*. Hanoi: FIG, 2019.

Jakovljević, G., M. Govedarica and F. Álvarez-Taboada. "Assessment of biological and physic chemical water quality parameters using Landsat 8 time series." *Proc. SPIE 10783, Remote Sensing for Agriculture, Ecosystems, and Hydrology XX*. Berlin: SPIE, 2018.

Jambeck, J.R., et al. "Challenges and emerging solutions to the land-based plastic waste issue in Africa." *Marine Policy* (2018): 256-263.

Jambeck, Jenna R, et al. "Plastic waste inputs from land into the ocean." *Science* (2015): 768–771.

Japitana, M.V. and M.E.C. Burc. " Satellite-basedRemote Sensing Technique for Surface Water Quality Estimation ." *Engineering, Technology & Applied Science Research* (2019): 3965-3970.

Japkowicz, N. and S. Stephen. "The class imbalance problem: A systematic study." *Intell. Data Anal. J.* (2002): 429–450.

Jeong, S.G., et al. "Mapping riparian habitat using a combination of remote-sensing techniques." *International Journal of Remote Sensing* (2016): 1069-1088.

Ji, L, et al. "Target Detection Method for Water Mapping Using Landsat 8 OLI/TIRS Imagery." *Water* (2015): 794–817.

Ji, L., et al. "Improving the Accuracy of the Water Surface Cover Type in the 30 m FROM-GLC Product." *Remote Sens.* (2015): 13507–13527.

Ji, L., L. Zhang and B. Wylie. "Analysis of Dynamic Thresholds for the Normalized Difference Water Index." *Photogrammetric Engineering and Remote Sensing* (2009): 1307–1317.

Johansen, K, et al. "Automatic Geographic Object Based Mapping of Streambed and Riparian Zone Extent from LiDAR Data in a Temperate Rural Urban Environment, Australia." *Remote Sens.* (2011): 1139-1156.

—. "Mapping riparian condition indicators in a sub-tropical savanna environment from discrete return LiDAR data using object-based image analysis." *Ecological Indicators* (2010): 796–807.

Johansen, K., S. Phinn and C. Wite. "Mapping of riparian zone attributes using discrete return LiDAR, QuickBird and SPOT-5 imagery: Assessing accuracy and costs." *Remote Sensing of Environment* (2010): 2679-2691.

Johnson, B. and K. Iizuka. "Integrating OpenStreetMap Crowdsourced Data and Landsat Time Series Imagery for Rapid Land Use/Land Cover (LULC) Mapping: Case Study of the Laguna De Bay Area of the Philippines." *Applied Geography* (2016): 140–149.

Joksić, D. and B. Bajat. "Elements of spatial data quality as information technology support for sustainable development planning." *Spatium* (2004): 77-83.

Jones, H.G. and Vaughan R.A. *Remote sensing of vegetation: Principles, techniques, and applications*. Oxford : Oxford University Press, 2010.

Joshi, I, et al. "Turbidity in Apalachicola Bay, Florida from Landsat 5 TM and Field Data: Seasonal Patterns and Response to Extreme Events." *Remote Sens.* (2017).

Jupyter. *Jupyter*. n.d. 01 06 2019. <https://jupyter.org/>.

Kanno, A and Y Tanaka. "Modified Lyzenga's Method for Estimating Generalized Coefficients of Satellite-Based Predictor of Shallow Water Depth." *IEEE GEOSCIENCE AND REMOTE SENSING LETTERS* (2012).

Kannoji, S.P. and G. Jaiswal. "Effects of Varying Resolution on Performance of CNN based Image Classification: An Experimental Study." *Int. J. Comput. Sci. Eng.* (2018): 451–456.

Kaplan, G. and U. Avdan. "Object-Based Water Body Extraction Model Using Sentinel-2." *European Journal of Remote Sensing* (2017): 137-143.

Karpatne, A, et al. "Global Monitoring of Inland Water Dynamics: State-of-the-Art, Challenges, and Opportunities." *Computational Sustainability, Studies in Computational Intelligence 645*. Cham: Springer International Publishing Switzerland , 2016. 121-147.

Kavzgoul, T. "Increasing the accuracy of neural network classification using refined training data. ." *Environ. Model. Softw.* (2009): 850–858.

Kay, S., J. Hedley and S. Lavender. "Sun Glint Correction of High and Low Spatial Resolution Images of Aquatic Scenes: A Review of Methods for Visible and Near-Infrared Wavelengths ." *Remote Sens.* (2009).

Ke, Y., L.J. Quackenbush and J. Im. "Synergistic use of QuickBird multispectral imagery and LIDAR data for object-based forest species classification." *Remote Sens. Environ.* (2010): 1141-1154.

Keith, D.J, R Lunetta and B.A Schaeffer. "Optical Models for Remote Sensing of Colored Dissolved Organic Matter Absorption and Salinity in New England, Middle Atlantic and Gulf Coast Estuaries USA." *Remote Sens.* (2016).

Kendall, A., V. Badrinarayanan and R. Cipolla. "Bayesian SegNet: Model Uncertainty in Deep Convolutional Encoder-Decoder Architectures for Scene Understanding." *arXiv: 1511.02680v2*. arXiv, 2016.

Kim, Y.H., et al. "Application of satellite remote sensing in monitoring dissolved oxygen variabilities: A case study for coastal waters in Korea." *Environment International* (2020).

Kingma, D.P. and J. Adam: Ba. "A Method for Stochastic Optimization." *arXiv*. arXiv:1412.6980v9, 2015.

Kinzel, P.J, C.J Legleiter and J.M Nelson. "Mapping River Bathymetry With a Small Footprint Green LiDAR: Application and challengdes." *Journala of the American water resources association* (2012).

Koedsin, W, et al. "An Integrated Field and Remote Sensing Method for Mapping Seagrass Species, Cover, and Biomass in Southern Thailand." *Remote Sens.* (2016).

Kooi, M., et al. "The effect of particle properties on the depth profile of buoyant plastics in the ocean." *Sci. Rep.* (2016).

Krasnopolsky, V.M., W.H. Gemmill and L.C. Breaker. "A neural network multipara meter algorithm for SSM/I ocean retrievals: Comparisons and validations." *Remote Sens. Environ.* (2000): 133-142.

Krizhevsky, A., I. Sutskever and G.E. Hinton. "ImageNet classification with deep convolutional neural networks." *Proceedings of the Advances in Neural Information Processing Systems*. Lake Tahoe, 2012. 1097–1105.

Kubat, M. and S. Matwin. "Addressing the curse of imbalanced training sets: One-sided selection." *Proceedings of the 14th International Conference on Machine Learning (ICML)*. Nashville , 1997. 179–186.

Kuenzer, C, et al. "Flood mapping and flood dynamics of the Mekong Delta: ENVISAT-ASAR-WSM based time series analyses." *Remote Sensing* (2013): 687-715.

Kutsar, T, et al. "Estimating lake carbon fractions from remote sensing data." *Remote Senisng of Environment* (2014).

Lagkvist, M., et al. "Classification and Segmentation of Satellite Orthoimagery Using Convolutional Neural Networks." *Remote Sens.* (2016).

Lague, D., N. Brodu and J. Leroux. "Accurate 3D comparison of complex topography with terrestrial laser scanners. Application to the Rangitikei canyon." *J. Photogramm. Remote Sens.* (2013): 10–26.

Laney, Doug. *3D Data Manafement: Controlling Data Volume, Valocity and Variety*. Stamford: Meta Group Inc, 2001.

Larsin, M, et al. "Multi-depth suspended sediment estimation using high resolution remote-sensing UAV in Maumee River, Ohio, ." *INTERNATIONAL JOURNAL OF REMOTE SENSING* (2018).

Lasier, M., L. Hubert-Moy and S. Dufour. "Mapping Riparian Vegetation Functions Using 3D Bispectral LiDAR Data." *Water* (2019).

Lebreton, L., et al. "River plastic emissions to the world's oceans." *Nat. Commun.* (2017).

Lee, J.S. "Refined filtering of image noise using local statistics." *Comput. Graph. Image Process* (1981): 380–389.

Lee, Z. P., K. L. Carder and R. A. Arnone. "Deriving inherent optical properties from water color: a multiband quasi-analytical algorithm for optically deep waters." *Applied Optics* (2002): 5755-5772.

Li, B. Y., H. Zhang and F. J. Xu. "Water Extraction in High Resolution Remote Sensing Image Based on Hierarchical Spectrum and Shape Features." *35th International Symposium on Remote Sensing of Environment*. 2014.

Li, J, X Huang and J Gong. "Deep neural network for remote-sensing image interpretation: status and perspectives." *National Science Review* (2019): 1082-1086.

Li, R., et al. "DeepUNet: A Deep Fully Convolutional Network for Pixel-level Sea-Land Segmentation ." *arXiv:1709.00201v1*. arXiv, 2017.

Li, X., et al. "Deep-water bathymetric features imaged by spaceborne SAR in the Gulf Stream regionLi,." *Geophysical Research Letters* (2010).

Li, Y, et al. "A Deep Learning Method for Change Detection in Synthetic Aperture Radar Images." *IEEE Transactions on Geoscience and Remote Sensing*. 2019. 5751-5763.

Li, Y., P. Gong and T. Sasagawa. "Integrated Shadow Removal Based on Photogrammetry and Image Analysis." *International Journal Remote Sensing* (2005): 3911–3929 .

Liao, H-Y and T-H Wen. "Extracting urban water bodies from high-resolution radar images: Measuring the urban surface morphology to control for radar's double-bounce effect, ." *International Journal of Applied Earth Observation and Geoinformation* (2020).

Lim, J and M Choi. "Assessment of water quality based on Landsat 8 operational land imager associated with human activities in Korea." *Environ Monit Assess* (2015).

Liu, H, et al. "Application of Sentinel 2 MSI Images to Retrieve Suspended Particulate Matter Concentrations in Poyang Lake." *Remote Sens.* (2017).

Liu, J, et al. "Empirical Estimation of Total Nitrogen and Total Phosphorus Concentration of Urban Water Bodies in China Using High Resolution IKONOS Multispectral Imagery." *Water* (2015): 6551-6573.

Liu, X., et al. "The effect of LiDAR data density on DEM accuracy." *Proceedings of the International Congress on Modelling and Simulation (MODSIM07)*. Christchurch, 2007. 1363–1369.

Long, J., E. Shelhamer and T. Darrell. "Fully convolutional networks for semantic segmentation." *Proceedings of the IEEE Conference on Computer Vision and Pattern Recognition*. Boston: IEEE, 2015. 3431–3440.

Lu, S., et al. "Water Body Mapping Method with HJ-1A/B Satellite Imagery." *International Journal of Applied Earth Observation and Geoinformatics* (2011): 428–434.

Macfarlane, W.W., et al. "High-resolution riparian vegetation mapping to prioritize conservation and restoration in an impaired desert river." *Journal of the Society for ecological restoration* (2016).

MAEP, Ministry of Agriculture and Environmental Protecti. *Transposition and implementation of environmental and climate change acquis - chapter 27: status and plans*. Belgrade: MAEP, 2015.

Mahdianpari, M., B. Salehi and F., Motagh, M. Mahammadimanesh. "Random forest wetland classification using ALOS-2 L-band, RADARSAT-2 C-band, and TerraSAR-X imagery." *ISPRS Journal of Photogrammetry and Remote Sensing* (2017): 13-31.

Maillard, P., N. Bercher and S. Clamant. "New processing approaches on the retrieval of water levels in Envisat and SARAL radar altimetry over rivers: A case study of the São Francisco River, Brazil ." *Remote Sensing of Environment* (2015): 226-241.

Mancino, G., et al. "Assessing water quality by remote sensing in small lakes: the case study of Monticchio lakes in southern Italy." *iForest* (2009).

Mandanici, E. and G. Bitelli. "Preliminary Comparison of Sentinel-2 and Landsat 8 Imagery for a Combined Use." *Remote Sens* (2016).

Mandlburger, G, et al. "Topo-Bathymetric LiDAR for Monitoring River Morphodynamics and Instream Habitats—A Case Study at the Pielach River." *Remote Sens.* (2015): 6160-6195.

Mandlburger, G., et al. "Evaluation of a novel UAV-born topo-bathymetric laser profiles." *The International Archives of the Photogrammetry, Remote Sensing and Spatial Information Sciences*. Prague: ISPRE, 2016. 933-936.

Maneewongvatana, M. and D. Mount. "Analysis of Approximate Nearest Neighbor Searching with Clusterd Point Sets." *arXiv:cs/9901013v1*. arXiv:cs, 1999.

Mao, Y., et al. "An advanced distributed automated extraction of draining network model on high-resolution DEM." *Hydrol. Earth Syst. Sci.* (2014): 7741-7467.

Martin, C., et al. "Use of unnamed aerial vehicle for efficient beach litter monitoring." *Mar. Pollut. Bull.* (2018): 662–673.

Marz, N and J Warren. *Big data - Principles and best practices of scalable realtime data systems*. Manning, 2014.

Massonnet, D and J.C Souyris. *Imaging with Synthetic Aperture Radar*. EPFL Press, 2008.

Matthews, M.W., S. Bernard and K. Winter. "Remote sensing of cyanobacteriadominant algal blooms and water quality parameters in Zeekoevlei, a small hypertrophic lake, using MERIS." *Remote Sens. Environ.* (2010): 2070–2087.

Mayer, B. and A. Kylling. "Technical note: The libRadtran software package for radiative transfer calculations - description and examples of use." *Atmos. Chem. Phys.,* (2005): 1855-1877.

McEliece, R., et al. "Evaluation of Nearshore and Offshore Water Quality Assessment Using UAV Multispectral Imagery." *Remote Sens.* (2020).

McFeeters, S. "The Use of the Normalized Difference Water Index (NDWI) in the Delineation of Open Water Features." *International Journal Remote Sensing* (1996): 1425–1432.

McKean, J., et al. "Remote Sensing of Channels and Riparian Zones with a Narrow-Beam Aquatic-Terrestrial LIDAR." *Remote Sens.* (2009): 1065-1096.

McQueen, D.J., J.R. Post and E.L. Mills. "Trophic relationships in freshwater pelagic ecosystems. ." *Can. J. Fish. Aquat. Sci.* (1986): 1571–1581.

Michey, A., et al. "Classification of riparian forest species and health condition using multi-temporal and hyperspatial imagery from unmanned aerial system." *Environ Monit Assess* (2016): 188-146.

Michez, A, et al. "LiDAR derived ecological integrity indicators for riparian zones: Application to the Houille river in Southern Belgium/Northern France." *Ecological Indicators* (2013): 627-640.

Michez, A., et al. "Mapping of riparian invasive species with supervised classification of Unmanned Aerial System (UAS) imagery." *International Journal of Applied Earth Observation and Geoinformation* (2016): 88-94.

Minchew, B, C.E Jones and B Holt. "Polarimetric Analysis of Backscatter From the Deepwater Horizon Oil Spill Using L-Band Synthetic Aperture Radar." *IEEE TRANSACTIONS ON GEOSCIENCE AND REMOTE SENSING* (2012).

Ministry of Construction, Transport and Infrastructure. *International and interstate waterways in the Republic of Serbia*. n.d. 03 06 2019. <http://www.plovput.rs/international-waterways>.

Ministry of Foreign Affairs of the Republic Serbia. *Proces EU integracija i regionalna saradnja*. n.d. 27 02 2017. <http://www.mfa.gov.rs,>.

Molkov, A.A, et al. "Regional Models for High-Resolution Retrieval of Chlorophyll a and TSM Concentrations in the Gorky Reservoir by Sentinel-2 Imagery." *Remote Sens.* (2019).

Monegaglia, F., et al. "Automated extraction of meandering river morphodynamics from multitemporal remotely sensed data." *Environmental Modelling & Software* (2018): 171-186.

Monteys, X, et al. "Spatial Prediction of Coastal Bathymetry Based on Multispectral Satellite Imagery and Multibeam Data." *Remote Sens.* (2015): 13782-13806.

Mooney, P, P Corcoran and A. C Winstanley. "Towards Quality Metrics for OpenStreetMap." *In Proceedings of the 18th SIGSPATIAL International Conference on Advances in Geographic Information*. New York, 2010.

Morsy, S, A Shaker and A El-Rabbany. "Using Multispectral Airborne LiDAR Data for Land/Water Discrimination: A Case Study at Lake Ontario, Canada." *applied sciences* (2018).

Moy, K., et al. "Mapping coastal marine debris using aerial imagery and spatial analysis." *Mar. Pollut. Bull.* (2018): 52–59.

Munyazneza, O., et al. "Water level monitoring using radar remote sensing data: Application to Lake KIvu, central Africa." *Physucs and Chemistry of the Earth* (2009): 722-728.

Mushtaq, F and M.G Nee Lala. "Remote estimation of water quality parameters of Himalayan lake (Kashmir) using Landsat 8 OLI imagery." *Geocarto International* (2016).

Nair, V. and G.E. Hinton. "Rectified Linear Units Improve Restricted Boltzmann Machines." *Proceedings of the 27th International Conference on Machine Learning*. Haifa, 2010.

Nas, B, et al. "An Application of Landsat-5TM Image Data for Water Quality Mapping in Lake Beysehir, Turkey." *Water Air Soil Pollut* (2010): 183–197.

Nazeer, M., et al. "Evaluation of Empirical and Machine Learning Algorithms for Estimation of Coastal Water Quality Parameters." *ISPRS Int. J. Geo-Inf.* (2017).

Neis, P. *How did you contribute to OpenStreetMap?* 2015. 08 05 2015. <http://hdyc.neis-one.org/>.

NIST. *Nist Cloud Computing Program—NCCP*. 2012. 25 04 2020. <https://www.nist.gov/programs-projects/>.

Obida, C.B., et al. "River network delineation from Sentinel-1 SAR data." *Int J Appl Earth Obs Geoinformatics* (2019).

OECD. *Land cover in countries and regions*. n.d. 15 07 2019. <https://stats.oecd.org/Index.aspx?DataSetCode=LAND_COVER>.

Olmanson, L., M. Bauer and P. Brezonik. "A 20-Year Landsat Water Clarity Census of Minnesota's 10,000 Lakes." *Remote Sensing of Environment* (2008): 4086–4097.

Opfer, S., C. Arthur and S. Lippiatt. *NOAA Marine Debris Shoreline Survey Field Guide*. 2012. 25 05 2020. <https://marinedebris.noaa.gov/sites/default/files/ShorelineFieldGuide2012.pdf>.

OSM. *OpenStreetMap*. n.d. 15 07 2017. <https://www.geofabrik.de/geofabrik/openstreetmap.html,>.

OSPAR , commission. *Guideline for Monitoring Marine Litter on the Beaches in the OSPAR Monitoring Area*. n.d. 22 04 2020. <https://www.ospar.org/documents?v=7260>.

Palmer, S.C.J, et al. "Ultraviolet Fluorescence LiDAR (UFL) as a Measurement Tool for Water Quality Parameters in Turbid Lake Conditions." *Remote Sens.* (2013): 4405-4422.

Pashaei, M., et al. "Review and Evaluation of Deep Learning Architectures for Efficient Land Cover Mapping with UAS Hyper-Spatial Imagery: A Case Study Over a Wetland." *Remote sens.* (2020).

Pavelsky, T.M. and L.C. Smith. "RivWidth: A Software Tool for the Calculation of River Width From Remote Sensed Imagery." *IEEE Geoscience and Remote Sensing Letters* (2008).

Peerbhay, K., et al. "Mapping Solanum mauritianum plant invasions using WorldView-2 imagery and unsupervised random forests." *Remote Sens. Environ* (2016): 39–48.

Pe'eri, S., et al. "Satellite Remote Sensing as a Reconnaissance Tool for Assessing Nautical Chart Adequacy and Completeness." *Marin Geodesy* (2014): 293-314.

Penatti, O. A. B., K. Nogueira and J. A. dos Santos. "Do Deep Features Generalize from Everyday Objects to Remote Sensing and Aerial Scenes Domains?" *IEEE Conference on Computer Vision and Pattern Recognition Workshops (CVPRW)*. IEEE, 2015.

Peng, J., et al. "A review of methods for downscaling remotely sensed soil moisture." *Rev. Geophys.* (2017): 341–366.

Peterson, K.T, V. Sagan and J.J Sloan. "Deep learning-based water quality estimation and anomaly detection using Landsat-8/Sentinel-2 virtual constellation and cloud computing." *GISCIENCE & REMOTE SENSING* (2019).

Peterson, V. S. and J. J. Sloan. "Deep learning-based water quality estimation and anomaly detection using Landsat-8/Sentinel-2 virtual constellation and cloud computing." *GIScience & Remote Sensing* (2020).

Pham-Duc, B, C Prigent and F Aires. "Surface Water Monitoring within Cambodia and the Vietnamese Mekong Delta over a Year, with Sentinel-1 SAR Observations." *Water* (2017).

Philipson, P, et al. "Satellite-based water quality monitoring in Lake Vänern, Sweden." *International Journal of Remote Sesning* (2016): 3938-3960.

Pierdicca, N, et al. "Observing floods from space: Experience gained from COSMO-SkyMed observations. ." *Acta Astronaut.* (2013): 122–133.

Plastics Europe. *Plastics Europe*. n.d. 27 04 2020. <https://www.plasticseurope.org/application/files/9715/7129/9584/FINAL_web_version_Plastics_the_facts2019_14102019.pdf>.

Poinani, T.H., et al. "Potential of Collaborative Mapping for Disaster Relief : A Case Study of OpenStreetMap in the Nepal Earthquake 2015." *HICSS 2016 – Hawaii International Conferenc on System Sciences*. Kauai, 2015.

Politi, E, M.E.J Cutler and J.S Rowan. "Evaluating the spatial transferability and temporal repeatability of remote-sensing-based lake water quality retrieval algorithms at the European scale: a meta-analysis approach." *International Journal of Remote Sensing* (2015): 2995-3023.

Prathap, G. and I. Afanasyev. "Deep Learning Approach for Building Detection in Satellite Multispectral Imagery." *2018 International Conference on Intelligent Systems (IS)*. arXiv, 2018.

Pratomo, D.G., Khomsin and B. F. E. Putranto. "Analysis of the green light penetration from Airborne LiDAR Bathymetry in Shallow Water Area." *IOP Conference Series: Earth and Environmental Science*. IOP, 2019.

Program, United Nations Environment. *UN declares war ocean plastic*. n.d. 27 04 2020. <https://www.unenvironment.org/news-and-stories/press-release/un-declares-war-ocean-plastic-0>.

Prosek, J, et al. "Integration of hyperspectral and LiDAR data for mapping small water bodies." *Int J Appl Earth Obs Geoinformation* (2020).

Pu, R, et al. "Mapping and assessing seagrass along the western coast of Florida using Landsat TM and EO-1 ALI/Hyperion imagery." *Estuarine, Coastal and Shelf Science* (2012): 234-245.

Pushparaj, J. and A.V. Hegde. "Estimation of bathymetry along the coast of Mangaluru using Landsat-8 imagery." *Journal of Ocean and Climate: Science, Technology and Impacts* (2017).

Python. n.d. 01 06 2019. <https://www.python.org/>.

Qi, C., et al. " PointNet: Deep Learning on Pont Sets for 3D Classification and Segmentation." *arXiv:1612.00593v2*. arXiv, 2017.

Qin, L., et al. "A River Channel Extraction Method for Urban Environments Based on Terrain Transition Lines." *Water Resources Research* (2018).

Quang, N.H, et al. "Spatiotemporal Variation of Turbidity Based on Landsat 8 OLI in Cam Ranh Bay and Thuy Trieu Lagoon, Vietnam." *Water* (2017).

Rashidi, P. and H. Rastiveis. "Extraction of ground points from LiDAR data based on slope and progressive window thresholding (SPWT). ." *Earth Obs. Geomat. Eng.* (2018): 36–44.

Ren, S., et al. "Faster R-CNN: Towards Real-Time Object Detection with Region Proposal Network." *arXiv:150601497*. arXiv, 2015.

Ribic, C.A., T.R. Dixon and I. Vining. " Marine Debris Survey Manual." NOAA Tech. Rep. 1992.

Richter, R. and D. Schläpfer. *Atmospheric/Topographic Correction for Satellite Imagery: ATCOR-2/3 UserGuide*. Wessling, Germany: DLR, 2011.

Ridolfi, E. and P. Manciola. "Water Level Measurements from Drones: A Pilot Case Study at a Dam Site ." *Water* (2018).

Rittinghouse, J. W. and J. F. Ransome. *Cloud Computing Implementation, Management and Security*. Boca Raton: CRC Press, 2010.

Rizaldy, A., et al. "Ground and Multi-Class Classification of Airborne Laser Scanner Point Clouds Using Fully Convolutional Networks." *Remote Sens.* (2018).

Rokni, K., et al. "A New Approach for Surface Water Change Detection: Integration of Pixel Level Image Fusion and Image Classification Techniques ." *International Journal Od Applied Earth Observation and Geoinformation* (2015): 226-234.

—. "Water Feature Extraction and Change Detection Using Multitemporal Landsat Imagery." *Remote Sensing* (2014): 4173–4189.

Ronneberger, O., P. Fischer and T. Brox. "U-Net: Convolutional Networks for Biomedical Image Segmentation." *In International Conference on Medical Image Computing and Computer-Assisted Intervention*. Cham: Springer, 2015. 234-241.

Russakovsky, O., et al. "ImageNet Large Scale Visual Recognition Challenge." *arXiv:1409.0575v3*. arXiv, 2015.

Sabater, S., et al. "Longitudinal development of chlorophyll and phytoplankton assemblages in a regulated large river (the Ebro River)." *Science of the Total Environment* (2008): 196–206.

Sakuno, Y, et al. "Evaluation of Unified Algorithms for Remote Sensing of Chlorophyll-a and Turbidity in Lake Shinji and Lake Nakaumi of Japan and the Vaal Dam Reservoir of South Affrica under Eutriophic and Ultra-Turbid Conditions." *Water* (2018).

Salach, A., et al. "Accuracy Assessment of Point Clouds from LiDAR and Dense Image Matching Acquired Using the UAV Platform for DTM Creation." *ISPRS Int. J. Geo-Inf.* (2018).

Santoro, M., et al. "Strengths and Weaknesses of Multi-Year Envisat ASAR Backscatter Measurements to Map Permanent Open Water Bodies at Global Scale." *Remote Sensing Environment* (2015): 185–201.

SATIMG, (Satellite Images). n.d. 14 8 2018. <http://www.satimagingcorp.com/satellitesensors/>.

Schelhorn, S.J., et al. "Identifying Elements at Risk from OpenStreetMap: The Case of Flooding." *11th International ISCRAM Conference*. Pennsylvania, 2014.

Schmidt, A., F. Rottensteiner and U. Sorgel. "Classification of airborne laser scanning data in Wadden Sea areas using Conditional Random Fields." *International Archives of the Photogrammetry, Remote Sensing and Spatial Information Sciences*. Melbourne: ISPRS, 2012. 161-166.

Schmidt, C., T. Krauth and S. Wagner. "Export of Plastic Debris by Rivers into the Sea." *Environ. Sci. Technol.* (2017): 12246–12253.

Schuegraf, P. and K. Bittner. "Automatic Building Footprint Extraction from Multi-Resolution Remote Sensing Images Using a Hybrid FCN." *ISPRS Int. J. Geo-inf.* (2019).

Schultz, Jeff. *How Much Data is Created on the Internet Each Day?* 8 6 2019. 14 7 2020. <https://blog.microfocus.com/how-much-data-is-created-on-the-internet-each-day/#:~:text=The%20Amount%20of%20Data%20Created%20Each%20Day%20on%20the%20Internet%20in%202019&text=That%20number%20grew%20to%203.4,million%20internet%20users%20were%20added.>.

Schwenk, J., et al. "High spatio-temporal resolution of river platform dynamics from Landsat: the RivMAP toolbox and results from ucayali river." *Earth and Space Sci.* (2016).

Sehira, S., J. Singh and H. Singh Rai. "Assessing the Topologic Consistency of Crowdsourced OpenStreetMap Data." *Human Computation* (2014): 267-282.

Servigne, S., et al. " A Methodology for Spatial Consistency Improvement of Geographic Databases." *GeoInformatica* (2000): 7-34.

Seyhan, E and A Dekker. "Application of remote sensing techniques for water quality monitoring." *Hydrobiol.Bull.* (1986): 41-50.

Shen, F. and W. Verhoef. "Suppression of local haze variations in MERIS images over turbid coastal waters for retrieval of suspended sediment concentration." *Optics Express* (2010): 12653-12662.

Shi, W and M Wang. "An assessment of the black ocean pixel assumption for MODIS SWIR bands. ." *Remote Sensing of Environment* (2009): 1587–1597.

Sieburth, J.M. and J.T. Conover. "Slicks associated with Trichodesmium Blooms in the Sargasso Sea." *Nature* (1965): 830-831.

Siles, G., et al. "Hydrological monitoring of high-latitude shallow water bodies from high-resolution space-borne D-InSAR." *Remote Sensing of Environment* (2020).

Simon, R.N, T Tormos and Danis P.-A. "Very high spatial resolution optical and radar imagery in tracking water level fluctuations of a small inland reservoir." *International Journal of Applied Earth Observation and* (2015): 36-39.

Simonyan, K. and A. Zisserman. "Very Deep Convolution Networks for Large-Scale Image Recognition." *arXiv:1409.1556v6*. arXiv, 2015.

sklearn. preprocessing. StandardScaler. . n.d. 1 7 2019. < https://scikit-learn.org/stable/modules/generated/sklearn.preprocessing.StandardScaler.html>.

Sl.glasnik RS br. 50/2012. *Uredba o graničnim vrednostima zagađujućih materija u površinskim i podzemnim vodama i sedimentu i rokovima za njihovo dostizanje*. Beograd: Sl.glasnik RS, 2012.

Sl.glasnik RS br. 74/2011. *Pravilnik o parametrima ekološkog i hemijskog statusa površinskih voda i parametrima hemijskog i kvantitativnog statusa podzemnih voda,*. Beograd: Sl.glasnik RS, 2011.

Sl.glasnik SRS, br.5/68. "Uredba o klasifikaciji voda,." 1986.

Smeeckaert, J, et al. "Large-scale water classification of coastal areas using airborne topographic LiDAR data." *IEEE International Geoscience and Remote Sensing Symposium*. Melbourne, Australia: VIC, 2013.

Smith, M.W., J.L. Carrivick and D.J. Quincey. "Structure from motion photogrammetry in physical geography." *Prog. in Phys. Geogr.* (2015): 1-29.

Sofman, B., et al. " Terrain Classification from Aerial Data to Support Ground Vehicle Navigation." 2003. 2 5 2019. <https://pdfs.semanticscholar.org/e94d/f03ec54e1c5b42c4ac50d4c8667d2e8cad6a.pdf?_ga=2.53795883.209>.

Song, H.S., Y.H. Kim and Y.I. Kim. "A Patch-Based Light Convolutional Neural Network for Land-Cover Mapping Using Landsat-8 Images." *Remote Sens.* (2019).

Song, K.S, et al. "Water quality monitoring using Landsat Themate Mapper data with empirical algorithms in Chagan Lake." *China. J. Appl. Remote Sens.* (2011): 1-16.

Stefan, S, et al. " Flood detection from multi-temporal SAR data using harmonic analysis and change detection. ." *Int. J. Appl. Earth Obs. Geoinf.* (2015): 15-24.

Strasser, T. and S. Lang. "Object-based class modelling for multi-scale riparian forest habitat mapping." *International Journal of Applied Earth Observation and Geoinformation* (2014).

Stumpf, R.P., Holderied, K. and M. Sinclair. "Determination of water depth with high-resolution satellite imagery over variable bottom types." *Limnology and Oceanography* (2003): 547–556.

Su, T.-C. "A study of a matching pixel by pixel (MPP) algorithm to establish an empirical model of water quality mapping, as based on unmanned aerial vehicle (UAV) images." *International Journal of Applied Earth Observation and Geoinformation* (2017): 213-224.

Su, T-C and H-T Chou. "Application of Multispectral Sensors Carried on Unmanned Aerial Vehicle (UAV) to Trophic State Mapping of Small Reservoirs: A Case Study of Tain-Pu Reservoir in Kinmen, Taiwan." *Remote Sens.* (2015): 10078-10097.

Sun, D, et al. "Detection of Total Phosphorus Concentrations of Turbid Inland Waters Using a Remote Sensing Method." *Water Air Soil Pollut* (2014).

Sun, D, Y Li and Q Wang. "A Unified Model for Remotely Estimating Chlorophyll a in Lake Taihu, China, Based on SVM and In Situ Hyperspectral Data." *IEEE transactions on geoscience and remote sensing* (2009).

Sun, Y., A.K. Wong and M.S. Kamel. "Classification of imbalanced data: A review." *Int. J. Pattern Recognit. Artif. Intell.* (2009): 687–719.

Swan, B. and R. Griffin. "A LiDAR–optical data fusion approach for identifying and measuring small stream impoundments and dams." *Transactions in GIS* (2019).

Szegedy, C., et al. "Going Deeper with Convolutions." *Proceedings of the IEEE Conference on Computer Vision and Pattern Recognition*. Boston: IEEE, 2015. 1-9.

—. "Inception-4, Inception-ResNet and the impact of residual connections on learning." *Proceedings of the Thirty-First AAAI Conference on Artificial Intelligence*. San Francisco, 2017.

Teo, T.A and C.H Huang. "Object-Based Land Cover Classification Using Airborne Lidar and Different Spectral Images." *Terr. Atmos. Ocean. Sci.* (2016): 491-504.

Teo, T.A. and C.H. Huang. "Object-Based Land Cover Classification Using Airborne Lidar and Different Spectral Images." *Terr. Atmos. Ocean. Sci.* (2016): 491-504.

Tetteh, G. and Schonert. M. "Automatic Generation of Water Masks from RapidEye Images." *Journal of Geoscience and Environment Protection* (2015): 17–23.

The guardian. *Terrawatch: the rivers taking plastic to the oceans*. n.d. 27 04 2020. <https://www.theguardian.com/science/2017/nov/05/terrawatch-the-rivers-taking-plastic-to-the-oceans>.

Thi Thu Ha, N, et al. "Selecting the Best Band Ratio to Estimate Chlorophyll-a Concentration in a Tropical Freshwater Lake Using Sentinel 2A Images from a Case Study of Lake Ba Be (Northern Vietnam)." *ISPRS Int. J. Geo-Inf.* (2017).

Thomas, I.A., et al. "Defining optimal DEM resolutions and point densities for modelling hydrologically sensitive areas in agricultural catchments dominated by microtopography. ." *Int. J. Appl. Earth Obs. Geoinf.* (2017): 36-44.

Topaloglu, R. H., E. Sertel and Musaoglu. " Assessment of Classification Accuracies of Sentinel 2 and Landsat 8 data for Land Cover/Use Mapping." *The International Arhives on Photogrammetry, Remote Sesning and Spatial Information Science* . Prague: ISPRS, 2016.

Topouzelis, K., A. Papakonstantinou and S.P. Garaba. "Detection of floating plastics from satellite and unmanned aerial systems (Plastic Litter Project 2018). ." *Int. J. Appl. Earth Obs. Geoinf.* (2019): 175–183.

Transposition and implementation of environmental and climate change acquis-chapter 27: status and plans. Beograd, 2015.

Trimble. *eCognition*. n.d. 12 01 2020. <http://www.ecognition.com/>.

TWG-HY, INSPIRE Thematic Working Group Hydrography. "INSPIRE Data Specification for the spatial data theme Hydrography." 2014.

Umar, M, B.L Rhoads and J Greenberg. "Use of multispectral satellite remote sensing to assess mixing of suspended sediment downstream of large river confluence." *Journal of Hydrology* (2018).

UN GGIM. "Future trends in geospatial information management: the five to ten years vision." 2020.

UN. "Transforming out world: The 2030 Agenda for Susatainable Development A/RES/70/1." 2015.

UNEP, United Nations Environment Program. *The state of plastic*. n.d. 27 04 2020. <https://wedocs.unep.org/bitstream/handle/20.500.11822/25513/state_plastics_WED.pdf?isA ll owed=y&sequence=1>.

UNEP, United Nations Environment Programme. *A Snapshot of the World's Water Quality: Towards a global assessment*. Nairobi, Kenya.: United Nations Environment Programme, 2016.

UNESC, United Nations Economic and Social Council. "Progress towards the Sustainable Development Goals." 2020.

UNESCO, UNWP. "Is wastewater the new black gold? Launch of the United Nations World Water Development Report ." 2017.

UNGA, United Nations General Assembly. "Resolution 64/292. The human right to water and sanitation." 2010. 4 7 2020. <https://undocs.org/pdf?symbol=en/a/res/64/292>.

UNICEF. *Topic: Water and sanitation: Drinking-water*. April 2019. 6 7 2020. <https://data.unicef.org/topic/water-and-sanitation/drinking-water/>.

UNSD, United Nations Sustainable Development. *Agenda 21*. Rio de Janerio, 1992.

UN-Water, UNESCO. *United Nations World Water Development Report 2020:Water and Climate Change*. Paris: UNESCO, 2020.

USGS. *Landsat 4-7 Collection 1 Surface Reflectance Code LEDAPS Product Guide*. n.d. 01 06 2019. <https://www.usgs.gov/media/files/landsat-4-7-collection-1-surface-reflectance-code-ledaps-product-guide>.

—. *Landsat Acquisition Tool*. n.d. 08 08 2020. <https://landsat.usgs.gov/landsat_acq>.

Verpoorter, C., et al. "A Global Inventory of Lakes Based on High-Resolution Satellite Imagery." *Geophysical Reasearch Letters* (2014): 6392–6402.

Verpoorter, C., T. Kutser and L. Tranvik. "Automated Mapping of Water Bodies Using Landsat Multispectral Data." *Limnology and Oceanography: Methods* (2012): 1037–1050.

Vickers, H., E. Malnes and K.-A. Hogda. "Long-Term Water Surface Area Monitoring and Derived Water Level Using Synthetic Aperture Radar (SAR) at Altevatn, a Medium-Sized Arctic Lake." *Remote Sens.* (2019).

Villa, A., J. Folster and K. Kyllmar. "Determining suspended solids and total phosphorus from turbidity: comparison of high-frequency sampling with conventional monitoring methods." *Environ Monit Assess* (2019).

Vinh Pham, Q, et al. "Using Landsat-8 Images for Quantifying Suspended Sediment Concentration in Red River (Northern Vietnam)." *Remote Sens.* (2018).

Wang, C-K and W.D Philpot. "Using airborne bathymetric lidar to detect bottom type variation in shallow waters." *Remote Sensing of Environment* (2007): 123-135.

Wang, F., S. Wang and Y. Zhou. "A Study of 6S Model Used for Atmospheric Correction of MODIS Image over Taihu Lake." *International Conference on Multimedia Technology*. 2011.

Wang, G, et al. "Monitoring cyanobacteria-dominant algal blooms in eutrophicated Taihu Lake in China with synthetic aperture radar images." *Chinese Journal of Oceanology and Limnology* (2015): 139-148.

—. "Water Identification from High-Resolution Remote Sensing Images Based on Multidimensional Densely Connected Convolutional Neural Networks." *Remote Sens* (2020).

Wang, L., et al. "Dynamic Inversion of Inland Aquaculture Water Quality Based on UAVs-WSN Spectral Analysis." *Remote Sens.* (2019).

Wang, Y, et al. "An Urban Water Extraction Method Combining Deep Learning and Google Earth Engine." *IEEE Journal of Selected Topics in Applied Earth Observations and Remote Sensing* (2020).

Wang, Y., et al. "Dense Semantic Labeling with Atrous Spatial Pyramid Pooling and Decoder for High-Resolution Remote Sensing Imagery." *Remote Sens.* (2019).

WDI, World Development Indicators. 2014. 7 5 2020. <http://datatopics.worldbank.org/world-development-indicators/themes/environment.html#water-and-sanitation_1>.

Webster, T. "Flood Risk Mapping Using LiDAR for Annapolis Royal, Nova Scotia, Canada." *Remote Sensing* (2010): 2060-2082.

Webster, W, et al. "Optimization of Data Collection and Refinement of Post-processing Techniques for Maritime Canada's First Shallow Water Topographic-bathymetric Lidar Survey." *Journal of coastal research* (2016): 31-43.

Weinmann, M., C. Mallet and N. Jutzi. " Involving different neighborhood types for the analysis of low-level geometric 2D and 3D features and their relevance for point cloud classification." *37. Wissenschaftlich-Technische Jahrestagung der DGPF*. Wurzburg: German Society for Photogrammetry, Remote Sensing and Geoinformation, 2017.

Westoby, M.J., et al. "Structure-from-motion' photogrammetry: A low-cost, effective tool for geoscience applications." *Geomorphology* (2012): 300-314.

Wiehle, S., A. Pleskachevsky and C. Gebhardt. "Automatic bathymetry retrieval from SAR images." *CEAS Space Journal* (2019): 105-114.

Wieldand, M., S. Martinis and Y. Li. "Semantic segmentation of water bodies in multi-spectral satellite images from situational awareness in emergency respons." *The International Archives*

of the Photogrammetry, Remote Sensing and Spatial Information Sciences. Muninch: ISPRS, 2019. 273-277.

Wikipedia. n.d. 22 1 2018. < https://sr.wikipedia.org/sr-el/%D0%91%D0%BE%D1%81%D1%83%D1%82_(%D1%80%D0%B5%D0%BA%D0%B0>.

WISE GIS Guidance. "Guidance on the reporting of spatial data to WISE." 2016.

Worrall, Les. *Spatial Analysis and Spatial Policy Using Geographic Information Systems*. London: Belhaven Press, 1991.

Wu, C, et al. "Empirical estimation of total phosphorus concentration in the mainstream of the Qiantang River in China using Landsat TM data." *International Journal of Remote Sensing* (2010): 2309-2324.

Wu, T., et al. "High-efficient extraction of drainage networks from digital elevation models constrained by enhanced flow enforcement from known river maps." *Geomorphology* (2019): 184-201.

WWAP, United Nations World Water Assessment Programme. *The United Nations World Water Development Report 2015: Water for a Sustainable World*. Paris: UNESCO, 2015.

Xie, H., et al. "Automated Subpixel Surface Water Mapping from Heterogeneous Urban Environments Using Landsat 8 OLI Imagery." *Remote Sensing* (2016).

Xie, S., et al. "Aggregated Residual Transformations for Deep Neural Network." *Proceedings of the IEEE Conference on Computer Vision and Pattern Recognition (CVPR)*. IEEE, 2017.

Xiong, J, et al. "Remote Sensing Estimation of Lake Total Phosphorus Concentration Based on MODIS: A Case Study of Lake Hongze." *Remote Sens.* (2019).

Xu, Y., et al. " Building Extraction in Very High Resolution Remote Sensing Imagery Using Deep Learning and Guided Filters." *Remote Sens.* (2018).

Yan, K., et al. " A review of low-cost space-borne data for flood modelling: topography, flood extent and water level." *Hydrological Processes* (2015): 3368-3387.

Yan, W.Y., A. Shaker and P.E. LaRocque. "Scan Line Intensity-Elevation Ratio (SLIER): An Airborne LiDAR Ratio Index for Automatic Water Surface Mapping." *Remote Sens.* (2019).

Yang, X. and L Chen. "Evaluation of Automated Urban Surface Water Extraction from Sentinel-2A Imagery Using different water indicies." *Journal Applications Remote Sensing* (2017).

Yang, X., et al. "Mapping of Urban Surface Water Bodies from Sentinel-2 MSI Imagery at 10 M Resolution via NDWI-Based Image Sharpening." *Remote Sensing* (2017).

—. "RivWidthCloud: An Automated Google Earth Engine Algorithm for River Width Extraction From Remotely Sensed Imagery." *IEEE Geoscience and Remote Sensing Letter* (2020): 217-221.

Yao, F., et al. "High-Resolution Mapping of Urban Surface Water Using ZY-3 Multi-Spectral Imagery." *Remote Sensing* (2015).

Yeu, Y., et al. "Evaluation of the Accuracy of Bathymetry on the Nearshore Coastlines of Western Korea from Satellite Altimetry, Multi-Beam, and Airborne Bathymetric LiDAR." *Sensor* (2018).

Yi, Y., et al. " Semantic Segmentation of Urban Buildings from VHR Remote Sensing Imagery Using a Deep Convolutional Neural Network." *Remote Sens.* (2019).

Yomwan, P, et al. "A study of waterborne diseases during flooding using Radarsat-2 imagery and a back propagation neural network algorithm." *Geomatics, Natural Hazards and Risk* (2013): 289-307.

Yoon, G.-W., et al. "Measurement of the water level in reservoirs from TerraSAR-X interferometry and amolitude images." *Remote Sensing Letters* (2013): 446-454.

Yosinski, J., et al. "How transferable are features in deep neural networks? ." *Advances in Neural Information Processing Systems 27 (NIPS '14)*. Montreal: NIPS Foundation, 2014.

Yousefi, S., et al. " Effects of an extreme flood on river morphology (case study: Karoon River, Iran)." *Geomorphology* (2018): 413-426.

Yu, F. and V. Koltun. "Multi-scale context aggregation by dilated convolution. ." *arXiv:1511.07122*. arXiv, 2016.

Yu, L, et al. "Convolutional Neural Networks for Water Body Extraction From Landsat Imagery." *International Journal of Computational Intelligence and Applications* (2017).

Yu, X., et al. "Deep learning in remote sensing scene classification: a data augmentation enhanced convolutional neural network framework." *GIScience and Remote Sensing* (2018).

Yuan, J, et al. "Automatic Extraction of Supraglacial Lakes in Southwest Greenland during the 2014–2018 Melt Seasons Based on Convolutional Neural Network." *Water* (2020).

Zaidi, A.Z., et al. "Indus river water level monitoring using satellite radar altimetry." *Advances in Space Reaserach* (2020).

Zhang, M., et al. "The backscattering characteristics of wetland vegetation and water-levle changes detection using multi-mode SAR: A case study." *International Journal of Applied Earth Observation and Geoinformation* (2016): 1-13.

Zhang, Y, et al. "Water Quality Retrievals From Combined Landsat TM Data and ERS-2 SAR Data in the Gulf of Finland." *IEEE TRANSACTIONS ON GEOSCIENCE AND REMOTE SENSING* (2003).

Zhang, Y., et al. "An Improved Boundary-Aware Perceptual Loss for Building Extraction from VHR Images." *Remote Sens.* (2020).

Zhao, H., et al. "Pyramid Scene Parsing Network." *arXiv:1612.011052v2*. arXiv, 2017.

Zhao, J, et al. "Shallow Water Measurements Using a Single Green Laser Corrected by Building a Near Water Surface Penetration Model." *Remote Sens.* (2017).

Zhao, X., et al. "Use of Unmanned Aerial Vehicle Imagery and Deep Learning UNet to Extract Rice Lodging." *Sensors* (2019).

Zhao, Y., et al. "Assessment of water quality in Baiyangdian Lake using multivariate statistical techniques." *Proc Environ Sci* (2012): 1213–1226.

Zheng, Z, et al. "Remote sensing of diffuse attenuation coefficient patterns from Landsat 8 OLI imagery of turbid inland waters: A case study of Dongting Lake." *Science of the Total Environment* (2016): 39-54.

Zhou, Z., et al. "UNet++: Redesigning Skip Connections to Exploit Multiscale Features in Image Segmentation." *IEEE Trans. Med. Imaging* (2020).

Zolfaghari, K and C.R Duguay. "Estimation of Water Quality Parameters in Lake Erie from MERIS Using Linear Mixed Effect Models." *Remote Sens.* (2016).

Appendix A
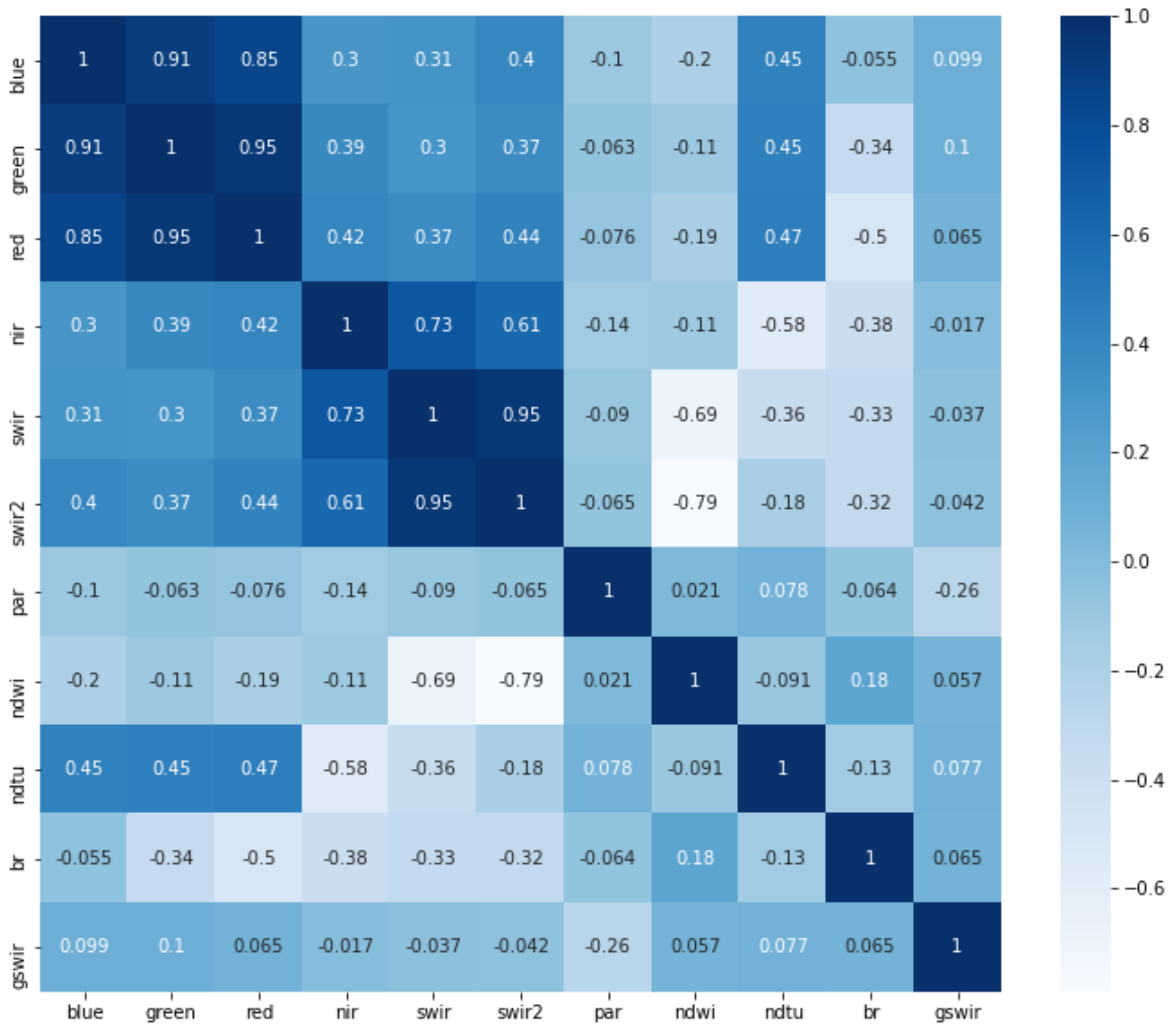
Figure 1A. Correlation matrix for chl-a
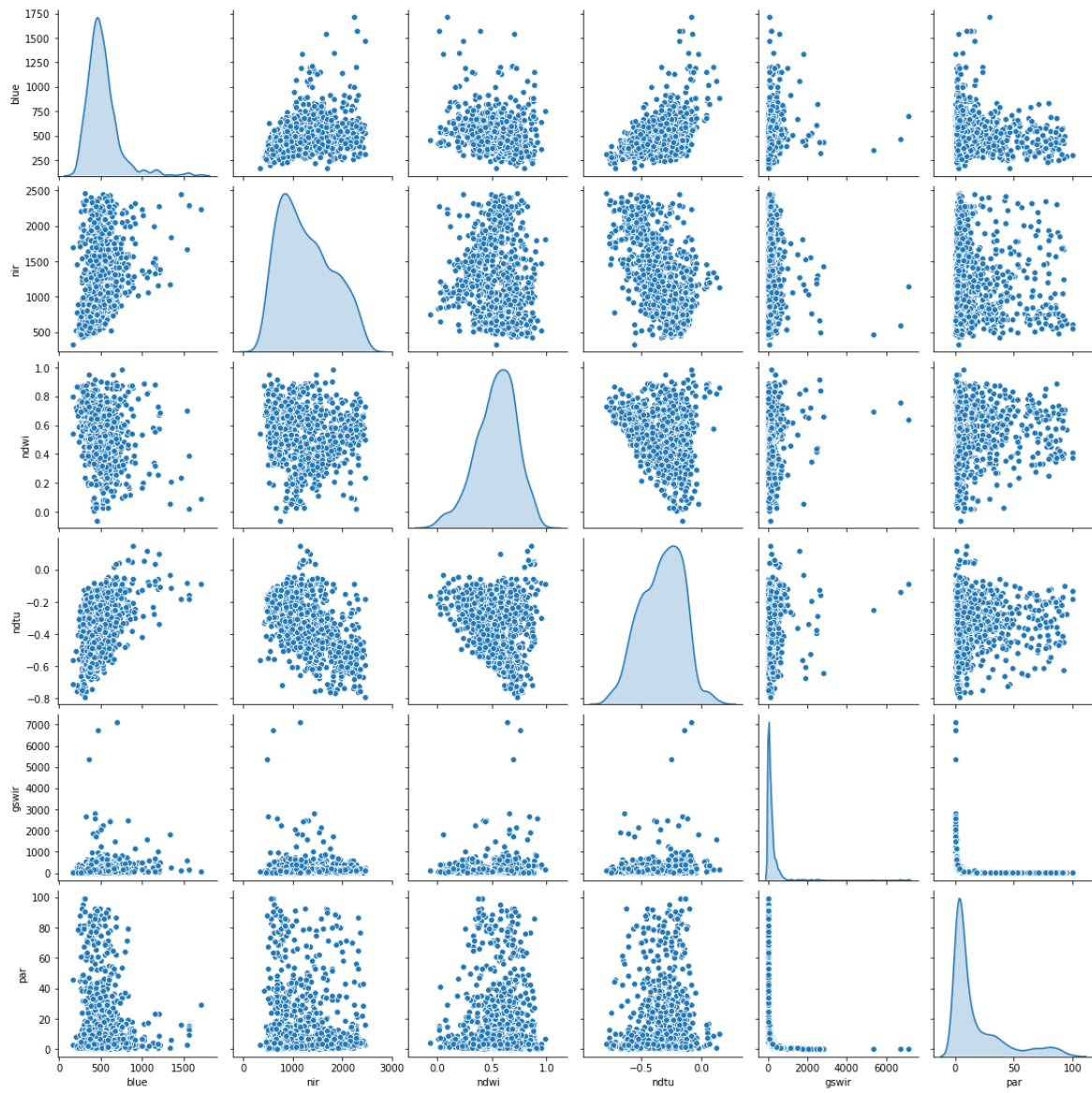
Figure 2A Scater plot for chl-a
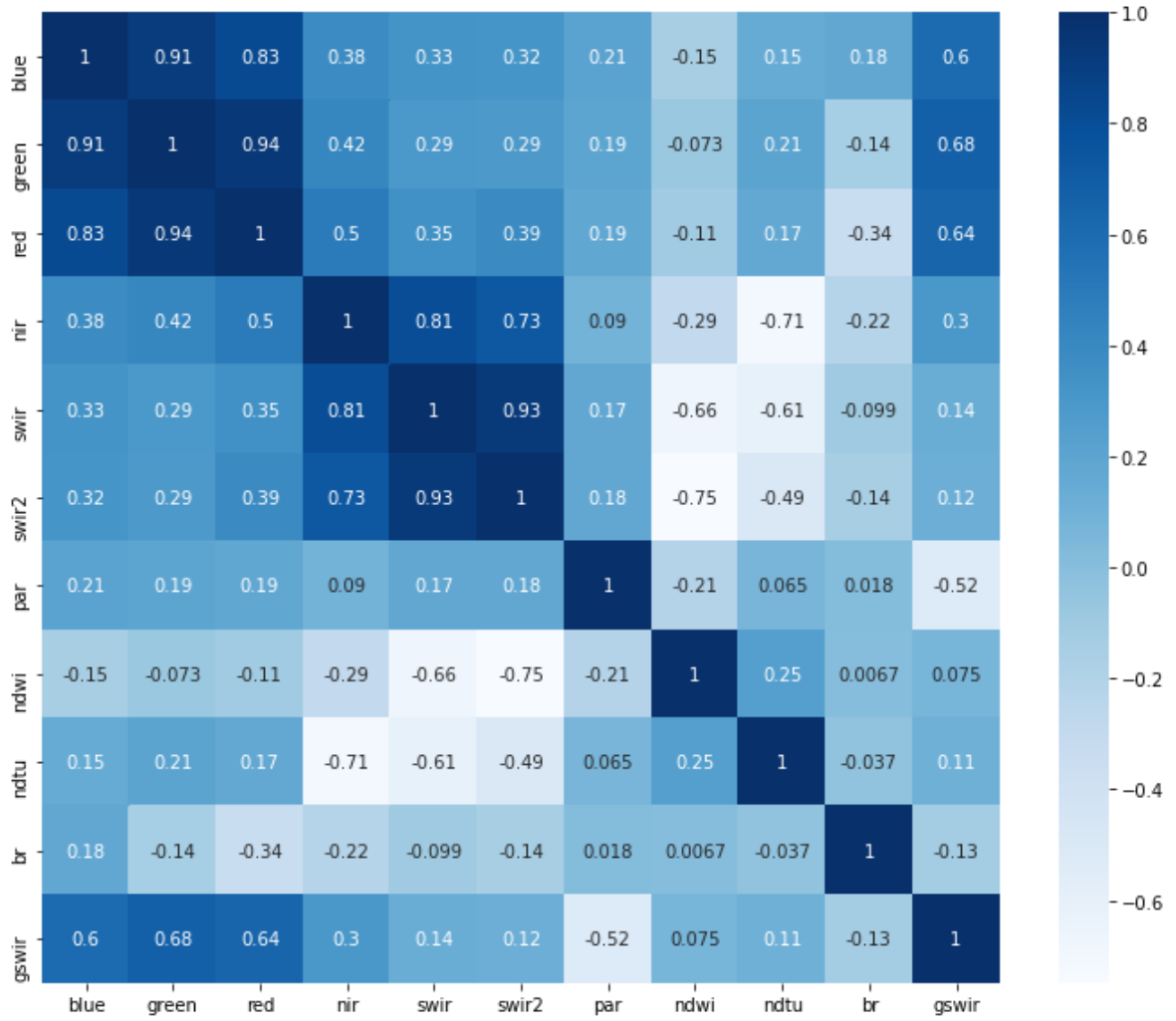
Figure 3A Correlation matrix for DO
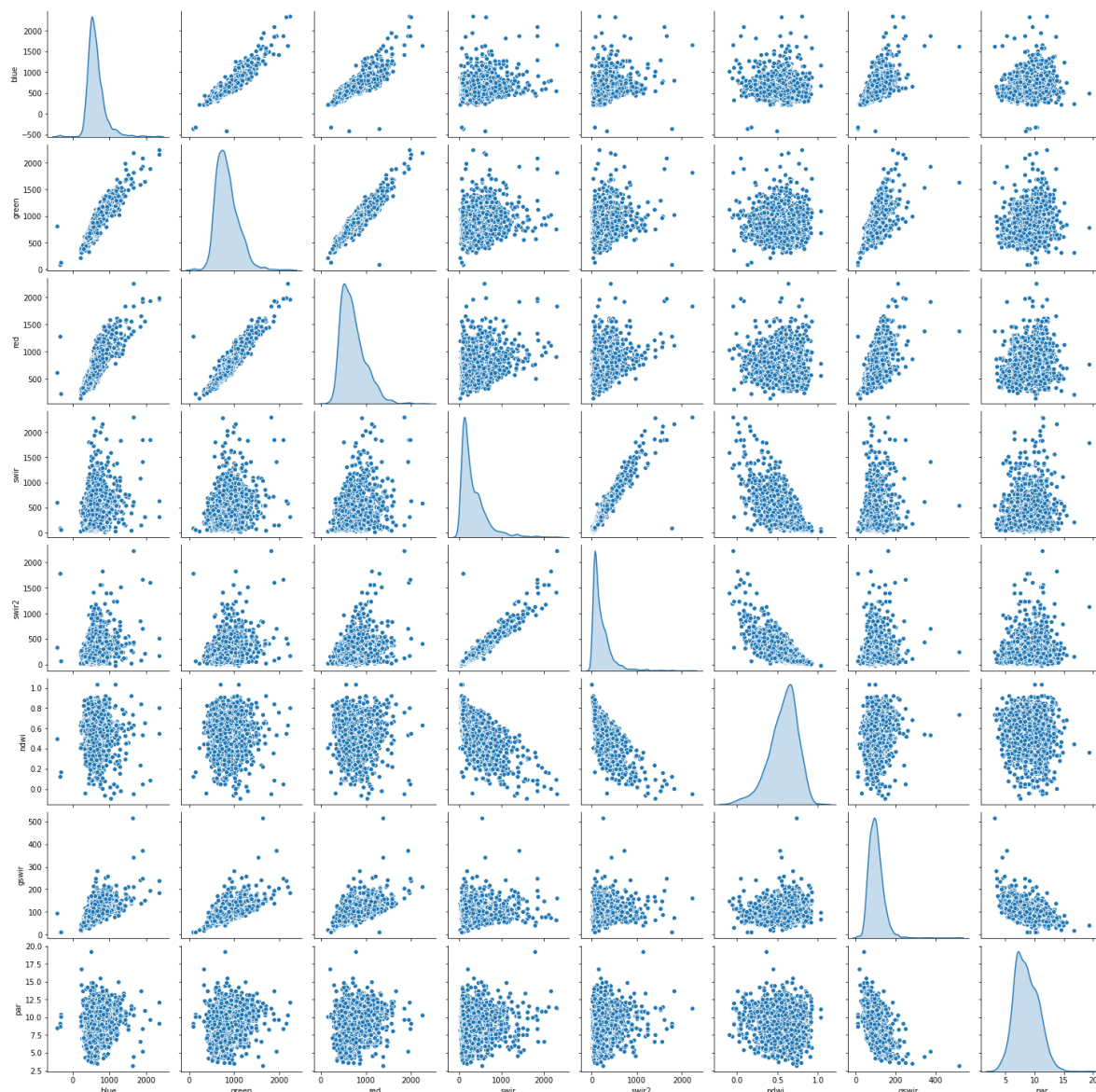
Figure 4A Scater plot for DO
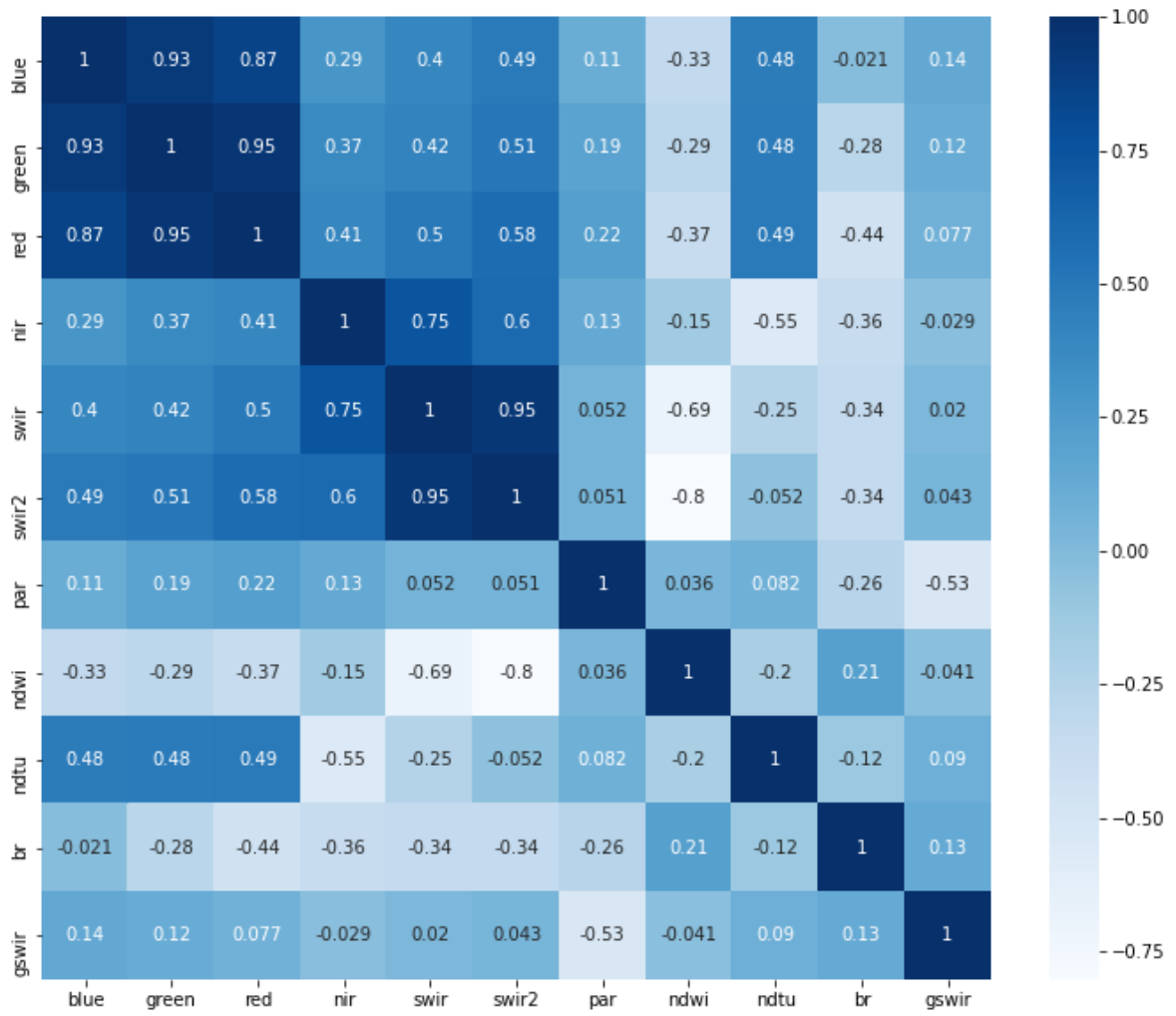
Figure 5A Correlation matrix for SS
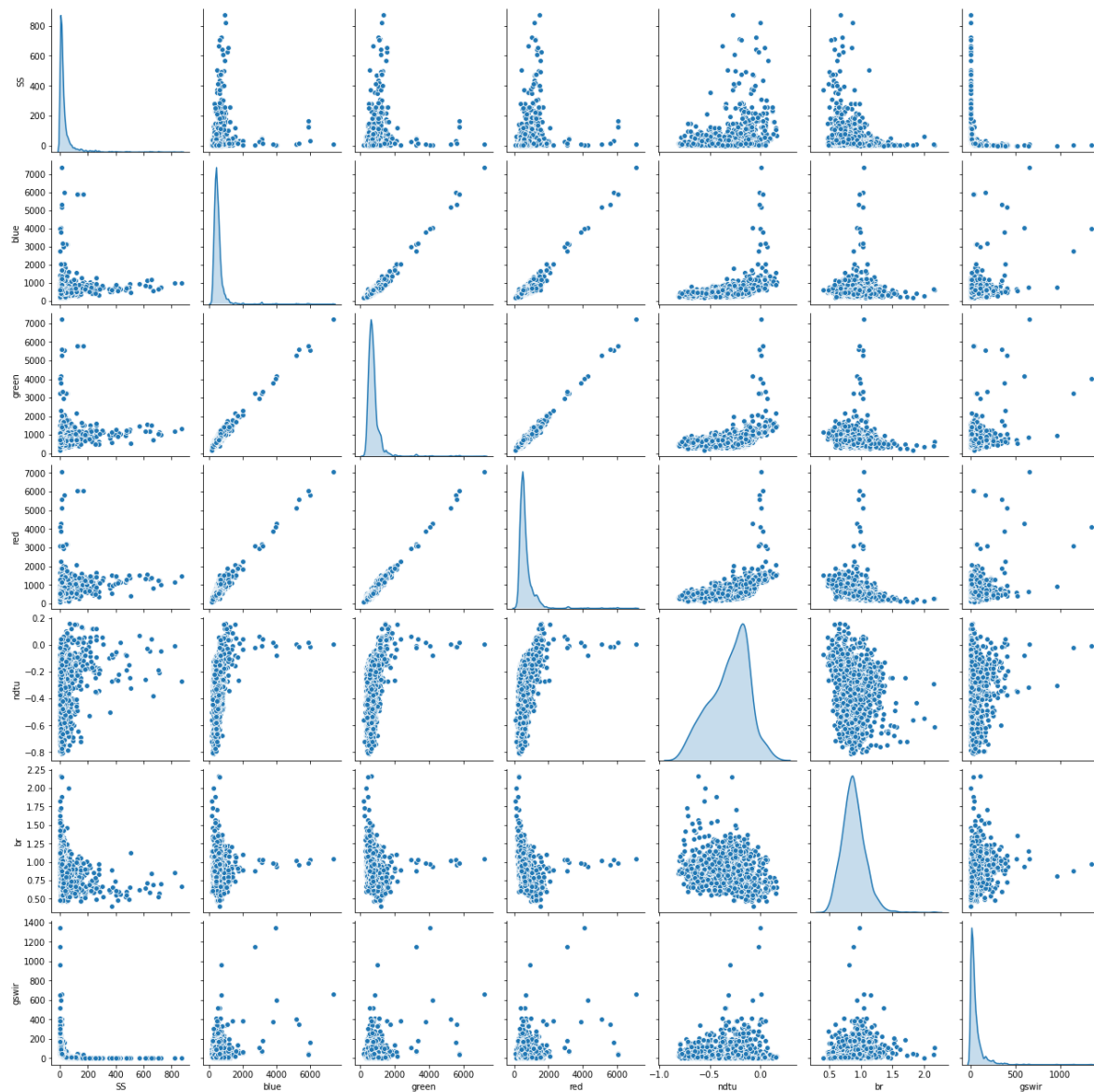
Figure 6A Scater plot for SS
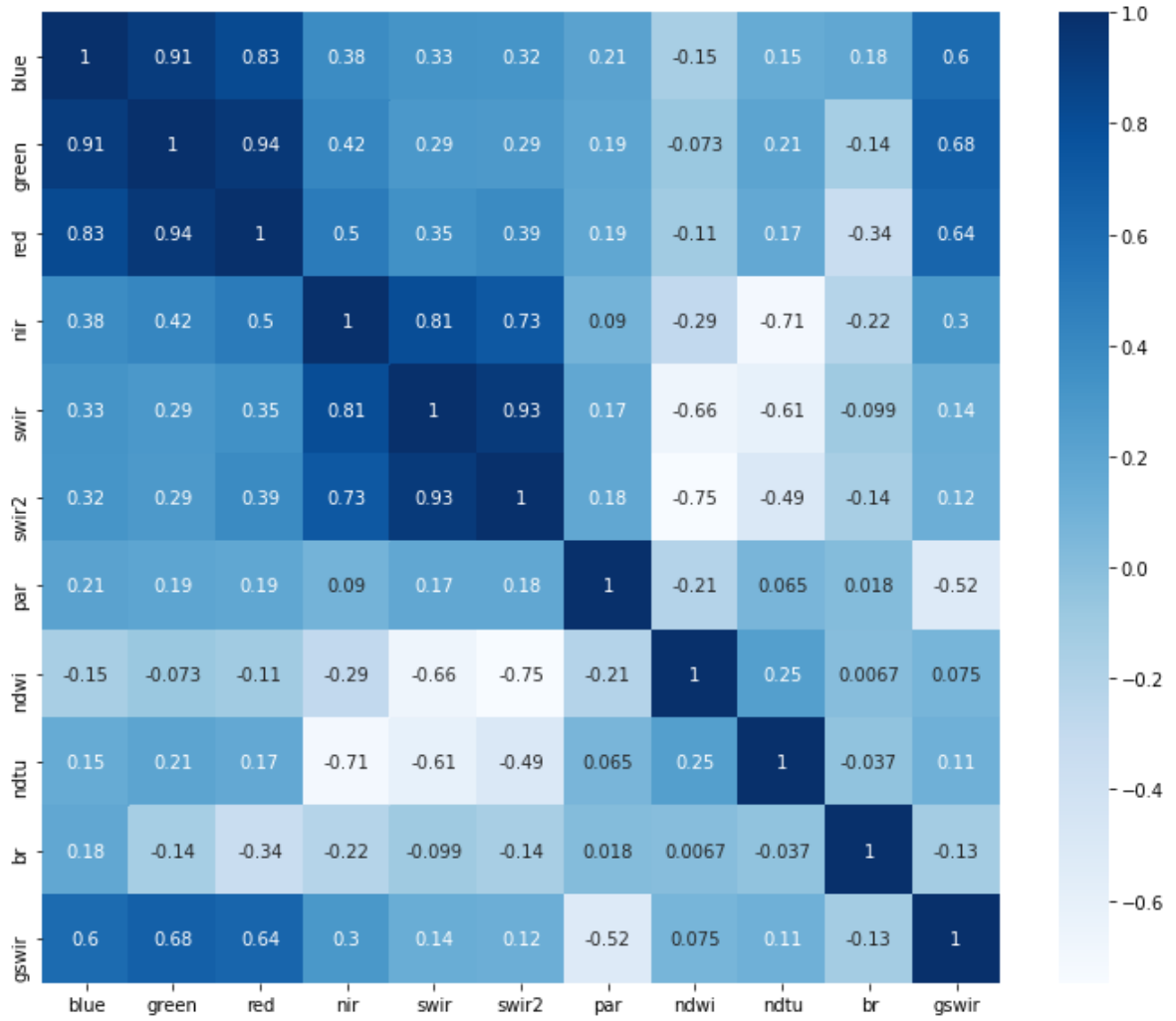
Figure 7A Correlation matrix TN
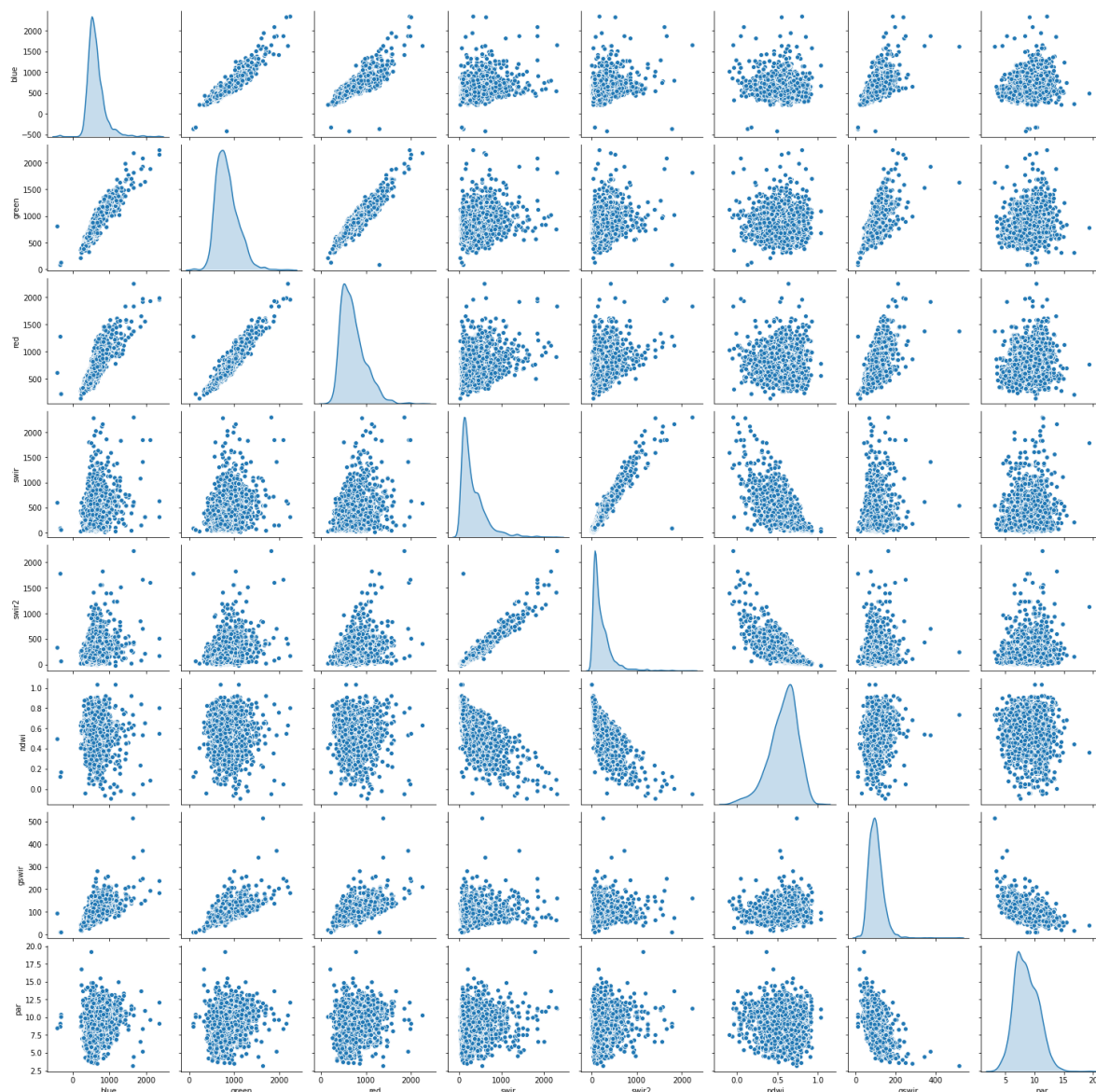
Figure 8A Scater plot TN
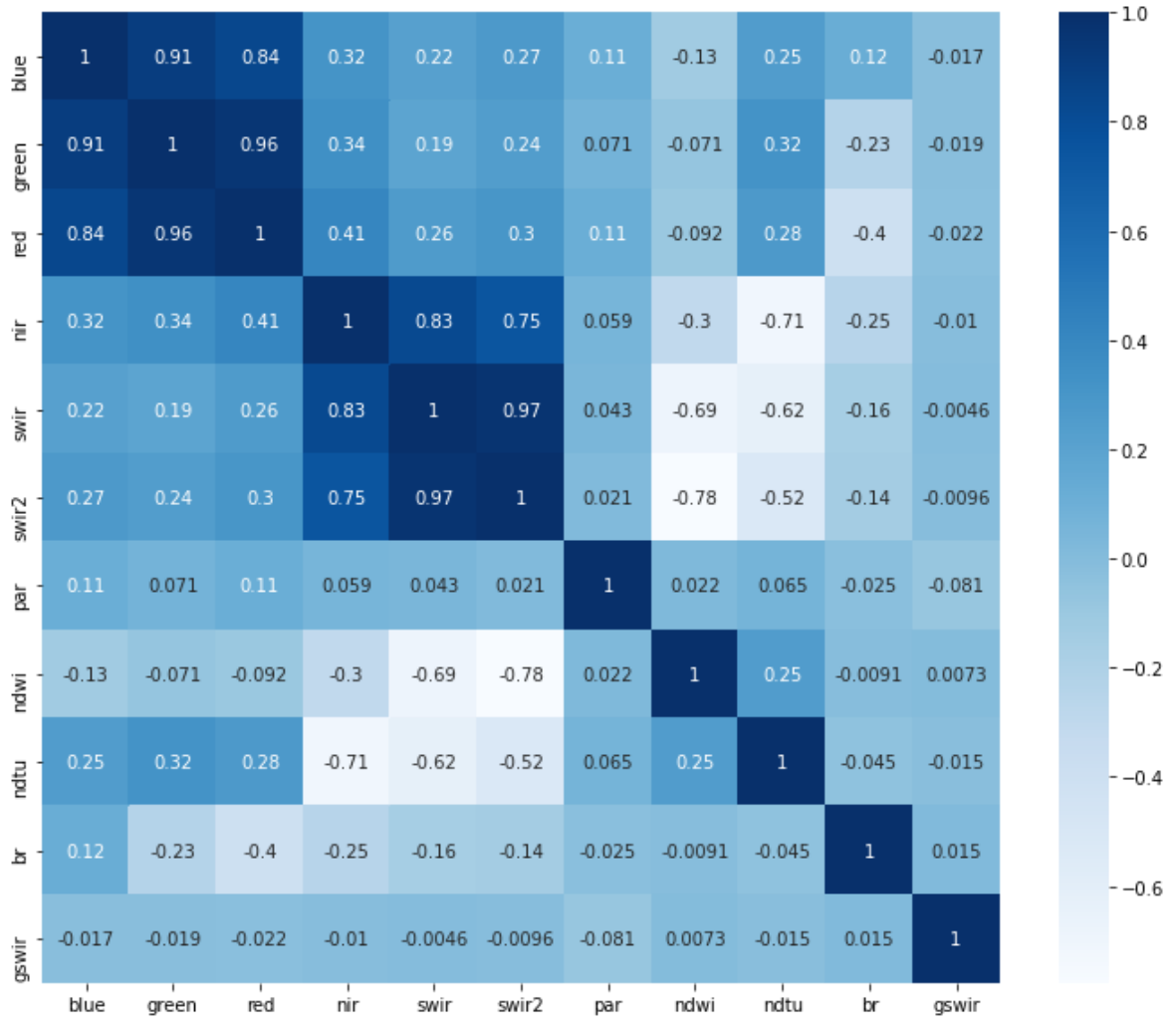
Figure 9A Correaltion matrix for TP
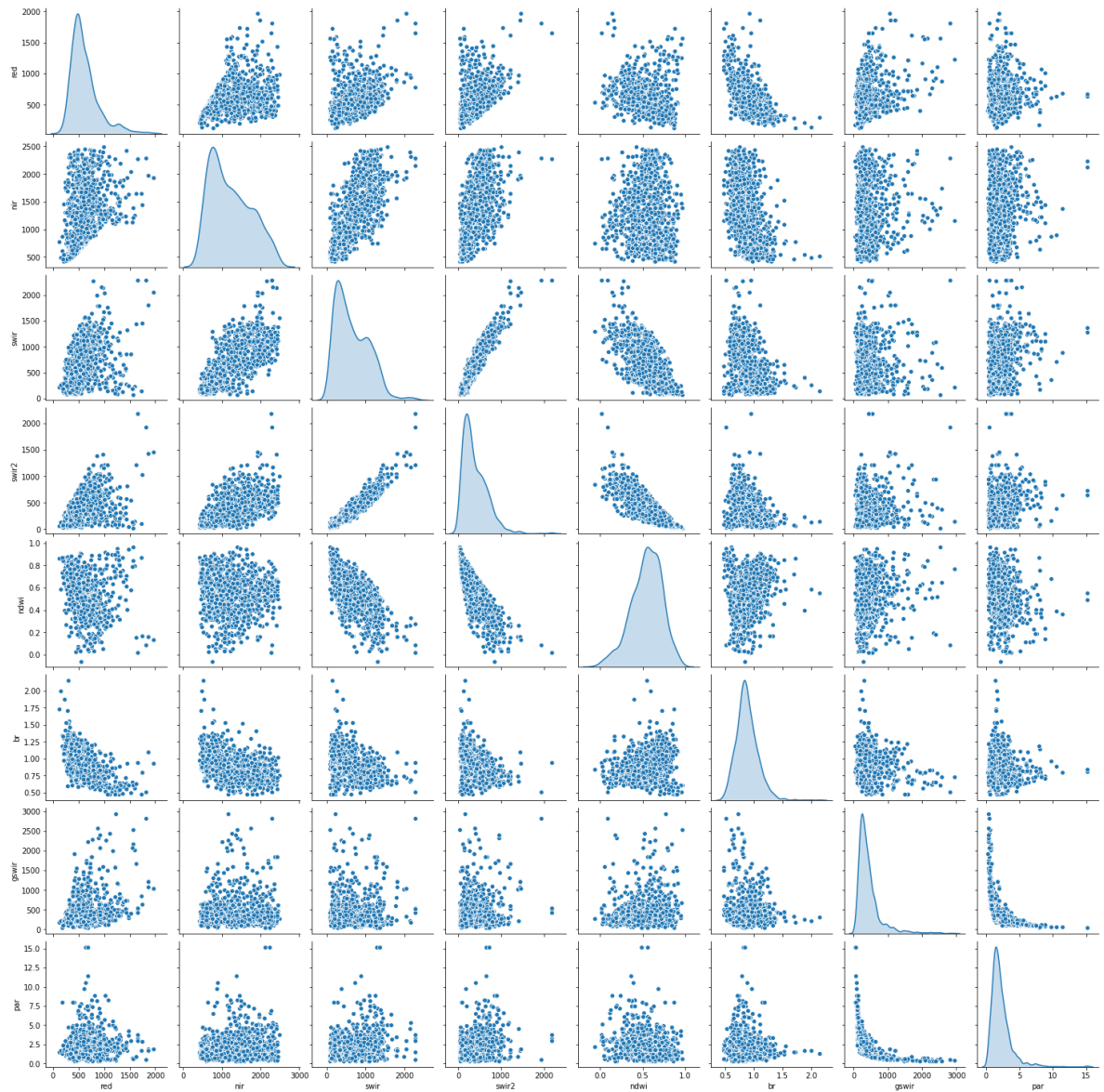
Figure 10A Scater plot for TP

Appendix B
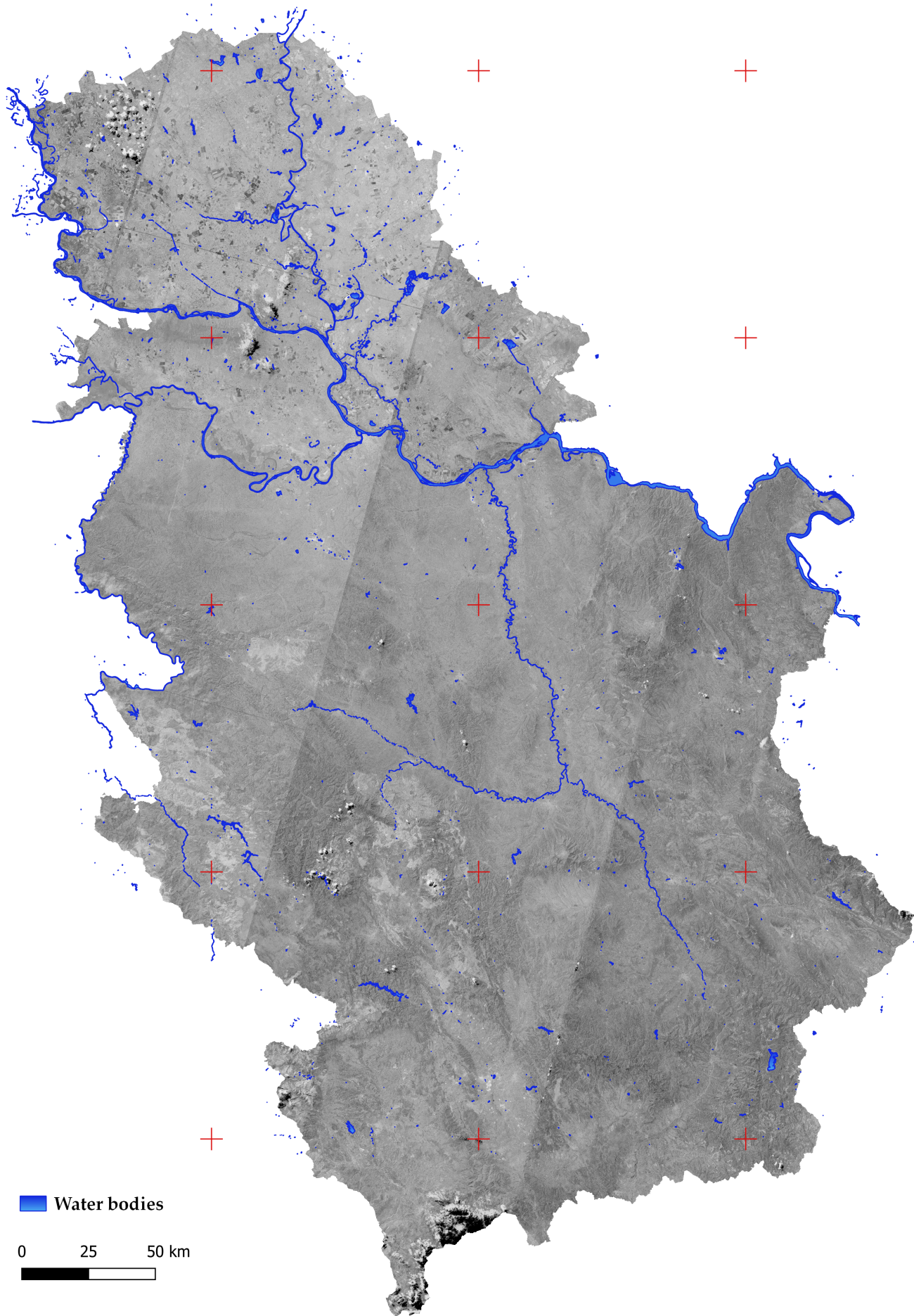
Water bodies in the Republic of Serbia

N

Water bodies

0	25	50 km

Appendix C

Ecological status of water bodies in the Republic of Serbia
-Chl-a-
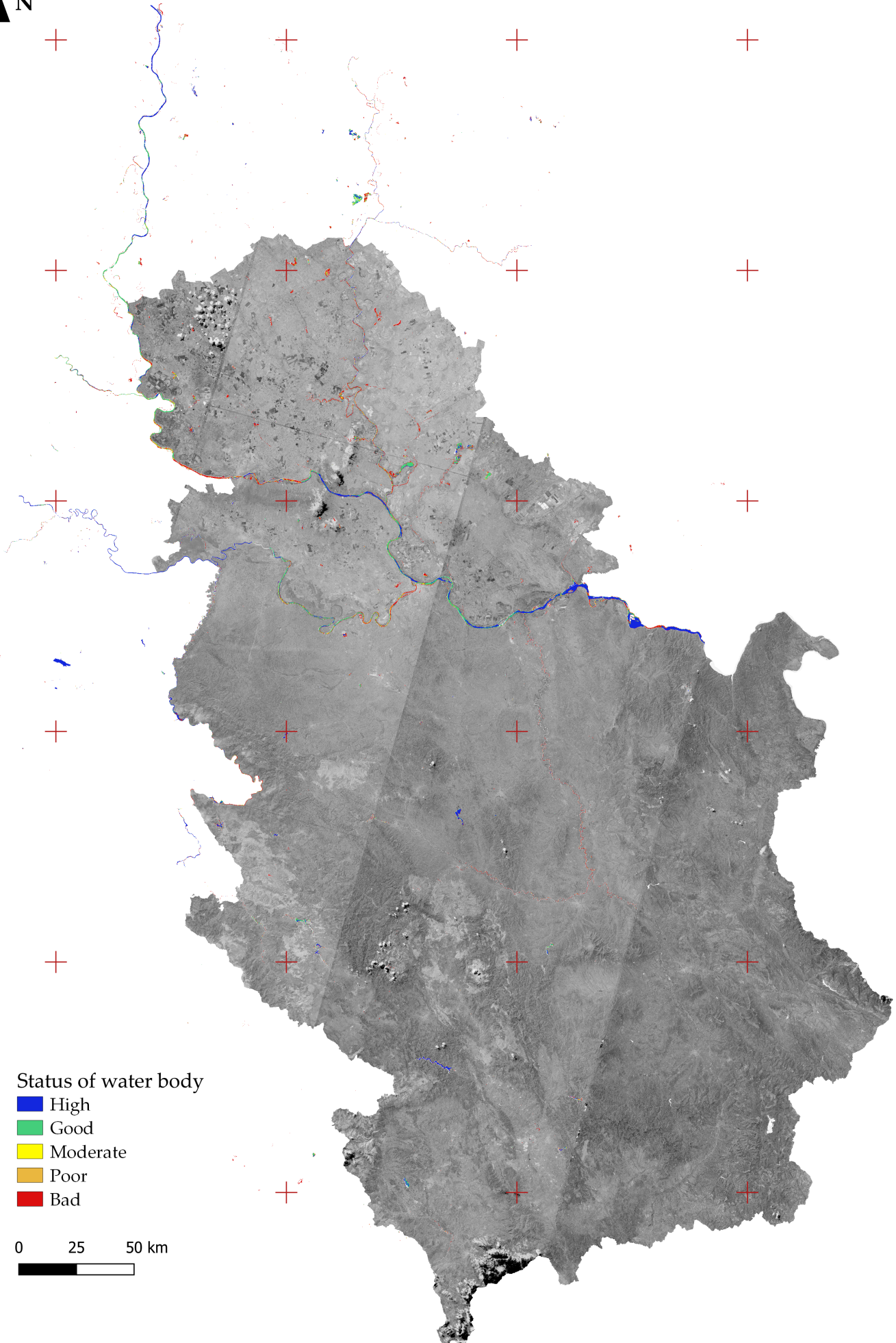
N

Status of water body

- ■ High
- ■ Good
- ■ Moderate
- ■ Poor
- ■ Bad

0   25   50 km

Ecological status of water bodies in the Republic of Serbia
-DO-

Status of water body
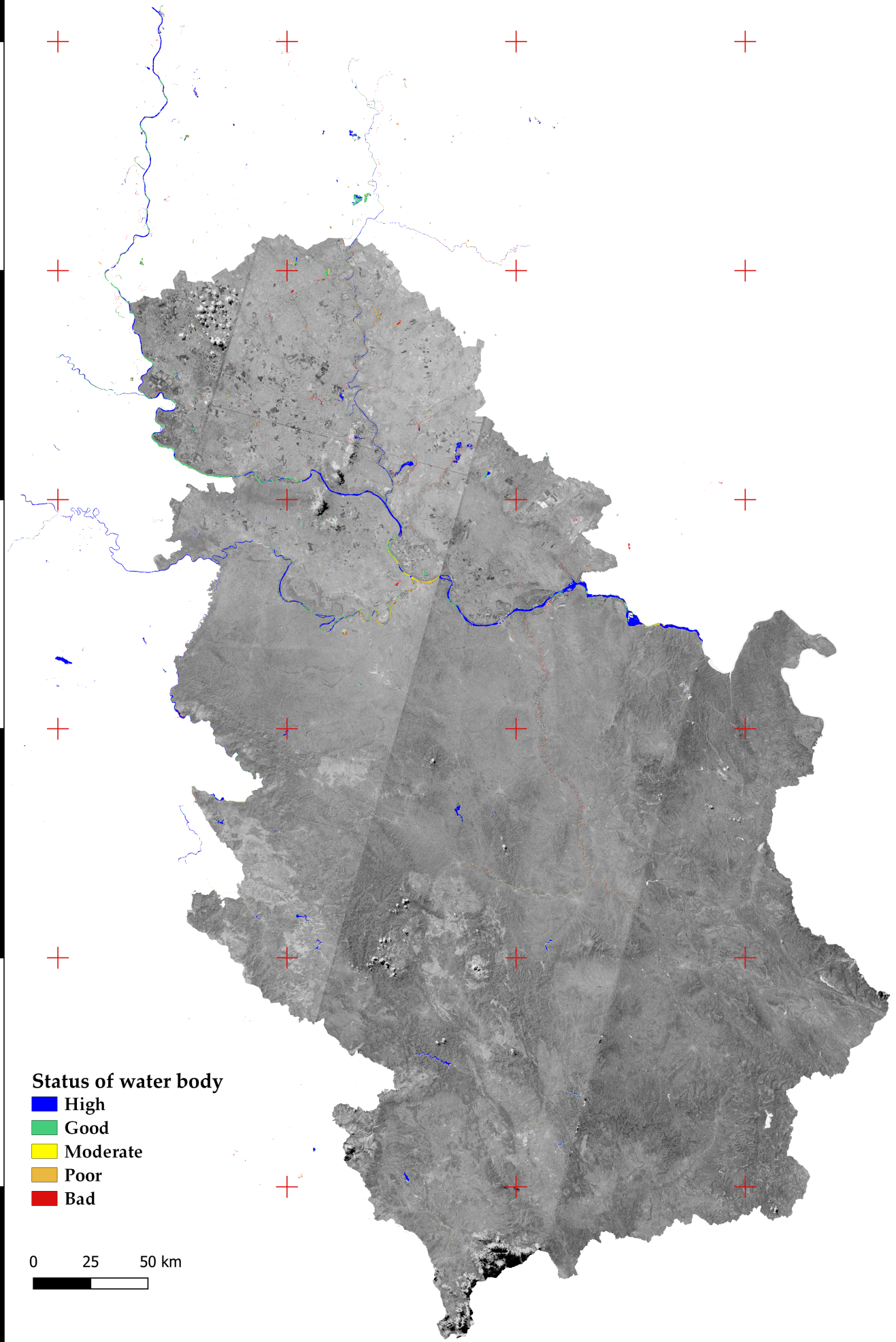
- ▮ High
- ▮ Good
- ▮ Moderate
- ▮ Poor
- ▮ Bad

0   25   50 km

Ecological status of water bodies in the Republic of Serbia
-SS-

N

Status of water body
- High
- Good
- Moderate
- Poor
- Bad

0   25   50 km

Ecological status of water bodies in the Republic of Serbia
-TN-

Status of water body
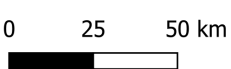- High
- Good
- Moderate
- Poor
- Bad

0   25   50 km

Ecological status of water bodies in the Republic of Serbia
-TP-

N

Status of water body
- High
- Good
- Moderate
- Poor
- Bad

0   25   50 km
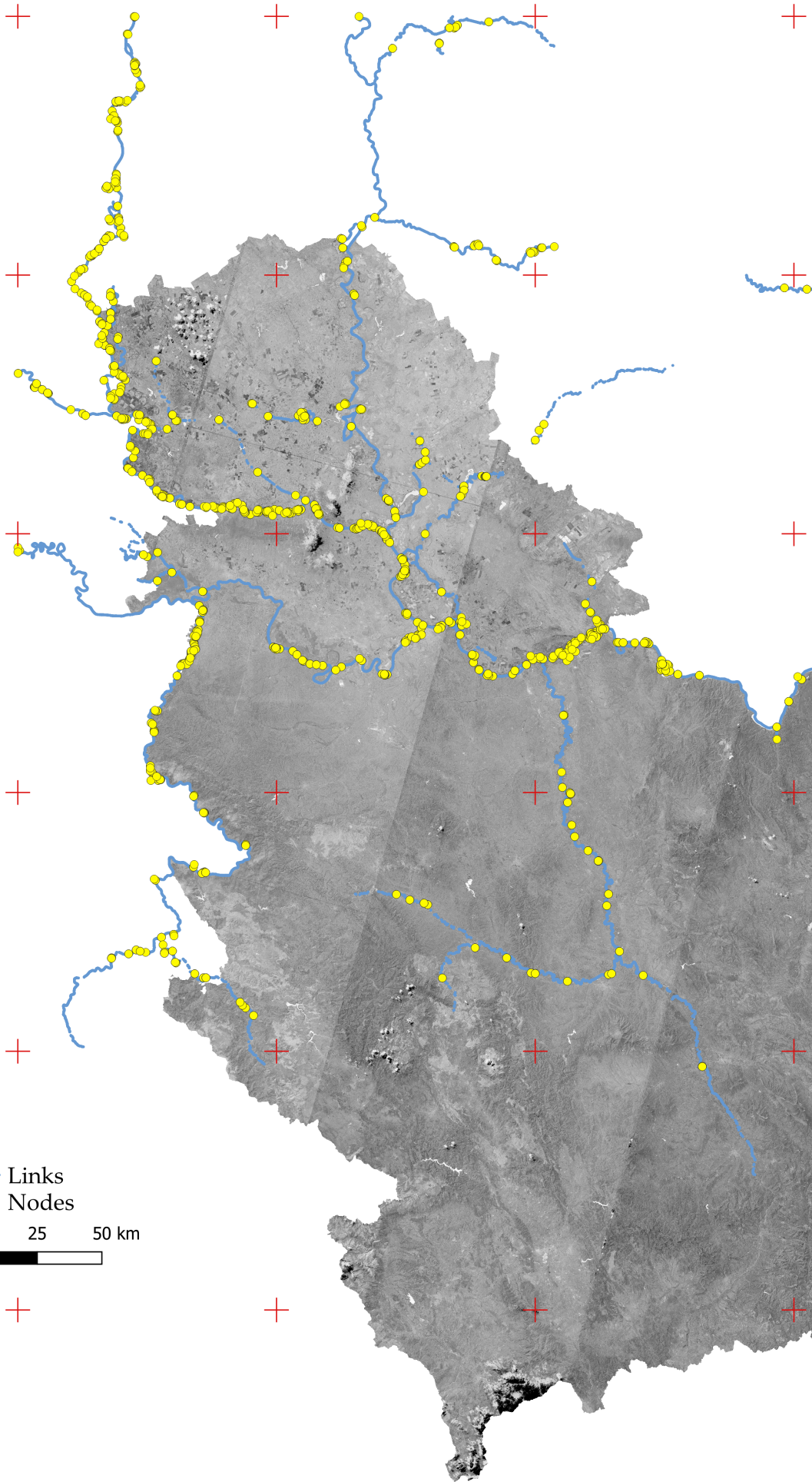
Appendex D

Topology of water bodies in the Republic of Serbia

Links

Nodes

0   25   50 km

Овај Образац чини саставни део докторске дисертације, односно докторског уметничког пројекта који се брани на Универзитету у Новом Саду. Попуњен Образац укоричити иза текста докторске дисертације, односно докторског уметничког пројекта.

План третмана података

Назив пројекта/истраживања
Мултидимензионални модел коришћена података даљинске детекције и геопросторних сервиса у управљању водним ресурсима сагласно INSPIRE и ОДВ специфукацијама Multidimensional model of use remote sensing data and geospatial services in water management according to INSPIRE and WFD specification

Назив институције/институција у оквиру којих се спроводи истраживање
а) Универзитет у Новом Саду, Факултет техничких наука, Департман за рачунарство и аутоматику

Назив програма у оквиру ког се реализује истраживање

1. Опис података

1.1 Врста студије

Укратко описати тип студије у оквиру које се подаци прикупљају

Докторска дисертација
_____

1.2 Врсте података

а) квантитативни

б) квалитативни

1.3. Начин прикупљања података

а) анкете, упитници, тестови

б) клиничке процене, медицински записи, електронски здравствени записи

в) генотипови: навести врсту _____

г) административни подаци: навести врсту ___Резултати испитивања квалитета воде___

д) узорци ткива: навести врсту_____

ђ) снимци, фотографије: навести врсту_____

е) текст, навести врсту_____Литературни извори_____

ж) мапа, навести врсту _____

з) остало: описати ___Сателитски снимци (Сентинел 1, Сентинел 2, Ландсат 8), снимци_____ беспилотном летјелицом, LiDAR подаци_____

1.3 Формат података, употребљене скале, количина података

1.3.1 Употребљени софтвер и формат датотеке:

а) Excel фајл, датотека _____.csv_____

b) SPSS фајл, датотека _____

c) PDF фајл, датотека _____

d) Текст фајл, датотека _____

e) JPG фајл, датотека _____

f) Остало, датотека _____.shp, .geotiff, .las____

1.3.2. Број записа (код квантитативних података)

а) број варијабли _____Велика количина_____

б) број мерења (испитаника, процена, снимака и сл.) ___Велика количина_____

1.3.3. Поновљена мерења

а) да

б) не

Уколико је одговор да, одговорити на следећа питања:

а)   временски размак измедју поновљених мера је _____

б)   варијабле које се више пута мере односе се на _____

в)   нове верзије фајлова који садрже поновљена мерења су именоване као _____

Напомене: _____

   Да ли формати и софтвер омогућавају дељење и дугорочну валидност података?

a) *Да*

б) *Не*

Ако је одговор не, образложити _____

_____

2. Прикупљање података

2.1 Методологија за прикупљање/генерисање података

2.1.1. У оквиру ког истраживачког нацрта су подаци прикупљени?

а) експеримент, навести тип _____ фотограметријски премјер беспилотом летјелицом _____

б) корелационо истраживање, навести тип _____

ц) анализа текста, навести тип _____

д) остало, навести шта _____

2.1.2 Навести врсте мерних инструмената или стандарде података специфичних за одређену научну дисциплину (ако постоје).

_____ Беспилотна летјелица DJI Mavic Pro _____

2.2 Квалитет података и стандарди

2.2.1. Третман недостајућих података

а) Да ли матрица садржи недостајуће податке? Да **Не**

Ако је одговор да, одговорити на следећа питања:

а)   Колики је број недостајућих података? _____

б)   Да ли се кориснику матрице препоручује замена недостајућих података? Да   Не

в)   Ако је одговор да, навести сугестије за третман замене недостајућих података

_____

2.2.2. На који начин је контролисан квалитет података? Описати

Квалитет података је контролисан при премјеру и обради прикупљених података у складу са стандардима у овој области.

2.2.3. На који начин је извршена контрола уноса података у матрицу?

Контрола уноса података у матрицу је изведена поређењем добијених података са литературним подацима.

3. Третман података и пратећа документација

3.1. Третман и чување података

3.1.1. Подаци ће бити депоновани у Репозиторијуму докторских дисертација на Универзитету у Новом Саду.

3.1.2. URL адреса _____ https://cris.uns.ac.rs/searchDissertations.jsf _____

3.1.3. DOI _____

3.1.4. Да ли ће подаци бити у отвореном приступу?

а) **Да**

б) *Да, али после ембарга који ће трајати до _____*

в) *Не*

Ако је одговор не, навести разлог _____

3.1.5. Подаци неће бити депоновани у репозиторијум, али ће бити чувани.

Образложење

_____

_____

3.2 Метаподаци и документација података

3.2.1. Који стандард за метаподатке ће бити примењен? _____

3.2.1. Навести метаподатке на основу којих су подаци депоновани у репозиторијум.

_____

_____

Ако је потребно, навести методе које се користе за преузимање података, аналитичке и процедуралне информације, њихово кодирање, детаљне описе варијабли, записа итд.

_____

_____

_____

_____

3.3 Стратегија и стандарди за чување података

3.3.1. До ког периода ће подаци бити чувани у репозиторијуму? _____

3.3.2. Да ли ће подаци бити депоновани под шифром? **Да**   Не

3.3.3. Да ли ће шифра бити доступна одређеном кругу истраживача? **Да**   Не

3.3.4. Да ли се подаци морају уклонити из отвореног приступа после извесног времена?

Да   **Не**

Образложити

_____

_____

4. Безбедност података и заштита поверљивих информација

Овај одељак МОРА бити попуњен ако ваши подаци укључују личне податке који се односе на учеснике у истраживању. За друга истраживања треба такође размотрити заштиту и сигурност података.

4.1 Формални стандарди за сигурност информација/података

Истраживачи који спроводе испитивања с људима морају да се придржавају Закона о заштити података о личности (*https://www.paragraf.rs/propisi/zakon_o_zastiti_podataka_o_licnosti.html*) и одговарајућег институционалног кодекса о академском интегритету.

4.1.2. Да ли је истраживање одобрено од стране етичке комисије? Да **Не**

Ако је одговор Да, навести датум и назив етичке комисије која је одобрила истраживање

_____

4.1.2. Да ли подаци укључују личне податке учесника у истраживању? Да **Не**

Ако је одговор да, наведите на који начин сте осигурали поверљивост и сигурност информација везаних за испитанике:

а)   Подаци нису у отвореном приступу

б)   Подаци су анонимизирани

ц)   Остало, навести шта

_____

_____

5. Доступност података

5.1. Подаци ће бити

а) јавно доступни

б) доступни само уском кругу истраживача у одређеној научној области

ц) затворени

Ако су подаци доступни само уском кругу истраживача, навести под којим условима могу да их користе:

_____

_____

Ако су подаци доступни само уском кругу истраживача, навести на који начин могу приступити подацима:

_____

_____

5.4. Навести лиценцу под којом ће прикупљени подаци бити архивирани.

_____

6. Улоге и одговорност

6.1. Навести име и презиме и мејл адресу власника (аутора) података

Гордана Јаковљевић gordana.jakovljevic@aggf.unibl.org _____

6.2. Навести име и презиме и мејл адресу особе која одржава матрицу с подацима

Гордана Јаковљевић gordana.jakovljevic@aggf.unibl.org

6.3. Навести име и презиме и мејл адресу особе која омогућује приступ подацима другим истраживачима

Гордана Јаковљевић gordana.jakovljevic@aggf.unibl.org